13 November 2009 $10

Science

IBEX
and the heliosphere's boundary

AAAS

Don't Take the Bait!

The herring off our shores are a vital food source for other fish and also for millions of birds and marine mammals. But industrial herring trawlers in New England now are urging the National Marine Fisheries Service to ignore the legal requirement to follow the advice of its science advisors, who recently recommended a reduction in the herring catch limit. Ignoring this advice would set a terrible precedent.

Message to NMFS: Base herring catch limits on the best available science, not industry pressure. It's not just a good idea, it's the law.

PewEnvironment.org/herring

THE PEW ENVIRONMENT GROUP

GE Healthcare
Life Sciences

Inspired Ägain

Who better to draw inspiration for the new ÄKTA™ avant system than from customers using the 30,000 ÄKTA systems already in use around the world? Well, you spoke and we listened. The new ÄKTA avant system for process development is faster — enabling quicker insights. It minimizes the chance of error, even while working at higher speeds. And it allows for direct, reliable scalability. At GE Healthcare, our focus is on helping scientists achieve even more, faster. It's a commitment we have in our genes. And all this is backed by the service, support, and investment in the future that being part of GE can bring.

Want to know more? Why not talk with us today. Visit **www.gelifesciences.com/aktaavant**

I **ÄKTA** I Amersham I Biacore I IN Cell Analyzer I Whatman I GE Service I

The New ÄKTA avant

imagination at work

First published September 2009
GE Healthcare Bio-Sciences AB, Björkgatan 30, 751 84 Uppsala, Sweden
GE12-09

EDITORIAL

NEWS OF THE WEEK

NEWS FOCUS

LETTERS

BOOKS ET AL.

POLICY FORUMS

PERSPECTIVES

VIEWPOINT

BREVIA

CONTENTS continued >>

page 926

page 938

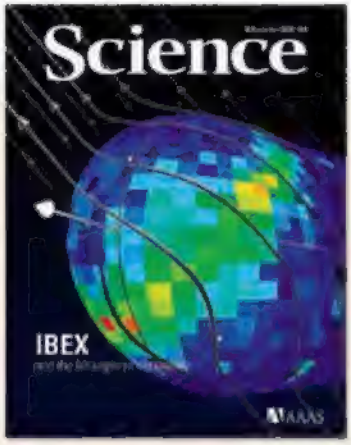

COVER

The Interstellar Boundary Explorer (IBEX) spacecraft has returned the first global images of the interaction of our heliosphere with the local interstellar medium. IBEX observations show a ribbon of energetic neutral atoms (reds to greens), snaking between the positions of the two Voyager spacecraft (white dots). This ribbon marks the region where the galactic magnetic field (gray lines) wraps most tightly around the heliosphere's boundary. See the series of Reports starting on page 959.

Image: Patrick McPike/Adler Planetarium

DEPARTMENTS

Analyzing genetic differences

Genotyping sample and assay technologies by QIAGEN

Rely on trusted automated and manual workflow solutions for:

- **Sample collection and stabilization**
- **Genomic DNA purification, DNA storage, and whole genome amplification**
- **PCR amplification and automated QIAxcel® fragment analysis**
- **HRM® and Pyrosequencing® detection**

Making improvements in life possible — www.qiagen.com

QIAGEN®

Sample & Assay Technologies

RESEARCH ARTICLE

REPORTS

CONTENTS continued >>

pages 942 & 980

page 954

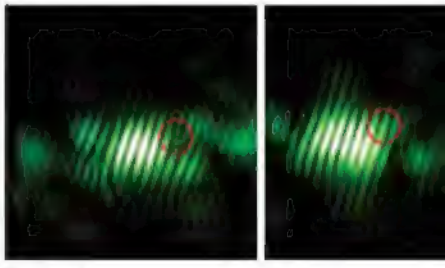

page 974

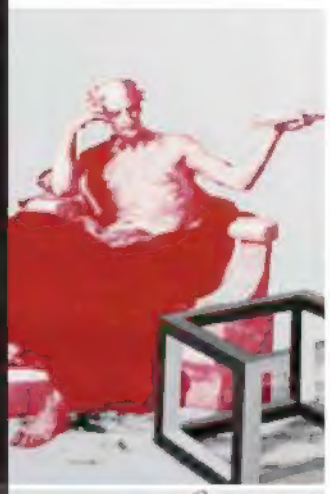

Dedication to Science
How is the light wavelength of knowledge calculated? Leica Microsystems has mapped its corporate values.
For more information, visit our website.

Professor Tanke, why is curiosity a building block of life?

Hans Tanke, a researcher and pioneer of digital fluorescence microscopy, is driven by passionate curiosity. He is Head of the Department of Molecular Cell Biology at Leiden University Medical Center, Netherlands, where he gives young scientists creative freedom: this enables them to develop the ethically responsible dedication with which he himself keeps tracking down the building blocks of life.

www.leica-microsystems.com

Living up to Life

Leica
MICROSYSTEMS

SCIENCEONLINE

SCIENCEXPRESS
www.sciencexpress.org

Real-Time Observation of Carbonic Acid Formation in Aqueous Solution
K. Adamczyk et al.

The use of a photoacid enables the long-sought characterization of the conjugate acid of bicarbonate.
10.1126/science.1180060

Two White Dwarfs with Oxygen-Rich Atmospheres
B. T. Gänsicke et al.

Two white dwarfs may have evolved from intermediate-mass stars that avoided exploding as supernovae.
10.1126/science.1180228

Structure of an RNA Polymerase II–TFIIB Complex and the Transcription Initiation Mechanism
X. Liu et al.

X-ray structures provide more details on the initiation of transcription.
10.1126/science.1182015

The Fanconi Anemia Pathway Promotes Replication-Dependent DNA Interstrand Cross-Link Repair
P. Knipscheer et al.

Insertion of a nucleotide during the repair of a complex lesion in DNA requires tagging of a lysine residue.
10.1126/science.1182372

Reproducibility Distinguishes Conscious from Nonconscious Neural Representations
A. Schurger et al.

Analysis of functional magnetic resonance imaging data reveals that neural activation patterns are more reproducible for seen versus unseen objects.
10.1126/science.1180029

SCIENCENOW
www.sciencenow.org
Highlights From Our Daily News Coverage

Arthritis on the Move

Scientists have pinpointed how rheumatoid arthritis spreads inside the body.

Chocolate Cake: The New Heroin?

Yo-yo diets may lead to food addiction.

Experts Criticize Nanoparticle Study

A paper that hints at dangers of nanoscopic particles has no relevance to human disease, they say.

SCIENCESIGNALING
www.sciencesignaling.org
The Signal Transduction Knowledge Environment

EDITORIAL GUIDE: Focus Issue—Coping with Cellular Stress
W. Wong

Cells use diverse signaling pathways to sense and respond to stress.

PERSPECTIVE: Aiming Straight for the Heart—Prolyl Hydroxylases Set the BAR
J. A. Garcia et al.

β2-adrenergic receptor density is regulated by oxygen availability.

PERSPECTIVE: A New Mechanism of Phosphoregulation in Signal Transduction Pathways
K. Jung and H. Jung

A protein kinase phosphorylates arginine residues in a transcriptional factor during the bacterial heat shock response.

PERSPECTIVE: A Gluconeogenic Tryst in the Nucleus, with ER Stress as the Third Wheel
D. T. Rutkowski

A transcriptional co-regulator links gluconeogenesis and ER stress responses in the liver.

PERSPECTIVE: FBXO31—A New Player in the Ever-Expanding DNA Damage Response Orchestra
Y. Shiloh et al.

FBXO31 is a damage-induced checkpoint protein that enhances cyclin D1 degradation in response to genotoxic stress.

PERSPECTIVE: Nutrition-Minded Cell Cycle
K. Shiozaki

Cross talk between TOR and MAPK signaling pathways determines mitotic onset in fission yeast during nutrition stress.

RESEARCH ARTICLE: H_2S Signals Through Protein S-Sulfhydration
A. K. Mustafa et al.

PODCAST
S. H. Snyder and A. M. VanHook

The gasotransmitter hydrogen sulfide signals by sulfhydrating target proteins.

SCIENCECAREERS
www.sciencecareers.org/career_magazine
Free Career Resources for Scientists

A Recipe for Collaboration
L. Chiu

An unlikely collaboration resulted in a new technique for measuring hormone levels.

Taken for Granted: Shocked, Shocked! to Find Disappointment on Campus
B. L. Benderly

A new book takes a revealing look at careers in academic science.

A Scientist Finds a Niche
S. Gaidos

Dean Pearson overcame a slow start and made a difference by observing ecological communities.

SCIENCETRANSLATIONAL MEDICINE
www.sciencetranslationalmedicine.org
Integrating Medicine and Science

PERSPECTIVE: Regulatory Considerations for Translating Gene Therapy—A European Union Perspective
M. C. Galli

Hypertrophy triggers discussions on the translational challenges of gene therapy.

RESEARCH ARTICLE: Follistatin Gene Delivery Enhances Muscle Growth and Strength in Nonhuman Primates
J. Kota et al.

Gene therapy in monkeys shows promise for muscle-wasting diseases.

RESEARCH ARTICLE: The Effect of Diet on the Human Gut Microbiome—A Metagenomic Analysis in Humanized Gnotobiotic Mice
P. J. Turnbaugh et al.

PERSPECTIVE: Gut Check—Testing a Role for the Intestinal Microbiome in Human Obesity
J. S. Flier and J. J. Mekalanos

The gut microbiome contributes to human metabolic disease and may yield new targets for preventative treatments.

SCIENCEPODCAST
www.sciencemag.org/multimedia/podcast
Free Weekly Show

Download the 13 November *Science* Podcast to hear about climate change predictions, creating hermaphroditic worms, and more.

ORIGINSBLOG
blogs.sciencemag.org/origins
A History of Beginnings

SCIENCEINSIDER
blogs.sciencemag.org/scienceinsider
Science Policy News and Analysis

SCIENCE (ISSN 0036-8075) is published weekly on Friday, except the last week in December, by the American Association for the Advancement of Science, 1200 New York Avenue, NW, Washington, DC 20005. Periodicals Mail postage (publication No. 484460) paid at Washington, DC, and additional mailing offices. Domestic individual membership and subscription (51 issues): $146 ($74 allocated to subscription). Domestic institutional subscription (51 issues): $835; Foreign postage extra: Mexico, Caribbean (surface mail) $55; other countries (air assist delivery) $85. First class, airmail, student, and emeritus rates on request. Canadian rates with GST available upon request, GST #1254 88122. Publications Mail Agreement Number 1069624. **Printed in the U.S.A.**

Change of address: Allow 4 weeks, giving old and new addresses and 8-digit account number. **Postmaster:** Send change of address to AAAS, P.O. Box 96178, Washington, DC 20090–6178. **Single-copy sales:** $10.00 current issue, $15.00 back issue prepaid includes surface postage; bulk rates on request. **Authorization to photocopy** material for internal or personal use under circumstances not falling within the fair use provisions of the Copyright Act is granted by AAAS to libraries and other users registered with the Copyright Clearance Center (CCC) Transactional Reporting Service, provided that $20.00 per article is paid directly to CCC, 222 Rosewood Drive, Danvers, MA 01923. The identification code for *Science* is 0036-8075. *Science* is indexed in the *Reader's Guide to Periodical Literature* and in several specialized indexes.

AAAS
ADVANCING SCIENCE, SERVING SOCIETY

You can deliver. We can help.

Invitrogen transfection solutions

"First and foremost, it works; second, it's convenient; and third, it's just a great machine."
– Dana Yoo
Osiris Therapeutics, Inc.

Invitrogen can help you deliver DNA or siRNA into virtually any cell type. In fact, the Neon™ Transfection System—our next-generation electroporation device—can successfully transfect even the most difficult-to-transfect primary and stem cells.

- Achieve 90% transfection efficiency and more than 80% viability in many mammalian cells
- Transfect DNA or siRNA into as few as 20,000 cells
- Benefit from exceptional value—a fast and simple workflow at half the initial purchase price compared to similar electroporation devices

Visit **www.invitrogen.com/neon4me** for details and to request a demonstration.

invitrogen

EDITED BY CAROLINE ASH

Sexual Blotch

Sexual conflicts may provide selection pressures that facilitate invasion of new genetic sex determiners. **Roberts *et al.*** (p. 998, published online 1 October) describe data obtained from several species of sexually dimorphic cichlid fishes found in Lake Malawi that support this model. An orange-blotch color pattern has evolved among the females of rock-dwelling species because it provides effective camouflage against the algae-coated rocks. Blotched males (OB) are rare, possibly because the trait interferes with the normal male color pattern of blue stripes that are important cues for mate selection. The pigmentation pattern that creates this conflict between natural selection in females and sexual selection in males is caused by mutation in the *cis*-regulatory region of the *Pax7* gene and is tightly linked to a dominant female sex determiner. When bred in the lab, the OB males inherit the intact maternal OB haplotype and their OB-carrying chromosome determines female sex in the offspring; the males seem to be sex-reversed by another mechanism.

Quantum Division

The notion of quantum mechanics is that variables are expressed as integer values. In quantum fluids, for instance, vortices are quantized in terms of the polarization and phase shifts observed as multiples of 2π, that is, full rotations of each variable around the vortex core. Theoretical work has predicted that in some instances there should be half-quantum vortices, where circumventing the vortex core is characterized by just π rotations of the phase and polarization. By observing exciton-polariton condensates **Lagoudakis *et al.*** (p. 974) present evidence for the existence of these long-predicted half-quantum vortices.

CREDITS (TOP TO BOTTOM): AD KONINGS, CHAUDHRY *ET AL.*, VAN DEN BROEKE *ET AL.*

Biffed into Shape

$BiFeO_3$ is known to have a very large ferroelectric polarization. Although the bulk ground state is rhombohedral (with the electrical polarization along the [111] direction), in thin films and under epitaxial strain, the material can be tetragonally distorted (polarization along [001]). **Zeches *et al.*** (p. 977) show that under compressive strain, these films are monoclinic, a phase that is highly stable because it comprises the same symmetry as the monoclinic phase which has been reported at the so-called morphotropic phase boundaries in technologically important ferroelectrics. This work offers the possibility of obtaining large piezoelectric responses in lead-free systems.

GRACE and Movement Together

Recent measurements of the rate of mass loss from the Greenland ice sheet vary approximately by a factor of three. Resolving these discrepancies is essential for determining the current mass balance of the ice sheet and to project sea level rise in the future. **Van den Broeke *et al.*** (p. 984) obtained consistent estimates from two independent methods, one based on observations of ice movement combined with model calculations and the other on remote gravity measurements made by the GRACE (Gravity Recovery and Climate Experiment) satellites. The combination of these approaches also resolves the separate contributions of surface processes and of ice dynamics, the two major routes of ice mass loss.

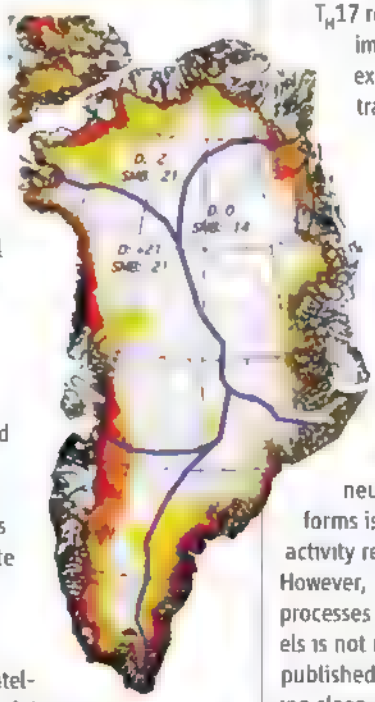

Outfoxing Immune Excess

Immune responses are kept in check by Foxp3-expressing $CD4^+$-regulatory T cells (T_{regs}) through a variety of mechanisms. Expression of specific transcription factors directs T_{reg} responses into distinct T helper cell lineages; however, the transcription factors that regulate particular helper lineages have not been completely characterized. **Chaudhry *et al.*** (p. 986, published online 1 October) show that the transcription factor Stat3, that is required for the initial differentiation of T_H17-effector T cells, is also required for T_{reg} cell-mediated suppression of T_H17-mediated immune responses. Mice carrying a T_{reg} cell-specific deletion in Stat3 succumb to an intestinal inflammatory disease driven by uncontrolled T_H17 responses. Thus, different classes of immune responses can result from the expression of helper lineage–specific transcription factors.

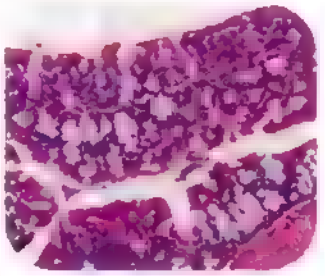

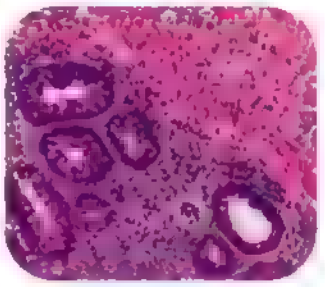

Sleep and Alzheimer's Disease

Accumulation of amyloid-β (Aβ) in the brain is thought to be the initiating event in the pathogenesis of Alzheimer's disease (AD). Aβ is a peptide secreted in a soluble monomeric form predominantly by neurons and its aggregation into toxic forms is concentration dependent. Synaptic activity regulates the release of Aβ in vivo. However, how physiological and environmental processes are involved in regulation of Aβ levels is not understood. **Kang *et al.*** (p. 1005, published online 24 September), by performing sleep-wake studies in freely behaving animals concomitant with in vivo microdialysis, found that brain interstitial fluid levels of Aβ were significantly correlated with wakefulness and negatively correlated with sleep. Furthermore, relatively short-term (3 weeks) sleep deprivation markedly accelerated amyloid plaque deposition in amyloid precursor protein transgenic mice. Thus, sleep-wake behavior is linked to Aβ levels and abnormal sleep may be linked to AD pathogenesis.

Bruce Alberts is Editor-in-Chief of *Science*.

On Becoming a Scientist

ONE NORMALLY BECOMES A SCIENTIST THROUGH A SERIES OF APPRENTICESHIPS, PURSUING research in laboratories directed by established scientists. My own scientific mentors were Jacques Fresco and Paul Doty at Harvard, where I learned not only technical skills but also how to think and function as a scientist. Both from them, and by making my own mistakes,* I learned how to identify important problems, how to think critically, and how to design effective research strategies. Because so much of one's scientific future is shaped by early experiences, it is critical that beginning scientists select their mentors wisely. Unfortunately, what constitutes a "good" choice is not always obvious. Here I offer some personal advice to help young scientists make these tough decisions wisely.

The exact project pursued for a Ph.D. degree is not nearly as important as finding the best place for learning how to push forward the frontier of knowledge as an independent investigator. My first piece of advice for graduate students is to begin research training in a laboratory led by a person with high scientific and ethical standards. It is by talking to people in that lab or those who have previously trained there, and by consulting other scientists in the same field, that one can gain this important insight.

It is also important to find an adviser who will pay close attention to your development as a scientist. Brilliant scientists sometimes make poor mentors. Often, an established leader who has no more than about a dozen people to manage can best nurture a creative, exciting, and supportive place to work. But carrying out research with an outstanding new professor with a very small group can frequently provide even better training.

Students enter graduate school both to learn how to do science well and to discover where their talents and interests lie. Success at either task requires that they be empowered to create new approaches and to generate new ideas. In my experience, beginning scientists will only gain the confidence needed to confront the unknown successfully by making discoveries through experiments of their own design. The best research advisers will therefore provide their graduate students with enough guidance to prevent them from wasting time on nonproductive pursuits, while giving them the freedom to innovate and to learn from their own mistakes.

In my field of biology, two apprenticeships are standard for beginning scientists, first while earning a Ph.D. degree and then in a second laboratory in a postdoctoral position. The choice of a postdoctoral laboratory is best made with a long-term career plan in mind. Scientists at this stage should intentionally try to choose a laboratory where they can acquire skills that complement those they already have. For example, a student whose Ph.D. thesis gave her strong skills as a yeast geneticist might choose to do postdoctoral research with an expert protein biochemist, planning to later use a combination of powerful genetic and biochemical tools to attack a biological problem in an area where very few scientists have the same abilities.

But success as an independent scientist will require much more than technical skills. It is critical to be able to design research strategies that are ambitious enough to be important and exciting, innovative enough to make unique contributions likely, and nevertheless have a good chance of producing valuable results. An enormous number of different experiments are possible, but only a tiny proportion will be really worthwhile. Choosing well requires great thought and creativity, and it involves taking risks.

Senior scientists have the responsibility of maintaining a system that provides talented young scientists with the opportunity to succeed in whatever career they choose. My next editorial addresses the importance of ensuring that innovation and risk-taking are rewarded for those pursuing a life of independent research. Also, a new series in *Science Careers* highlights conversations with audacious scientists who give their own advice about selecting institutions, mentors, and projects.†

– Bruce Alberts

10.1126/science.1184202

*B. Alberts, *Nature* **431**, 1041 (2004). †http://dx.doi.org/10.1126/science.caredit.a0900139.

CREDITS: (TOP) TOM KOCHEL; (LEFT) GETTY IMAGES

EDITED BY GILBERT CHIN AND JAKE YESTON

EVOLUTION

No *b* to Rule Them All

The dependence of basal metabolic rate (BMR) on body mass (*M*) in mammals is generally expressed as $BMR = aM^b$, but the value of the exponent *b* has long been disputed. Some researchers argue for geometric scaling ($b = 0.67$), as predicted by surface area–to–volume ratios. Others claim quarter-power scaling ($b = 0.75$), which has been supported by theoretical analyses of nutrient supply networks. However, most empirical "mouse-to-elephant" studies have not accounted for the shared evolutionary history of the sampled species. To do so, White *et al.* use two methods: phylogenetic generalized least squares and independent contrasts. They consider high-quality BMR data from 585 species (which include only measurements on inactive, fasted, nonreproductive adults in a thermoneutral environment) and a subset of 537 species that excludes lineages for which BMR may not be measurable. Their phylogenetically informed estimates of *b* fall between 0.67 and 0.75, and all of their statistically valid analyses reject both values. In addition, they find that *b* differs among lineages. Their results reinforce doubts as to the existence of a universal allometric relationship between mammalian BMR and body mass. — SJS

Evolution **63**, 2658 (2009)

CHEMISTRY

Poison Probe

The toxic compound methylmercury often bioaccumulates in fish tissues, where it can exceed recommended maximum levels for human consumption. There is thus a need for simple screening procedures to rapidly detect methylmercury in samples of fish intended for human consumption. Climent *et al.* now report such a method, in which the presence of methylmercury triggers the opening of pores in a mesoporous inorganic material by liberating a tethered capping group. Upon opening, the pores release multiple dye molecules previously trapped inside, thereby amplifying the detection signal. The authors tested their method on fish samples with known methylmercury content, straightforwardly processed by acid digestion and subsequent toluene extraction. The results showed that the method yields accurate results and is selective for methylmercury even in the presence of Hg^{2+} and numerous other metal ions. — JFU

Angew. Chem. Int. Ed. **48**, 8519 (2009).

MATERIALS SCIENCE

Up, Up and Away

When hot vapor comes in contact with a cold surface, such as a shower wall, liquid droplets are created that quickly coalesce and form a film. This condensation process is ubiquitous in natural as well as artificial environments. In industrial settings, preventing film formation is generally desirable because liquid films are poor heat conductors. However, it can be challenging to remove the droplets more quickly than they coalesce, particularly when nonvertical sample orientations preclude help from gravity. Boreyko and Chen demonstrate the spontaneous elimination of droplets from a horizontal surface. They prepare a superhydrophobic substrate consisting of carbon nanotubes deposited on silicon micropillars (shown at right). Video imaging of the condensation of ambient moisture reveals that, after the droplets are formed, they initially coalesce without moving, then eventually reach a mobile phase where several droplets fuse and leave the surface of the sample in a dramatic out-of-plane jump. The energy for the jump is provided by the decrease in surface energy gained by coalescence; the average condensed droplet size is an order of magnitude smaller than that observed in gravitational removal. Interestingly, a similar mechanism is thought to be used by a type of mushroom to eject a spore from its stengma. — JS

Phys. Rev. Lett. **103**, 184501 (2009).

CELL BIOLOGY

As It Happens

RNA polymerase moves information from the genome (DNA) into pre-messenger RNA (pre-mRNA), from which introns are removed and exons are ligated to make a mature mRNA. To follow the progress of transcription on single genes from start to finish, Wada *et al.* chose five long human genes whose expression could be switched on by the cytokine tumor necrosis factor–α. Putting together snapshots taken at 7.5-min intervals for 3 hours, they documented the waves of RNA synthesized by polymerase, with each molecule of enzyme jumping on at the transcription start site and hopping off over 100 kb away. During each round, upstream introns were excised as the polymerase moved downstream, often before the next intron was reached. Furthermore, it appeared that later rounds of transcription were begun and continued for a few kilobases before being aborted, as if the polymerases were colliding with a checkpoint that kept track of downstream occupancy of the gene. Each wave of transcription traveled at ~3 kb m^{-1}, although the accumulation of polymerase at regions bound by the insulator proteins CTCF and cohesion, both of which are involved in chromosome looping, suggested that polymerase may be held up at specific sites. — HP

Proc. Natl. Acad. Sci. U.S.A. **106**, 18357 (2009).

CREDITS (TOP TO BOTTOM): ISTOCK PHOTO; BOREYKO AND CHEN

www.sciencemag.org

Science

1200 New York Avenue, NW
Washington, DC 20005
Editorial: 202-326-6550, FAX 202-289-7562
News: 202-326-6581, FAX 202-371-9227
Bateman House, 82-88 Hills Road
Cambridge, UK CB2 1LQ
+44 (0) 1223 326500, FAX +44 (0) 1223 326501

SUBSCRIPTION SERVICES For change of address, missing issues, new orders and renewals, and payment questions: 866-434-AAAS (2227) or 202-326-6417, FAX 202-842-1065. Mailing addresses: AAAS, PO Box 96178, Washington, DC 20090-6178 or AAAS Member Services, 1200 New York Avenue, NW, Washington, DC 20005

INSTITUTIONAL SITE LICENSES please call 202-326-6755 for any questions or information

REPRINTS: Author Inquiries 800-635-7181
Commercial Inquiries 803-359-4578

PERMISSIONS 202-326-7074, FAX 202-682-0816

MEMBER BENEFITS AAAS/Barnes&Noble.com bookstore www.aaas.org/bn, AAAS Online Store www.apisource.com/aaas/ code MKB6; AAAS Travels: Betchart Expeditions 800-252-4910; Apple Store www.apple.com/eppstore/aaas, Bank of America MasterCard 1-800-833-6262 priority code FAA3YU, Cold Spring Harbor Laboratory Press Publications www.cshlpress.com/affiliates/aaas.htm, GEICO Auto Insurance www.geico.com/landingpage/go51.htm?logo=17624, Hertz 800-654-2200 CDP#343457, Office Depot https://bsd.officedepot.com/portalLogin.do; Seabury & Smith Life Insurance 800-424-9883, Subaru VIP Program 202-326-6417; VIP Moving Services www.vipmayflower.com/domestic/index.html; Other Benefits: AAAS Member Services 202-326-6417 or www.aaasmember.org.

science_editors@aaas.org	(for general editorial queries)
science_letters@aaas.org	(for queries about letters)
science_reviews@aaas.org	(for returning manuscript reviews)
science_bookrevs@aaas.org	(for book review queries)

Published by the American Association for the Advancement of Science (AAAS), *Science* serves its readers as a forum for the presentation and discussion of important issues related to the advancement of science, including the presentation of minority or conflicting points of view, rather than by publishing only material on which a consensus has been reached. Accordingly, all articles published in *Science*—including editorials, news and comment, and book reviews—are signed and reflect the individual views of the authors and not official points of view adopted by AAAS or the institutions with which the authors are affiliated.

AAAS was founded in 1848 and incorporated in 1874. Its mission is to advance science, engineering, and innovation throughout the world for the benefit of all people. The goals of the association are to: enhance communication among scientists, engineers, and the public; promote and defend the integrity of science and its use; strengthen support for the science and technology enterprise; provide a voice for science on societal issues; promote the responsible use of science in public policy; strengthen and diversify the science and technology workforce; foster education in science and technology for everyone; increase public engagement with science and technology; and advance international cooperation in science.

INFORMATION FOR AUTHORS
See pages 807 and 808 of the 6 February 2009 issue or access www.sciencemag.org/about/authors

HOPE FOR MONGOLIAN HORSES

The Przewalski's horse—the world's last remaining truly wild horse—may be gaining traction in the Gobi desert.

Many projects have attempted unsuccessfully to reintroduce zoo horses to their original habitat on the central Asian steppes. Now, scientists have announced at the recent Society for Conservation Biology meeting in Beijing that in two cases the horses may have turned the corner.

Veterinarian Chris Walzer of the University of Veterinary Medicine in Vienna says that horses at two projects in Mongolia have been upgraded from "extinct in the wild" to "critically endangered," according to criteria set by the International Union for Conservation of Nature, which requires that more than 50 mature individuals spend 5 years free-living in the wild. The horses are at Hustai National Park, which had 171 living on their own in 2006, and Takhin Tal, which had 115 in 2007.

Walzer has calculated that 140 is "a robust starting population" for a group's long-term survival. He and colleagues say the current 58% foal survival rate in Takhin Tal is enough to sustain the population, even through the Gobi's harsh winters.

Weikang Yang, an ecologist at Mongolia's Kalameili reserve, says some horses were released in Kalameili in 2001, but survival is difficult because livestock push the horses off their land in winter and the thick snow makes food hard to find. At Takhin Tal, local herdsmen are paid to keep their animals off the reserve.

Who's That Swine?

Pigs belong to the elite group of animals that can use mirrors, researchers say. "We knew that pigs have sophisticated social behaviors," says zoologist Donald Broom of the University of Cambridge in the United Kingdom, so he and colleagues decided to test their mirror awareness. First, they left eight pigs, in pairs, with a mirror for 5 hours. "They initially interpret the image as another pig," says Broom—the error most species make. But then they began to recognize the reflections of their own movements.

Proof of their mirror smarts came in the next test: The researchers hid a bowl of food behind a barrier so that it could be seen only in the mirror. An overhead fan circulated the food's scent so that the pigs could not simply use their noses. In less than 25 seconds, seven of the pigs correctly interpreted the image, turned away from the mirror, and ran to the bowl. The eighth pig flunked the test, looking behind the mirror for the food.

The experiments show that pigs can make sense of mirror images and have some degree of self-awareness, the researchers report in the current issue of *Animal Behavior*. The findings are "very significant," says Marc Bekoff, a cognitive ethologist at the University of Colorado, Boulder, and "extend the range of animals who are self-aware." That includes elephants, dolphins, magpies, gray parrots, and some primates.

Miss Piggy has mirror smarts.

CREDITS (TOP TO BOTTOM): ART WOLFE/GETTY IMAGES; ESO; GETTY IMAGES; REDFERN/GETTY IMAGES

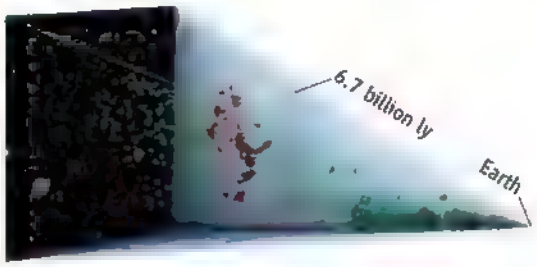

Putting Things in Perspective

Astronomers are reaching ever deeper into the distant universe. A team led by Masayuki Tanaka of the European Southern Observatory near Munich, Germany, has created a 3D image of a chunk of the universe that shows a huge, previously unknown cluster of galaxies almost 7 billion light-years away. The galaxies (in red), revealed by powerful optical telescopes in Chile and Hawaii, extend over at least 60 million light-years.

End of an Era

Anthropologist Claude Lévi-Strauss, a towering figure in 20th century anthropology, died in Paris on 31 October, a few weeks shy of his 101st birthday.

Lévi-Strauss in Amazonia circa 1936.

Lévi-Strauss introduced "structuralism" to anthropology: the concept that all societies follow certain universal patterns of thought and behavior, as exemplified in their myths. "The ultimate original principle of structuralism [is] that the forms of cultural order reflect general underlying laws of the human mind," says social anthropologist Marshall Sahlins of the University of Chicago in Illinois.

Born in Belgium, Lévi-Strauss taught sociology in Brazil in the 1930s and spent 3 years studying tribes in the Brazilian interior. During World War II, he fled to the United States, where he taught at New York City's New School for Social Research. In 1959, Lévi-Strauss was named to a chair in social anthropology at Paris's Collège de France, where he remained until his retirement in 1982.

Confusion over H1N1 vaccination for kids
922

A pause in the retreat of Himalayan glaciers
924

Islamic outreach. U.S. Secretary of State Hillary Clinton unveiled a new science initiative to the 57 Muslim-majority countries (*below*) during a trip to Morocco

DIPLOMACY

U.S. Takes Steps to Use Science To Improve Ties to Muslim World

In a surprise announcement, U.S. Secretary of State Hillary Clinton last week named three prominent scientists as special envoys to assess the potential for scientific partnerships with Muslim-majority countries. The move is the first concrete step in a broader U.S. effort to expand the role of science in diplomacy.

Speaking in Morocco on 3 November, Clinton said the new envoys will help "to fulfill President Obama's mandate to foster scientific and technological collaboration" and to "develop the capacity to meet economic, social, and ecological challenges." She announced the selection of Egyptian-born Ahmed H. Zewail, a chemistry Nobelist at the California Institute of Technology in Pasadena; Algerian-born Elias Zerhouni, a radiologist who stepped down last fall as director of the National Institutes of Health (NIH); and biochemist Bruce Alberts, former president of the U.S. National Academy of Sciences (NAS) and current editor-in-chief of *Science*. Clinton said that the State Department is also bolstering its scientific and environmental expertise at embassies around the world.

Clinton's speech to the Forum for the Future, a group that fosters dialogue between countries in the region and industrialized nations, builds upon Obama's highly publicized 4 June speech at Cairo University that called for a "new beginning" in relations with the Muslim world. Within the scientific realm, the president also promised to establish at least three technology "centers of excellence" in the Middle East, North Africa, and Muslim-majority regions in Asia, an idea now under discussion by an interagency group.

While these initiatives are aimed at the 57 Muslim-majority countries, officials at both

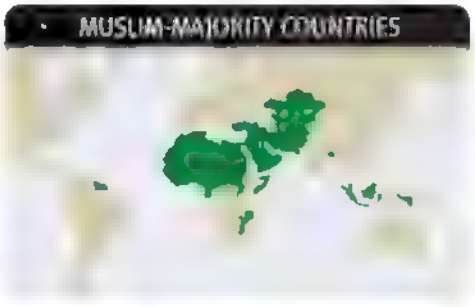

the State Department and the White House told *Science* that the goal is to bolster the department's science capacity across the board. Assistant Secretary of State Kerri-Ann Jones, who directs the Bureau of Oceans and International Environmental and Scientific Affairs, says the department wants "to better engage science as part of our diplomacy."

Pradeep Ramamurthy, senior director for global engagement at the National Security Council, says the envoys program and the expansion of science diplomats "reflects a broader, long-term commitment by this Administration to the role of S&T in global engagement." A bill (S.838) to create such envoys cleared the Senate Foreign Relations Committee this spring, and its sponsor, Senator Richard Lugar (R–IN), praised the initial appointments and said that he "look[s] forward to more envoys that will be announced in the coming months."

The trio was selected from a list, drawn up by the White House Office of Science and Technology Policy and the State Department, of "illustrious scientists who have shown global leadership and the ability to build partnerships with excellent research institutes abroad," Jones said. The National Academies helped winnow down the list, she said, and the final selection was made by Jones, White House science adviser John Holdren, and State Department science adviser Nina Fedoroff.

Zewail, who earned his initial degrees at Egypt's Alexandria University, plans to travel to the Middle East next month to ask government officials and scientists "to help come up with a visionary road map of how to create new partnerships." He has called for "scientopolitical" initiatives (*Science*, 12 September 2008, p. 1417) that focus on education and science to advance political and social goals.

Zerhouni, a graduate of the University of Algiers Medical School, says, "We want to open doors that others cannot." A senior adviser to the Johns Hopkins University School of Medicine and a senior fellow at the Bill and Melinda Gates Foundation, Zerhouni notes that "we've made great strides in 'health diplomacy' worldwide, and we hope to extend that success to science diplomacy."

As NAS president, Alberts helped create and co-chaired the InterAcademy Council in Amsterdam, an international organization of science academies that produces reports on major science, technological, and health issues. A strong advocate for increased international science cooperation, he has also been

CREDITS (TOP TO BOTTOM): JEAN BLOND/REUTERS/LANDOV (SOURCE) ORGANIZATION OF THE ISLAMIC CONFERENCE

active in reforming science education in the United States and around the world.

Arden Bement, director of the National Science Foundation, thinks the envoys initiative is a good concept but suggested adding an engineer to the list to help evaluate potential technology collaborations. "It is critically important to establish closer ties with Muslim-majority countries and to make use of science diplomacy to identify research areas of mutual interest," says Bement, a nuclear engineer who led the U.S. delegation that attended this fall's opening ceremonies for the King Abdullah University of Science and Technology in Saudi Arabia (*Science*, 16 October, p. 354). Officials say they expect some future envoys to have backgrounds in engineering and the physical sciences.

In the meantime, senior officials from the White House, State Department, U.S. Agency for International Development, and NIH are working to implement Obama's centers-of-excellence pledge. Options range from traditional "brick and mortar" institutes to virtual centers of excellence. "We're trying to figure out which models work best, where they should be located, and what their primary focus should be—such as water or energy or climate change," says Ramamurthy. The new envoys will help to define the best foci for such centers.

Zerhouni says improving the quality of science officers at embassies "is long overdue. There is a scarcity of S&T–capable diplomats around the world." Jones says the department plans to increase the number of diplomats who focus primarily on science, the environment, and health. There are 42 full-time science and environmental officers at embassies and a dozen more at the 12 "regional hubs" around the world, including one in Jordan. They supervise other diplomats who devote part of their time to science issues.

Last month, the White House followed up on yet another promise that Obama made in Cairo. The government's Overseas Private Investment Corp. (OPIC) has issued a call for proposals to manage one or more funds to promote the growth of technology in the Middle East, North Africa, and Asia. Depending on how much private capital is raised, OPIC would provide financing of between $25 million and $150 million.

–ROBERT KOENIG

PHILANTHROPY

Wellcome Trust to Shift From Projects to People

Scientists often complain that they spend too much time chasing after their next grant and not enough time doing research. Now the Wellcome Trust, the giant biomedical research charity in the United Kingdom, wants to remove those constraints by giving no-strings-attached funding to nearly all the independent researchers it supports.

This week, Wellcome officials announced that they are phasing out their biomedical research grants for U.K. scientists, which consists of 3-year to 5-year awards focused on a specific problem. Instead, starting in 2011, the organization will put that money, about 20% of its total budget, or $183 million, into a new program called Investigator Awards. The awards will be bigger, more flexible, and longer—up to 7 years.

"The idea is to empower the very best scientists to tackle difficult, long-term questions," says Wellcome Trust Director Mark Walport. Although the trust already provides this kind of support, including salaries, through fellowships, the new awards will expand this model to researchers who receive their salary from their institutions.

The change puts the $21 billion Wellcome Trust in line with the policies of the smaller Howard Hughes Medical Institute (HHMI) in Chevy Chase, Maryland, to fund "people, not projects." More than 350 Hughes investigators each receive $1 million a year (including overhead costs) for 5 years under the institute's major program to support research, and that support can be extended indefinitely. The U.S. National Institutes of Health supports nearly 200 researchers with similar programs it began a few years ago.

Wellcome already offers fellowships that provide salaries and research funds for more than 500 independent researchers for 4 to 7 years. But the foundation also funds about 200 investigators a year with 3-year project grants that range from $250,000 to $500,000 in total. It awards another 45 or so program grants for up to $2 million over 5 years. Wellcome will hold one more competition next summer for these awards before taking applications in the fall for the new program.

Whereas HHMI selects its investigators through paper applications, Walport says that, as with the fellows, Wellcome plans to interview candidates in person to "test their mettle." Reviewers will focus less on paperwork and more on qualifications and the importance of the research. The trust hopes this interaction will create a "community of scientists," says Walport. Researchers will remain free to seek grants from other sources as well.

Cutting strings. The Wellcome Trust's Mark Walport hopes that phasing out project-based research grants will encourage creativity.

Walport declined to specify the annual funding level per investigator, noting that researchers will request what they need. But the total number of researchers supported is expected to be lower than the 245 or so now with project or program grants. (Although the grants may be smaller than HHMI's, investigators can also apply for supplemental grants for equipment, travel, and other expenses.) A subset of the new program will be reserved for early-career scientists.

"I fully support the move," says Paul Nurse, a British Nobel Prize–winner who is now president of Rockefeller University in New York City. "I think it's the most effective way to fund science." Molecular biologist Angus Lamond of the University of Dundee in the United Kingdom, a Wellcome fellow and grants review panel chair, predicts that the reaction of U.K. scientists will be mixed. Dundee, who was not part of the decision, says it will be important for the trust to "listen to feedback" and address any problems that crop up. –JOCELYN KAISER

CREDIT: WELLCOME IMAGES

PANDEMIC INFLUENZA

Europe Reconsiders H1N1 Flu Shots for Children

PARIS—On 27 October, the White House announced that President Barack Obama's daughters, Sasha and Malia, had received their shots against the H1N1 pandemic virus, at the same time that the vaccine became available to other children in Washington, D.C. No European leader has made a similar announcement, for a simple reason: Until recently, no European country had included healthy children in the priority groups targeted for vaccination. But as the outbreak gathers speed and more vaccine becomes available, some countries are now telling families that healthy children—or at least infants—are candidates for vaccination after all. The change of mind did not reassure a jittery public.

In France, where vaccination has just begun, the government announced a plan this weekend to offer the vaccine to children from preschool through high school starting on 25 November. In the Netherlands, health minister Ab Klink promised on Monday to follow fresh advice from the Health Council to start vaccinating children between ages 6 months and 4 years as soon as possible. The United Kingdom is considering an expansion of its vaccination program as well but is awaiting scientific advice.

Ouch. Irish 7-year-old Aoife Maher, who's in one of the risk groups, gets a swine flu shot. But Ireland is not yet vaccinating healthy children.

CREDIT: PA PHOTOS/ANDOV

How many European children will eventually be vaccinated remains to be seen, partly because distrust of the new vaccines is running high. In France, for instance, polls show that fewer than one in five people would take it, and even Jean-François Copé, leader of the ruling party in the National Assembly, has acknowledged having qualms. In Germany, prominent doctors have denounced pandemic hype that benefits big pharma. Amid the confusion, many parents may ignore the new advice to vaccinate children.

Like the public response, the availability of vaccines varies widely. Some countries such as Norway and the Netherlands have erred on the side of caution by ordering two doses of vaccine for every resident—much more than they now think they will use. Spain, by contrast, has bought 37 million doses for more than 46 million people. Economic stragglers along the European Union's eastern flank have purchased none at all. But even those who had plenty did not at first include healthy children among the priority groups. "They have a very different outlook," says Lone Simonsen, a Danish-born epidemiologist at George Washington University in Washington, D.C.

That may seem strange, given the fact that the same epidemiological and clinical trial data prompted U.S. officials to recommend the vaccine for everyone from 6 months through 24 years of age. Their reasoning: The risk of severe disease, hospitalization, and death is the highest in these groups. But European experts tend to point out that the risk is still very small and has to be weighed against the small risk of serious side effects. "With pandemic vaccines, which are being developed in a relatively short amount of time and tested in a limited number of subjects, you've got to be extra-careful," says André Knottnerus, chair of the Dutch Health Council. Until last week, his panel had recommended against vaccinating small children; the group changed course after experience in Australia and New Zealand suggested that pediatric intensive care units in Holland may be overwhelmed.

One reason behind Europe's reticence is that, unlike the United States, it is using vaccines containing potency-enhancing compounds called adjuvants. Although one such vaccine for seasonal flu, Novartis's Fluad, has been on the market for over a decade, there's limited data on its safety in children. Experience with GlaxoSmithKline's adjuvanted pandemic vaccine, Pandemrix, is limited to just several tens of thousands of people.

Experience with seasonal flu also helps explain the different responses, says Simonsen. Since 2002, the United States has vaccinated healthy children under 2 against seasonal flu, and since 2008 it has recommended the seasonal shot for anyone under 18. In Europe, only five countries, with a combined population of 15 million, recommend giving healthy children annual flu shots, and none of them beyond 6 years of age. As a result, protecting children against the pandemic was less obvious in Europe, she says.

U.S. health officials have cited another benefit of vaccinating children: Studies have suggested that, because they contribute most to the spread of the disease, protecting them may offer some protection to the rest of the population as well (*Science*, 12 November 2004, p. 1123). But the evidence for this herd immunity effect is not very strong, says epidemiologist Arnold Monto of the University of Michigan School of Public Health in Ann Arbor, who calls it an "added bonus" at best. European countries generally did not find the argument persuasive, says Johannes Löwer, head of the Paul Ehrlich Institute, which is responsible for licensing vaccines in Germany.

Whatever the reasoning, the jump in H1N1 cases in Europe over the past few weeks—and the deaths of some previously healthy people—has contributed to a changed view in several countries. In Germany, the Association of Pediatricians had strongly opposed vaccination of children under 3 but reversed itself last week in the face of increasing numbers of pediatric cases and growing confidence in the vaccine. "Everybody reads the same literature," Monto says, "but when you have the disease in your own country, the impact is greater."

Another transatlantic contrast has emerged. The U.S. is satisfied with data from clinical trials indicating that one dose of unadjuvanted vaccine suffices for persons 10 years and older, a view endorsed by an expert panel at the World Health Organization. But the European Medicines Agency isn't sure yet, and most European countries are sticking to two doses for all age brackets for now. There's a certain irony in that, because European policymakers pride themselves on buying adjuvanted vaccine, which requires less antigen per shot, allowing for the production of more vaccines and a more equitable global distribution. By recommending two shots, they're hogging more of the precious resource than they had hoped.

—MARTIN ENSERINK

With reporting by Gretchen Vogel in Berlin.

CREDIT: SERGEI RUBLIOV/WIKIMEDIA

RUSSIA

Restructuring Physics Labs Brings Delight and Despair

MOSCOW—Four of Russia's most prominent physics labs are to be merged into a new national research center. The institutes, which have languished in the post-Soviet era, have cautiously welcomed the raised profile the merger will bring. But a different reform aimed at separating basic and applied research at one of the institutes—the Kurchatov Institute in Moscow, Russia's premier lab for nuclear energy research—has researchers up in arms.

The merger, announced in a presidential decree last month, will combine the Institute for High Energy Physics (IHEP) in Protvino, 100 kilometers south of Moscow; the B. P. Konstantinov Petersburg Nuclear Physics Institute (PNPI) in St. Petersburg; and two Moscow labs—the Institute for Theoretical and Experimental Physics (ITEP) and the Kurchatov. The reorganization is aimed at smoothing the path of innovations into industry, says Sergei Kiriyenko, chief of the nuclear energy agency Rosatom and one of the key officials behind the decree.

ITEP and IHEP are currently managed by Rosatom, a state corporation created out of the Ministry of Atomic Energy. Many researchers felt uncomfortable as part of a body geared toward the energy industry. "For us and for IHEP, it has crucial significance. This is the way for us to get away from Rosatom's aegis," says ITEP's Boris Ioffe.

PNPI also sees a positive side to the merger. The institute, which is part of the Russian Academy of Sciences, is desperate to complete a reactor-based neutron source that began construction in 1976. "It was impossible with an academic budget," says Ioffe, who hopes the prospects will be better in the combined center.

Although Kurchatov researchers appear content with the merger plans, the ongoing internal restructuring has prompted dissent. The newspaper *Troitsky Variant*, published in the town of Troitsk near Moscow that is home to many physics institutes, ran a letter last month from 59 researchers in the Kurchatov's Nuclear Fusion Institute (NFI). The letter protested against splitting the institute into three parts, fusion, applied science, and production.

"At the very least," says NFI Director Valentin Smirnov, such a division, "would seriously complicate our part of work on the [international ITER fusion] project." Those who signed the letter argued that the same specialists previously worked on fusion research and applied issues, which made the staff flexible and made it easier to hold onto highly qualified personnel when funding was scarce. Ksenia Razumova, who signed the letter, cites the example of two groups that used to work on plasma-wall interactions in tokamak fusion reactors. "As a result of the division, our group doesn't exist any longer: All the staff left for the national agency in charge of ITER. They now have highly paid managerial positions," Razumova says.

Although the merger of the four institutes is already in motion, some think it may flounder through lack of funding. "Financial plans for the coming year are already finalized, and they don't stipulate any merger," says Nikolay Ponomarev-Stepnoy, honorary vice president of the Kurchatov Institute. "The plans for 2011 are being made at the moment, but even there it's impossible to envisage anything of this kind."

–ANDREY ALLAKHVERDOV AND VLADIMIR POKROVSKY

Allakhverdov and Pokrovsky are reporters in Moscow.

*Science*Insider

From the *Science* Policy Blog

*Science*Insider explored why academic biomedical scientists report that they are receiving less **corporate support for their research** now than in the 1990s. Possible reasons for the shift include the 5-year doubling of the National Institutes of Health budget and a public debate over whether funding from drug companies can distort research results. http://bit.ly/3WwfLX

The Dutch House of Representatives rejected a motion asking the government to sever all ties with virologist Albert Osterhaus of Erasmus Medical Center in Rotterdam, who had been **accused of conflicts of interest** in his role as a health adviser. http://bit.ly/BTYUE

The U.S. Senate rejected an attempt to strip funding for **political science research** out of the National Science Foundation's (NSF's) 2010 budget. http://bit.ly/19DCKr

A planned meeting in March of 150 scientists to discuss **governance issues related to geoengineering** drew praise but also some criticism from scientists who believe that some of the organizers are tainted by ties to companies with an interest in the technology. http://bit.ly/39cQQ

African science academies have released a joint report that suggests a 20% increase in the use of **affordable medical interventions** such as immunizations could save the lives of about 770,000 children and young mothers each year in nine countries in sub-Saharan Africa. http://bit.ly/2TADZG

U.S. Energy Secretary Steven Chu seems to have stretched the truth when he said that scientists at a DOE lab he once led had been wasting energy by forgetting to unplug equipment that hadn't been used in many years. http://bit.ly/3YVXgU

Biofuels experts Tim Searchinger and John Sheehan debated **whether biofuels could be carbon friendly** in a six-part e-mail conversation. http://bit.ly/3G5bzF

For more science policy news, visit **blogs.sciencemag.org/scienceinsider.**

CLIMATE CHANGE

No Sign Yet of Himalayan Meltdown, Indian Report Finds

NEW DELHI—Are Himalayan glaciers beating a rapid retreat in the face of global warming? That would seem to be the case, according to a flurry of recent reports by BBC and other mass media. But the picture is more complex—and poses scientific puzzles, according to a review of satellite and ground measurements released by India's Ministry of Environment and Forests earlier this week.

The report, by senior glaciologist Vijay Kumar Raina, formerly of the Geological Survey of India, seeks to correct a widely held misimpression based on measurements of a handful of glaciers: that India's 10,000 or so Himalayan glaciers are shrinking rapidly in response to climate change. That's not so, Raina says. Even if it were, other researchers argue that severe loss of ice mass would not entail drastic water shortages in the Indian heartland, as some fear. Both concerns were cited in the Asia chapter of the U.N. Intergovernmental Panel on Climate Change's (IPCC's) 2007 Working Group II report, which asserted that Himalayan glaciers "are receding faster than in any other part of the world and, if the present rate continues, the likelihood of them disappearing by the year 2035 and perhaps sooner is very high if the Earth keeps warming at the current rate."

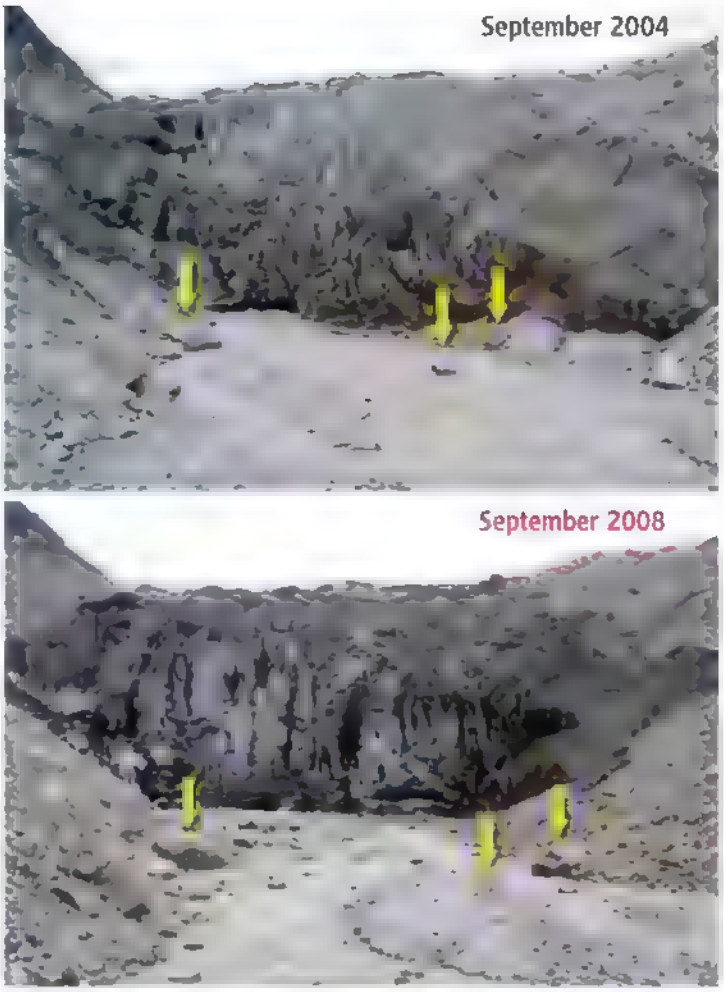

Hanging tough. Gangotri glacier, source of the Ganges River, retreated a few dozen meters from 2004 to 2008—"hardly an abnormal retreat" that would have been expected from rising temperatures, states a provocative new report.

Some glaciologists hew to IPCC's view, disputing Raina's conclusions. Any suggestion that the retreat of Himalayan glaciers has slowed is "unscientific," charges Syed Iqbal Hasnain, a senior fellow at the Energy and Resources Institute in New Delhi. He says the Indian government has an "ostrichlike attitude in the face of impending apocalypse."

However, India's environment minister, Jairam Ramesh, told *Science*, "We don't need to write the epitaph for the glaciers, but we need a concentrated scientific and policy focus on the Himalayan ecosystem since the truth is incredibly complex." India, he says, needs to measure and monitor Himalayan glaciers as a matter of national security.

With ice and snowfields covering more than 30,000 square kilometers, the Himalayas are often called the "third pole." Records that began in the 19th century show that most glaciers advanced through that century as the Little Ice Age that gripped the Northern Hemisphere tapered off. Glaciers began to retreat in the early 20th century. Since 1960, almost a fifth of the Indian Himalayas' ice coverage has disappeared, says Anil V. Kulkarni of the Space Applications Centre in Ahmedabad, who has mapped more than 1000 glaciers using satellite data.

Raina's report, *Himalayan Glaciers: A State-of-Art Review of Glacial Studies, Glacial Retreat and Climate Change*, concurs with that assessment. But it questions a link to global warming. Findings in the past few years, it states, demonstrate that "many" Himalayan glaciers are stable or have advanced and that the rate of retreat for "many others" has slowed. The report does not enumerate glaciers in either category.

The Raina report draws on published studies and unpublished findings from half a dozen Indian groups who have analyzed remote-sensing satellite data or conducted arduous surveys at remote sites often higher than 5000 meters. The report revises perceptions of a number of glaciers, including two iconic ones. For example, the 30-kilometer-long Gangotri glacier, source of the Ganges River, retreated an average of 22 meters a year and shed a total of 5% of its length from 1934 to 2003. But in 2004 and 2005, the retreat slowed to about 12 meters a year, and since September 2007 Gangotri has been "practically at a standstill," according to Raina's report, which cites, among other observations, field measurements by ecologist Kireet Kumar of the G. B. Pant Institute of Himalayan Environment and Development in Almora. Even more stable is Siachin glacier in Kashmir, where Indian and Pakistani forces are stationed eyeball to eyeball at 6000 meters. Claims reported in the popular press that Siachin has shrunk as much as 50% are simply wrong, says Raina, whose report notes that the glacier has "not shown any remarkable retreat in the last 50 years."

Several Western experts who have conducted studies in the region agree with Raina's nuanced analysis—even if it clashes with IPCC's take on the Himalayas. The "extremely provocative" findings "are consistent with what I have learned independently," says Jeffrey S. Kargel, a glaciologist at the University of Arizona, Tucson. Many glaciers in the Karakoram Mountains, which straddle India and Pakistan, have "stabilized or undergone an aggressive advance," he says, citing new evidence gathered by a team led by Michael Bishop, a mountain geomorphologist at the University of Nebraska, Omaha. Kenneth Hewitt, a glaciologist at Wilfrid Laurier University in Waterloo, Canada, who just returned from an expedition to mountain K2, says he observed five glacier advances and a single retreat in the

CREDITS (TOP TO BOTTOM): IIT MUMBAI ISHWAR SINGH (PROVIDED BY V. K. RAINA)

Could Glacier Research Help Thaw Himalayan Standoff?

NEW DELHI—On climate change policy, India and China are on the same page: They oppose mandatory carbon emissions reductions. But they don't see eye to eye on the Himalayas. Both countries claim a swath of the mountains as their own, a dispute that sparked a brief war in 1962. Because of lingering tensions, a diplomatic initiative to get Chinese and Indian scientists working together on glaciers has quietly been put on ice.

Last August, officials from the Wadia Institute of Himalayan Geology in Dehradun, India, and the Cold and Arid Regions Environmental and Engineering Research Institute in Lanzhou, China, were preparing to ink an agreement in Beijing that would have paved the way for the sharing of glacier data and hosting of research exchanges. But the signing ceremony was nixed at the last minute. An Indian diplomat says the territorial dispute would have "led to limited ground access for the joint teams of researchers in the disputed regions." A Chinese government official places the blame squarely on India: "Indian scientists can receive permits for research expeditions with Chinese colleagues [in the Tibetan Himalayas], but India refuses to allow Chinese scientists to join fieldwork in its territory," he says.

The impasse frustrates scientists. "Unless we combine data sets from both sides of the Himalayas, a holistic understanding of the 'third pole' will just not emerge," says former Wadia Institute Director Baldev Raj Arora. He says both sides are now crafting a legal framework that would allow academic exchanges. Neither side will speculate on when an accord might be reached. **–P.B.**

With reporting by Richard Stone in Beijing.

Karakoram. Such evidence "challenges the view that the upper Indus glaciers are 'disappearing' quickly and will be gone in 30 years," Hewitt says. "There is no evidence to support this view and, indeed, rates of retreat have been less in the past 30 years than the previous 60 years," he says.

Why are many Himalayan glaciers bucking the trend of rapid retreat seen in the Alps, for example, or at Mount Kilimanjaro as reported in the *Proceedings of the National Academy of Sciences* last week? "Glaciers at lower elevations are going to respond faster to a warming climate than those at the highest elevations," says Richard Armstrong, a glaciologist at the National Snow and Ice Data Center in Boulder, Colorado. Snowfall patterns are more important to Himalayan glacier stability than temperatures, adds Rajinder Kumar Ganjoo, a glaciologist at the University of Jammu in India. "If rising temperatures were the real cause for the retreat, then all ice masses across the Himalayas should be wasting away uniformly," he says. "At issue in scientific circles," Kargel notes, "is how lengthy the response time is, and how it varies among glaciers."

The bottom line is that IPCC's Himalaya assessment got it "horribly wrong," asserts John "Jack" Shroder, a Himalayan glacier specialist at the University of Nebraska, Omaha. "They were too quick to jump to conclusions on too little data." IPCC also erred in its forecast of the impact of glacier melting on water supply, claims Donald Alford, a Montana-based hydrologist who recently completed a water study for the World Bank. "Our data indicate the Ganges results primarily from monsoon rainfall, and until the monsoon fails completely, there will be a Ganges river, very similar to the present river." Glacier melt contributes 3% to 4% of the Ganges's annual flow, says Kireet Kumar.

Atmospheric scientist Murari Lal, chair of the Climate, Energy and Sustainable Development Analysis Centre in New Delhi and coordinating lead author of the 2007 IPCC report's Asia chapter, rejects the notion that IPCC was off the mark on Himalayan glaciers. But he acknowledges that the report's 10-author team relied on unpublished work when assessing the status of the glaciers. India's U.N. delegation had objected to the wording, Lal recalls, but in the IPCC plenary session the analysis got wide support.

Raina's report is by no means the last word. The surprising stability of some glaciers may be a temporary phenomenon, says Hewitt: Melting may have been reduced by a change in summer weather, such as increased cloudiness, and possibly unusually heavy snowfall, he says. "There needs to be a lot of research on [Asia's] mountain glaciers," adds glaciologist Lonnie G. Thompson of Ohio State University, Columbus. "Truly, we know less about them than any other place on Earth." Both sides of the debate agree on one point: Forecasts hold little water, so only a robust observation campaign will reveal whether the third pole's resistance to climate change is durable—or ephemeral.

–PALLAVA BAGLA

CREDIT: ORTHOPEDIC SPECIALTY HOSPITAL

ScienceNOW.org

From *Science*'s Online Daily News Site

Experts Criticize Nanoparticle Study
The headlines are laced with fear. All of them seem to suggest that a new study has found that nanoscale materials, used in everything from medical imaging to cancer treatments, can damage genetic material in our bodies. But this particular study has little relevance to human exposure risks, experts say, and it is deeply flawed in other ways http://bit.ly/nanoparticles

More Support for Human Role in Chinese Quake
When the Wenchuan earthquake killed some 80,000 people in southwest China in May of last year, suspicion immediately fell on the reservoir behind the nearby Zipingpu Dam. Seismologists knew that several hundred million tons of water had filled the reservoir in the preceding few years and that either the water itself or its weight might have weakened a nearby fault and unleashed the quake. A new analysis finds that both scenarios are plausible, but further insight will require the cooperation of the Chinese government. http://bit.ly/Wenchuan

No Sprinting Advantage With Prosthetic Limbs

In 2007, South African double-amputee sprinter Oscar Pistorius became the first disabled athlete to compete against able-bodied runners, placing seventh in the British Grand Prix. But his J-shaped, carbon-fiber prostheses, called the Össur Flex-Foot Cheetah, sparked a debate within the athletic world: Do the devices give him an unfair advantage over able-bodied competitors? The answer, according to a new study of six amputee sprinters, is no. http://bit.ly/prosthetics

Don't Shush That Baby; It's Learning
A newborn's cry is a call to action. "Quick, somebody help me!" But bawling babies are getting something else besides attention: language practice. A new study finds that, in the first few days of life, babies produce cries that mimic the melodies of their native language. http://bit.ly/babycries

Read the full postings, comments, and more on **sciencenow.sciencemag.org**.

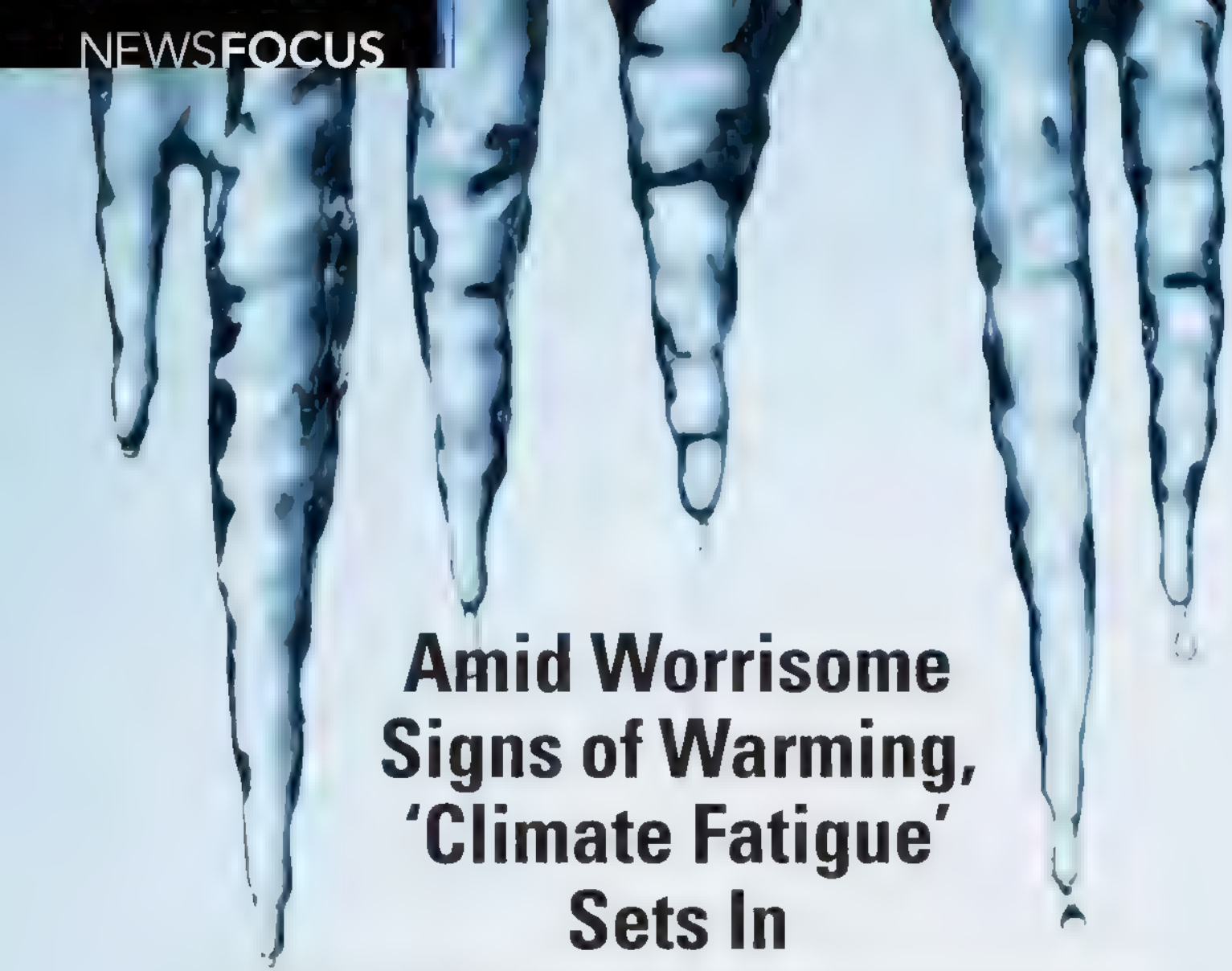

Amid Worrisome Signs of Warming, 'Climate Fatigue' Sets In

As scientists debate whether climate is changing faster than anticipated, some worry that a drumbeat of dire warnings may be helping to erode U.S. public concerns about global warming

CLIMATE NEWS SEEMS TO HAVE BEEN ALL bad since the Nobel Prize–winning Intergovernmental Panel on Climate Change (IPCC) came out with its fourth assessment in February 2007. Within months of the sober but disquieting report, Arctic summer sea ice coverage plunged to a dramatic new record low, prompting talk about catastrophic tipping points. Glaciologists watched as record meltwater on the Greenland ice plunged into chasms, slicking the bottoms of glaciers and sending them racing to the sea. Swelled by glacier losses both north and south, the sea had been rising as fast as IPCC's worst-case scenario predicted, researchers reported. Lacking ice to hunt on, gaunt polar bears roamed Arctic lands in search of food. And newly crunched numbers showed that greenhouse gas emissions had shot up in the previous 5 years to exceed IPCC's worst scenarios.

"We are basically looking now at a future climate that is beyond anything that we've considered seriously," ecologist and IPCC author Christopher Field of Stanford University in Palo Alto, California, said in February at the annual meeting of the American Association for the Advancement of Science (which publishes *Science*), according to a media report. In March, a meeting of 2000 climate scientists in Copenhagen prompted the headline "Projections of Climate Change Go From Bad to Worse, Scientists Report" (*Science*, 20 March, p. 1546).

This September, the United Nations Environment Programme issued an IPCC-like report that, according to a UNEP press release, showed that "the pace and scale of climate change may now be outstripping even the most sobering predictions of the last report of the … IPCC." In the foreword of the UNEP report, U.N. Secretary-General Ban Ki-moon delivered the intended take-home message: The report "is a wake-up call. The time for hesitation is over." In the run-up to next month's climate summit in Copenhagen, some researchers have argued that the worsening prospects for Earth's climate system make the negotiations all the more urgent.

Others, however, say the picture since the IPCC report is more complicated than that—though no brighter. "Things are looking much worse than was thought in the 1970s and '80s," says climate scientist Stephen Schneider of Stanford University, who has been deeply involved in global climate issues since the 1970s. "But 'much worse than IPCC 2007' is only true for a few things." And some anticipated climate changes are actually behind schedule, at least for the time being, notes the U.K. Meteorological Office's head of climate change advice, Vicky Pope. "It's at least as bad as expected," she says. "I don't think it's worse."

CREDIT: GAZ MAL/GETTY IMAGES

Almost all climate scientists are of one mind about the threat of global warming: It's real, it's dangerous, and the world needs to take action immediately. But they disagree about the best way to convey the urgency of the situation to the public and policymakers. "Where do you go after 'unequivocal'?" asks Roger Pielke Jr., a science policy scholar at the University of Colorado, Boulder, referring to the measure of certainty IPCC applied to its core findings in 2007. By sounding the alarm too loudly, Pielke and others say, scientific climate campaigners could be driving potentially sympathetic audiences to tune them out or could even provoke a backlash. Recent surveys in the United States show such "climate fatigue" may indeed be on the rise.

Online
sciencemag.org
Podcast interview with author Richard A. Kerr

A glass half-empty

The UNEP report entitled *Climate Change Science Compendium 2009* (www.unep.org/compendium2009) presents the latest and perhaps most comprehensive case for heightened climate concerns. It is not the exhaustively peer-reviewed consensus assessment of peer-reviewed literature that IPCC produces every 5 or 6 years, but UNEP did compile its report "in association with scientists around the world" as a review of "some 400 major scientific contributions … released through peer-reviewed literature or from research institutions over the last three years," according to its press release.

The UNEP update finds more sobering, even scarier, climate changes under way than IPCC did. The prime driver of global warming, emissions of carbon dioxide from burning fossil fuel, surged between 2000 and 2006, the report notes. The rate of emissions growth nearly tripled compared with the 1990s as economic growth surged, particularly in China and India. According to the report, that spurt has already contributed to a host of sooner-than-expected climate impacts, including "faster sea-level rise, ocean acidification, melting of Arctic sea-ice cover, warming of polar land masses, freshening in ocean currents, and shifts in circulation patterns in the atmosphere and the oceans."

The UNEP report also appears to update IPCC 2007 by citing an unofficial but peer-reviewed revision of IPCC 2001's "reasons for concern." The 2001 assessment used a color-coded diagram to lay out the risk of five climate-change consequences expected for a range of possible future warmings. The risk of having more extreme-weather events, for example, was considered low at small warmings of 1°C or less (coded yellow at the bottom of a column), but it would be high (red at the top of a column) at large warmings of more than 3°C or 4°C (see figure).

IPCC 2007 didn't update the "burning embers diagram." But 15 climate scientists, including some of the 2001 IPCC authors, did so in a March 2009 paper in the *Proceedings of the National Academy of Sciences* (*PNAS*). Things now look worse in all five risk categories; the red of high risk has inched down to smaller warmings in each column. Several factors caused the reassessments, says *PNAS* author Gary Yohe of Wesleyan University in Middletown, Connecticut. After Hurricane Katrina struck in 2005, for example, the group realized that developing countries aren't the only ones at considerable risk of intensified coastal storms aggravated by rising sea level.

Many climate scientists share the heightened sense of urgency. A group of 25 or so researchers has prepared a document "very similar in tone" to the UNEP report. They will deliver it in a press conference to attendees in Copenhagen next month, says longtime climate researcher Richard Somerville, a professor emeritus at Scripps Institution of Oceanography in San Diego, California, and an author of the report. "We're seeing things happen more rapidly" than IPCC 2007 anticipated, he says. "I think IPCC has done a very responsible job, but now we know more, and the trends are all in the wrong direction." Especially worrying, Somerville says, is that greenhouse-gas emissions have increased faster than in IPCC's most pessimistic scenario, leaving even less time to rein them in before great harm is done. The world's ice also seems to be in particular trouble, threatening to raise sea level by a meter or more by the end of the century instead of the few tens of centimeters that IPCC projected

No more, no less concerned

Amid the calls for action, other climate researchers—equally concerned but less vocal—are advising caution in interpreting recent trends. The departures from IPCC 2007, they say, are not that large, not that unexpected, or not that indicative of future trends. Accelerating emissions growth is a case in point, says economist James Edmonds of the Joint Global Change Research Institute in College Park, Maryland. The speedup of the past 5 to 10 years marked a spurt in the world economy. Soon, Edmonds says, "we're going to see the effects of the recession." Such near-term fluctuations are a bad basis for forecasting far-future emissions, he says, and the IPCC scenarios were never intended to track them. Over the long term, however, "the trend is really clear: If there's no intervention, emissions are going to rise. Up, up, up is inconsistent with stabilization" of atmospheric greenhouse gases below dangerous levels, which is the stated goal of "every country on the face of the earth."

Most of UNEP's other "sooner-than-expected" climate effects—from ocean acidification to shifts in ocean circulation—have likewise failed to heighten concern among more guarded scientists. The lone exception,

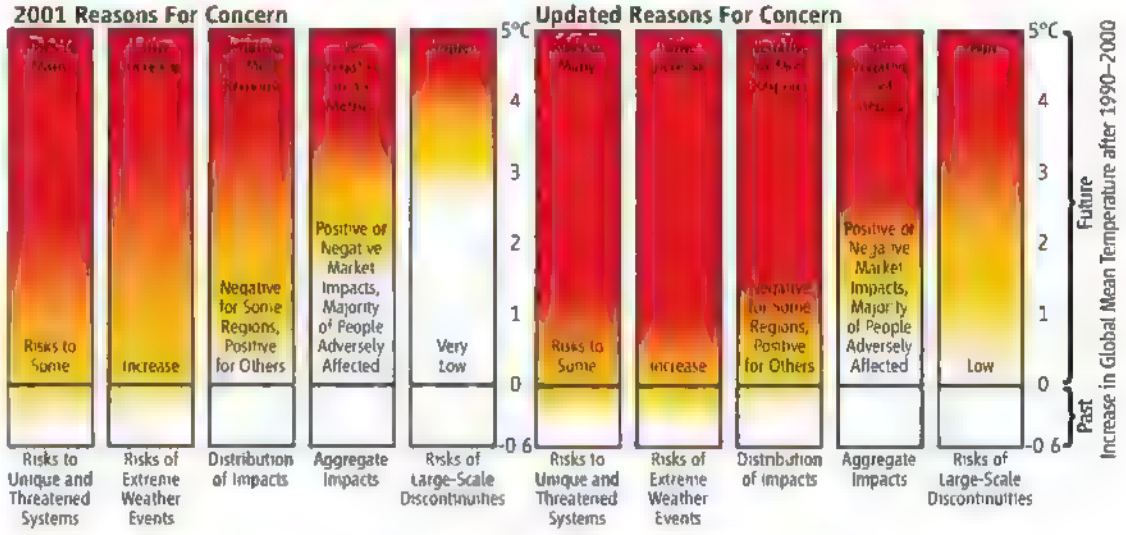

Burning brighter. The red denoting high risk has crept down to smaller warmings since 2001.

SOURCE: J. B. SMITH ET AL./PNAS

says glaciologist and IPCC author Richard Alley of Pennsylvania State University, University Park, is dwindling ice. The cryosphere—both floating sea ice and ice sheets on land—is reacting to the warming faster than IPCC projected, Alley says. In the Arctic, the 2007 report noted that some model projections had late-summer sea ice almost entirely disappearing "by the latter part of the 21st century." Models and sea-ice specialists now point to summer sea ice being gone by about 2030 (*Science*, 27 March, p. 1655).

On land, IPCC authors did recognize that losses from both the Greenland and West Antarctic ice sheets had picked up in recent years, owing in part to a surprising acceleration of glacier tongues draining ice to the sea (*Science*, 9 October, p. 217). But even with the observed accelerations factored in, IPCC projected that sea level would rise by only a few tenths of a meter by the end of the century. Subsequent analysis has suggested that the rise in sea level is running near the extreme high end of IPCC projections and could reach about a meter by century's end (*Science*, 8 June 2007, p. 1412).

The UNEP report dwells in detail on such fast ice responses. But some researchers say that the plight of the ice—although serious—is old news and is symptomatic of deeper concerns. Pope, for one, sees Arctic sea ice decline as a combination of a long-term loss due to global warming and bursts of ice loss like 2007's that are due to natural, temporary changes such as wind shifts. The long-term threat was already obvious to IPCC authors, Pope says.

Likewise, the recent faster rise in sea level fed by wasting ice sheets certainly concerns geoscientist Michael Oppenheimer of Princeton University, but he's long had a greater fear. "We still can't project sea-level rise," he says. "That worries me." A major problem is understanding how glaciers would behave in a warmer world—faster or slower than today's—and getting them to act that way in predictive models. Compounding the uncertainty is the slow response of kilometers-thick ice sheets to warming. Humans could put enough greenhouse gases in the atmosphere this century to guarantee that Greenland's ice will melt centuries from now, Oppenheimer says. The UNEP report discussed such irrevocable climate commitments, but they got little public attention.

And finally, the new "burning embers" do indeed tell an ominous story, says Schneider, who was second author on the *PNAS* paper that presented the updated graph. But it is a story, he says, of which the IPCC 2007 was already largely aware.

Unintended consequences?

Why does it matter whether the bad news is old news or new? Climate scientists feel that they are speaking with two voices, one much louder than the other. That worries Arctic climate researcher John Walsh of the University of Alaska, Fairbanks. "We have a delicate task of conveying the seriousness of the situation without overselling it as a done deal. We have a [climate] process that comes in fits and spurts," he says, referring to the big loss of summer sea ice in 2007 as well as recent losses from Greenland. "We have to be careful not to extrapolate" a short spurt far into the future. With all the attention given Arctic ice after the heavy 2007 loss, "I am a little concerned the imminence of rapid [Arctic] change is being oversold or the uncertainties aren't being conveyed," he says.

And Pielke wonders whether the louder, more insistent voice is the best one for the job. "One of the strengths of the IPCC is it can make a pretty solid claim to be a consensus process," he says. "I'm a little bit leery of the process at [the meeting in] Copenhagen earlier this year and the UNEP effort. They don't have the same institutional legitimacy" as IPCC.

Whether or not the public is hearing the right tone of voice from the right places, it doesn't seem to be getting the message anymore. Recent polling suggests that U.S. citizens, at least, are if anything less concerned about global warming than they were a few years ago. In polling at the end of September conducted by the Pew Research Center for the People and the Press, the proportion of Americans who "think there is solid evidence that the average temperature on earth has been getting warmer over the past few decades" dropped to 57% from 71% in April 2008, according to Pew pollsters. The proportion of the American public that views global warming as a very serious or somewhat serious problem dropped from 73% to 65%. And in a Gallup poll released in March, the proportion of Americans who believe that the seriousness of global warming is exaggerated hit 41%, a record high in the 12 years Gallup has asked that question.

Declining concern. Gallup polls suggest that more Americans feel that the seriousness of global warming is exaggerated and fewer are worried about it.

Apparently, anxious warnings of imminent climate crises are no longer getting through. Matthew Nisbet thinks he knows why. The political communications researcher at American University in Washington, D.C., says that "it's very difficult for any single [climate] event to break through competing issues and information." For Americans, those issues now include two wars, a lurching economy, and health care reform.

"Given the complexity of climate change," Nisbet says, "any one event will be downplayed [by partisan critics]. I think the real long-term challenge is public education, to prepare people. What does it mean to be an American in an era of climate change?" Climate scientists need to refocus their message, he says, from the broad sweep of global warming to small regions such as New England and the Southwest and to immediate issues such as personal health. At the same time, new conduits to individuals need to be created to replace crumbling traditional media. A tall order. **–RICHARD A. KERR**

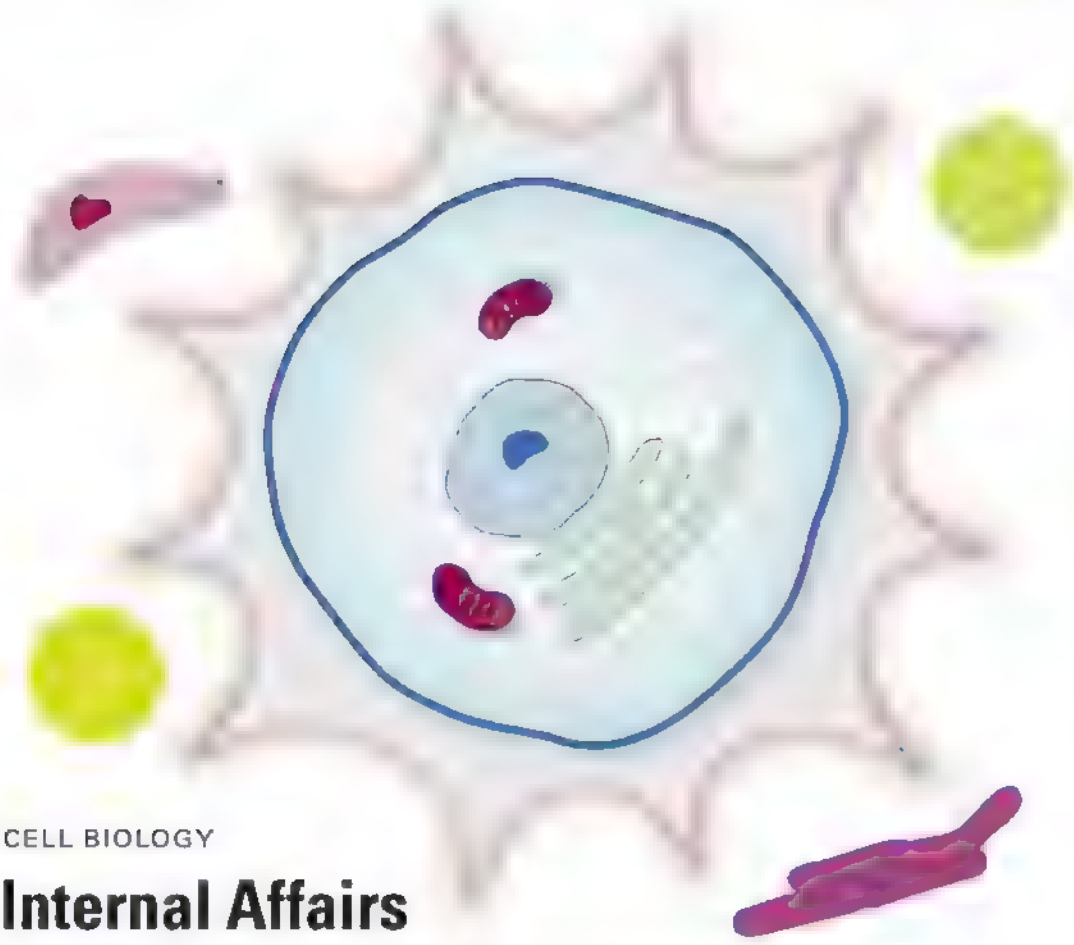

Enemies within. Our cells' internal defenses keep busy warding off intruding pathogens.

CREDIT: J. NEWFIELD/SCIENCE

CELL BIOLOGY

Internal Affairs

Newly discovered cytoplasmic defenses sound the alarm when pathogens penetrate our cells

For many pathogens, the interior of the cell is a prime place to settle down and start a family. Once they sneak into our cells, bacteria can plunder nutrients and duck the immune system. Viral intruders gain access to the molecular machinery they need to replicate. No wonder, then, that myriad microbes, including the germs responsible for the world's biggest infectious killers—AIDS, tuberculosis, and malaria—barge into our cells.

Our cells fight back against these intrusions, relying on a network of novel internal alarms that can trigger an infected cell to try to save itself, or to at least provoke the body to defend other cells. The ultimate goal is to ensure "the sanctity of the cytoplasm is preserved," says immunologist Katherine Fitzgerald of the University of Massachusetts Medical School in Worcester. Although researchers have long known that cells attempt to repel invaders—for example, by blocking viral replication—over the past decade or so, scientists have discovered protections that are more elaborate and have a much broader impact than anyone suspected.

To keep watch for internal intruders, a cell deploys a cytoplasmic surveillance system that parallels the one detecting menaces outside of its membrane. When infiltrating pathogens trip one of these alarms, the cell retaliates with measures that range from instigating inflammation to committing suicide in a way that alerts other cells to the threat. In turn, microbes have evolved a plethora of countermeasures to disrupt, deceive, and dodge these intracellular weapons.

The medical importance of our cells' internal defenses goes beyond battling pathogens. Errant responses by these alarm systems underlie illnesses such as gout, Crohn's disease, which is a type of intestinal inflammation, and the lung deterioration provoked by asbestos. Some of what scientists have learned about the mechanisms of such diseases has already made it to the clinic: The discovery that faulty microbial receptors inside the cell are behind several rare but debilitating "fever syndromes" inspired a successful new treatment for those conditions. Researchers have been testing the same drug against gout. Furthermore, scientists have just realized that a chemical long used to boost the effectiveness of vaccines might work by activating one of the cell's internal tripwires. This insight could lead to the production of better, safer ingredients for future immunizations. "We lack vaccines for many infections," says immunologist Russell Vance of the University of California, Berkeley, but understanding our cytoplasmic defenses "might help us trigger the right kind of immune responses to get protection."

Looking inward

Many animal cells, especially immune sentinels such as dendritic cells and macrophages, scrutinize their surroundings with Toll-like receptors (TLRs), more than a dozen of which have been identified. These cell-surface proteins recognize specific conserved features of broad classes of microbes, so-called pathogen-associated molecular patterns (PAMPs). For example, the PAMP for TLR-5 is the protein flagellin, a component of the flagellum that propels many kinds of bacteria. When triggered, TLRs unleash the primary, or innate, immune response and also help guide the subsequent adaptive response from T and B cells, which rely on microbe-specific receptors.

The study of plant defenses sparked the discovery that the cytoplasm of animal cells contains equivalents of TLRs. Plants detect invaders inside their cells with so-called resistance, or R, proteins (*Science*, 8 May, p. 744), and nearly a decade ago researchers began searching mammalian genome databases for analogs of these proteins. They found plenty. In animals, "there's an elaborate intracellular detection array, just like there's an elaborate extracellular array," says immunopathologist Brad Cookson of the University of Washington (UW), Seattle. So far, the intracellular array in humans numbers more than 20 pathogen sensors called nucleotide-binding domain and leucine-rich repeat containing proteins (NLRs) that distinguish bacteria, parasites, and other interlopers. Other pathogen detectors within cells include at least three so-called RIG-I-like receptors, which

check mainly for the genetic material—RNA or DNA—of viruses, and proteins called AIM2 and DAI, which scan for the DNA of microbial interlopers. Identifying these cytoplasmic molecules "gave us the tools to examine more rigorously the role of these mechanisms in host defense," says immunopathologist Gabriel Nuñez of the University of Michigan, Ann Arbor, whose team was one of the first to demonstrate that an NLR could discern a pathogen.

"There's an elaborate intracellular detection array, just like there's an elaborate extracellular array."

—BRAD COOKSON, UNIVERSITY OF WASHINGTON, SEATTLE

What the pathogen detectors actually sense is one of the field's biggest questions. Scientists have notched progress in understanding how particular intracellular receptors identify invaders. Like TLRs, some intracellular receptors bind PAMPs. RIG-I, for instance, homes in on viral RNA molecules, allowing it to spot killers such as HIV and the hepatitis C virus.

A cellular trick expands the range of pathogens that RIG-I can detect, biochemist Zhijian Chen of the University of Texas Southwestern Medical Center at Dallas and colleagues reported in the 7 August issue of *Cell*. In a cell's nucleus, the enzyme RNA polymerase naturally makes an RNA copy of a gene, the first step in synthesizing the protein the gene encodes. Chen and colleagues found, however, that in the cytoplasm, RNA polymerase copies any stray DNA it encounters—which likely comes not from the cell but from a pathogen—into double-stranded RNA that RIG-I can recognize. This mechanism enables RIG-I to discern not only DNA-carrying viruses such as adenoviruses and the Epstein-Barr virus but also certain bacteria. "Cells have found a way to take advantage of the RIG-I pathway to sense DNA in the cytosol," says Chen.

Still, researchers remain in the dark about how most of the cytoplasmic receptors spot their microbial targets. A prime example is the intracellular protein NLRP3, which responds not only to bits of bacterial cell wall within the cytoplasm but also to stimuli as diverse as the monosodium urate crystals that torture gout patients and the industrial toxicants asbestos and silica (*Science*, 2 May 2008, p. 674). "You can't find a binding place on this protein for all these activators," says biochemist Jürg Tschopp of the University of Lausanne in Switzerland.

Undiscovered receptors might serve as the actual detectors of each stimulus, with NLRs functioning as their intermediaries, suggests biologist Ed Miao of UW Seattle. If so, a cell might have one internal sensor for monosodium urate, one for bacterial cell walls, and one for asbestos—all of which relay their status to NLRP3.

Alternatively, says Vance, the triggers that activate NLRs might be internal cell changes that result from attack or from injury by toxicants such as asbestos. "Instead of sensing microbes or microbial products directly, it [the receptor] would sense some kind of damage that the microbe causes," he suggests. An example of these "danger signals," Tschopp says, is monosodium urate, which forms when dying cells discharge the metabolic waste product uric acid. If the danger signal mechanism is valid, researchers still need to explain how NLRs are able to respond to such diffuse activators. Tschopp suspects that the common trigger for NLRP3 is the reactive oxygen species that cells produce in their cytoplasm when under stress, such as when they attempt to swallow asbestos fibers or encounter monosodium urate.

Gotcha—now what?

Once a cell perceives an internal invasion, it has several options. The cell might attempt to destroy the interloper. For example, an assortment of bacteria and viruses can provoke autophagy, a "self-eating" mechanism in which cells envelop and digest part of their cytoplasm—and any microbes it contains. Infected cells can also call for help that may prevent other cells from succumbing to their fate. As Tschopp and colleagues discovered in 2002, activated NLRs can convene several kinds of cytoplasmic proteins to form what the scientists dubbed an inflammasome. Joining the NLRP3 inflammasome, for instance, are multiple copies of NLRP3, an adaptor protein called ASC, and an inactive form of the enzyme caspase-1. Non-NLR receptors such as AIM2 can also induce inflammasomes. These protein clusters appear to be crucial for immune defenses. Without them, mice die from what are normally nonlethal doses of influenza virus, researchers reported earlier this year.

An inflammasome furnishes an editing platform

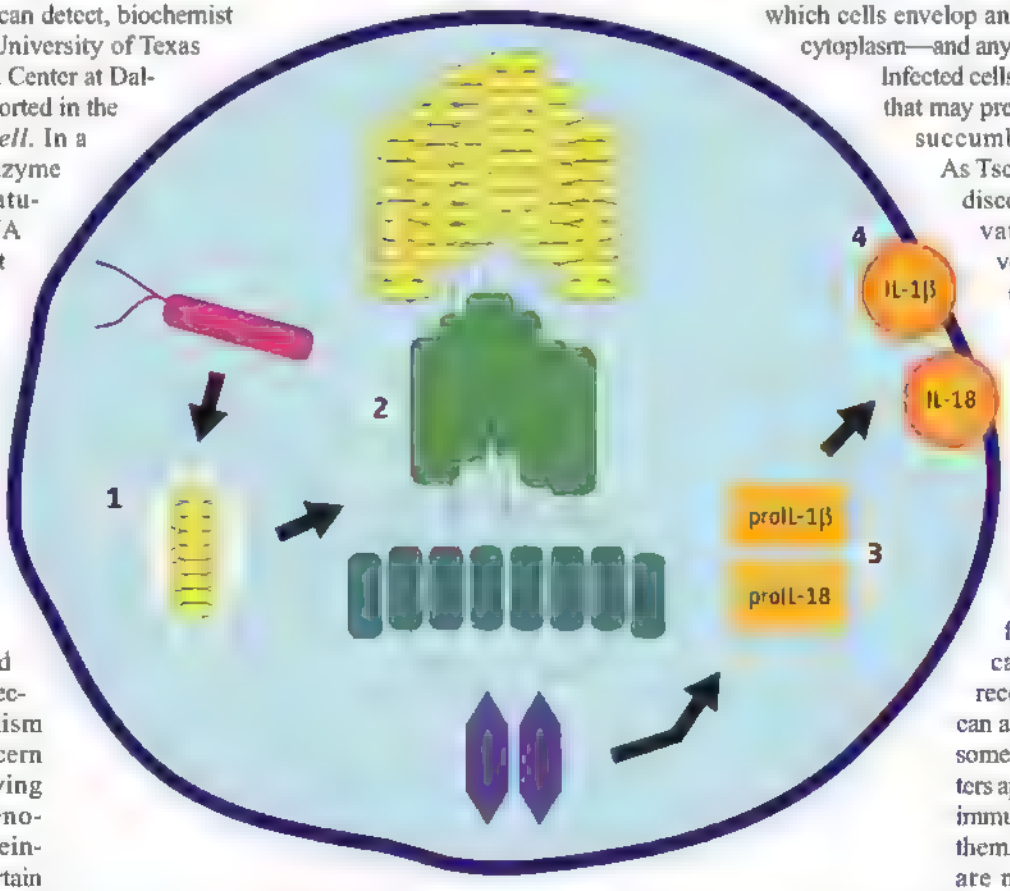

Triggering the alarm. When the cytoplasmic sensor NLRP3 recognizes a pathogen (1), it sets off a chain of events that lead to inflammation. The activated sensor draws in more NLRP3 molecules and other kinds of proteins to form an inflammasome (2). After the enzyme caspase-1 (purple) switches on, it activates the cytokines IL-1β and IL-18 (3). The end result is the release of these inflammation-promoting molecules (4).

CREDIT: J. NEWFIELD/SCIENCE

where caspase-1 activates itself and then prunes and switches on the cytokines interleukin-1β (IL-1β) and IL-18, which the cell then releases. Both cytokines, but particularly IL-1β, are formidable pathogen-fighters, triggering inflammation and attracting other immune cells to battle. They can even draw in T and B lymphocytes, potentially unleashing the adaptive immune system on the invader. Although these responses may not save the infected cell, they can prevent other cells from falling victim.

The multistep system for activating cytokines might seem baroque, but it makes sense from a safety perspective, says systems biologist Alan Aderem of UW Seattle. "The innate immune system is very dangerous," he says. Inflammation helps stanch infection, but it also promotes many of our most deadly illnesses, including heart disease, Alzheimer's disease, cancer, and diabetes. Triggering cytokines through the inflammasome, rather than directly from an NLR, adds another safeguard against inappropriate inflammation, says Aderem.

Stimulation of NLRs can even prompt cells to sacrifice themselves by committing suicide. "If they can't clear the pathogen and remain viable, they clear it by dying," says microbiologist Craig Roy of Yale University. The most familiar kind of cell suicide—apoptosis—doesn't result in the release of cytokines or the immune system being alerted. But when certain NLRs detect intracellular invaders, they switch on caspase-1 in a manner that instigates the cell death program and the production of IL-1β and IL-18. Cookson and his then–grad student Molly Bergman dubbed this process pyroptosis; essentially, a fiery death. Not only does a pyroptotic cell pour out cytokines that spur inflammation and fever, but it also spills its insides, which also rouse the immune system. The combination sends out a stronger warning signal than cytokines alone. A further benefit is the elimination of "a 'Trojan horse' loaded with pathogenic invaders," Cookson says.

Cheaters do prosper

Our survival depends on cytoplasmic defenses, and microbes' survival depends on evading them. Researchers have already compiled several examples of bacterial and viral chicanery. For example, Chen and colleagues have discovered that when RIG-I senses a viral invader, it transmits the alarm through MAVS, a protein they named in honor of their local pro basketball team, the Dallas Mavericks. Just as the Mavericks have the Los Angeles Lakers, MAVS also has its nemesis—an enzyme carried by the hepatitis C virus that snips the protein off at the base. This ability to cut the receptor's line of communication helps make the virus a killer, says Chen.

Other microbes attempt to stymie intracellular defenses by defusing the inflammatory cytokine IL-1β or blocking activation of caspase-1. The tuberculosis bacterium prevents the inflammasome from switching on, researchers discovered last year, although they don't know how. To avoid being digested, the bacterium that causes Legionnaire's disease hinders autophagy, as microbiologist Michele Swanson of the University of Michigan, Ann Arbor, and colleagues have found.

So far, the most important medical insight to emerge from research on NLRs involves the little-known fever syndromes, which affect about 500 people worldwide. Patients with familial cold autoinflammatory syndrome, for example, can develop a fever, skin rash, and joint pain after only a few minutes outside on a chilly day. The more severe Muckle-Wells syndrome often brings on kidney damage and deafness. About 10 years ago, researchers discovered that this disease family stems from different mutations in the *NLRP3* gene. When Tschopp and colleagues discovered that NLRP3 spurs IL-1 production through the inflammasome, other researchers decided to treat patients with what was then a new drug, known as anakinra. This substance blocks the IL-1 receptor and was originally developed to soothe rheumatoid arthritis. It worked against the fever syndromes, and in 2007 the U.S. Food and Drug Administration approved it for that purpose. Nuñez describes this case as "a beautiful example" of how a basic science discovery can lead to a new treatment.

But patients with these rare illnesses aren't the only ones who could benefit. Nearly half of people with Crohn's disease carry mutations in an NLR called NOD2. Scientists have yet to discover how faulty NOD2 foments the condition's intestinal agony; it may undermine intestinal protections against bacteria or provoke excess inflammation. Faulty internal defenses might even contribute to chronic diseases such as heart disease and diabetes that involve inflammation. "There's some evidence but no definitive studies," Nuñez says. Nonetheless, researchers have reported that anakinra benefits patients with type 2 diabetes.

Hot and cold. In people with a rare condition called familial cold autoinflammatory syndrome, chilly temperatures trigger a rash, fever, and joint pain. A faulty inflammasome protein is the culprit.

Better vaccines will be another payoff from this field, several researchers predict. Vaccines contain additives called adjuvants that amplify the immune response. In the United States, the only approved adjuvant is aluminum hydroxide, or alum. Although alum can boost immunity, it can also trigger fever and other side effects. One obstacle blocking vaccine improvements is that researchers didn't know how alum tweaks the immune system. But some recent studies suggest that alum provokes the inflammasome. If so, researchers might be able to fine-tune adjuvants to induce a strong inflammasome response while provoking fewer side effects.

Whether we will be able to manipulate cytoplasmic defenses for our benefit is unresolved. However, natural selection will keep tinkering with our internal defenses to ensure that our cells aren't hopelessly defeated for long. But in this evolutionary arms race, the microbes that want to settle inside our cells have the advantage, Roy says. "Because the bugs evolve faster, they are always going to stay a few steps ahead."

–MITCH LESLIE

CREDITS (LEFT TO RIGHT): WIKIPEDIA; JES ERV. BERGMAN/CORBIS; WIKIPEDIA

Ready to roll. Ground is prepared at the ITER site in France. Cement mixers are due next spring.

FUSION

ITER Blueprints Near Completion, But Financial Hurdles Lie Ahead

As staff put finishing touches to the fusion project's final design, member governments mull over the latest cost estimates and prepare to raid piggybanks

CADARACHE, FRANCE—When diplomat Kaname Ikeda took the job of director-general of the ITER fusion reactor project in 2006, he quickly realized that he was building something literally from the ground up. "There was just a forest here when I started and six or seven people working," he says. Now a large, if temporary, office building houses more than 400 staff members and another one is taking shape next door. Meters away, beyond a fence and up a bank, stretches a vast flat expanse of gravel, 1 kilometer long and 500 meters wide, made by slicing off the top of a hill. Next spring, this area—which ITER staff members jokingly liken to a huge terrain for pétanque, the game of bowls played in towns and villages across France—will be a bustling construction site as the world's largest scientific experiment takes shape. But for now, quiet expectation reigns.

But this quiet is not a sign of inactivity. Inside headquarters, researchers are working feverishly toward one of the project's early milestones: completion of the Project Baseline, a complete description of the machine's scope, design, construction schedule, and cost. This set of documents, which runs to thousands of pages, will be presented for approval on 18 November to the ITER Council, representing the project's seven international partners: China, the European Union, India, Japan, South Korea, Russia, and the United States. The meeting will be a turning point for the project. "It's a bit like a starting pistol. It [the baseline] is a big framework on which to hang the work of the next 10 years," says David Campbell, deputy head of ITER's fusion science and technology department. From the point of view of the project's paymasters, one part of the baseline will be subject to special scrutiny: the cost.

ITER, or the International Thermonuclear Experimental Reactor, seeks to demonstrate that nuclear fusion—the power source of the sun and stars—can be tamed on Earth to generate electricity. In the 3 years since the partners formally agreed to work together on the project, its estimated cost has ballooned. Earlier underestimates, rising construction costs, and design and schedule changes aimed at reducing risks have landed the partners with bills substantially higher than they were expecting. Although all appear committed to the project, tough discussion is likely at this month's council meeting. "Everyone's concerned about cost containment," says Campbell. "There's a tension between cost and time to completion, but if you move too fast you can get technical difficulties. You have to strike the right balance."

First milestone. Staff from ITER and French and European agencies celebrate the end of site preparation.

Plasma physicists have been working on the design of ITER since the mid-1980s. When the agreement was signed to set the ball rolling in 2006, the estimated cost was roughly €5 billion to build the reactor and another €5 billion to operate it for 20 years. Those figures, however, were based on a 5-year-old design drawn up before the site was decided (Cadarache was chosen in 2005) and when only three partners (the European Union, Japan, and Russia) were on board. In addition, fusion science had moved on since 2001, and researchers were itching to make changes to ensure that the project was a success.

So even as the ink was drying on the ITER agreement, the seven partners called for a design review. "We asked the whole international community to say what their worries were" by filling out "issue cards," says Campbell. By early 2007, researchers had registered about 500 issues. ITER staff and external experts were assembled into eight panels that worked through all the issues. Some problems required only minor tweaks and some could be discounted, Campbell says. By the end of 2007, the panels had whittled the number down to 13 major issues that needed more effort. "We spent another 6 to 12 months working on them. Some significant changes in design were needed," Campbell says.

One of the most significant changes was a new system to help control the plasma, a maelstrom of ionized hydrogen gas heated to 150 million degrees so that nuclei will have enough energy to smash together and fuse. But instabilities in the plasma called edge-localized modes (ELMs) act like quakes at the plasma boundary. They can make it bulge out unpredictably, damaging the wall of the doughnut-shaped reactor, known as a tokamak, or the divertor, a structure around the bottom of the reactor that extracts helium, the spent fuel of fusion. "ELMs have a devastating effect. A reliable mitigation technique would have tremendous value,"

CREDITS: ITER ORGANIZATION

says Norbert Holtkamp, ITER's second in command and construction leader.

ITER already had one system for combating ELMs, firing small pellets of frozen deuterium into the plasma at regular intervals to provoke small quakes, which do less damage and seem to suppress the larger ones. But researchers working with the U.S. tokamak DIII-D in San Diego, California, discovered that they could suppress ELMs with an extra magnetic field. So the review team modified the design to include magnetic coils for quelling ELMs behind the blanket tiles that line the inside of the reactor vessel.

The blanket also came under scrutiny in the design review. It absorbs the heat and fast-moving neutrons flying out of the plasma once fusion is taking place, protecting components, and people, outside. It is made up of 440 tiles, most of them 4.6-tonne slabs of copper and steel measuring 1 meter by 1.5 meters. The plasma-facing side of the tiles is key. It must be tough enough to withstand the touch of plasma at 150 million degrees but also made of a material that won't pollute the plasma if it does get burned off. This "first wall" will be made of beryllium, but other materials may be tested later. The first wall of the divertor, which faces a higher heat load, will be carbon composite and tungsten. "We needed to review the heat loads and make corrections to the design," says Gary Johnson, head of ITER's tokamak department.

Another key change to come out of the design review was a requirement to test all of ITER's magnets at cryogenic temperatures. ITER uses 48 huge magnet coils to control the plasma. Each of the 18 toroidal field magnets, which loop through the center of the tokamak, weighs more than 360 tonnes, as much as a fully laden Boeing 747. The magnets are made of superconducting cable that works at about 4 kelvin. Thorough testing "can reduce the risk of installing a flawed device," says Johnson, so new facilities will be built on site and elsewhere in Europe to test each magnet at low temperature.

These and other changes resulting from the design review "have a major impact scientifically," says Holtkamp, but they increase the project's cost by less than 15%. As work progressed, however, it emerged that the 2001 design had seriously underestimated the cost. And as staff continued refining the design and drawing up the project baseline, it soon became obvious that the planned construction and schedule was "too risky," Holtkamp says. "Certain things needed to be added or adjusted to ensure the scientific goals were achieved." But such changes would bring higher costs, delays, or both.

The issue came to a head at the council meeting in June 2008 when the partners told ITER staff members that they had to get a better handle on costs and not let the start date slip. "We received clear guidance," Holtkamp says. "Make a schedule to reach first plasma by 2018, quantify the risk, and report back." At the same time, the council formed two independent panels to assess the work of the ITER organization: one looking at how costs are estimated and managed, the other at systems engineering and management.

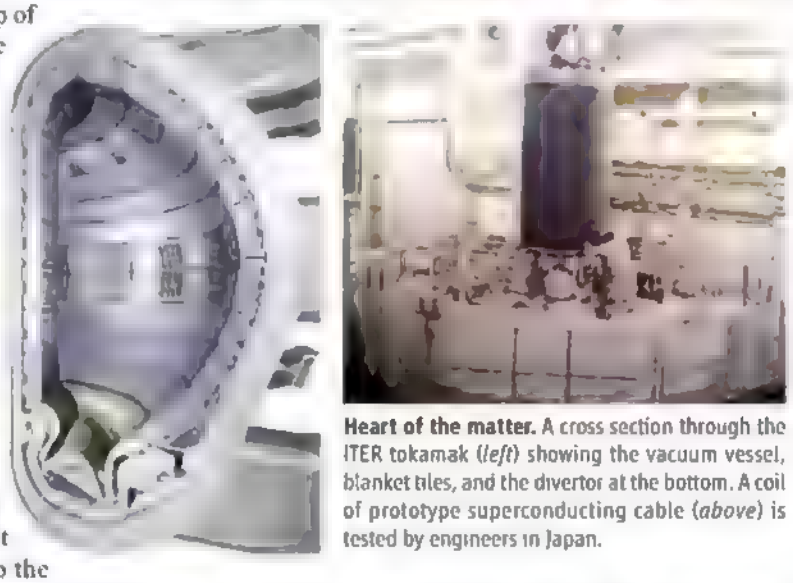

Heart of the matter. A cross section through the ITER tokamak (*left*) showing the vacuum vessel, blanket tiles, and the divertor at the bottom. A coil of prototype superconducting cable (*above*) is tested by engineers in Japan.

CREDITS: ITER ORGANIZATION

One reason for the uncertainty in ITER's cost is the way in which the reactor is constructed and paid for. The ITER organization does not have a large sum of money to buy all the parts. Instead, partner countries carve up the design and then each pays its own industries to make their share of the components and ship them to Cadarache. Hence ITER staff members control only 10% of the machine's cost, the rest comes as these in-kind contributions. As a result, ITER's true cost is very hard to pin down. The 2001 design had put a value on each component so they could be shared out fairly and then calculated an overall cost from those values. But "different countries [cost things] in different ways," Campbell says, and the 2001 estimates have proved inaccurate. Because of the different systems in different parts of the world, "a simple addition of the cost in each country is an unfair representation of the cost of ITER," Holtkamp says.

Another factor pushing up the cost is the ITER collaboration's principle that all partners get an equal share in the knowledge of how to build the reactor. "Each member wants to learn how to make everything," says Ikeda. So large items, such as the magnets and the vacuum vessel, are not built in one place but are divided between the partners. That approach seemed reasonable for three partners in 2001, but with seven partners economies of scale are lost. ITER staff members have negotiated some cost-saving rationalizations with relevant agencies in the seven partner countries, although Holtkamp emphasizes that the council has yet to approve them.

Over the past year, as staff members continued to analyze the construction schedule, "it became clear we had to change something in the sequence of assembly. We had to take an approach that reduces risk for the project," says Holtkamp. To reduce pressure on the schedule, ITER planners proposed firing up a stripped-down version of the reactor in 2018 without many components needed for later power-producing plasmas. "If something is wrong, it will be easier to repair," says Holtkamp. "Once we know this is okay, we can install the rest." Some 15% to 20% of components would be installed later, and the scheduled start date of 2026 for power production is little changed.

In June, the council approved the new schedule, contingent on its approving the full baseline this month. The issue of cost still hangs heavy in the air. E.U. documents suggest it may need to fork out twice what was originally forecast. (The European Union, as host, must pay a 45% share of ITER's construction costs; the others pay 9% each.) A few months ago, "the E.U. had asked for a number of remedial measures for cost containment and improved management to be put in place. This is work in progress," says E.U. research spokesperson Catherine Ray. "We need a realistic timetable, we need to be sure that we are basing our decisions on credible cost estimates, and we need to be sure that responsible organizations will be able to deliver on it."

"The fact that it will cost more is more or less accepted. Parties are carefully addressing how to handle the increase, such as through cost optimization," says Ikeda, though he concedes that "some partners may be struggling." "The partners want to understand the risk," says Holtkamp. "All countries want to find a comfort level. Has [all our work] provided comfort? I hope so. We'll find out soon."

–DANIEL CLERY

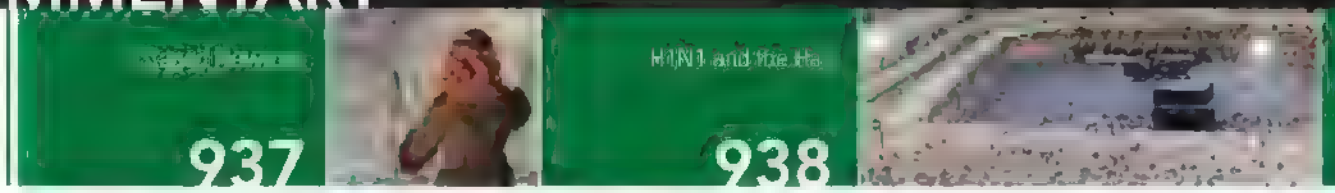

LETTERS

edited by Jennifer Sills

Protecting the Herd from H1N1

HERD IMMUNITY—THE CONCEPT THAT HIGH VACCINATION COVERage can provide partial or even complete protection to those not vaccinated—has been a component of vaccination policy for more than 50 years (*1*, *2*). J. Medlock and A. P. Galvani ("Optimizing influenza vaccine distribution," Reports, 25 September, p. 1705) applied this concept to the current H1N1 situation and concluded that officials should target vaccination to those that contribute the greatest transmission (schoolage children and their parents) rather than focusing on high-risk individuals, thus indirectly protecting high-risk groups through herd immunity. Herd immunity, however, may not be attained at the predicted levels because the authors failed to adequately consider vaccine coverage and the reproductive number, R_0, a measure of the epidemic potential.

Using all vaccine supplies on schoolchildren and particularly their parents suggests unrealistically high coverage within these groups given that vaccination is voluntary. There is a growing awareness that R_0 is highly heterogeneous (depending on mixing patterns, host susceptibility, pathogen characteristics, and environment) (*3*). R_0 may be large in certain social contexts (e.g., schools and vulnerable populations) and small in others. High-risk individuals might be socially clustered, thus ignoring them in vaccine policy may put this group at higher risk. Coverage level determined by mean R_0 may therefore result in local herd immunity in some groups but not others.

Using transmission models to address optimal vaccination strategies is a powerful approach to inform policy when the inferences derived from them are robust to uncertainty and variability in disease processes. In the analysis by Medlock and Galvani, we are unconvinced that there is sufficient justification for the Advisory Committee on Immunization Practices to alter their targeting of high-risk individuals. We do agree that the U.S. Centers for Disease Control and Prevention should take into consideration the results of multiple analyses that point toward indirect benefits of vaccine coverage (*2*, *4*). Future transmission models would be more robust if they consider more realistic social mixing patterns within communities.

JOSEPH N. S. EISENBERG,[1]* ALLISON E. AIELLO,[1] IAN H. SPICKNALL,[1] ARNOLD S. MONTO,[1] ARTHUR REINGOLD[2]

[1]Department of Epidemiology, University of Michigan, Ann Arbor, MI 48109, USA. [2]Epidemiology Division, School of Public Health, University of California, Berkeley, CA 94720, USA.

*To whom correspondence should be addressed. E-mail: jnse@umich.edu

References

1. A. S. Monto, F. M. Davenport, J. A. Napier, T. Francis Jr., *J. Infect. Dis.* **122**, 16 (1970)
2. D. Weycker *et al.*, *Vaccine* **23**, 1284 (2005)
3. J. O. Lloyd-Smith, S. J. Schreiber, P. E. Kopp, W. M. Getz, *Nature* **438**, 355 (2005)
4. Y. Yang *et al.*, *Science* **326**, 729 (2009)

Response

EISENBERG *ET AL*. ARGUE THAT OUR ANALYSIS is insufficient to warrant a change in vaccination policy because of questions regarding the ability to achieve high coverage in schoolchildren and the effect of variation between individuals in transmission potential.

The feasibility of achieving optimal vaccine allocation is demonstrated by the coverage of more than 90% routinely achieved in children for vaccines, such as those against measles, polio, and pertussis in the United States (*1*). On the basis of our analysis, most optimal influenza vaccine allocations require coverage levels that are indeed lower than 90% in schoolchildren [e.g., less than 75% coverage for $R_0 = 1.4$ when minimizing deaths (fig. S7 in our Report)]. Therefore, the levels of influenza vaccine coverage optimally required in schoolchildren seem achievable, although parental concern about the safety of vaccines may be an impediment.

Individuals of the same age vary in their propensity to transmit infection to others. However, identifying "superspreaders" by the behavioral, immunological, or genetic factors that lead to an elevated transmission potential is highly challenging in epidemic and pandemic outbreaks. By contrast, age-specific allocations are easier to implement and could be administered, for example, by offering vaccines that target schoolchildren in schools. In addition, modeling studies that include variation in contact rate based on detailed simulation of mixing patterns have also found vaccination of schoolchildren to improve population-level outcomes (*2*–*5*). Therefore, we do not believe that heterogeneity in transmission potential would significantly affect our results, although this remains to be tested.

JAN MEDLOCK[1]* AND ALISON P. GALVANI[2]

[1]Department of Mathematical Sciences, Clemson University, Box 340975, Clemson, SC 29634, USA. [2]Epidemiology and Public Health, Yale University School of Medicine, New Haven, CT 06520, USA.

*To whom correspondence should be addressed. E-mail: medlock@clemson.edu

References

1. World Health Organization, *Immunization Coverage* (www.who.int/immunization_monitoring/routine/immunization_coverage/en/index.html)
2. D. Weycker *et al.*, *Vaccine* **23**, 1284 (2005)
3. I. M. Longini, M. E. Halloran, *Am. J. Epidemiol.* **161**, 303 (2005)
4. R. Patel, I. M. Longini, M. E. Halloran, *J. Theor. Biol.* **234**, 201 (2005)
5. E. Goldstein *et al.*, *J. R. Soc. Interface*, 10.1098/rsif.2009.0393 (2009).

942

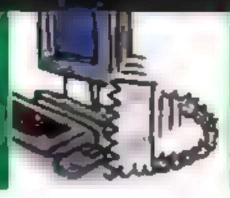

are not secure
943

Repurposing for Neglected Diseases

IN THEIR POLICY FORUM "REPURPOSING with a difference" (12 June, p. 1394), M. S. Boguski *et al.* predict that changes in pharmacovigilance procedures will increase the opportunities for drug "repurposing." We agree with the authors' proposition but note that this strategy is restricted to first-world needs and resources. The gap in R&D when diseases of poverty are concerned is unlikely to be modified by changes in pharmacovigilance, given that populations affected by these diseases are mostly excluded from medical care.

Nonetheless, we believe that the foundations of repurposing, with new perspectives and strategies, can represent an invaluable tool worldwide, including the so-called "neglected diseases" (*1*). For example, the description of unexpected similarities between unicellular pathogenic parasites and cancer cells led to efforts to define antiparasitic effects of drugs originally developed for treating cancer. Hexadecylphosphocholine (Miltefosine) (*2*) was developed as an antineoplastic drug in the early 1980s, but its anti-leishmanial activity ultimately led to its approval as the first oral drug for the treatment of visceral leishmaniasis in India (*3*). Tamoxifen, a drug used to treat breast cancer for more than 30 years, has been shown to be effective in experimental models of cutaneous and visceral leishmaniasis (*4*–*6*). These are striking examples that represent academic research initiatives.

In spite of the enormous decrease in cost of repurposing projects, as compared to a conventional R&D program, they too need funding and support. Public policies to allow repurposing for neglected diseases are urgently needed to reduce another (perhaps narrower) gap: the one between the laboratory and the sick.

SILVIA RENI BORTOLIN ULIANA AND MARCELLO ANDRÉ BARCINSKI*

Departamento de Parasitologia, Universidade de São Paulo, São Paulo 05508-000, Brazil

*To whom correspondence should be addressed. E-mail: barcinsk@icb.usp.br

Letters to the Editor

Letters (~300 words) discuss material published in *Science* in the previous 3 months or issues of general interest. They can be submitted thr[illegible] [illegible]ence.org) or [illegible] mail (1200 Ne[illegible] 20005, USA). Lette[illegible] [illegible] publication[illegible] lished in full [illegible] [illegible]ing for clarity and [illegible]

References

1. P. J. Hotez *et al.*, *Lancet* **373**, 1570 (2009).
2. S. L. Croft, J. Engel, *Trans. R. Soc. Trop. Med. Hyg.* **100**, 54 (2006).
3. S. K. Bhattacharya *et al.*, *J. Infect. Dis.* **96**, 591 (2007).
4. D. C. Miguel *et al.*, *J. Antimicrob. Chemother.* **60**, 526 (2007).
5. D. C. Miguel *et al.*, *PLoS Negl. Trop. Dis.* **2**, e249 (2008).
6. D. C. Miguel *et al.*, *J. Antimicrob. Chemother.* **63**, 365 (2009).

Response

ALTHOUGH WE PROPOSED SOME TECHNOlogical approaches to repurposing pharmacovigilance, the fundamental, underlying challenge is the conceptual reorientation from seeking adverse effects to being equally vigilant about identifying unexpected beneficial effects. This new concept can be applied in a number of "low-tech" ways as well and, indeed, none of the examples cited by Uliana and Barcinski required online social networks or sophisticated data-mining but rather (to paraphrase Louis Pasteur) chance observations entering a prepared mind.

Uliana and Barcinski's point about the "cost of repurposing projects" underscores the real need for novel business models and/or regulatory and legal reforms in order to capitalize on the candidate drugs that are identified. This is especially true in the case of generic drugs or drugs that cannot otherwise be patented or have small markets. In such cases, where there is inadequate or uncertain financial return on the investment needed to conduct rigorous clinical studies to validate a new use, a not-for-profit model may be the only current, practical solution. This approach is being tested by OneWorld Health and Global Cures, Inc. (*1*). Innovative public-private partnerships might also address this issue. Other solutions may require reforms of patent law and/or changes in FDA doctrine that create new financial incentives for pharmaceutical and biotechnology companies to invest in such clinical studies. If the cost of drug development could be substantially decreased by such approaches, the barriers to entry for new companies might not require "first-world" resource levels and make economically feasible the development of new treatments for neglected diseases.

MARK S. BOGUSKI,[1]* KENNETH D. MANDL,[2] VIKAS P. SUKHATME[3]

[1]Center for Biomedical Informatics, Harvard Medical School, Boston, MA 02115, USA. [2]Children's Hospital Informatics Program, Children's Hospital Boston, Boston, MA 02115, USA. [3]Department of Medicine and the Cancer Center, Beth Israel Deaconess Medical Center, Boston, MA 02215, USA.

*To whom correspondence should be addressed. E-mail: Mark_Boguski@hms.harvard.edu

Note

1. Global Cures, Inc. was cofounded by V.P.S.

A SMART Plan for New Investigators

IT IS ENCOURAGING TO NOTE THAT NIH HAS chosen to focus on funding "new" investigators (*1*). However, I foresee some dangers in the specific means adopted ("Grants 'below payline' rise to help new investigators," J. Kaiser, News of the Week, 25 September, p. 1607). Increasing the grants funded below the quality cutoff to nearly one-fifth of all funded grants will not serve the goal of helping new investigators. If such applicants are not held to the stringent process of producing a grant that meets R01 quality requirements, what will happen to them when they are no longer new investigators and are then subject to the same rigors as the rest of the field? How will they have learned the science and craft of grant preparation? The (indirect) quota practice compromises scientific quality in favor of age, gender, and other subsidiary criteria.

This practice is reminiscent of the R23 and its replacement, the R29 First Independent Research Support and Transition (FIRST) award (*2*). However, these two early-investigator programs were discontinued by NIH because of unacceptable differences between these awards and R01s, including evidence that awardees of the R29 were less likely to secure subsequent R01 funding than were early-career investigators starting with an R01. The R29 mechanism was also under-resourced (*3*). Grant writing is an academic skill that we mostly learn from the grant peer-review system. If compromised, the NIH system will slip in overall quality.

Senior faculty often contract junior faculty to conduct at least part of their research

Instead of providing special funding directly to new faculty, we should make sure that they receive sufficient mentoring as they work on the projects of more experienced investigators. I propose a new type of grant: the Senior Mentor-initiated Academic Research Training (SMART) award. To obtain this funding, senior faculty must apply to recruit junior faculty or new investigators and groom them for future independent work. If the university or the equivalent research institute provides a fostering environment and scientific resources, NIH should match the SMART funding. In this way the grant could be used to better new scientists, with the help of senior faculty, instead of representing just another revenue-generating scheme for institutions.

DEBOMOY K. LAHIRI

Laboratory of Molecular Neurogenetics, Departments of Psychiatry and of Medical and Molecular Genetics, Institute of Psychiatric Research, Indiana University School of Medicine, Indianapolis, IN 46202, USA. E-mail: dlahiri@iupui.edu

References

1. J. Kaiser, *Science* 322, 834 (2008).
2. NIH Guide Notice, Vol. 26, No. 38 (21 November 1997); http://grants.nih.gov/grants/policy/r29policychange.htm
3. NIH 2007–2008 Peer Review Self-Study Final Draft (29 February 2008), http://enhancing-peer-review.nih.gov/meetings/NIHPeerReviewReportFINALDRAFT.pdf

CORRECTIONS AND CLARIFICATIONS

Brevia: "Oceanic spawning migration of the European eel (*Anguilla anguilla*)" by K. Aarestrup *et al.* (25 September, p. 1660). There were two errors in Fig. 1A. The first text label in the key should read "Pop-up position," and an arrow indicating the direction of the Sargasso Sea was missing. The corrected panel is shown here.

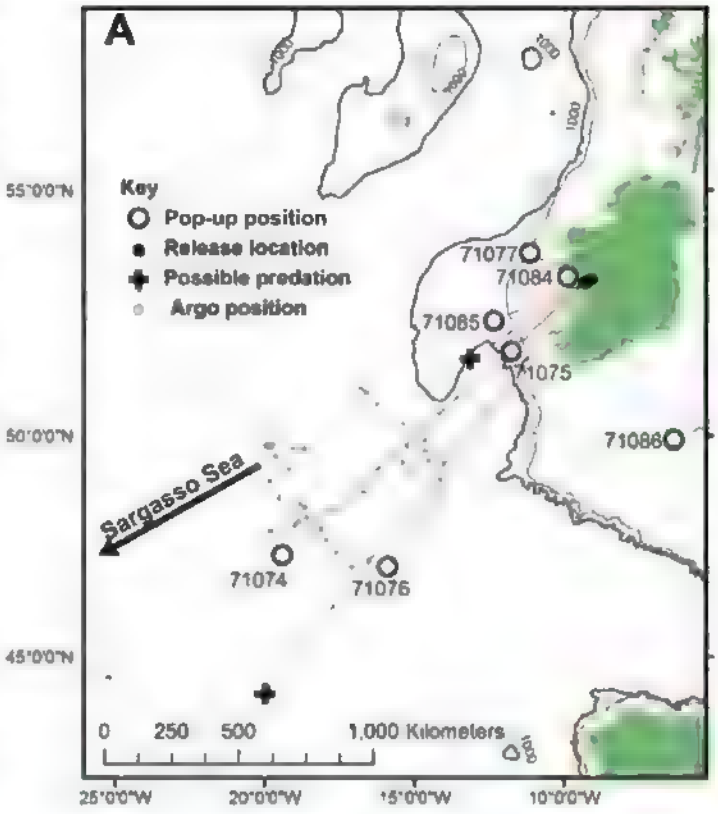

THEATER: HISTORY OF SCIENCE

Newton in Three Dimensions

Rebecca Stott[1] and Hannah Morrish[2]

Two hours after the end of the play *Let Newton Be!*, we were still deep in conversation about it in a Cambridge pub. One of us is the author of *Ghostwalk*, a historical thriller about Newton's alchemy (*1*); the other, a theater student and actress. We went with different expectations and interests but came out equally excited. And we've gone on talking about the play since, as a body of ideas and as a theatrical experience. It deserves to be seen internationally.

Craig Baxter's new play premiered in late October at Newton's old college, Trinity. The performance we attended was introduced by the just-retired Lucasian professor of mathematics, theoretical physicist Stephen Hawking, and by Denis Alexander, director of the Faraday Institute for Religion and Science, which had sponsored the production as part of the celebration of Cambridge University's 800th anniversary and the International Year of Astronomy.

Baxter is unique. A playwright with a degree in zoology, he has been writing drama for 15 years. He has written ten plays, several adaptations, and a brace of radio dramas. But he has come into his own with his return to science in the past five years. His recent work includes *The Altruists*, about 20th-century evolutionary biologists, and *Re:Design*, a daring play based on Darwin's letters, composed entirely from Darwin's words and the words of his correspondents [reviewed in (*2*)].

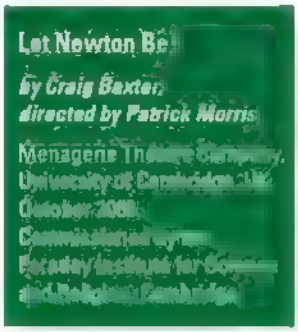

Bringing Darwin to the stage was all very well. That was the 19th century, Darwin was liked and prolific, and there were thousands of genial and engaging letters from which Baxter could cut his material. Newton, however, is another country. He was troublesome. He was guarded, secretive, and paranoid. There is no consensus about his personality from his biographers. There are gaps in the historical record. There were few letters for Baxter to work with.

But there were words. Millions of them, from notebooks and personal accounts. The incomparable Newton Project, which over the past ten years has put four million of Newton's words online (making them widely accessible for the first time), has revolutionized the ways in which we can understand Newton. And Baxter has quarried these millions of words on theology, alchemy, mathematics, and physics to produce a Newton whom brilliantly he chose to split.

Baxter gives us a trinity of Newtons: the child Isack (played by Caroline Rippin), who runs and jumps and measures and records, the man Newton (played by Neil Jones), at war with himself, contemplative, constantly list-writing, driven, and on the brink of breakdown; and the mature Sir Isaac (played by Paul McCleary), self-possessed master of the mint. It would have been easy to present Newton's life chronologically, one Newton after the other. But Baxter has all three on stage all the time, challenging and questioning one another. That produces a multidimensional Newton—one who is indeed torn among selves, split, divided, energetic, and spilling over, but whom we see as a complete being. The result is a play that barely contains its own subject. This is the theater of ideas at its very finest. It is mesmerizing, inventive, and provocative.

Director Patrick Morris brilliantly choreographed the actors to orbit one another, constantly recomposing the geometry of a disordered mind. The young Newton keeps returning to his desk and to his accounts book, recording and repeating lists—of accounts of sins, of daily routines. This was a Newton who did not know how to stop and who was always preoccupied with theology, with defining a God and defining for God. Somewhere around the middle of the play, the anguished energy spills over into nightmare, and Newton breaks down. He is held down by his servants, only to get up moments later and start all over again. This is intelligent and psychologically perceptive direction, and the result is moving.

Newton's extraordinary mind is embodied not only in the text and the trinity of selves but also in the wonderfully effective and visually exciting set designed by Issam Kourbaj, artist in residence at Christ's College. The set transforms endlessly using Newton-like contraptions that open out into chairs, then to desks, then bookcases, then into models of windmills. Flecked with red velvet and the scribblings of the Lucasian professor's handwriting, the set folds and unfolds in and out of itself: windows within windows, wheels within wheels. If Newton's mind could be represented visually, this would be it.

Can theater be a platform for science? In the hands of Baxter, Morris, and Menagerie Theatre—yes. Spectacularly yes. Baxter cuts a man of science from the cloth of his own words, seeking to persuade us that Newton's science was always driven by a belief in an all-powerful and ever-present "God of Dominion." From the ramblings, jottings, accounts, and notebooks—the spillings over of Newton's strange inner world—Baxter creates a unified Newton who will awe and move modern audiences. This is Newton fully in three dimensions.

School of Literature and Creative Writing, University of East Anglia, Norwich NR4 7TJ, UK. E-mail: rebecca.stott@uea.ac.uk. [2]Hills Road Sixth Form College, Cambridge CB2 8PE, UK.

References

1. R. Stott, *Ghostwalk* (Weidenfeld and Nicolson, London, 2007); reviewed in (*3*).
2. C. Thomas, *Science* **325**, 679 (2009).
3. J. Golinski, *Science* **321**, 40 (2008).

10.1126/science.1183342

PUBLIC HEALTH

Pandemic H1N1 and the 2009 Hajj

Shahul H. Ebrahim,[1]* Ziad A. Memish,[2] Timothy M. Uyeki,[1] Tawfik A. M. Khoja,[3] Nina Marano,[1] Scott J. N. McNabb[1]

It will take vigilance, commitment, and action by all global stakeholders to reduce the potential impact of pandemic influenza during the upcoming Hajj pilgrimage.

The annual Hajj pilgrimage of more than 2.5 million pilgrims from more than 160 countries is held in the Kingdom of Saudi Arabia (KSA) (*1*) (see the figure). Hajj is a deeply spiritual journey undertaken by Muslims at least once in their lifetimes. Hajj-related infectious disease outbreaks in recent decades have focused attention on Hajj as a global public health security challenge of extraordinary dimensions (*1*–*5*). This past summer, a KSA–World Health Organization (WHO) consultation process developed the Jeddah recommendations on mitigation for the effects of the current pandemic influenza A (H1N1) virus during the 2009 Hajj, which is the last week of November (*6*). Here, we outline some of the realities associated with meeting those recommendations and the most recent plans to help mitigate the transmission burden.

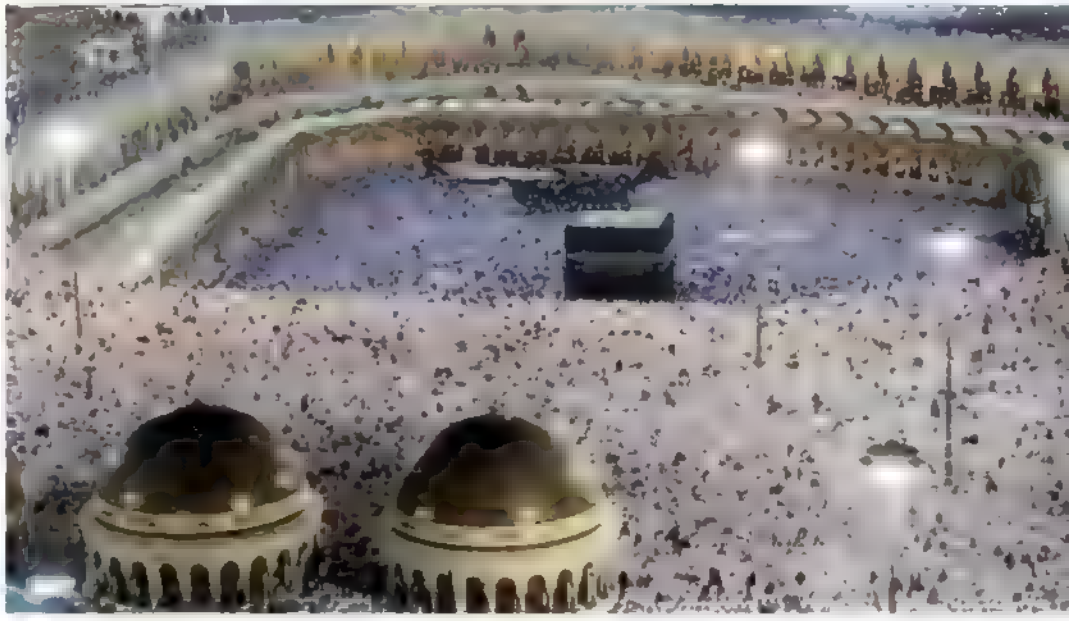

Pilgrims encircling Kaaba, the main mosque in Mecca, during Hajj.

Hajj-related exportation of H1N1 virus by returning pilgrims could potentially initiate waves of outbreaks worldwide and burden health-care systems. No region can be considered free from risk. For example, pilgrims originating from North America (more than 15,000) and Europe (more than 45,000) pass though major airline hubs of the world on their journey, which increases the risk of international spread of the virus.

Although the impact of the current pandemic on Hajj pilgrims is unpredictable, preparedness is clearly indicated. Participation, cooperation, and commitment by home countries will be critical. Because many pilgrims originate from resource-poor countries (*7*), all stakeholders should support specific pre- and post-Hajj preparedness efforts.

Of the Jeddah recommendations, the most challenging is that the population groups considered to be at high risk for complications from influenza (pregnant women, those with chronic diseases, and people under 12 or over 65 years of age) voluntarily refrain from the 2009 Hajj. Roughly 25% of the pilgrims are expected to be at least 65 years old (see the graph). These recommendations were based on information available in June. Recent epidemiologic data indicate that children and young adults are at high risk for H1N1 complications. However, because of the relatively low mortality observed with H1N1, compliance with any recommendation to voluntarily abstain from Hajj by young adults is unlikely. KSA will not restrict anyone from performing Hajj based on their age but endorses the Jeddah recommendations and urges authorities in the home countries of pilgrims to communicate risk information.

Reactions to the pandemic and the recommendations have been mixed from Muslim communities and governments (*8*, *9*). Egypt became the first Arab country to claim that Hajj and the ritual of Umrah (both of which center around Mecca) were a threat to its citizens' lives. Oman issued a warning on 6 July for high-risk groups to postpone Hajj. On 10 August, Iran suspended all flights to KSA as a precautionary measure during the peak Umrah season (*10*). Indonesia has advised Indonesians age 65 years and older to refrain from Hajj (*11*). Tunisia suspended the Umrah pilgrimage on 5 July and extended the ban to Hajj on 6 October (*12*).

Nonpharmaceutical Options for Mitigation

Influenza is potentially spread by large droplets, small particles, droplet nuclei, and contact transmission. The density of pilgrims, the nature of the rituals, and the shoulder-to-shoulder contact recommended during prayers provide a perfect transmission atmosphere. Floors or carpets and objects of religious significance are routinely touched. Standard social distancing measures will not to be practical (*13*).

Face masks, cough etiquette, and hand hygiene are nonpharmaceutical measures that could be realistically implemented during Hajj and are recommended by the Ministry of Health of the KSA (MoH) (*10*, *14*). However, the effectiveness of these interventions to prevent pandemic influenza transmission among pilgrims is unknown, and compliance with mask use may be challenging because of factors that include hot weather and religious considerations. The specific dress code for men during Hajj excludes stitched clothes, and women are required to expose their faces. Some pilgrims would interpret the use of face masks as prohibited by religion.

On a positive note, washing of hands, face, and nostrils is required before the five obligatory daily prayers. Use of soap and hand sanitizers needs to be encouraged. Private organizations in KSA will be donating personal hygiene kits for each arriving pilgrim that contain face masks, hand sanitizers, and information materials. However, they should be made available to pilgrims before their departure and used during the journey. Some pilgrims may consider using alcohol-containing products (e.g., hand sanitizers) as prohibited by religion. Religious advisories exist that allow the use of alcohol for

CREDIT: MINISTRY OF INTERIOR, KSA

[1]Centers for Disease Control and Prevention, Atlanta, GA 30333, USA. [2]Ministry of Health, Riyadh, Saudi Arabia. [3]Executive Board, Health Ministers' Council for Cooperation, Council of Gulf States, Riyadh, Saudi Arabia. *Corresponding author. E-mail: Sbe2@cdc.gov

medical purposes (*15*). Therefore, social marketing and endorsement by religious leadership of personal protection as part of pilgrims' religious duty to avoid harm to themselves and others may help improve compliance.

Screening, Quarantine, and Surveillance

Thermal screening equipment to detect febrile passengers are in place at KSA airport terminals receiving pilgrims. However, some infected travelers may not yet be symptomatic at entry, some will never be febrile, and some will have fever suppressed by antipyretics. Another challenge to organized screening at arrival is the fact that there are multiple routes of entry for pilgrims.

With respect to quarantine and isolation measures, the MoH has recommended that each receiving airport have the holding capacity for 200 to 300 pilgrims to evaluate those who are symptomatic with influenza-like illness (ILI). Publicized large-scale quarantine of healthy pilgrims or isolation of symptomatic pilgrims may become a deterrent to self-reporting of illness. KSA's strategy is to ensure screening, confirmation, and comprehensive treatment of all pilgrims who become ill and to help them rejoin their groups when it is safe to do so. At Jeddah, it was recommended that the MoH provide each pilgrim with a wristband containing identifying information to enable surveillance, medical care, and notification of illnesses. International Health Regulation mechanisms would be used for reporting events to the WHO. A complicating factor is that there are other infectious etiologies for acute respiratory or ILI expected among pilgrims (*16*), and current influenza tests that produce timely results have suboptimal sensitivities for H1N1 (*17*, *18*).

KSA, in collaboration with the U.S. Centers for Disease Control and Prevention (CDC), is operationalizing an Internet-enabled mobile-technology–based surveillance system. Laboratory analysis of specimens from patients who seek care in clinical facilities is being implemented through collaboration between the KSA MoH and the U.S. Naval Medical Research Laboratory. WHO regional laboratories will facilitate rapid diagnosis of patients with ILI. Whereas surveillance for antiviral drug resistance may not provide timely data during Hajj, such data are important for global public health.

Although most ill persons infected with the new H1N1 virus have experienced mild to moderate disease, some require hospitalization, and severe acute respiratory distress syndrome has been reported (*19*). Saving these lives depends on specialized and demanding care in intensive care units, usually with long and costly stays. This will put an additional strain on the KSA's Hajj medical infrastructure. Surge capacity is being assured through hospitals in Jeddah. Infection-control plans for hospital and primary care settings are being implemented for the full Umrah and Hajj periods.

Role of Influenza Vaccines in Hajj

One positive development is that limited quantities of monovalent pandemic H1N1-specific vaccine are becoming available, and early evidence suggests protection of adults 14 days after vaccination with a single dose (*20*, *21*). However, vaccination of pilgrims in their home countries at least 14 days before departure will be unlikely because of variation in the ability of countries of origin to afford vaccine, as well as limitations in production and distribution capacity.

Yang *et al.* (*22*) have estimated that a 70% coverage requirement by H1N1 vaccine could mitigate of pandemic spread in the United States (*23*). China is aiming at 30% vaccination coverage among school children (*23*). These estimates for protection may not be relevant for mass gatherings such as Hajj that involve diverse risk and age groups.

Ensuring high pandemic vaccine uptake is likely to be a challenge unless it is mandatory; only 4.7% of Hajj pilgrims over 65 years and 5.9% of health workers in the 2003 Hajj followed the recommendation for seasonal influenza vaccination (*24*). KSA has requested an official response from Ministries of Health in each country sending pilgrims regarding availability of vaccines for seasonal influenza and H1N1. If official information that vaccine supplies are available in a country is received by KSA authorities in a reasonable time frame, then proof of vaccination may be required for pilgrims from that country in order to receive a Hajj visa. Because of the delay in acquiring H1N1 vaccines as of 22 October 2009, only four countries have indicated to the KSA that they plan to vaccinate their pilgrims.

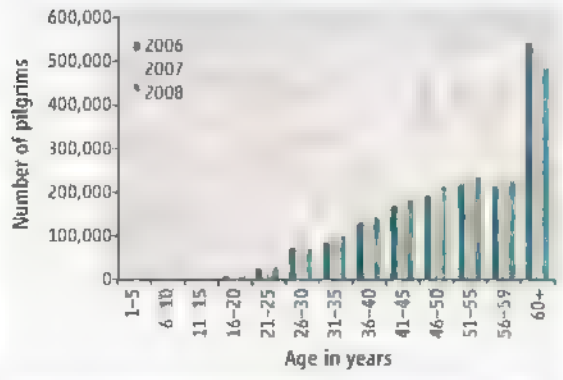

PHOTO CREDIT: MINISTRY OF INTERIOR, KSA

Distribution of Hajj pilgrims by age, 2006 through 2008.

Antiviral Use During Hajj

Antiviral treatment as soon as possible is recommended for all hospitalized persons and outpatients in high-risk groups, but routine chemoprophylaxis is not recommended by WHO (*25*). KSA has allocated courses of neuraminidase inhibitors to be offered to all pilgrims free of charge during Hajj, irrespective of national origin. Antiviral treatment will also be allocated for health-care workers supporting Hajj operations.

Preparedness

Surveillance hospital capacity and other aspects of preparedness were field-tested during the part of August that is the peak Umrah season, which brought close to 2 million pilgrims to Mecca. The MoH confirmed only 26 cases of H1N1 (and no deaths) during this period, which does not indicate an upsurge from what is expected among more than 2 million people. As a continuation of preparedness plans for Hajj, efforts are under way to assure live linkages between the public health and emergency services operations under the MoH and the Ministry of Civil Defense. These two entities will jointly determine potential triggers for activating the "Civil Defense Emergency Plan" should the pandemic pattern change

Final Words

Research during the 2009 Hajj would be a critical investment to address future challenges of this nature. Hajj provides us an unprecedented opportunity to study many unknowns that affect mass gatherings, including transmission dynamics and the effectiveness of medical and other mitigation strategies.

Health care for pilgrims is a top priority for the government of KSA. Despite the use of an early-warning system to monitor an upsurge in influenza, it is assumed that most of the transmission would have occurred before the detection of cases. Efforts in KSA would largely help mitigate suffering once cases are detected.

Endorsement of the Jeddah recommendations by credible Islamic religious entities and political leaders in countries from which pilgrims originate can lead to wider acceptance of these recommendations. Resource-poor countries will need political will and external support to ensure availability of resources and logistics to implement pre-departure prevention measures. After Hajj, surge capacity for returning pilgrims who might be ill should be ensured.

As a cautionary note, the safeguards and

preparedness that have been recommended, planned, or implemented to date are based on current information. Changes in viral characteristics or epidemiological/geographical trends may call for modification of recommendations. Authorities in home countries of pilgrims and the global public health community should monitor the situation and advise potential pilgrims and all stakeholders accordingly. Pilgrims can receive updated information from the Web sites of the MoH (www.moh.gov.sa) and the Ministry of Hajj (www.hajinformation.com)

For a summary of recommendations in this paper and information about H1N1, see Flu Prevention Advice in the supporting online material and freely available on *Science* Express.

References and Notes

1. Q. A. Ahmed *et al.*, *Lancet* **367**, 1008 (2006)
2. A. Wilder-Smith *et al.*, *Lancet* **360**, 644 (2002)
3. H. H. Bakhy, Z. A. Memish, *Int. J. Antimicrob. Agents* **21**, 153 (2003)
4. CDC, *JAMA* **284**, 2989 (2000)
5. A. Alzeer *et al.*, *J. Infect.* **36**, 303 (1998)
6. World Health Organization, *International Consultation: Infectious Disease Prevention and Control at Umra and Hajj*, Technical meeting report, Jeddah, Kingdom of Saudi Arabia, 28 to 30 June 2009 (WHO, Geneva, 2009), www.emro.who.int/csr/h1n1/pdf/infectiousdiseases_hajj_umra.pdf
7. E. C. Hayden, *Nature* **459**, 756 (2009)
8. B. A. Al-Naja, "Millions converge on Makkah for Khatm prayers," *Arab News*, 19 September 2009; www.arabnews.com/?page=1&section=0&article=126549&d=19&m=9&y=2009
9. W. Mahdi, "Saudi Arabia questions reasons for Haj ban," *The National* (Abu Dhabi), 28 July 2009; www.thenational.ae/apps/pbcs.dll/article?AID=/20090728/FOREIGN/707279806
10. "Iran cancels all Saudi flights in Ramadan," *Arab News*, 11 August 2009; www.arabnews.com/?page=1&section=0&article=125340
11. "H1N1 prompts Hajj restrictions," Aljazeera.net, 23 July 2009; http://english.aljazeera.net/news/middleeast/2009/07
12. "Tunisia bars citizens from performing Haj," *Arab News*, 7 October 2009; www.arabnews.com/?page=4&section=0&article=127153&d=7&m=10&y=2009
13. H. Markel *et al.*, *JAMA* **298**, 644 (2007)
14. MoH, Kingdom of Saudi Arabia, www.moh.gov.sa/en/modules/mysections/article.php?id=10
15. Muslim World League, "Resolutions of the Islamic Fiqh Council," in *Proceedings of the Six Resolutions of the 16th Session*, Makkah Mukarramah, Saudi Arabia, 5 to 10 January 2002; www.themwl.org.
16. A. Alborzi *et al.*, *J. Travel Med.* **16**, 239 (2009)
17. S. Vasoo, J. Stevens, K. Singh, *Clin. Infect. Dis.* **49**, 1090 (2009)
18. D. J. Fiax *et al.*, *N. Engl. J. Med.* **361**, 728 (2009)
19. R. Perez-Padilla *et al.*, *N. Engl. J. Med.* **361**, 680 (2009).
20. U.S. Centers for Disease Control and Prevention, *MMWR Recomm. Rep.* **58**(RR-10), 1 (2009)
21. K. M. Neuzil, *N. Engl. J. Med.*, 10.1056/NEJMe0908224, 10 September 2009
22. Y. Yang *et al.*, **326**, 729 (2009); published online 10 September 2009
23. R. Stone, *Science* **325**, 1482 (2009)
24. H. Rashid *et al.*, *Vaccine* **26**, 4809 (2008).
25. WHO, *WHO Guidelines for Pharmacological Management of Pandemic (H1N1) 2009 Influenza and other Influenza Viruses* (WHO, Geneva, 2009)

Flu Prevention Advice

www.sciencemag.org/cgi/content/full/1183210/DC1

Published online 29 October 2009

10.1126/science.1183210

CLIMATE CHANGE

Bridging the Montreal-Kyoto Gap

Using carbon markets to eliminate substances that deplete stratospheric ozone could pay huge dividends in combating global warming.

Jeff Cohen,[1]* Alex Rau,[2] Kristian Brüning[2]

Because of the growing need for near-term, feasible, greenhouse gas (GHG) abatement options (*1*), there is increasing interest in the scale and cost-effectiveness of potential emission reductions from destruction of ozone-depleting substances (ODSs) (*2*). Chlorofluorocarbons (CFCs) and other ODSs not only damage stratospheric ozone, but also are powerful GHGs, with global warming potentials (GWPs) up to 11,000 times that of carbon dioxide (CO_2) (*3*). The Montreal Protocol eliminates production of these chemicals but does not control their emissions or require destruction of ODSs produced before phase-out deadlines. The Kyoto Protocol targets emissions of CO_2 and other non-ODS GHGs. Because of these regulatory gaps, large quantities of ODSs remain in legal use or storage in older refrigeration and air-conditioning equipment, building and appliance insulation, fire suppression systems, and government and industrial stockpiles (*4*). Without requirements or incentives for destruction, these ODSs will ultimately be released to the atmosphere and contribute to anthropogenic climate change.

Current global ODS banks (not yet emitted into the atmosphere) are estimated to represent (in terms of GWP) the equivalent of 16 to 18 billion tons of CO_2 (CO_2 eq) (*4*) (see the graph, page 941 and table S1). Of this total, refrigerants and other "reachable banks" are ~8.8 billion tons of CO_2 eq (*5*); most of which (6 billion tons of CO_2 eq) is expected to be lost to the atmosphere by 2015 (*4*).

Reachable banks can be collected and destroyed in accordance with industry standards (*6*) by using technologies and infrastructure available in industrialized countries and feasible for developing countries. Highly regulated destruction technologies, such as rotary and cement kilns, plasma arc, and waste-to-energy conversion, provide sufficient capacity, with removal efficiencies above 99%. Remaining ODS banks are in less accessible, but more stable, sources, such as building insulation, that are less prone to rapid leaking.

Governments may be tempted simply to mandate destruction of ODS banks. However, given their dispersed nature and continued demand for recycled ODSs to service older equipment, direct financial incentives are essential. This could be accomplished by issuing GHG emission reduction credits (offsets) for permanent, certified removal of ODS banks. These credits could then be traded in carbon markets as a mitigation alternative alongside other targeted GHGs.

ODS destruction can be precisely monitored and is verifiable (*7*), "additional" (*8*), and permanent, representing the highest-quality GHG reduction. Projects can be implemented quickly, on the order of months. Voluntary carbon markets that commercialize GHG emission reductions outside government-mandated programs have spurred the development of protocols, verification systems, infrastructure, and financing (*9*, *10*). However, the size of global ODS banks far exceeds the capacity of voluntary carbon markets alone to create enough incentive for collection and destruction of ODSs. Instead, ODS destruction credits should be included in national and global mandatory compliance carbon markets.

Parties to the Montreal Protocol are considering a systematic, international approach to management of ODS banks, with incentives leveraging private capital from carbon markets to promote destruction of ODS banks (*11*). The Kyoto Protocol's Clean Development Mechanism may serve as a guide for such a system (*12*). Parties will also receive recommendations from the Technology and Economic Assessment Panel (TEAP) of the United Nations Environment Programme

[1]EOS Climate, South San Francisco, CA 94080, USA. [2]Climate Wedge Ltd., San Francisco, CA 94080, and 00120 Helsinki, Finland.
*Author for correspondence. E-mail: jcohen@eosclimate

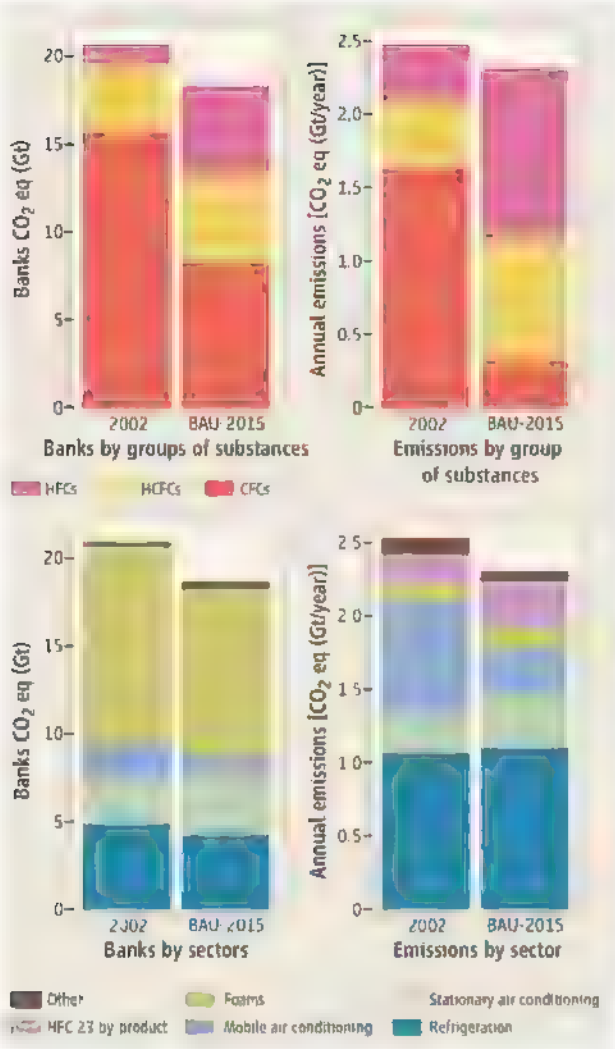

Historic data for 2002 and business-as-usual (BAU) projections for 2015 of GHG CO_2 eq banks (left) and direct annual emissions (right) related to the use of CFCs, HCFCs, and HFCs. "Other" includes medical aerosols, fire protection, nonmedical aerosols and solvents. [Source: figure SPM-4 from (*4*)]

(UNEP) and World Bank on funding mechanisms, including carbon finance (*13*).

Average costs to separate, collect, and destroy ODSS from "low-" and "medium-effort" sources, such as refrigeration and air-conditioning equipment, are estimated to range between U.S. $15 and $35 per ton of CO_2 eq; between now and 2013 to 2014, costs could fall below $10 per ton of CO_2 eq (*5*). These costs are comparable to and, for the low-effort sources, well below the cost of abatement for the majority of GHG reduction measures (*14*), as well as projected prices of emissions permits in the European Union Emissions Trading Scheme (*15*) and a likely U.S. cap-and-trade system (*16*)

Pending U.S. cap-and-trade legislation (*17*, *18*) recognizes the climate benefits of destroying ODSs by allowing the U.S. Environmental Protection Agency (EPA) to allocate additional allowances for production and import of hydrofluorocarbons (HFCs; non–ozone-depleting substitutes for CFCs) in exchange for destruction of CFCs. Unfortunately, demand for HFCs will represent only a small fraction of the total U.S. ODS bank (*19*). Thus, these bills, in their current forms, would not substantively slow ongoing, preventable ODS release. Instead, making ODS destruction eligible under cap-and-trade provisions as a general GHG offset available to all regulated businesses would expand financing needed to prevent these emissions, and provide a much-needed source of near-term carbon abatement. In the United States, ODS destruction could rapidly scale to generate several hundred million tons per year of verifiable reductions by 2015 to 2020, helping to contain overall costs to the economy.

As domestic and international climate negotiations go into high gear, policy-makers worldwide have an immediate, cost-effective opportunity to prevent release of hundreds of millions of tons of CO_2 eq, by incorporating the following measures:

1. Count banked ODSs that have been phased out of production as controlled GHGs and allow creation of GHG offsets from verified ODS extraction and destruction.

2. Require rigorous protocols so that only verified ODS extraction and/or destruction projects, with clear additionality and emission reductions, qualify for offsets.

3. Include incentives for accelerated development and adoption of advanced replacement technologies that avoid substitution with other high-GWP GHGs.

Banks of ODSs represent a potential source of emissions that could undo climate protection achieved by phasing out production of these chemicals (*20*). There is little time in which to address this issue: Most easily reachable ODS banks, under business as usual, will be released to the atmosphere in 5 to 10 years (*4*). By recognizing ODS banks as GHGs in domestic legislation and international agreements, ODS destruction projects would be rapidly mobilized, the transition to more advanced technologies would be accelerated, and the legacy of the Montreal Protocol secured.

References and Notes

1. Commission of the European Communities, *Proposal for Decision of the European Parliament and of the Council on the Effort of Member States to Reduce Their Green-House Gas Emissions to Meet the Community's Green-House Gas Emission Reduction Commitments by 2020* (CEC, Brussels, 2008)
2. E. Kintisch, *Science* **324**, 323 (2009)
3. U.S. Climate Change Science Program, *Trends in Emissions of Ozone-Depleting Substances, Ozone Layer Recovery, and Implications for Ultraviolet Radiation Exposure*, A. R. Ravishankara, M. J. Kurylo, C. A. Ennis, Eds. (National Oceanographic and Atmospheric Agency, Asheville, NC, 2008), 240 pp.
4. Intergovernmental Panel on Climate Change, *IPCC/TEAP Special Report: Safeguarding the Ozone Layer and the Global Climate System* (IPCC, Geneva, 2005); www.ipcc.ch/publications_and_data/publications_and_data_reports.htm#2
5. UNEP TEAP, *Task Force Decision XX/7 Report. Environmentally Sound Management of Ozone-Depleting Substances* (UNEP, Ozone Secretariat, Nairobi, 2009) (phase 2, advance copy), http://ozone.unep.org/Assessment_Panels/TEAP/Reports/TEAP_Reports/teap-june-2009-decisionXX-7-task-force-report.pdf
6. RAL Quality Assurance Association, Minimum standards for quality assurance and test specifications, www.ral-online.org/html_engl/mindest.htm.
7. Each reduction unit must be monitored, tracked, and verified by a third party before any credit is issued.
8. Additionality indicates that offset-generating activities would not have occurred under "business as usual." (see, e.g., http://cdm.unfccc.int/methodologies/PAmethodologies/tools/am-tool-01-v5.2.pdf
9. The Chicago Climate Exchange, ODSs Destruction Emission Offsets, www.chicagoclimatex.com.
10. The Climate Action Reserve and the Voluntary Carbon Standard have ODS destruction protocols in development (available online).
11. Montreal Protocol, Meeting of the Parties, Port Ghalib, Egypt, 4 to 8 November 2009, http://ozone.unep.org/Meeting_Documents/mop/21mop/index.shtml.
12. Clean Development Mechanism, http://cdm.unfccc.int/index.html
13. Montreal Protocol, *Decision XX/7 Environmentally Sound Management of Banks of Ozone-Depleting Substances* (UNEP, Ozone Secretariat, Nairobi, 2008).
14. McKinsey&Co, *Pathways to a Low-Carbon Economy: Version 2 of the Global Greenhouse Gas Abatement Cost Curve* (McKinsey&Co., 2009), www.mckinsey.com/clientservice/ccsi/pathways_low_carbon_economy.asp
15. See e.g., Point Carbon, www.pointcarbon.com.
16. EPA, *Analysis of the American Clean Energy and Security Act* (EPA, Washington, DC, 2009); www.epa.gov/climatechange/economics/economicanalyses.html
17. Clean Energy Jobs and American Power Act, S. 1733.
18. American Clean Energy and Security Act of 2009, H.R. 2454
19. Assuming EPA would authorize 10% additional HFC import and production beyond a baseline of 330 million metric tons (MMT) of CO_2 eq per year, expected annual demand for CFC destruction offsets would be of order 30 MMT of CO_2 eq, which we estimate is at least two orders of magnitude less than total U.S. ODS banks (e.g., assuming U.S. ODS banks are 25% of total global banks or 4 to 5 Gt of CO_2 eq)
20. G. J. M. Velders, S. O. Andersen, J. S. Daniel, D. W. Fahey, M. McFarland, *Proc. Natl. Acad. Sci. U.S.A.* **104**, 4814 (2007)

Supporting Online Material
www.sciencemag.org/cgi/content/full/1176958/DC1

10.1126/science.1176958

MATERIALS SCIENCE

Viewing the Seeds of Crystallization

Electron microscopy is providing glimpses of the complex structural processes that precede crystal nucleation.

J. Murray Gibson

All materials search for the lowest accessible energy state. As temperature is increased in disordered materials, atoms diffuse and explore different chemical and structural configurations. Crystalline phases may be favored, but a very small crystal is unstable, so there is a "nucleation barrier" to overcome; only after reaching a critical size can the nucleus grow. Although we understand the thermodynamics of the nucleation process [e.g., (*1*)], observation of the actual atomic-scale complexity during nucleation has remained elusive, despite its importance to the properties of materials. Taking nucleation out of the "black box" is one of the grand challenges to "materials by design" that is seen as the future solution to major societal problems such as sustainable energy (*2*). On page 980 of this issue, Lee *et al.* (*3*) use fluctuation electron microscopy to image subcritical nuclei in a solid material, observing metastable structural states that facilitate later nucleation in amorphous films. Their study is applied to a technologically important case of "phase-change memory" and therefore may facilitate efforts to design faster higher-density nonvolatile memory.

Nucleation is ubiquitous. It determines when a menacing cloud will start to pour out rain, or when a pan on the stove will boil. Suppressing ice nucleation helps fish live in ice-cold water (*4*). Nucleation of amyloid fibers is suspected to be critical to the development of neurodegenerative diseases (*5*). Nucleation of crystalline ice is dependent on impurities and other conditions, and this has been used to produce beautiful ice "paintings" (*6*) (see the figure). The nucleation of crystals in amorphous materials or liquids, as studied by Lee *et al.*, is often a determining step in the processing of materials. Crystal nucleation is responsible for the write cycle in a DVD, but it is also key to steel production, manufacturing of solar cells, and the production of food.

Although very small crystalline nuclei have been observed on exposed crystal surfaces (*7*), reports of subcritical nucleation observation in bulk materials are scarce (*8*). The scale and density of crystal nucleation sites inside liquids or disordered materials is usually very small, typically on the atomic scale, which makes them very difficult to probe. It is hard to distinguish crystalline structure from disorder when the correlation length of the crystals is just a few atomic spacings. Fluctuation microscopy was developed to address this problem (*9*, *10*).

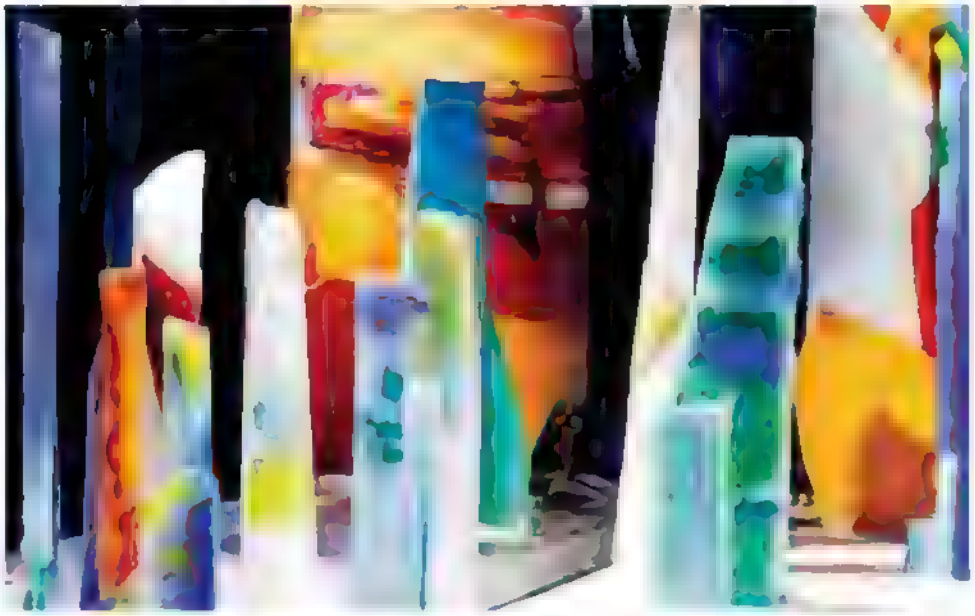

Ice paintings. Exploiting the complexity of ice crystal nucleation to produce beautiful art (*6*). Nucleation is controlled through cooling rates and impurities, which also lend color to the ice.

CREDITS: GORDON HAMORAN/WWW.ICEPAINTINGPROJECT.COM. PHOTO: ALLAN BURNS

Scattering techniques with diffracting radiation such as x-rays, neutrons, and electrons tell us most of what we know about the atomic configurations in solids. Yet averaging techniques are not well suited for detecting nucleation that begins with vanishing volume fraction. Today, fast electrons are unique in their subsurface sensitivity and spatial resolution, permitting diffraction from highly localized nanoscale volumes, and thus could detect nucleation. The difficulty in doing so, however, is that crystal nucleation often occurs in highly disordered or amorphous matrices. In this case we have to contend with the quasi-random scattering fluctuations ("speckle") that arise from nanoscale volumes. Fluctuation microscopy focuses on statistical analysis of fluctuations to overcome the limitations of visual inspection. It can reveal prototypical crystalline order through sensitivity to higher-order atomic correlations that pick out crystalline topology (*9*). The first experimental use showed that amorphous elemental semiconductors contain more crystalline topological order than expected from a random network model, and that upon gentle annealing the order dissolves (*11*). Since then there have been growing applications to other amorphous materials (*10*).

"Phase-change" materials (*12*) are now widely used in optical and electronic memories (*13*). Certain chalcogenide amorphous semiconductors exhibit a change in reflectivity (and electrical resistivity) between crystal and amorphous phases and can be rapidly and reversibly switched between the two states by heating. Slower heating yields the crystalline phase, whereas fast heating and cooling leaves the amorphous phase. A recent use of these materials is in solid-state circuits for nonvolatile high-speed, high-density memory, where thermal switching uses resistive heating and the change in resistivity between states is exploited as a memory. Key to the application is control of crystal nucleation during switching, and the stochastic nature of this limits the speed and density of the memory. There are many handles to turn in the material's stoichiometry and processing that can affect nucleation, but the results to date have been mostly empirical. A better understanding of nucleation will lead to new approaches to control and improve the process. Lee *et al.* show that preannealing favors faster nucleation because it leaves subcritical seeds in the material.

We expect to see further application of techniques that probe higher-order correlations as a tool to understand nucleation and

Advanced Photon Source, Argonne National Laboratory, Argonne, IL 60439, USA. E-mail: jmgibson@aps.anl.gov

structure in disordered and partially crystalline substances. Beyond fluctuation microscopy, there are related approaches that also look promising (*14*). Revolutions in focusing and brightness make related techniques accessible with penetrating x-rays. Fluctuation microscopy is a fingerprint technique. It is sensitive enough to allow one to distinguish models, but it is difficult to directly interpret data. Further advances will occur by combining fluctuation microscopy data and other structural data in Monte Carlo structural refinements. Progress is needed in the theory underlying interpretation, with the ultimate goal that high-order correlation functions can be directly determined without modeling (*15*). Such developments will provide a better fundamental understanding of amorphous materials and crystal nucleation, resulting in better phase-change memory and other technologies.

References and Notes

1. D. Kaschiev, *Nucleation: Basic Theory with Applications* (Butterworth-Heinemann, Oxford, 2000)
2. U.S. Department of Energy Basic Sciences Advisory Committee, *New Science for a Secure and Sustainable Energy Future* (2008) (www.sc.doe.gov/bes/reports/files/NSSSEF_rpt.pdf)
3. B.-S. Lee *et al.*, *Science* **326**, 980 (2009)
4. J. Peterson, *Sci. News* **130**, 330 (1986)
5. J. T. Jarrett, P. T. Lansbury, *Cell* **73**, 1055 (1993)
6. The artwork of Gordon Halloran (see, for example, www.icepainbagproject.com)
7. O. E. Jesson, M. Kastner, B. Voightlander, *Phys. Rev. Lett.* **84**, 330 (2000)
8. K. F. Kelton *et al.*, *Phys. Rev. Lett.* **90**, 195504 (2003)
9. M. M. J. Treacy, J. M. Gibson, *Acta Crystallogr.* **A52**, 212 (1996)
10. M. M. J. Treacy *et al.*, *Rep. Prog. Phys.* **68**, 2899 (2005)
11. J. M. Gibson, M. M. J. Treacy, *Phys. Rev. Lett.* **78**, 1074 (1997)
12. S. Ovshinsky, *Phys. Rev. Lett.* **21**, 1450 (1968).
13. S. Raoux, *Annu. Rev. Mater. Res.* **39**, 25 (2009)
14. P. Wolchner *et al.*, *Proc. Natl. Acad. Sci. U.S.A.* **106**, 11611 (2009)
15. T. Iwai *et al.*, *Phys. Rev. B* **60**, 191 (1999)

10.1126/science.1182817

COMPUTER SCIENCE

Reflections on Cybersecurity

The lack of security in cyberspace may be addressed by learning from the strengths of the Internet.

William A. Wulf and Anita K. Jones

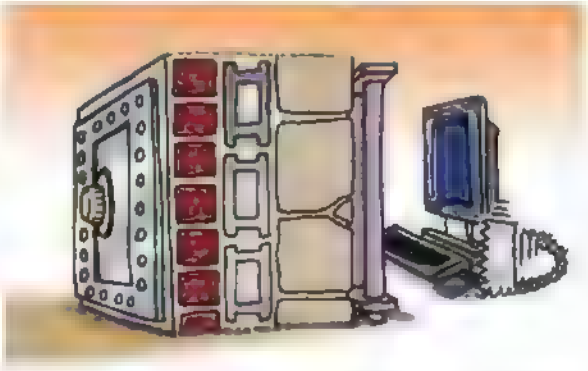

> Perfection is achieved, not when there is nothing more to add, but when there is nothing left to take away.
>
> –Antoine de Saint-Exupéry
> in *The Little Prince*

Cyberspace is less secure than it was 40 years ago. That is not to say that no progress has been made—cryptography is much better, for example. But more vital information is accessible on networked computers, and the consequences of intrusion can therefore be much higher. A fresh approach is needed if the situation is to improve materially.

The prevailing assumption continues to be that if systems were implemented correctly, the problem would be solved. Yet, software engineers have tried to do that for 40 years and have failed. A 1993 report from the Naval Research Laboratory (*1*) points to a deeper problem. It analyzed some 50 security breaches, and found that in 22 of those cases, the code correctly implemented the specifications—it was the specifications that were wrong. They handled the usual cases just fine, but did not appreciate that under some circumstances, permitted actions or outcomes were, in fact, security breaches.

A natural tendency is to declare a crisis and convene task forces and an army of programmers to "fix" the security problem(s). But, as detailed in Fred Brooks' *The Mythical Man-Month* (*2*), trying to get more "man months per calendar month" can actually make the situation worse, not better. We conjecture that a similar phenomenon is occurring for cybersecurity. The security model has remained the same since the 1960s, and software engineers have added more and more patches and widgets to try to enforce that security model. The complex interaction of this additional code with the extant code just provides more opportunities for security failures. The cybersecurity community must thus ask whether the problem has been formulated in the right way.

The current model for most cybersecurity is "perimeter defense": The "good stuff" is on the "inside," the attacker is on the "outside," and the job of the security system is to keep the attacker out. The perimeter defense model is built deeply into the very language used to discuss security: Hackers try to "break in," "firewalls" protect the system, "intrusion" must be detected, etc. But is perimeter defense the right underlying model?

We do not think so, for several reasons. First, perimeter defense does not protect against the compromised insider. The Federal Bureau of Investigation (FBI) has reported that in one sample of financial systems intrusions, attacks by insiders were twice as likely as ones from outsiders—and the cost of an intrusion by an insider was 30 times as great (*3*).

Second, it is fragile; once the perimeter has been breached, the attacker has free access. Some will say that this is why "defense in depth" is needed—but if each layer is just another perimeter defense, all layers will have the same problems.

Third, and most important, it has never worked. It did not work for ancient walled cities or for the French in World War II (at 20 to 25 km deep, the Maginot Line was the most formidable military defense ever built, yet France was overrun in 35 days). And it has not worked for cybersecurity. To our knowledge no one has ever built a secure, nontrivial computer system based on this model.

So, what might be an alternative approach? We think we should take our cue from the Internet. That is, there should not be just one model. Rather, there should be a minimal central mechanism that enables implementation of many security policies in application code—systems attuned to the needs of differing applications and organizations.

It is worth noting that the Internet succeeded so well precisely because it does so little. At its core, the TCP/IP protocols, all the Internet does is to promise "best effort" message delivery. It does not promise that the messages will arrive in the order in which they were sent, that they will ever arrive at all, or even that the same message will not

Department of Computer Science, University of Virginia, Charlottesville, VA 22903, USA. E-mail: wulf@virginia.edu, jones@virginia.edu

arrive multiple times. All of the "smarts" of the net are at its periphery and embedded in "end-to-end" protocols (*4*) that are defined by applications.

Dave Parnas, one of the early software engineers, made a provocative and, we think, deeply important observation that helps to explain the success of the TCP/IP protocols. He pointed out that, when doing a design, the hardest decision to change is the one you make first, because all the subsequent ones to some extent depend on it (*5*). The decision for the TCP/IP protocols to do so little never had to be reconsidered, because it precluded so little.

Is there an analogy to the Internet message delivery design for security? Is there some minimal mechanism that would allow the construction of arbitrary end-to-end security protocols and allow an arbitrary number of these security protocols to coexist simultaneously? Is there a mechanism so simple that, while adequate to support the construction of security policies, does not preempt any decisions on the definition of security or how it is achieved? We think the answer is yes.

But why build multiple "end-to-end security protocols" rather than one really good one? We offer three reasons. First, different applications have different security needs: The requirements of law enforcement emphasize the integrity of the trail of evidence, the intelligence community is most concerned with disclosure of sources and methods, legitimate access to electronic medical records may change dramatically in emergencies, and so on. The point is that desirable security policy is a natural extension of the application; there is no single security policy that serves all needs equally well.

Second, multiple security protocols ensure that if one is broken, the others are not, or at least not in the same way. The current Internet clients form a predominantly Wintel/Cisco monoculture, so a single flaw can make almost the entire net vulnerable to the same attack. Incorporating multiple security policies and multiple implementations of the same policy can dramatically reduce this monoculture-induced vulnerability.

Third, the requirements of future applications cannot be predicted. In the same way as user-defined, end-to-end communications protocols allowed new applications that were not anticipated (such as the Web, search engines, and e-commerce), application-defined security protocols could accommodate unanticipated security requirements.

The lack of cybersecurity has been a consistent concern for 40 years. From time to time that concern flares up, and society resolves to "try harder," but the number of intrusions and their cost have only increased exponentially. It is time to reexamine the basic assumptions, like perimeter defense. Systems based on those assumptions have consistently failed. At least one alternative is an Internet-like minimal mechanism that enables application-defined security definitions.

Is such a minimal mechanism feasible? We think so. In particular, at the network level, an application can use any computable function to decide whether or not to provide its service to a client if it can be absolutely certain who is requesting it. There is a class of algorithms known as "cryptographic protocols" for doing this that require knowing the public key of an object—so we conjecture that by providing just a way of accessing the public key of an object, one could build an arbitrary end-to-end security policy.

References and Notes

1. "A Taxonomy of Computer Program Security Flaws, with Examples," Naval Research Laboratory Report, NRL/FR/5542–93/9591, November 1993
2. F. Brooks, *The Mythical Man-Month* (Addison-Wesley, Reading, MA, 1975)
3. Testimony of Keith Lourdeau, Deputy Assistant Director, Cyber Division, FBI, before the Senate Judiciary Subcommittee on Terrorism, Technology, and Homeland Security, February 2004
4. J. H. Saltzer *et al.*, *ACM Trans. Comput. Syst.* **2**, 277 (1984)
5. D. L. Parnas, *Commun. ACM* **15**, 1053 (1972).

10.1126/science.1181643

DEVELOPMENTAL BIOLOGY

Strategies to Get Arrested

Two gene families in the worm control survival strategies in response to stressful environmental conditions.

Akira Ogawa and Ralf J. Sommer

From bacteria to vertebrates, organisms can respond to changing environmental conditions by arresting their development. Animals in particular have invented a repertoire of diapause programs. As the environment can change at any step of an organism's life cycle, many independent strategies have evolved even within one species. Studies in the nematode *Caenorhabditis elegans* are beginning to show not only the diversity of these strategies, but also the genetic and genomic mechanisms mediating the response. On pages 994 and 954 of this issue, Kim *et al.* (*1*) and Angelo and Van Gilst (*2*) reveal how members of two multigene families—nuclear hormone receptors and G protein–coupled receptors—perceive and translate environmental cues to regulate diapause stages in the larval and adult reproductive stages, respectively.

C. elegans became a model organism in part because of the ease with which it can be cultured in the laboratory. On petri dishes with *Escherichia coli* as food source, this animal can complete its life cycle in as little as 3 days (see the figure). However, this is only observed when food is unlimited, a scenario that is unrealistic in the natural world. Not surprisingly, therefore, recent studies suggest that in nature, *C. elegans* follows a different path. Animals are most often found in the so-called dauer stage, a developmentally arrested stage (*3*). Lab-based studies revealed that the dauer stage occurs when larvae have little food or are exposed to high temperature or a high concentration of dauer pheromone, which is secreted constitutively by the members of a population (*4*). Although the existence of a pheromone was shown more than three decades ago, only recently have studies characterized it as a complex mixture of chemicals. Ascarosides, a class of glycosides with a dideoxysugar moiety and variable side chains, regulate entry of larvae into the dauer phase and also social behaviors in adults (*5–8*). Genetic studies have identified signaling systems involved in dauer regulation, including insulin and transforming growth factor–β signaling (*9*). However, how the dauer pheromone is sensed and how it is coupled to signal transduction have not been clear.

Kim *et al.* report that two chemoreceptors that are G protein–coupled receptors—*srbc-64* and *srbc-66*—mediate the effects of the dauer pheromone. When these two receptors, which are expressed in a pair of sensory neurons, were mutated, responses to ascarosides were impaired. However, a nematode strain carrying a mutation in both genes still retained some responsiveness to ascarosides, indicating that dauer pheromone perception involves multiple receptors. The results also reveal unexpected complexity in both pheromone production and sensing.

Max Planck Institute for Developmental Biology, 72076 Tübingen, Germany. E-mail: akira.ogawa@tuebingen.mpg.de; ralf.sommer@tuebingen.mpg.de

A worm's life. Self-fertilizing *C. elegans* lay eggs that complete embryogenesis in 14 hours (25°C). Four larval stages (L1 to L4) follow before a worm becomes an adult. Under stress conditions, young larvae enter the dauer stage, an arrested long-living dispersal stage. Young larvae can also arrest at the L1 stage, and adults can enter reproductive diapause.

The dauer stage of *C. elegans* is not only a survival strategy; it also helps dispersal of the organism by facilitating association with invertebrates. This phenomenon is thought to represent an evolutionary trend toward parasitism (*10*). Indeed, experimental support for a conserved endocrine mechanism that controls the formation of dauer and infective larvae in nematodes (*11*, *12*) indicates that a more detailed understanding of *C. elegans* dauer regulation might result in long-term practical applications.

Despite the long-standing interest in dauer development, *C. elegans* researchers have focused little on other survival strategies. This is surprising, as the dauer stage is an option to escape unfavorable conditions only for young larvae. Animals in other stages must find different means to cope with the environment. Angelo and Van Gilst describe an additional survival strategy of adult *C. elegans*. Starvation induces adult reproductive diapause, a delay of reproduction that results in increased longevity and protection of germ stem cells. By contrast, most other germ cells undergo programmed cell death (apoptosis), possibly providing nutrition (through resorption) required for survival. The gene *nhr-49*, which encodes a nuclear hormone receptor, controls adult reproductive diapause entry and exit, whereas the gene *daf-12* encodes another nuclear hormone receptor that controls dauer formation (*13*). These similarities strongly illustrate the importance of endocrine signaling in nematode survival strategies.

These two studies further establish nematodes as a unique model for studying animal survival strategies and the environmental regulation of life histories. One interesting aspect is that the genes involved in dauer pheromone sensing and adult reproductive diapause both belong to gene families that have undergone recent gene duplication (*14*, *15*). Such duplicated genes are believed to supply building blocks for new features without affecting preexisting biological systems. However, the function of duplicated genes is often hidden by redundancy, leaving open the possibility that the full complexity of environmental regulation escapes genetic analysis.

References

1. K. Kim *et al.*, *Science* **326**, 994 (2009); published online 1 October 2009 (10.1126/science.1176331)
2. G. Angelo, M. R. Van Gilst, *Science* **326**, 954 (2009); published online 27 August 2009 (10.1126/science.1178343)
3. A. Barriere, M. A. Felix, *Curr. Biol.* **15**, 1176 (2005)
4. J. W. Golden, D. L. Riddle, *Science* **218**, 578 (1982)
5. P. Y. Jeong *et al.*, *Nature* **433**, 541 (2005).
6. R. A. Butcher *et al.*, *Nat. Chem. Biol.* **3**, 420 (2007)
7. E. Z. Macosko *et al.*, *Nature* **458**, 1171 (2009)
8. J. Srinivasan *et al.*, *Nature* **454**, 1115 (2008)
9. P. J. Hu, *WormBook* 1 (2007) 10.1895/wormbook.1.144.1
10. R. C. Anderson, *Can. J. Zool.* **62**, 317 (1984)
11. A. Ogawa *et al.*, *Curr. Biol.* **19**, 67 (2009)
12. Z. Wang *et al.*, *Proc. Natl. Acad. Sci. U.S.A.* **106**, 9138 (2009)
13. A. Antebi *et al.*, *Genes Dev.* **14**, 1512 (2000)
14. M. Robinson-Rechavi *et al.*, *J. Mol. Evol.* **60**, 577 (2005)
15. J. H. Thomas, H. M. Robertson, *BMC Biol.* **6**, 42 (2008).

10.1126/science.1183272

OCEAN SCIENCE

Photosynthesis in the Open Ocean

A little-understood electron flow pathway helps cyanobacteria to adapt to high-light, low-nutrient ocean environments.

Jonathan P. Zehr and Raphael M. Kudela

Global primary productivity (the fixation of carbon dioxide, CO_2, into organic matter) fuels food production on land and in the sea. About half of this CO_2 fixation occurs in the sea, mainly by a type of phytoplankton called cyanobacteria (*1*). Recent reports (*2*–*4*) have shown that a key characteristic of oxygenic photosynthesis—the electron flux through photosynthetic reaction centers coupled to oxygen (O_2) evolution—is variable, thus uncoupling oxygen cycling from CO_2 fixation. This insight has implications for how phytoplankton have adapted to the marine environment and for how we measure the productivity of the oceans.

During oxygenic photosynthesis, energy is captured by linear electron transfer through two multiprotein reaction centers, or photosystems, coupled with reduction of CO_2 to sugars in the Calvin cycle. In a perfect world, the coordinated linear electron flow reactions (see the figure, panel A) would stoichiometrically couple O_2 production with CO_2 fixation, without a need for alternate pathways, and measurements of O_2 production or CO_2 fixation would estimate primary productivity, whereas fluctuations in fluorescence intensities would directly represent electron transport rates between photosystems (*5*). However, although linear electron flow from water to carbon is the most important pathway, because it results in CO_2 fixation, other pathways become important under suboptimal growth conditions, allowing photosynthetic organisms to balance input of light energy with production of adenosine triphosphate (ATP) and reductant.

Well-known examples of such pathways include the Mehler reaction, in which electrons are cycled around the photosystem I (PSI) complex, and the use of cytochrome oxidase to reduce O_2, forming water and ATP. Previously reported light-stimulated oxidation of photosynthetic electron carriers, or chlororespiration (*6*), was found to at least partially involve a third pathway using plastoquinol oxidase (PTOX). Recent papers (*2*, *3*) suggest that this pathway (see the figure, panel B) may be more widespread in open

Department of Ocean Sciences, University of California, 1156 High Street, Santa Cruz, CA 95064, USA. E-mail: zehr@ucsc.edu

CREDIT: AKIRA OGAWA AND RALF J. SOMMER

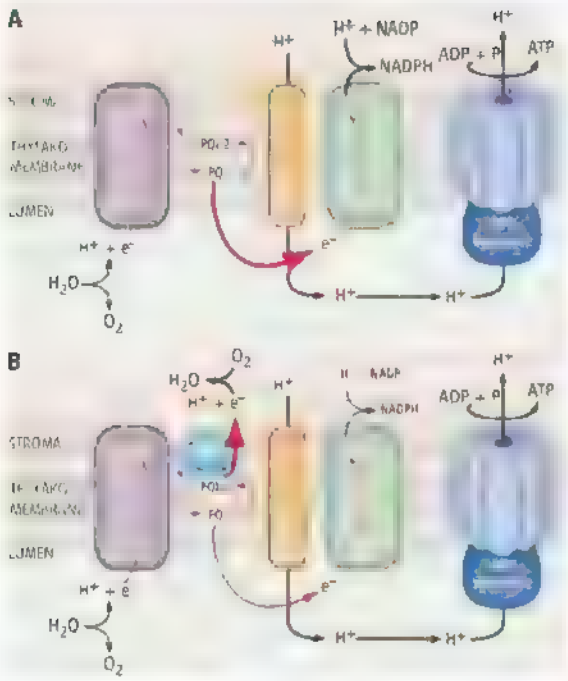

Photosynthesis with a difference. Light harvesting leads to linear electron transport through photosystems PSI and PSII. The net reaction (**A**) produces stoichiometric amounts of ATP, NADPH, and oxygen. When the PTOX electron valve is activated (**B**), electrons are siphoned away from PSI to PTOX, mediating the reduction of oxygen back to water. The result is dissipation of light energy with reduced O_2 and NADPH production and reduced CO_2 consumption while maintaining ATP production.

ocean cyanobacteria than previously recognized. The PTOX pathway provides an electron valve after PSII, allowing the cell to avoid photoinhibition and photosystem damage while producing ATP. This electron valve bypasses PSI, uncoupling PSII and PSI activities and thus changing the stoichiometry of O_2 production and CO_2 fixation.

Photosynthesis is affected by various environmental factors. In the sea, temperature, light quality and quantity, and nutrient availability are the main variables that determine the ability or efficiency of organisms to transform light energy into chemical energy and fixed carbon. Nutrients and trace elements, especially iron, are at vanishingly low concentrations in much of the open ocean, and iron limits photosynthetic production over large regions of the ocean (*7*). In these regions, the ratio of PSII to iron-rich PSI is lower than it is in iron-replete regions (*8*).

To maximize efficiency, the rate of light harvesting at PSII has to equal the rates of electron transfer from water to the PSI reaction center. If electrons are not transferred fast enough, the gateway between light harvesting and electron transfer in PSII is closed or reduced, given that single-celled algae cannot easily escape high light intensities, photodamage occurs if the electrons are not shunted to another acceptor. Various organisms take advantage of PTOX as an electron valve between PSII and PSI (*2*–*4*). PTOX only requires 2 iron molecules (compared with 6 for cytochrome b6f and 12 for PSI), allowing the cells to survive in low-iron environments. When necessary, linear electron flow is reduced, and the electrons are transferred from PSII through PTOX back to O_2 in a closed loop, reducing the electron flux to the Calvin cycle and consuming O_2.

These alternate electron flows provide ecological advantages for organisms in the high-light, low-nutrient environment of the open ocean. O_2 cycling around the photosystems does not change the fundamental operation of light energy harvesting and carbon fixation; its importance lies mainly in enabling phytoplankton to adapt to variable light environments. However, these seemingly minor molecular-scale changes can also have implications on ocean basin scales, because they affect the efficiency of photosynthesis and provide a mechanism for protecting the photosynthetic apparatus, while also impacting measurements of oceanic production.

The PTOX pathway may have implications for photosynthesis rate measurements. Although the pathway provides an ecological advantage, measured changes in O_2 concentrations should still be correlated with CO_2 fixation, because electrons simply cycle through PTOX (with no net change in O_2 and no CO_2 fixation). Carbon fixation is associated with linear electron flow, which produces stoichiometric amounts of O_2. Thus, the net change in O_2 should still be correlated with net CO_2 fixation.

Chlorophyll fluorescence data have been widely used to measure the rate of energy transfer from photosynthetic pigments to the reaction centers, allowing electrons to be tracked directly. These data are generally well correlated with O_2 evolution. By keeping PSII oxidized, the PTOX electron shunt effectively decouples fluorescence from oxygenic photosynthesis. Even though the PTOX pathway thus complicates primary productivity rate measurements using fluorescence, it appears that at global scales, fluorescence measurements remain a robust proxy for assessing phytoplankton physiology and productivity (*9*).

Both prokaryotic (*2*, *3*) and eukaryotic (*4*) algae can generate ATP from the PTOX pathway without producing reductant. This source of ATP could be physiologically advantageous to support processes such as active transport of ions (especially nutrients), synthesis of macromolecules, nitrogen fixation, and activation of metabolic pathways.

Ultimately, NADPH is needed for both carbon and nitrogen assimilation, and it remains unclear how the cell uses the excess ATP to maintain chemical and energy balance. The ratio of electron transfer and oxygen production to carbon fixation is flexible, ranging from O_2 production to CO_2 fixation ratios of ~1 to 1.6 or greater (*10*); this highlights the many uses for ATP and reductant in the cell besides CO_2 fixation (*11*). Fluorescence measurements track the total electron flow, not the number of electrons diverted to PTOX, and fluorescence exceeds measured CO_2 fixation rates by a factor of five or more, with a surprisingly diverse rates and ratios among algal species (*10*). Taken together, the recent reports (*2*–*4*, *10*) provide a mechanistic basis for deviations between electron transfer and CO_2 fixation and highlight the need to think carefully about how these measurements relate to CO_2 fixation.

The PTOX pathway may be a ubiquitous feature of high-light, low-nutrient ocean regimes, but many details remain elusive. Which organisms use alternate electron pathways, and how often do they do so? Is this process restricted to well-lit surface waters and mainly cyanobacteria, and does this change our interpretation of vertical profiles of photosynthetic processes, or satellite-derived proxies? Does iron limitation really lead to reduced PSII:PSI ratios in natural populations of cyanobacteria that are limited by other nutrients as well as iron? Intriguing possibilities for the PTOX pathway include mitigation of chronic iron limitation, enhanced nitrogen fixation, or acquisition of scarce macro- and micronutrients. These adaptations should be considered in any scenario of how the ocean's biogeochemical cycles are likely to operate in the near future.

References

1. E. F. DeLong, D. M. Karl, *Nature* **437**, 336 (2005)
2. S. Bailey *et al.*, *Biochim. Biophys. Acta* **1777**, 269 (2008)
3. K. Mackey *et al.*, *Limnol. Oceanogr.* **53**, 900 (2008)
4. P. Cardol *et al.*, *Proc. Natl. Acad. Sci. U.S.A.* **105**, 7881 (2008)
5. J. C. Kromkamp, R. M. Forster, *Eur. J. Phycol.* **38**, 103 (2003)
6. G. Peltier, L. Cournac, *Annu. Rev. Plant Biol.* **53**, 523 (2002)
7. J. Martin *et al.*, *Limnol. Oceanogr.* **36**, 1793 (1991)
8. R. F. Strzepek, P. J. Harrison, *Nature* **431**, 689 (2004)
9. M. Behrenfeld *et al.*, *Biogeosciences* **6**, 779 (2009).
10. D. J. Suggett *et al.*, *Aquat. Microb. Ecol.* **56**, 147 (2009)
11. M. J. Behrenfeld *et al.*, *Philos. Trans. R. Soc. B* **363**, 2687 (2008)

10.1126/science.1181277

RETROSPECTIVE

Ruth L. Kirschstein (1926–2009)

The leadership, political skills, and commitment of the first woman director at the U.S. National Institutes of Health are unrivaled.

Howard K. Schachman[1] and Marvin Cassman[2]

In a discussion about the U.S. National Institutes of Health (NIH) several years ago, Ruth Kirschstein commented, "I love it." And it showed. She served with distinction in countless positions and her imprint is evident in virtually all NIH policies and practices. With her passing last month from cancer, the world has lost a creative and dedicated public servant.

In 1974, as the newly appointed director of the National Institute of General Medical Sciences (NIGMS), Ruth found a grossly inadequate budget. Because of the poor funding prospects by NIGMS, some scientists began twisting their proposals so as to be assigned to other "richer" NIH institutes. Ruth recognized that general medical problems had little impact on the U.S. Congress, in contrast to cancer or heart disease. Accordingly, she initiated an education campaign about the importance of basic research. Convincing Congress that basic research was the path to improved health was an unrivaled accomplishment. That success has had a lasting impact. By 1998, Congress approved a budget for NIGMS exceeding $1 billion dollars, thereby demonstrating that its members recognized the crucial role of basic research in maintaining health. NIGMS is now the fourth largest institute at NIH.

Whatever the problem, Ruth Kirschstein was there with a creative contribution toward its solution. She was born in 1926, in Brooklyn, New York, and aspired to be a physician. With a medical degree in hand in 1951 from Tulane University, she joined the NIH in 1955 as a pathology resident, and was to spend the next 54 years there. Her innumerable contacts within the scientific community and in government, along with her remarkable memory and comprehensive understanding of NIH and how it functioned, made her the indispensable person to deal with emergencies and provide advice when problems arose. She had a key role in improving the peer review system for NIH grants and in having an acceptable definition of "misconduct in science" adopted by all government agencies. From 2002 to 2009, she was a senior advisor to the NIH director; previously she served as acting associate director of the Office of Research on Women's Health. In 1993 and from 2000 to 2002, Ruth was acting director of NIH, as well as principal deputy director of NIH from 1994 to 2000. It cannot be overemphasized that her success in these roles came not only from her knowledge and abilities, but also from the confidence that Congress placed in her. That confidence was the result of decades of interactions where her qualities of mind were matched by her common sense and unquestioned integrity. As she repeatedly told her staff, "Don't do anything that you wouldn't want to see in *The Washington Post*." (This was usually after some especially egregious behavior of a federal employee or member of Congress was reported in the newspaper.) Her ethical standards were sufficiently ingrained that she needed no such reminders, and she expected nothing less from the people who worked with her. However, a few reminders couldn't hurt.

It is no accident that NIGMS has been the primary focus within NIH for minority programs and for training in general, another reflection of Ruth's interest in individual scientists and their importance in society. One of her first acts as director was to establish the Minority Access to Research Careers (MARC) program in 1975, aimed at improving undergraduate training at minority institutions. Over the years, MARC, the existing Minority Biomedical Research Support program, along with new initiatives, was folded into a new division at NIGMS, Minority Opportunities in Research. The impact of these programs is incalculable. Ruth's belief in the importance of training and the encouragement of students also contributed to the development of predoctoral training programs. Today, these programs are a staple of the academic environment and their value is unquestioned, but it is worth recalling that they were eliminated in 1973 because many government officials did not consider training to be a legitimate function of NIH. They were reestablished in 1974 as the National Research Service Awards. The NIGMS has always been the primary source for these programs, which under Ruth's guidance evolved and grew as the needs of science changed. Her contribution was recognized in 2002 when Congress renamed them "The Ruth L. Kirschstein National Research Service Awards."

Ruth believed that scientific research progressed best when left to the unfettered imagination of the investigator, with as little direction and control as possible. She was firmly committed to the Research Project Grant Program (R01), the heart and soul of basic research funding at NIH. When the issue of determining the human genome sequence emerged, there was a debate between those advocating a centralized, highly directed program versus others proposing individual, loosely coordinated grants. Ruth, knowing that the basic knowledge and many of the techniques had already become available through NIGMS support through individual grants, favored continuing the latter approach. In the end, the decision was made to go with a centralized administrative mechanism, and it became evident that for such a quasi-industrial effort, this was the appropriate choice. The biological sciences had taken their first steps into a Big Science era, whose benefits Ruth readily admitted but with which she was not entirely comfortable. The NIGMS under her direction remained committed to research performed by small groups following their scientific intuitions. It is a strong argument for that vision that NIGMS, through R01 grants, has supported the work of 73 Nobel laureates, including all six of the 2009 laureates in biology or medicine and in chemistry.

It is impossible to write about Ruth's life and career without mentioning her husband and colleague, Alan Rabson, the long-time deputy director of the National Cancer Institute. They both arrived at NIH in the 1950s and stayed there—with a home on the campus—ever since. They have contributed enormously to making NIH a national treasure. Her death leaves a void that cannot be filled at NIH or in the lives of the people who knew her.

10.1126/science.1183756

CREDIT: ERNIE BRANSON/NATIONAL INSTITUTES OF HEALTH

[1]Department of Molecular and Cell Biology, QB3, Stanley Hall, University of California, Berkeley, CA 94720–3220, USA. [2]Former director of NIGMS. E-mail: howardschachman@berkeley.edu; mcassman@sbcglobal.net

How Telomeres Solve the End-Protection Problem

Titia de Lange

The ends of eukaryotic chromosomes have the potential to be mistaken for damaged or broken DNA and must therefore be protected from cellular DNA damage response pathways. Otherwise, cells might permanently arrest in the cell cycle, and attempts to "repair" the chromosome ends would have devastating consequences for genome integrity. This end-protection problem is solved by protein-DNA complexes called telomeres. Studies of mammalian cells have recently uncovered the mechanism by which telomeres disguise the chromosome ends. Comparison to unicellular eukaryotes reveals key differences in the DNA damage response systems that inadvertently threaten chromosome ends. Telomeres appear to be tailored to these variations, explaining their variable structure and composition.

Of the three major questions in telomere biology, two were solved in the 1980s. First, the nature of the DNA sequences that confer telomere function onto chromosome ends was revealed when Blackburn and Szostak showed that the short G-rich repeats from the ends of yeast chromosomes were sufficient to stabilize a linear plasmid (*1*, *2*). Since then it has become clear that G-rich repeats cap the ends of most eukaryotic chromosomes, including mammalian chromosomes that end in TTAGGG repeats.

Second, the mechanism by which telomeric DNA is maintained was resolved when Blackburn and Greider showed that telomeric DNA is synthesized by telomerase. Telomerase is a reverse transcriptase that adds telomeric repeats to the 3′ ends of each chromosome (*3*). In doing so, telomerase makes up for the shortcomings of semiconservative DNA replication, which cannot complete the synthesis of chromosome ends. Other solutions to this end-replication problem exist, notably in *Drosophila* and other dipterans, but it is now clear that telomerase is the main method by which eukaryotes avoid sequence loss at the ends of their chromosomes.

It has been suggested that early eukaryotes used a primitive form of telomeres without telomerase to solve the end-replication problem (*4*). The later acquisition of telomerase not only solved the end-replication problem but ensured the presence of the same sequence at all chromosome ends. Once all telomeres in the cell had the same sequence, telomeric DNA binding factors could evolve, thereby enabling cells to distinguish natural chromosome ends from sites of DNA damage.

The End-Protection Problem

Research on the third major issue in telomere biology, how telomeres solve the end-protection problem, stagnated until the 1990s. The end-protection problem first surfaced early last century, when Muller and McClintock observed a critical distinction between the behavior of broken chromosome ends and telomeres. Muller found that chromosomes lacking their natural ends were unstable; McClintock documented the propensity of broken ends, but not telomeres, to fuse. However, the full extent of the end-protection problem remained obscure until the principles of the DNA damage response were revealed in the 1980s.

The first insight came when Szostak, Rothstein, and Orr-Weaver found that linear DNA introduced into eukaryotic cells is unstable because the DNA ends recombine with the genome (*5*). It is now clear that introduced linear DNA falls victim to two important DNA repair pathways that mend broken chromosomes: homology-directed repair (HDR) and nonhomologous end joining (NHEJ). The observation that DNA ends (also known as double-strand breaks) are processed by these DNA repair reactions raised the question of whether the natural ends of chromosomes are also attacked by HDR and NHEJ, and if not, why not.

A second question arose from the work of Hartwell and Weinert, who found that budding yeast lacking the *RAD9* gene failed to arrest the cell division cycle in response to double-strand breaks (*6*). This experiment, and earlier observations on fission yeast and mammalian cells (*7*), revealed that the cell cycle arrest normally associated with DNA damage is not due to the DNA damage itself. Rather, cells arrest because of the activation of a pathway that detects DNA damage and blocks cell cycle progression in response. Why, then, are these pathways not activated by the natural ends of linear chromosomes?

These findings on how eukaryotes respond to DNA damage shaped the current molecular definition of the end-protection problem: How do telomeres prevent the activation of the DNA damage signaling pathways, and why are they resistant to the repair pathways that act on DNA ends?

In the context of mammalian cells, the end-protection problem can be rephrased in more precise terms, based on current knowledge of the molecular pathways that recognize and repair double-strand breaks (Fig. 1). Mammalian cells have two independent signaling pathways that are activated by double-strand breaks: (i) the ATM (ataxia telangiectasia mutated) kinase path-

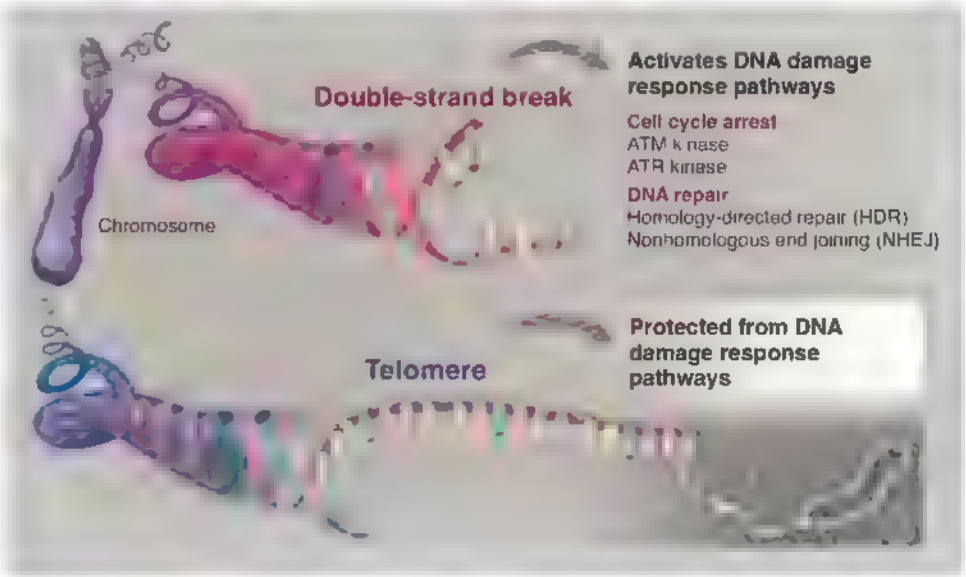

Fig. 1. The end-protection problem. When a mammalian chromosome breaks (top), the exposed DNA ends can activate two signaling pathways (the ATM and ATR kinase pathways) that arrest the cell division cycle and can induce cell death. The broken chromosome is usually repaired by one of two different DNA repair pathways (NHEJ and HDR), allowing cells to continue their divisions with an intact genome. The presence of these DNA damage response pathways poses a problem for the ends of linear chromosomes (telomeres, bottom) because activation of DNA damage signaling or DNA repair at telomeres would be disastrous. Mammalian telomeres solve this end-protection problem through the use of a telomere-specific protein complex (shelterin) and an altered structure (the t-loop) that together ensure that all four pathways remain blocked.

Laboratory of Cell Biology and Genetics, Rockefeller University, New York, NY 10021, USA. E-mail: delange@mail.rockefeller.edu.

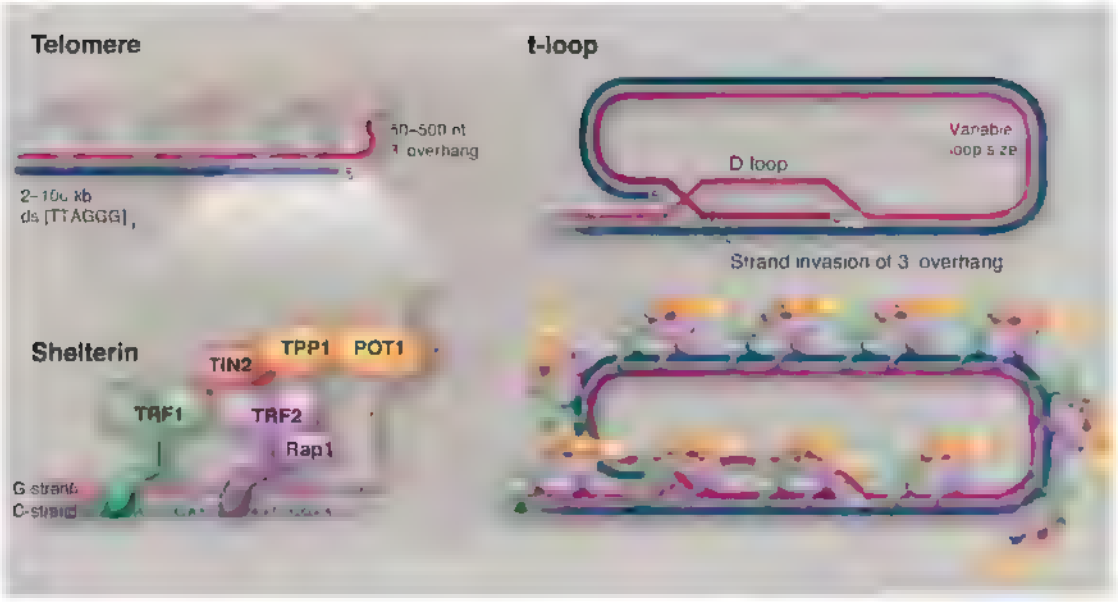

Fig. 2. Mammalian telomeres. Human and mouse telomeres are composed of long stretches of the repetitive sequence TTAGGG and a telomere-specific protein complex, shelterin (upper left). Shelterin derives its specificity for telomeric DNA from three DNA binding proteins (lower left). TRF1 and TRF2 are two similar proteins that bind to the double-stranded telomeric repeats while POT1 interacts with TTAGGG repeats in single-stranded form. TIN2 and TPP1 connect POT1 to TRF1 and TRF2. Rap1 is bound to TRF2. Telomeres are found in a lariat conformation (upper right), the t-loop, which results from the strand invasion of the 3′ single-stranded overhang into the double-stranded telomeric DNA. Shelterin is sufficiently abundant to cover most of the double-stranded telomeric DNA, and there is sufficient POT1 to cover single-stranded telomeric DNA either in the 3′ overhang or in the D loop. Telomeres also contain nucleosomes and numerous shelterin-associated proteins (not shown).

way, which is activated directly by DNA ends, and (ii) the ATR (ataxia telangiectasia and Rad3 related) kinase pathway, which is activated by the single-stranded DNA formed when the 5′ end of a double-strand break gets trimmed back, or resected. Solutions to the end-protection problem must include mechanisms that keep both kinases dormant at telomeres, because mammalian telomeres have features (both a DNA end and a constitutive region of single-stranded DNA) that could activate ATM and ATR. A second set of reactions also needs to be blocked at telomeres: Mammalian cells can repair double-strand breaks via either HDR or NHEJ, and therefore a mechanism must exist that allows telomeres to avoid these reactions.

The end-protection problem of mammalian chromosomes thus involves escaping the potential harmful effects of four different pathways (Fig. 1). Failure to do so will result in cell cycle arrest (under the command of ATM and/or ATR), chromosome end-to-end fusions (a product of NHEJ), or sequence exchanges (mediated by HDR) that involve two telomeres or a telomere and another part of the genome.

How Shelterin Solves the End-Protection Problem in Mammals

Mammalian telomeres solve the end-protection problem through the agency of a six-subunit protein complex called shelterin (*8*) (Fig. 2). Shelterin is endowed with specificity for telomeres through the DNA sequence preference of several DNA binding proteins in the complex. Two shelterin subunits, TRF1 and TRF2, bind to the TTAGGG sequences in double-stranded DNA, and one subunit, POT1, binds to these sequences in single-stranded form. Because these three proteins are held together by TIN2 and TPP1, the selectivity of shelterin for telomeric DNA is exquisite.

The logic of the mammalian telomere system is that the repeats synthesized by telomerase function as binding sites for shelterin. As a consequence, shelterin accumulates at all natural chromosome ends, where it prevents the activation of the DNA damage response. In turn, shelterin is thought to be required for the recruitment of telomerase (*9*), ensuring that this enzyme does not add telomeric DNA to broken ends that lack shelterin binding sites. The sequence specificity of shelterin is critical: If it accumulated at chromosome-internal sites, it could interfere with the normal steps of the DNA damage response in case of local damage, and it might promote inappropriate "healing" of the broken ends by telomerase.

The repression of the ATM kinase pathway at telomeres is the assignment of the TRF2 subunit (Fig. 3A). Loss of TRF2 leads to activation of the ATM kinase at the natural ends of mouse or human chromosomes (*10*, *11*). The consequences of ATM activation can be directly visualized at chromosome ends in the form of DNA damage foci containing DNA damage response factors such as γ-H2AX, MDC1, and 53BP1 (*12*, *13*). Cells lacking TRF2 at their telomeres arrest in the cell cycle because of up-regulation of p53 and show other hallmarks of ATM signaling, including the phosphorylation of ATM and Chk2. The DNA damage response at these dysfunctional telomeres is not only completely dependent on ATM, but also requires a DNA end binding complex [the MRN (Mre11/Rad50/Nbs1) complex] that senses double-strand breaks and activates ATM (*14*–*16*).

The threat of the ATR signaling pathway is handled by POT1 (*17*) (Fig. 3B). Deletion of the two mouse *POT1* genes results in a telomere damage response, as evidenced by DNA damage foci at telomeres and phosphorylation of the ATR target Chk1 (*18*, *19*). The response to loss of POT1 is dependent on the ATR kinase but not on ATM. The ATM kinase remains repressed when POT1 is removed, because TRF2 is still associated with the telomeres. Thus, two different shelterin subunits independently repress the two main DNA damage signaling pathways. Together, TRF2 and POT1 distinguish telomeres from the chromosome-internal double-strand breaks that require DNA repair and modulation of cell cycle transitions.

The TRF2 and POT1 subunits are also instrumental in blocking the two DNA repair pathways that could harm telomeres (Figs. 3 and 4). The NHEJ pathway is a major threat to telomeres because it could create dicentric chromosomes when two telomeres fuse. Dicentric chromosomes are unstable in mitosis, the time when cells segregate their chromosomes during cell division, and thereby promote genome instability. In the G_1 phase of the cell cycle, before DNA replication starts, TRF2 is the main repressor of NHEJ at telomeres (*11*, *20*), whereas in the G_2 phase, after DNA replication, both TRF2 and POT1 contribute to blocking this type of repair (*18*, *21*). In addition, TRF2 and POT1 inhibit the processing of telomeres by HDR (*21*–*24*). However, HDR at telomeres can also be repressed by the Ku70/80 heterodimer, a DNA repair factor that binds to DNA ends. Thus, HDR between telomeres is only fully unleashed when both Ku70/80 is absent and either TRF2 or POT1 is deleted (*22*, *23*).

The protective role of Ku70/80 at telomeres brings up a dilemma that has fascinated the field, because Ku70/80 is a component of the NHEJ pathway. Ku70/80 forms a ring-shaped complex that loads onto DNA ends and promotes the association of double-strand breaks in preparation for their ligation (*25*). Given its role in NHEJ, Ku70/80 could reasonably be expected to be barred from telomeres. Yet this factor binds to telomeres, probably not by loading onto the end, but rather through an interaction with shelterin (*26*). The current interpretation of this paradox is that shelterin might curb the actions of Ku70/80

in such a way that it becomes helpful in repressing HDR without being able to initiate NHEJ. Ku70/80 is one of several DNA repair factors that seem to have been "tamed" by shelterin to protect telomeres without engaging in activities that could pose a threat to telomeres (*27*).

How TRF2 and POT1 Hide the End

How does a DNA binding protein such as TRF2 prevent activation of the ATM kinase at telomere termini? A possible answer arose from an analysis of the structure of telomeric DNA in human and mouse cells, which revealed that the telomere terminus can be hidden in a configuration termed the t-loop (*28*) (Fig. 2). T-loops appear to form through strand invasion of the 3′ telomeric overhang into the duplex part of the telomere. Consistent with such a strand invasion, there is a short segment of single-stranded telomeric DNA at the base of the loop (the D loop). T-loops have also been found in chickens, *Caenorhabditis elegans*, plants, and protozoa (*29*–*32*).

Given that t-loops hide the telomere terminus, their formation and maintenance is expected to block DNA end-binding factors from gaining access to the chromosome end (Fig. 3A). In particular, t-loops could provide an architectural solution to the repression of the ATM kinase pathway, which relies on a sensor (the MRN complex) with DNA end-binding activity. In addition, t-loops could prevent the Ku70/80 heterodimer from loading onto the telomere terminus, thereby blocking the initiation of the NHEJ pathway (Fig. 3A). TRF2, which is dedicated to the repression of ATM and is a key factor for the repression of NHEJ, has the unusual ability to generate t-loop like structures in vitro (*28*, *33*, *34*). Thus, a model can be proposed wherein TRF2, through its ability to remodel telomeres into the t-loop configuration, takes the telomere terminus into custody, sheltering it from the potentially ruinous actions of MRN/ATM and the NHEJ pathways (Fig. 3A).

The above t-loop model does not explain how telomeres deter the ATR kinase, which is activated by replication protein A (RPA), which binds to single-stranded DNA. Although the t-loop sequesters the telomere terminus, binding of RPA to the single-stranded D loop could lead to the activation of the ATR kinase at telomeres.

A likely model for how telomeres block the activation of ATR is based on competition between POT1 and RPA for single-stranded DNA (*17*) (Fig. 3B). POT1 has the advantage over RPA that, as a component of shelterin, it can accumulate in excess of its single-stranded target sequences at telomeres. In agreement with this competition model, RPA is not normally observed at mammalian telomeres but becomes readily detectable when POT1 is impaired (*35*). Furthermore, POT1 can only repress the ATR kinase pathway when linked to the rest of shelterin. Inhibition of TPP1, the tether between POT1 and the rest of shelterin, also activates the ATR kinase pathway (*19*, *36*, *17*). The ability of POT1 to compete with single-strand DNA binding proteins might also play an important role in the repression of HDR, which involves binding of both RPA and the HDR factor Rad51 to single-stranded DNA.

These are speculative models that are influenced by the current understanding of the earliest steps in ATM and ATR signaling and NHEJ, and many issues remain to be addressed (Box 1). As insights into the mammalian DNA damage signaling pathways deepen, more sophisticated models and accompanying tests will emerge. Similarly, future insights into the initiation of HDR in mammalian cells will help to elucidate at which step this pathway is blocked by shelterin and the Ku70/80 heterodimer.

True for an Elephant, but Is It True for...?

In the context of the eukaryotic genomes, the essence of Jacques Monod's dictum ("what is true for *E. coli* is true for an elephant") clearly pertains to one aspect of telomeres: the end-replication problem. Both the problem itself and its telomerase-based solution have been highly conserved during eukaryotic evolution. In contrast, the manner in which telomeres solve the end-protection problem appears to be much less conserved—most likely because the problem itself is not identical in different eukaryotes (Fig. 4).

Telomeres have been studied extensively in two types of single-celled eukaryotes to which we owe much of our current knowledge of telomerase: ciliates and yeast. These organisms

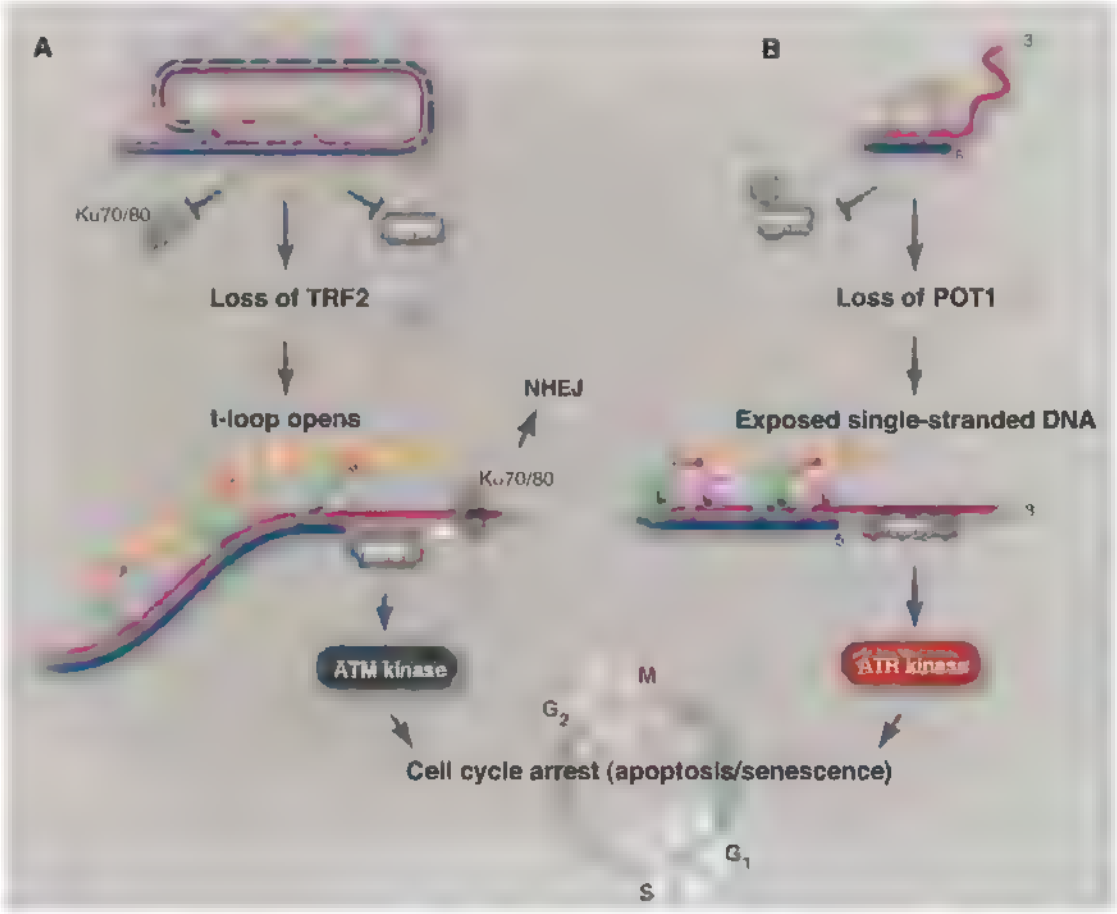

Fig. 3. Different components of shelterin are dedicated to different aspects of the end-protection problem. TRF2 represses the ATM kinase signaling pathway (**A**), whereas POT1 ensures that the ATR kinase is not activated (**B**). In addition, TRF2 is the main repressor of NHEJ at telomeres, although POT1 contributes to the repression of NHEJ, especially after DNA replication. Both TRF2 and POT1 function to block HDR at telomeres (not shown). TRF2 is proposed to block NHEJ and ATM kinase signaling by forming the t-loop. In the t-loop structure (A), the telomere end is hidden from the DNA end sensor MRN that activates the ATM kinase pathway (MRN), and the Ku70/80 ring (which initiates NHEJ) will not be able to load onto the chromosome end. In (B), POT1 is proposed to block ATR kinase signaling by preventing the binding of RPA, the single-stranded DNA binding protein that activates the ATR kinase pathway. POT1 could block RPA from binding to the single-stranded telomeric DNA either when present at the telomere terminus (as shown) or when exposed in the D loop of the t-loop configuration.

also provided early hints about telomere binding proteins, the first of which was found in *Oxytricha*, a hypotrichous ciliate. In their vegetative nucleus (the macronucleus), these ciliates have very short telomeres (one-thousandth the length of mammalian telomeres) that are capped by a single protein dimer, TEBPα/β. TEBPα/β is distantly related to POT1 and its binding partner TPP1 in the shelterin complex (*37*, *38*), although little is known about its function.

Two yeasts (budding yeast and fission yeast), on the other hand, have delivered both the proteins that bind to their telomeres and the phenotypes associated with their functional impairment. Fission yeast telomeres associate with a protein complex that bears similarity to shelterin (*39*). In this complex, a TRF-like module, Taz1, connects to a TPP1/POT1-like dimer, Tpz1/Pot1, through protein-protein interactions. The Rap1 subunit is also conserved and, as in shelterin, it binds to the TRF module, Taz1. Like mammalian TRF2, Taz1 represses the NHEJ pathway at telomeres and also acts with Ku70/80 to inhibit telomere recombination, specifically in cells lacking telomerase (*40*, *41*). NHEJ threatens fission yeast primarily when cells are nitrogen-starved and arrest in the G_1 phase of the cell cycle; when growing in rich medium, fission yeast spends most of its time in the G_2 phase, where HDR dominates (*42*). A corollary of lingering in the G_2 phase is the constant threat of telomere resection, which is blocked by Pot1 (*37*). Cells lacking Pot1 rapidly lose all telomeric DNA, a disastrous phenotype not (yet?) observed at mammalian chromosome ends. How fission yeast avoids the activation of Rad3 (the ATR homolog) and Tel1 (related to ATM) at its chromosome ends is not yet clear. Given that the details of the DNA damage signaling pathways are well-defined in this system, it will be particularly informative to understand at which steps fission yeast telomeres intervene.

The most extensively studied telomeres are those of budding yeast (Fig. 4). These telomeres contain two distinct telomeric complexes, one on the double-stranded telomeric DNA and one at the telomere terminus; neither of them resemble shelterin. The double-stranded DNA binding complex is formed by Rap1, the only shelterin component conserved in budding yeast (*43*-*45*), and its interacting partners Rif1 and Rif2. Unlike mammalian and fission yeast Rap1, however, budding yeast Rap1 binds directly to telomeric DNA (*46*, *47*). Furthermore, budding yeast Rap1 has a prominent nontelomeric function in regulating transcription of numerous genes (*48*). At telomeres, the Rap1 complex has a well-described and highly conserved role in the regulation of telomere length (*49*) and contributes to the repression of NHEJ (*50*), a function it shares with fission yeast Rap1 (*51*). Whether mammalian Rap1 also inhibits NHEJ of chromosome ends remains to be determined (*52*).

The complex that binds to the termini of budding yeast telomeres is composed of three subunits: Cdc13, Stn1, and Ten1 (*53*-*56*). This complex binds to single-stranded telomeric DNA and appears to be a telomere-specific version of RPA, rather than being related to TPP1/POT1 (*57*). The Cdc13 complex is prominent at telomeres during DNA replication, when it has a role in the telomerase pathway (*49*) and—relevant to the end-protection problem—it limits resection of the telomere end, preventing formation of a region of single-stranded DNA. Without the Cdc13 complex, exonucleolytic attack on the 5′ end generates long regions of single-stranded DNA that activate the Mec1 kinase (related to ATR), resulting in arrest after DNA synthesis in the G_2 phase (*58*). It is not yet clear whether Cdc13 prevents Mec1 activation primarily through limiting end resection or whether it also blocks RPA binding to the single-stranded telomeric DNA (as proposed for ATR inhibition by POT1 in mammals).

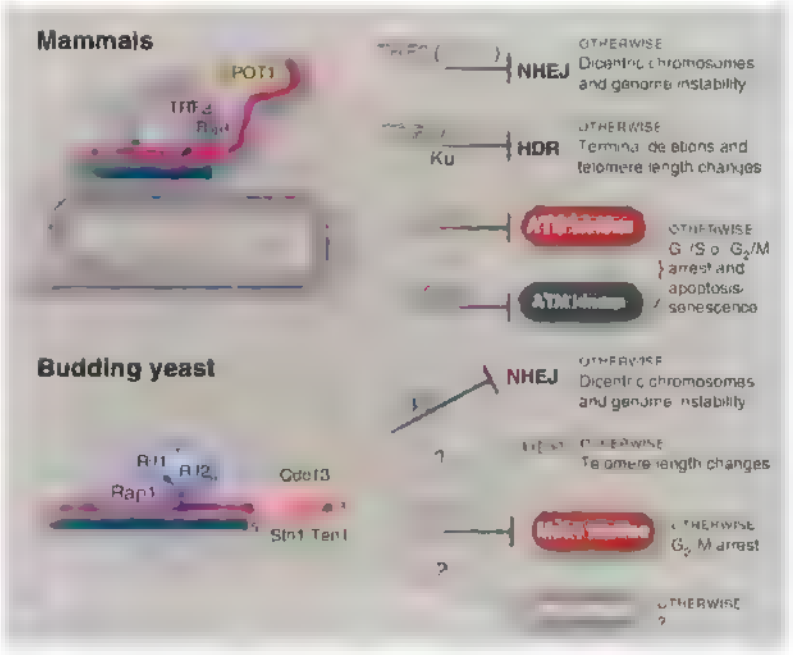

Fig. 4. Different solutions to the end-protection problem. At mammalian telomeres, the presence of shelterin and the t-loop structure together ensure the repression of the four pathways that threaten telomeres throughout the cell cycle (top). The DNA damage response in budding yeast is not the same as in mammalian cells, hence budding yeast telomeres face a different set of threats (bottom). Whereas Mec1 (ATR equivalent) is a major threat, Tel1 (ATM-like) is not, and HDR is less stringently repressed at budding yeast telomeres than in mammals. Budding yeast telomeres appear tailored to cope with this simpler set of problems, which may explain why none of the shelterin components, except for Rap1, are conserved (bottom). Shelterin is at telomeres throughout the cell cycle, whereas Cdc13/Stn1/Ten1 is not at telomeres before the initiation of DNA replication (not shown).

Unlike TRF2 and POT1, which are required to repress ATM and ATR throughout the mammalian cell cycle (*20*), budding yeast Cdc13 complex is not needed for the protection of telomeres in the G_1 phase (*59*). How then do yeast telomeres prevent the activation of the DNA damage signaling pathways during G_1? One pertinent consideration is that the budding yeast version of ATM, Tel1, like its fission yeast counterpart, has a very limited ability to enforce a G_1 arrest; it may thus not pose a threat to cell cycle progression (and hence viability) when it is activated at telomeres. The task for budding yeast telomeres in the G_1 phase is therefore primarily to prevent the activation of Mec1.

The dependence of Mec1 activation on single-stranded DNA may have given budding yeast a reasonable way to avoid its activation in the G_1 phase: limiting the single-stranded DNA at chromosome ends. Indeed, before their replication, budding yeast telomeres do not contain enough single-stranded DNA for RPA binding and hence avoid activation of Mec1 (*60*). Furthermore, end-resection activities are minimal in the G_1 phase, so telomeres may not be at risk in terms of activating Mec1 even when the Cdc13 complex is not bound. According to this logic, the Cdc13 complex is only needed to prevent the activation of Mec1 in the S/G_2 phases, when end-resection activities rise and telomeres gain transient long 3′ overhangs (*61*).

How budding yeast represses HDR at its telomeres is not yet clear, but it appears that the repression is weaker than in mammalian cells. HDR events can occur spontaneously at budding yeast telomeres (*62*), and telomere-telomere recombination can readily compensate for telomerase deficiency (*63*). HDR at mammalian telomeres is more tightly restricted, and mammalian cells are consequently poor at escaping replicative senescence without telomerase (*64*). Unlike the large vertebrate genomes, the budding yeast chromosomes lack substantial chromosome-internal telomeric DNA; therefore, disastrous recombination events between telomeres and chromosome-internal sites should be rare, perhaps obviating the need for stringent HDR control.

These insights suggest interesting differences between budding yeast and vertebrates (and fission yeast) with regard to the end-protection problem and its solutions. Consistent with this divergence, the composition of the telomeric protein complex is distinct. TRF1 and TRF2

Box 1. Outstanding issues concerning the mammalian end-protection problem.

- What are the molecular mechanisms by which TRF2 and POT1 control ATM and ATR signaling and prevent repair by NHEJ and HDR?
- How do t-loops contribute to end protection? Are the loops lost when shelterin is impaired? Are they resolved by passage of the replication fork in the S phase of the cell cycle, or are they present throughout the cycle?
- What is the role of the many shelterin accessory factors that also function in DNA damage signaling and DNA repair? How are their potentially harmful actions repressed at telomeres?
- How is the 3′ overhang of mammalian telomeres generated? Is this process responsible for the high rate of telomere shortening in mammalian cells?
- Does telomeric repeat–containing RNA (TERRA) contribute to end protection? (TERRA has recently been observed in several eukaryotes. Its function and regulation are of potential interest in all aspects of telomere biology.)
- What happens at human telomeres during replicative senescence and crisis? What type of DNA damage response takes place at critically shortened telomeres? Which signal transducers enforce arrest? What repair pathways act on short telomeres? What are the key differences between a critically short telomere and a functional one?
- How is the length of mammalian telomeres regulated, and how is telomerase recruited? Does temporary loss of end protection (for example, in the S phase of the cell cycle) contribute to these pathways?
- How do human ALT cells bypass the repression of HDR at their telomeres? (Alternative lengthening of telomeres, or ALT, is a mechanism of telomere maintenance that relies on HDR.)

have been lost in budding yeast, and part of the role of POT1 has been taken over by the Cdc13 complex. The telomeric DNA itself is also quite different. Although t-loops have been demonstrated directly and indirectly in budding yeasts with unusual telomere length (*65*, *66*), t-loops are unlikely to occur in the wild-type cells. Budding yeast telomeres have three features that may restrict the formation of t-loops: They are short (~300 base pairs), lack a long 3′ overhang in most of the cell cycle, and are made up of imprecise repeats, limiting the options for strand invasion. It could also be argued that the advantages the t-loop has to offer as a solution to the budding yeast end-protection problem are minimal, because the t-loop structure would block the weak Tel1 pathway but is helpless against the bigger threat of the Mec1 pathway.

In addition to ciliates, yeast, and mammals, telomeres are being analyzed in chickens, *Xenopus*, *Drosophila*, *C. elegans*, plants, and assorted protozoa. The resulting comparative telomere biology should lead to a deeper understanding of the spectrum of challenges faced by chromosome ends and how these end-protection problems are solved by variations on the themes observed so far.

Tackling Human Telomeres

Several of the outstanding questions about mammalian telomeres (Box 1) are currently being addressed using genetic tools in the mouse. Although mouse genetics is the only way of assessing null phenotypes in the context of different genetic backgrounds (a prerequisite for understanding how telomeres work), mice have the drawback that they are not human. Human and mouse telomeres, although the same in broad strokes, differ in some detailed aspects that should caution against facile extrapolations from one system to another. For instance, whereas TRF2 and POT1 appear to work very similarly in human and mouse cells, the single *POT1* gene in human cells combines the two distinct functions of the two mouse *POT1* genes (*18*, *23*), and whereas mice survive without Ku70/80, human cells perish without Ku70/80 because of deletion of their telomeres (*67*). These examples imply that subtle differences in the DNA damage response of human and mouse cells may dictate variations in how telomeres solve the end-protection problem.

References and Notes

1. J. W. Szostak, E. H. Blackburn, *Cell* **29**, 245 (1982).
2. J. Shampay, J. W. Szostak, E. H. Blackburn, *Nature* **310**, 154 (1984).
3. C. W. Greider, E. H. Blackburn, *Cell* **43**, 405 (1985).
4. T. de Lange, *Nat. Rev. Mol. Cell Biol.* **5**, 323 (2004).
5. T. L. Orr-Weaver, J. W. Szostak, R. J. Rothstein, *Proc. Natl. Acad. Sci. U.S.A.* **78**, 6354 (1981).
6. T. A. Weinert, L. H. Hartwell, *Science* **241**, 317 (1988).
7. A. J. Callegari, T. J. Kelly, *Cell Cycle* **6**, 660 (2007).
8. T. de Lange, *Genes Dev.* **19**, 2100 (2005).
9. J. L. Stern, T. M. Bryan, *Cytogenet. Genome Res.* **122**, 243 (2008).
10. J. Karlseder, D. Broccoli, Y. Dai, S. Hardy, T. de Lange, *Science* **283**, 1321 (1999).
11. G. B. Celli, T. de Lange, *Nat. Cell Biol.* **7**, 712 (2005).
12. F. d'Adda di Fagagna *et al.*, *Nature* **426**, 194 (2003).
13. H. Takai, A. Smogorzewska, T. de Lange, *Curr. Biol.* **13**, 1549 (2003).
14. C. L. Attwooll, M. Akpinar, J. H. J. Petrini, *Mol. Cell. Biol.* **29**, 5540 (2009).
15. N. Dimitrova, T. de Lange, *Mol. Cell. Biol.* **29**, 5552 (2009).
16. Y. Deng, X. Guo, D. O. Ferguson, S. Chang, *Nature* **460**, 914 (2009).
17. E. Lazzerini Denchi, T. de Lange, *Nature* **448**, 1068 (2007).
18. D. Hockemeyer, J. P. Daniels, H. Takai, T. de Lange, *Cell* **126**, 63 (2006).
19. X. Guo *et al.*, *EMBO J.* **26**, 4709 (2007).
20. A. Konishi, T. de Lange, *Genes Dev.* **22**, 1221 (2008).
21. L. Wu *et al.*, *Cell* **126**, 49 (2006).
22. G. B. Celli, E. Lazzerini Denchi, T. de Lange, *Nat. Cell Biol.* **8**, 885 (2006).
23. W. Palm, D. Hockemeyer, T. Kibe, T. de Lange, *Mol. Cell. Biol.* **29**, 471 (2009).
24. R. C. Wang, A. Smogorzewska, T. de Lange, *Cell* **119**, 355 (2004).
25. M. R. Lieber, Y. Ma, U. Pannicke, K. Schwarz, *Nat. Rev. Mol. Cell Biol.* **4**, 712 (2003).
26. H. L. Hsu *et al.*, *Genes Dev.* **14**, 2807 (2000).
27. W. Palm, T. de Lange, *Annu. Rev. Genet.* **42**, 301 (2008).
28. J. D. Griffith *et al.*, *Cell* **97**, 503 (1999).
29. A. J. Cesare, N. Quinney, S. Wilcox, D. Subramanian, J. D. Griffith, *Plant J.* **36**, 271 (2003).
30. J. L. Muñoz-Jordán, G. A. Cross, T. de Lange, J. D. Griffith, *EMBO J.* **20**, 579 (2001).
31. K. G. Murti, D. M. Prescott, *Proc. Natl. Acad. Sci. U.S.A.* **96**, 14436 (1999).
32. M. Raices *et al.*, *Cell* **132**, 745 (2008).
33. R. M. Stansel, T. de Lange, J. D. Griffith, *EMBO J.* **20**, 5532 (2001).
34. A. Poulet *et al.*, *EMBO J.* **28**, 641 (2009).
35. K. S. Barrientos *et al.*, *Mol. Cell. Biol.* **28**, 5251 (2008).
36. D. Hockemeyer *et al.*, *Nat. Struct. Mol. Biol.* **14**, 754 (2007).
37. P. Baumann, T. R. Cech, *Science* **292**, 1171 (2001).
38. F. Wang *et al.*, *Nature* **445**, 506 (2007).
39. T. Miyoshi, J. Kanoh, M. Saito, F. Ishikawa, *Science* **320**, 1341 (2008).
40. M. G. Ferreira, J. P. Cooper, *Mol. Cell* **7**, 55 (2001).
41. L. Subramanian, B. A. Moser, T. M. Nakamura, *Mol. Cell. Biol.* **28**, 1443 (2008).
42. M. G. Ferreira, J. P. Cooper, *Genes Dev.* **18**, 2249 (2004).
43. M. S. Longtine, N. M. Wilson, M. E. Petracek, J. Berman, *Curr. Genet.* **16**, 225 (1989).
44. M. N. Conrad, J. H. Wright, A. J. Wolf, V. A. Zakian, *Cell* **63**, 739 (1990).
45. A. J. Lustig, S. Kurtz, D. Shore, *Science* **250**, 549 (1990).
46. A. R. Buchman, W. J. Kimmerly, J. Rine, R. D. Kornberg, *Mol. Cell. Biol.* **8**, 210 (1988).
47. B. Li, S. Oestreich, T. de Lange, *Cell* **101**, 471 (2000).
48. D. Shore, K. Nasmyth, *Cell* **51**, 721 (1987).
49. A. Bianchi, D. Shore, *Mol. Cell* **31**, 153 (2008).
50. S. Marcand, B. Pardo, A. Gratias, S. Cahun, I. Callebaut, *Genes Dev.* **22**, 1153 (2008).
51. K. M. Miller, M. G. Ferreira, J. P. Cooper, *EMBO J.* **24**, 3128 (2005).
52. N. S. Bae, P. Baumann, *Mol. Cell* **26**, 323 (2007).
53. J. J. Lin, V. A. Zakian, *Proc. Natl. Acad. Sci. U.S.A.* **93**, 13760 (1996).
54. C. I. Nugent, T. R. Hughes, N. F. Lue, V. Lundblad, *Science* **274**, 249 (1996).
55. N. Grandin, S. I. Reed, M. Charbonneau, *Genes Dev.* **11**, 512 (1997).
56. N. Grandin, C. Damon, M. Charbonneau, *EMBO J.* **20**, 1173 (2001).
57. H. Gao, R. B. Cervantes, E. K. Mandel, J. H. Otero, V. Lundblad, *Nat. Struct. Mol. Biol.* **14**, 208 (2007).
58. B. Garvik, M. Carson, L. Hartwell, *Mol. Cell. Biol.* **15** 6128 (1995).
59. M. D. Vodenicharov, R. J. Wellinger, *Cell Cycle* **6**, 1161 (2007).
60. M. D. Vodenicharov, R. J. Wellinger, *Mol. Cell* **24**, 127 (2006).
61. R. J. Wellinger, A. J. Wolf, V. A. Zakian, *Cell* **72**, 51 (1993).
62. M. T. Teixeira, M. Arneric, P. Sperisen, J. Lingner, *Cell* **117**, 323 (2004).
63. V. Lundblad, E. H. Blackburn, *Cell* **73**, 347 (1993).
64. A. G. Bodnar *et al.*, *Science* **279**, 349 (1998).
65. B. Li, A. J. Lustig, *Genes Dev.* **10**, 1310 (1996).
66. A. J. Cesare, C. Groff-Vindman, S. A. Compton, M. J. McEachern, J. D. Griffith, *Mol. Cell. Biol.* **28**, 20 (2008).
67. Y. Wang, G. Ghosh, E. A. Hendrickson, *Proc. Natl. Acad. Sci. U.S.A.* **106**, 12430 (2009).

68. I thank M. Wellinger, J. Petrini, J. Haber, V. Lundblad, and M. Godinho Ferreira for helpful discussion; Y. Doksani, P. Wu, F. Lottersberger, and A. Sfeir for their comments on this manuscript; and J. Griffith for providing the t-loop EM in Fig. 1. Supported by NIH grants CA076027, GM049046, and AG016642.

10.1126/science.1170633

Widespread Occurrence of Self-Cleaving Ribozymes

Chiu-Ho T. Webb,[1]* Nathan J. Riccitelli,[2]* Dana J. Ruminski,[3] Andrej Lupták[1,2,3]†

Self-cleaving ribozymes are autocatalytic RNAs that include the hammerhead, hepatitis delta virus (HDV), hairpin, the *Neurospora* Varkud satellite, and the bacterial *GlmS* motifs (*1*). Recently, an HDV ribozyme-like fold was found in the human *CPEB3* gene, but sequence-based searches were unable to identify this class of RNAs outside of mammals (*2*). Because in HDV and *CPEB3* ribozymes only six nucleotides (nt) are invariant, whereas about 60 nt are required to form the minimal fold, the conserved nested double-pseudoknot secondary structure (Fig. 1A and fig. S1) was used to search genomic databases for RNAs capable of magnesium-dependent self-cleavage (*3*–*5*).

In vitro self-scission was initially confirmed in six eukaryotes, one bacterium, and one insect virus (Fig. 1B, table S1, and figs. S2 to S18). All eukaryotes harbor several HDV-like ribozymes, and some contain multiple sequence families (figs. S2 to S11). These sequences were used to search the GenBank Expressed Sequence Tags database (dbEST), where additional ribozymes, often in apparently self-cleaved form, were identified in plants, fungi, fish, insects, a tapeworm, and a unicellular ciliate (table S2).

In *Anopheles gambiae*, representatives of two ribozyme families were tested in vitro (Fig. 1 and figs. S2 to S5). The drz-Agam-1 ribozymes were found by using a restrictive structure descriptor and closely resemble HDV and *CPEB3* ribozymes, whereas the drz-Agam-2 family was found by using a descriptor that permitted extended J1/2 and P4 regions. Although previous work demonstrated that a variable P4 helix does not affect catalytic activity (*6*), an expanded J1/2 region has not been observed. This feature appears to stabilize the overall structure, with a fast cleavage rate constant of $1.7 \pm 0.4\ min^{-1}$ at 37°C (Fig. 1C). Rapid amplification of cDNA ends (5′ RACE) experiments performed on total RNA extracts from basic developmental stages of *A. gambiae* showed that the sequenced 5′ ends map to the in vitro verified self-cleavage sites. Reverse transcription quantitative polymerase chain reaction (RT-qPCR) revealed highly differential expression and self-cleavage of the ribozymes (Fig. 1D and figs. S2 to S5), suggesting that both processes are regulated.

Several other sequence families contain features unusual for HDV and *CPEB3* ribozymes. In drz-Spur-3, the P1 helix is only six base pairs long, yet the ribozyme undergoes efficient self-cleavage (Fig. 1B and fig. S8). Drz-Spur-4, drz-Ppac-1, and drz-Dpap-1 contain only one adenosine in the J4 and J2 section (figs. S9, S14, and S19).

Although in vivo analysis of other ribozymes has not been conducted, several findings indicate potential biological activity. In nematodes, the ribozymes (drz-Ppac-1 and drz-Cjap-1; figs. S12 to S15) are intergenic and widely distributed, with drz-Cjap-1, or its fragments, composing up to 1/10,000 of the animal's genome. These copies reside between conserved downstream sequences and diverse upstream sequences and likely play a part in retrotransposition. A similar role is hypothesized for *Strongylocentrotus purpuratus* and *A. gambiae* ribozymes, which appear within or near genes coding for reverse transcriptase–like proteins. Other ribozymes likely partake in RNA processing: drz-CIV-1 resides between predicted transcription and translation start sites of an RNA polymerase large-subunit gene, drz-Fpra-1 maps between two metabolic genes, and drz-Dpap-1 bisects a transcript containing an upstream splice-leader sequence and downstream 5*S* ribosomal RNA (figs. S17 to 19).

Our results indicate that HDV-like ribozymes, and likely ribozymes in general, are widely distributed in nature and may play a variety of biological roles. Although alignment-based sequence searching can uncover conserved regions of these molecules, a structure-based approach has proven more effective at finding new functional RNAs.

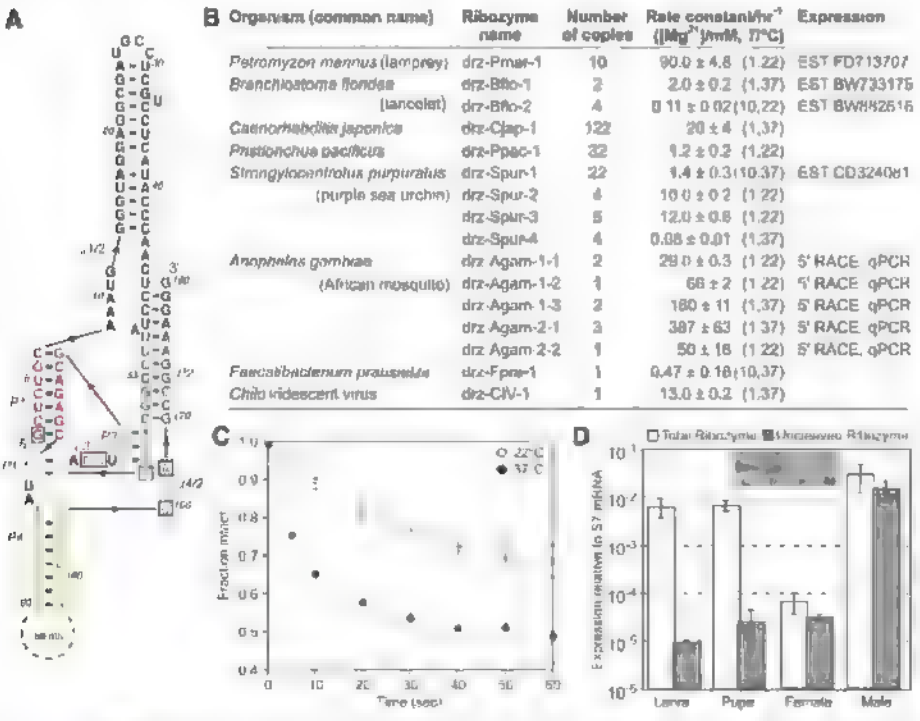

Fig. 1. *A. gambiae* drz-Agam-2-1 ribozyme. (**A**) Core elements are colored by region corresponding to the HDV ribozyme (*1*). Boxed letters are the six invariant positions used in secondary structure searches that identified the ribozymes listed in (**B**). (**C**) Graph of in vitro self-cleavage in 1 mM $MgCl_2$ and (**D**) RT-qPCR of drz-Agam-2-1 isolated from indicated developmental stages. (Inset) 5′ RACE of the ribozyme. All data are average values ± average deviations.

References and Notes

1. M. J. Fedor, *Annu. Rev. Biophys.* **38**, 271 (2009).
2. K. Salehi-Ashtiani, A. Lupták, A. Litovchick, J. W. Szostak, *Science* **313**, 1788 (2006).
3. A. R. Ferre-D'Amare, K. Zhou, J. A. Doudna, *Nature* **395**, 567 (1998).
4. Materials and methods are available as supporting material on *Science* Online.
5. D. Gautheret, F. Major, R. Cedergren, *Comput. Appl. Biosci.* **6**, 325 (1990).
6. M. D. Been, A. T. Perrotta, S. P. Rosenstein, *Biochemistry* **31**, 11843 (1992).

7. We thank the Lupták laboratory, G. Weiss, and J. Kieft for comments and A. James for *A. gambiae* samples. This work was supported by the University of California, Irvine. A.L. is a member of the Chao Family Comprehensive Cancer Center. The GenBank accession numbers for the confirmed ribozymes are BK006878 to BK006897.

Supporting Online Material

www.sciencemag.org/cgi/content/full/326/5955/953/DC1
Materials and Methods
Figs. S1 to S19
Tables S1 and S2
References

22 June 2009; accepted 17 September 2009
10.1126/science.1178084

[1]Department of Molecular Biology and Biochemistry, University of California, Irvine, CA 92697 USA. [2]Department of Chemistry, University of California, Irvine, CA 92697 USA. [3]Department of Pharmaceutical Sciences, University of California, Irvine, CA 92697 USA.

*These authors contributed equally to this work.
†To whom correspondence should be addressed. E-mail: aluptak@uci.edu

Starvation Protects Germline Stem Cells and Extends Reproductive Longevity in *C. elegans*

Giana Angelo and Marc R. Van Gilst*

The study of starvation-resistant biological programs has elucidated numerous mechanisms influencing aging. Here we present the discovery and characterization of starvation-induced adult reproductive diapause (ARD) in *Caenorhabditis elegans*. ARD differs from the *C. elegans* dauer diapause in that it enables sexually mature adults to delay reproductive onset 15-fold and extend total adult life span at least threefold. The effectiveness of ARD requires apoptotic death of the entire germ line, except for a small population of protected germline stem cells (GSCs). When feeding is resumed, surviving GSCs regenerate a new germ line capable of offspring production near the level of nonstarved animals. The starvation-sensing nuclear receptor NHR-49 is required for ARD entry and recovery. Our findings establish mechanisms for preserving stem cell potency and reproductive potential during prolonged starvation.

Upon severe dietary restriction, many organisms, including some mammals, initiate programs of developmental or reproductive diapause, which are reversible states of dormancy (*1*-*3*). In these states, animals often respond to prolonged starvation by considerably extending their normal life span and reproductive period (*3*-*5*). Consequently, studying starvation-mediated diapause has provided a wealth of insight into nutritional control of development, reproduction, and aging (*6*-*9*).

When starved, the soil nematode *Caenorhabditis elegans* can developmentally arrest at multiple larval stages. The most-studied arrests are the larval stage one (L1) and dauer diapauses. Embryos that hatch in the absence of food can survive at least 2 weeks of starvation by entering an L1 diapause (*5*). Worms entering dauer arrest, an alternative developmental fate specialized for enduring long periods of starvation and stress, can withstand several months of nutrient deprivation (*3*). In both cases, worms delay their developmental progression from larvae to adults, which occurs in only 2 days under favorable conditions, by weeks or months. When food is restored, animals exit the diapause, resume larval development, and mature into adults with full reproductive capacity and a normal adult life span, implying that developmental diapause also halts the aging process in arrested larvae (*3*, *5*, *10*).

Discovery of an adult reproductive diapause (ARD). While studying starvation response in late development, we observed adult reproductive arrest. When a population of wild-type (WT) hermaphrodites was completely removed from its bacterial food source during the fourth and final stage of larval development (L4), many animals transitioned into adults and halted reproductive activities, therefore establishing an ARD (Fig. 1A). ARD initiation was optimal if a developmentally synchronized population of animals was removed from food when the majority of animals were in the mid-L4 stage of development (fig. S1, A to C). In this case, there were three distinct fates: (i) Animals arrested as L4 larvae; (ii) animals arrested as adults harboring no more than one live embryo per gonad arm; or (iii) animals developed into adults with multiple embryos in utero, which hatched and caused death through facultative vivipary, more commonly known as "bagging" (*11*) (Fig. 1, C to E). The relative ratio of these three fates differed depending on when starvation was started. For example, Fig. 1B shows the percentage of each outcome when starvation was initiated at the optimal developmental stage. However, if starvation was initiated late in L4 development, the majority of animals would miss the adult arrest and adopt the bagging fate, whereas food withdrawal early in L4 development primarily resulted in animals that arrested as L4 larvae (fig. S1D). ARD was dependent, in some fashion, on population density, because high densities of worms were required for optimal ARD establishment (see supporting online materials and methods). Additionally, isolation of individual ARD animals from a dense population of starved worms led to premature diapause exit and bagging (table S1).

A distinguishing feature of ARD was inhibition of embryo development and facultative

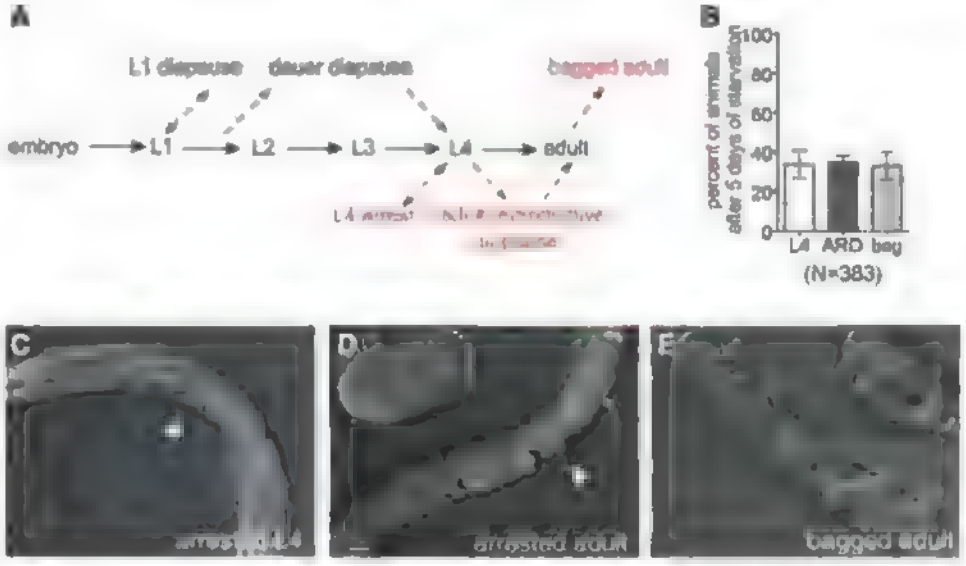

Fig. 1. (**A**) Starvation at receptive periods during early larval development in *C. elegans* leads to the previously characterized L1 and dauer developmental arrests. Acute starvation during the fourth larval stage (L4) leads to the formation of ARD, whereas starvation during late L4 or adulthood results in hermaphrodite bagging. (**B**) When a population of hermaphrodites in the middle of L4 was acutely starved, we observed three potential outcomes: L4 larval arrest, ARD, and bagged adults. The data are presented as the mean (±SEM) percentage of animals that adopted each of the three fates. Data are compiled from nine independent starvations ($n = 9$). The total number of animals scored in all nine experiments is also shown. (**C**) An arrested WT L4 after 5 days of starvation. The vulva is marked with an arrowhead. (**D**) A typical WT hermaphrodite in the fifth day of ARD. This animal contained two embryos in utero (indicated with arrows). The vulva is marked with an arrowhead. The inset shows an enlargement of one of the two uterine embryos (red arrow); it is in a premorphogenic stage of embryogenesis, when cells have not yet begun to differentiate. (**E**) A WT hermaphrodite in the process of bagging with five embryos in utero (indicated with arrows). The inset shows an enlargement of one of these embryos in the morphogenic stage of embryogenesis, when cells terminally differentiate and tissues and organs begin taking shape (red arrow). Scale bars = 20 μm.

Division of Basic Sciences, Fred Hutchinson Cancer Research Center, 1100 Fairview Avenue North, Seattle, WA 98109, USA.

*To whom correspondence should be addressed. E-mail: vangilst@fhcrc.org

vivipary (Fig. 1D). Under standard laboratory conditions, embryos develop and hatch within 14 hours of fertilization. If adult worms are starved and do not establish ARD, egg laying is inhibited and hatching of multiple embryos will occur in the uterus within 24 to 48 hours (*11*). In contrast, up to two embryos were retained within the uterus of ARD animals for at least 30 days. These embryos were viable for at least the first 5 days of starvation. For example, if ARD animals were isolated 3 or 5 days after starvation, thereby promoting diapause exit, embryos resumed a more normal rate of development and hatched inside the adult within 24 hours (table S1). Differential interference contrast (DIC) images suggested that the viability of uterine embryos, as determined by embryo morphology, started to decrease around day 7 of starvation. Inviable embryo remains then occupied the uterus as "corpses" (*12*) (Fig. 3F). These data argue that the ARD mechanism involves slowing or arresting the development of uterine embryos for at least 5 days of starvation, so that they can resume normal development and hatching upon ARD exit.

The mechanism for preventing embryonic development in ARD animals is still not apparent. Starvation-induced embryonic diapause is common in many animals, and it has recently been shown that hypoxia can cause embryonic diapause in *C. elegans* (*2*, *13*). However, because isolation of individual animals in ARD led to diapause release, we were unable to monitor embryonic development in arrested adults; therefore, it is not clear whether embryos in these animals fail to hatch because they are in an embryonic diapause or development is simply slowed down.

The adult diapause extends life span and reproductive longevity. In theory, the effectiveness of a starvation-induced diapause depends on the ability of arrested worms to survive extended periods of starvation, search for improved nutritional conditions, and recover to produce offspring. To characterize the survivability characteristics of ARD, we measured two parameters in animals rescued from ARD after periods of starvation of up to 30 days. First, we quantified brood size, a parameter indicative of how well reproductive potential is maintained during starvation (Fig. 2A). Second, we determined how well ARD protected the "youth" of somatic tissues by measuring the life span of worms after food restoration (Fig. 2B).

Entry into ARD offered notable survival advantages over worms that underwent the bagging fate. Even at 30 days of starvation, arrested adults recovered when returned to food and produced up to 20 progeny through self-fertilization (Fig. 2A). Much larger broods (>100 progeny when starved up to 15 days and >50 at 30 days) were obtained when animals were reintroduced to food and mated with well-fed males. This result suggests that viable oocytes are produced even after very long periods of starvation; however, the fecundity of recovered hermaphrodites that self-fertilize is limited by the survival of functional sperm. Consistent with this hypothesis, very few sperm are observed in worms starved for extended periods, even after rescue (Fig. 3, D and G). The normal reproductive period of *C. elegans* begins at the onset of adulthood (~2 days after

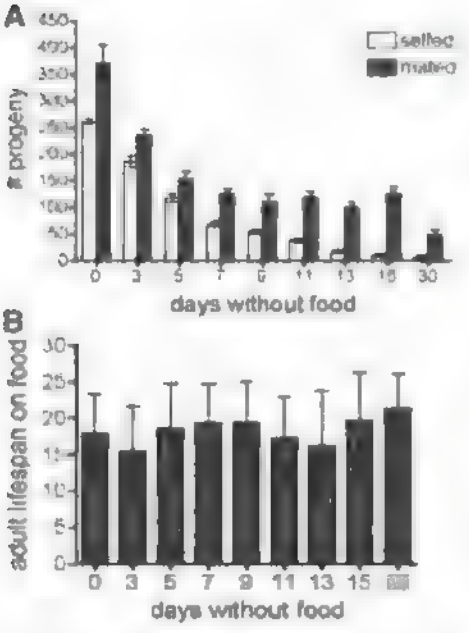

Fig. 2. (**A**) The number of progeny produced by WT animals rescued from ARD after various periods of starvation. Hermaphrodites were allowed to self-fertilize (white bars) or mate with fed males (gray bars). Data represent the mean brood size (±SEM) per animal (n = 19 to 24 animals per time point). Worms were obtained from three independent starvations. (**B**) The mean adult life span (±SD) of animals rescued from ARD after various periods of starvation on nematode growth media plates (n > 23 animals per time point).

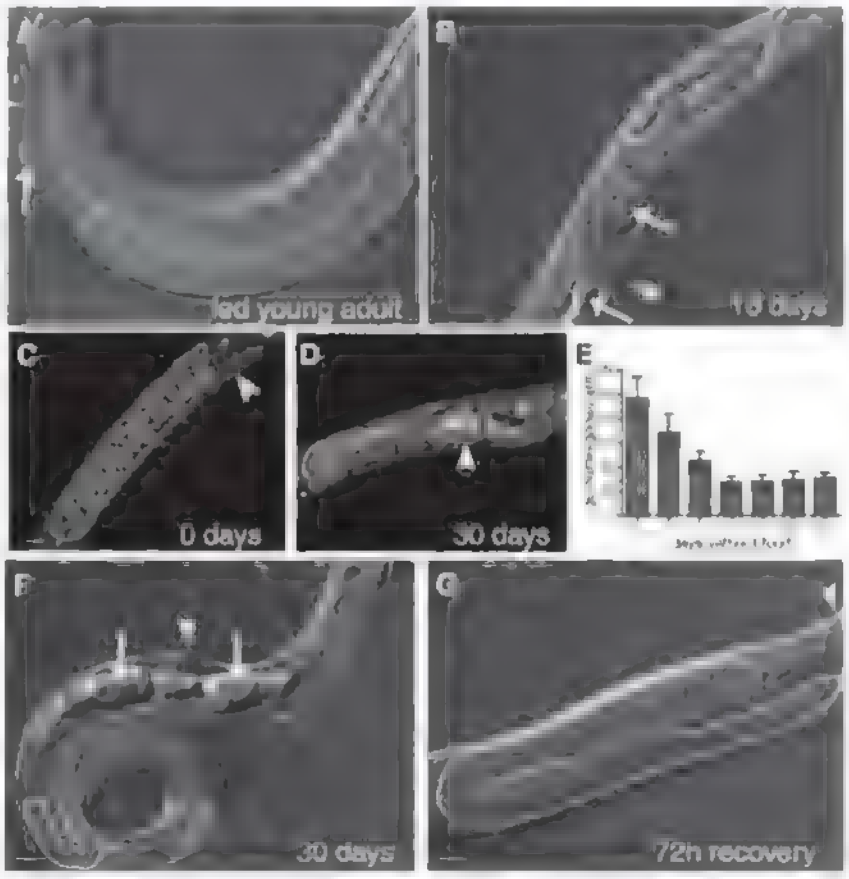

Fig. 3. (**A**) A typical WT hermaphrodite germ line shortly after reaching adulthood. In all images the gonad is outlined in white, the vulva is marked with an arrowhead, and uterine embryos are marked with arrows. The distal tip cell is opposite the vulva in (A), (C), and (G). (**B**) By 10 days of ARD, the gonad was considerably condensed and the embryos appear inviable. (**C**) DAPI (4′,6′-diamidino-2-phenylindole) staining of L4 worms at the time of food withdrawal. (**D**) DAPI staining of arrested adults after 30 days in ARD. (**E**) Quantification of germ cell nuclei by DAPI staining showed a significant reduction in germ cell nuclei over time. Time course data are displayed as the mean (±SD) number of surviving germ cells per gonad arm (n > 16 gonad arms per time point for days 5 to 30, and n = 5 gonad arms per time point for days 0 and 3). Worms were obtained from three independent starvations. The loss of germ cell nuclei plateaus when about 35 germ cells remain. (**F**) After 30 days of starvation, the gonad was considerably condensed, and the embryos remained as corpses (arrows). (**G**) After 72 hours of refeeding, a remarkable recovery was observed, and the germ line had regenerated and appeared similar to that of a well-fed young adult. No sperm are visible in the spermatheca, adjacent to the proximal end of the gonad. Scale bars = 20 μm.

hatching from embryos); thus, the initiation of reproduction can be extended by at least 15 fold when animals enter ARD.

ARD also appears to share the anti-aging properties of other developmental diapauses (Fig. 2B). Animals starved for up to 30 days were able to exit ARD and still live a normal adult life span (~18 days at 20°C) when returned to food. These results are consistent with prior studies showing that starvation of sterilized *C. elegans* adults can dramatically extend total life span (*14*). Our results are distinct from these studies, however, in that we observed the extension of life span and reproductive longevity in fertile WT animals. Nonetheless, it is possible that sterilization of adult nematodes mimics a component of the adult arrest and thereby leads to the extension of life span through a similar mechanism

Protection of germline stem cells (GSCs) and germline regeneration. Perhaps the most striking feature of ARD was plasticity of the germ line during maintenance and recovery. Shortly after ARD initiation, we observed substantial loss of cellular volume and germ cell number in the gonad (Fig. 3, A to D). After more prolonged starvation (>10 days), the germ line was reduced to a small population of ~35 germ cell nuclei per gonad arm (Fig. 3E). This surviving population of germ cells was maintained at a relatively constant level for another 20 days, implying that these cells were protected from the mechanism that precipitated death of the rest of the germ line (Fig. 3E). Changes in somatic gonad morphology were also marked by retreat of the distal tip cell (Fig. 3B and fig. S3, A to C).

Reintroduction to food resulted in robust recovery, so that the germ line of an animal rescued after 30 days of starvation appeared similar to that of a young adult that had never been starved (Fig. 3G). Consequently, exit from ARD must involve processes that stimulate the proliferation and differentiation of GSCs in order to regenerate a fully mature and functional female germ line. Thus, the population of germ cells protected during extended starvation must contain functional GSCs.

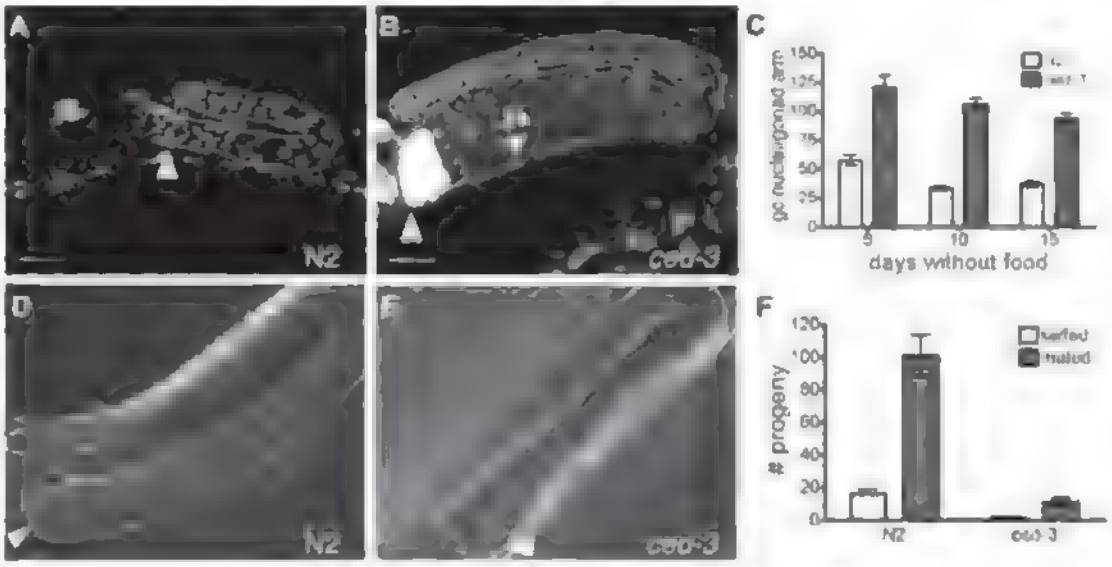

Fig. 4. (**A** and **B**) Whole-animal DAPI staining revealed that *ced-3(n1286)* mutants possess more germ cell nuclei than WT worms after 15 days of starvation in ARD. The proximal end of the gonad is indicated with a white arrowhead. The mass of DAPI staining in the *ced-3(n1286)* animal represents endomitotic nuclei in the proximal gonad. (**C**) The bar graph represents the mean (±SEM) number of germ cell nuclei present in arrested WT (white bars) and *ced-3(n1286)* (gray bars) adults after increasing days of starvation (n = 8 to 10 gonad arms per data point). (**D** and **E**) DIC images of recovered adults that had spent 15 days in ARD were taken after recovery. (**F**) Rescued *ced-3* adults produced fewer progeny by both self-fertilization (white bars) and mating with well-fed WT males (gray bars). Bars represent the mean (±SEM) number of progeny produced per animal (n > 15 animals per data point) upon recovery on food after 15 days of starvation. Scale bar = 20 μm.

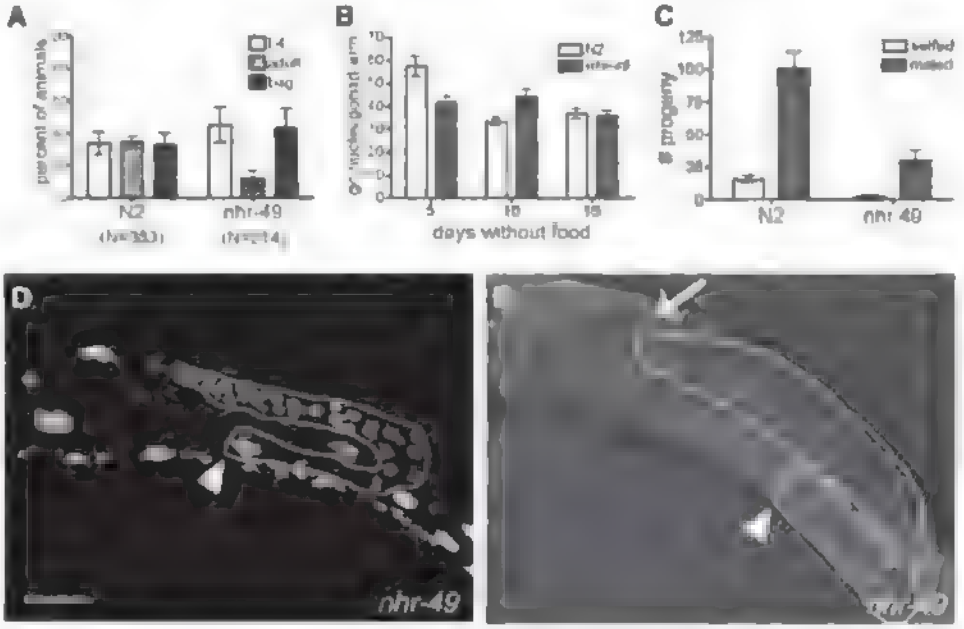

Fig. 5. (**A**) *nhr-49(nr2041)* mutants were severely impaired in their ability to form a normal ARD. Data are presented as the percent of animals (±SEM, n = 5) that arrested as L4s (white bars), bagged (black bars), or remained adults in ARD or some other form (gray bars). Total numbers of worms assayed in all five experiments are indicated on the graph. Of the 12% of *nhr-49(nr2041)* animals that did not arrest as L4s or die by bagging, fewer than 1% showed the primary characteristics of ARD (fig. S5). (**B**) The bar graph represents the mean (±SEM) number of germ cell nuclei per gonad arm (n = 7 to 10 gonad arms per time point) in arrested WT (white bars) and *nhr-49(nr2041)* adults (gray bars) after increasing days of starvation. (**C**) Rescued *nhr-49(nr2041)* mutants produced fewer progeny by both self-fertilization (white bars) and mating with well-fed WT males (gray bars). Bars represent the mean number of progeny (±SEM, n > 14 animals per time point) produced per recovered animal after 15 days of starvation. (**D**) A representative image of a DAPI-stained *nhr-49(nr2041)* adult after 15 days of starvation. The gonad is outlined, and the proximal end of the gonad is indicated with a white arrowhead. (**E**) A representative DIC image of a recovered *nhr-49(nr2041)* adult that had spent 15 days in starvation before rescue. The yolklike substance in the body cavity is indicated with a white arrow. Scale bar = 20 μm.

Programmed cell death (PCD) or apoptosis in *C. elegans* is active during adulthood as a means to control total germ cell number in healthy animals and also to mediate germ cell death in response to pathogens, stress, and short-term starvation (*15*–*18*). To determine whether apoptosis was responsible for the germline atrophy observed during ARD, we examined the apoptosis-deficient *ced-3(n1286)* mutant. The *ced-3* gene encodes a caspase essential for apoptosis. We found that inactivation of *ced-3* did not inhibit ARD entry but did prevent the reduction in germ cell nuclei normally observed during the course of ARD (Fig. 4, A to C). Although *ced-3(n1286)* mutants appeared healthy when starved for 15 days in ARD, these mutants were unable to successfully recover upon refeeding, because germ cell proliferation resumed in the distal gonad, but oocyte formation and embryo production were severely impaired (Fig. 4, D to F, and fig. S4, A to D).

These results demonstrate that the PCD mechanism is a critical factor for extending the reproductive potential of animals rescued from prolonged starvation in ARD. The germ cell loss observed in ARD could potentially be explained by the normal rate of germline apoptosis in combination with a failure to replace dead germ cells with new germ cell proliferation (*15*). However, there are clear differences between starvation-mediated cell death, which results in the death of nearly all differentiated cells, and the apoptosis mechanism that functions in the gonad of well-fed animals, which targets only some germline cells in order to nurse growing oocytes (*15*). Thus, it is likely that the ARD mechanism is specifically regulating germ cell proliferation and apoptosis.

NHR-49 is required for ARD. In mammals, both the peroxisome proliferator–activated receptor α (PPARα) and hepatocyte *nuclear* factor-4α (HNF-4α) nuclear receptors (NRs) mediate metabolic response to food withdrawal, implying that NRs function in starvation physiology (*19*, *20*). The *C. elegans* counterpart of these receptors is the NHR-49 protein, which is an HNF-4α homolog that mediates the induction of fatty acid oxidation and gluconeogenesis genes in response to food deprivation (*21*).

We found that NHR-49 was required for the establishment of ARD. When *nhr-49* loss-of-function animals [*nhr-49(nr2041)*] were starved at the same point in the L4 program as WT animals, approximately 12% did not arrest as L4s or bag as adults (Fig. 5A). However, less than 1% of these animals entered a normal ARD. First, in all *nhr-49(nr2041)* animals that failed to bag, embryos in the uterus were inviable (fig. S5, A to B). This observation raises the question of whether *nhr-49* mutants are able to arrest embryonic development, and consequently only survive extended starvation if dead embryos are produced, thus preventing death via bagging. Second, in surviving *nhr-49(nr2041)* adults, sperm were strongly attracted to the proximal oocyte, whereas in WT animals in the reproductive diapause, sperm were primarily confined to the spermatheca (fig. S5, C to E). Finally, *nhr-49(nr2041)* animals were severely impaired in their ability to recover from starvation and produce offspring (Fig. 5C and table S2). Two days after rescue of starved *nhr-49(nr2041)* adults, the uterus of these mutants was filled with cellular debris, and yolk-like material was present throughout the body cavity (Fig. 5E and fig. S6C). The rate of cell death in *nhr-49(nr2041)* mutants was comparable to that of WT animals, however, implying that the accumulation of cellular debris is likely to be a consequence of impaired autophagy or phagocytic mechanisms normally required for maintaining a clean proximal gonad (Fig. 5, B and D, and fig. S6D).

The fact that *nhr-49(nr2041)* mutants could not properly mediate ARD entry brought up the question of whether the loss of *nhr-49* function and poor ARD establishment would also interfere with the protection of GSCs. However, we found that *nhr-49* and normal ARD establishment were not required for the survival of GSCs and for their ability to proliferate upon recovery from starvation (Fig. 5, D and E, and figs. S5G and S6C), implying that these components of the ARD are separable from the NHR-49 mediated mechanism that facilitates ARD establishment.

It is clear that NHR-49 mediates numerous changes in glucose and fat metabolism upon starvation; how NHR-49 senses these changes and responds is not yet understood (*21*, *22*). The *Drosophila* homolog of NHR-49, HNF-4α, has been shown to interact with free fatty acids released from lipases immediately after the initiation of starvation (*23*). Given the strong homology of these two NRs both in structure and in function, it is likely that a similar mechanism occurs in *C. elegans*. Consequently, we expect that lipases and the upstream signals that activate lipases in response to starvation will also be key features in this overall signaling network. Recent studies have shown that GSC arrest leads to the activation of lipid hydrolysis in *C. elegans* (*24*).

Discussion. We have shown that the initiation of ARD enables the formation of a starvation-resistant adult that can extend reproductive potential for at least 30 days. Based on our findings, we propose a "disposable germline" hypothesis: As ARD progresses, nutrient deprivation leads to a loss of oocytes and meiotic germ cell nuclei. Meanwhile, a small population of mitotic germ cells is maintained in the stem cell niche in quiescence or self-renewal. Mitotic germ cells in general are protected from apoptosis in the *C. elegans* germ line (*15*). Because these cells are generally held in mitosis by Notch signaling from the stem cell niche, we predict a role for Notch signaling in ARD (*15*, *16*). In support of this hypothesis, a $P_{lag\text{-}2}$::GFP (P, promoter; GFP, green fluorescent protein) promoter shows that expression of the *lag-2* gene, which encodes the Notch ligand necessary for inhibiting exit from mitosis, is expressed at high levels even after 90 days of starvation (fig. S3). We also predict that autophagy and/or phagocytosis of apoptotic germ cells provides fuel necessary for supporting viability during starvation. As a whole, this model implies that worms have adapted a mechanism to exploit differentiated germ cells for fuel while preserving pluripotent stem cells for tissue regeneration when conditions improve. Although the ecological advantage of the ARD is not yet clear, we suggest that this alternative diapause may exist because it is specially adapted to survive starvation in environmental contexts where the dauer diapause is not as effective, or it functions simply as an added layer of protection against harsh environmental conditions. Like the *C. elegans* dauer diapause, our results show that ARD is dependent on population density, implying that pheromones and/or other signals may also be an important part of this process. However, we cannot yet rule out the possibility that a crowded population facilitates ARD by depleting important nutrients from the growth media.

The effect of ARD on the reproductive system is quite distinct from the prevailing models of the impact of caloric restriction on somatic cells, which posit that reduced calorie intake leads to slowing of somatic cell aging (*9*). We have observed here that starvation of adult *C. elegans* leads to a "reversal" of the aging process in the reproductive system, because a new differentiated germ line is regenerated when food is restored. Our characterization of this reproductive diapause presents *C. elegans* as a model for this process and for understanding how stem cells and their host tissues survive and recover from prolonged periods of nutrient deprivation. Studies in fruit flies show that this phenomenon may be conserved across metazoan species, because nutrient deprivation leads to changes in germline proliferation and apoptosis in *Drosophila* (*25*, *26*). Vitamin A levels can control GSC death and proliferation in rodent testes in a process that may mirror that of germline plasticity in *C. elegans* ARD (*27*). Finally, starvation of cultured cancer cell lines results in the death of differentiated cancer cells, whereas side populations of cancer stem cells survive (*28*). Altogether these findings suggest a provocative mechanism for how calorically restricted animals in general, including mammals, may extend their reproductive period (*29*), and we expect that studies of the *C. elegans* ARD will reveal essential factors involved in somatic cell and GSC aging, as well as factors involved in controlling germline resurrection in response to nutritional signals. Our implication of NHR-49 reveals a NR important for robust ARD establishment, and our characterization of a *ced-3* mutant reveals an important role for apoptosis in ARD maintenance and recovery.

References and Notes

1. F. L. Lopes, J. A. Desmarais, B. D. Murphy, *Reproduction* **128**, 669 (2004)
2. M. B. Renfree, G. Shaw, *Annu. Rev. Physiol.* **62**, 353 (2000)

3. D. L. Riddle, *C. elegans II* (Cold Spring Harbor Laboratory Press, Cold Spring Harbor, NY, 1997), pp. 739–768.
4. M. Tatar, C. Yin, *Exp. Gerontol.* **36**, 723 (2001)
5. T. E. Johnson, D. H. Mitchell, S. Kline, R. Kemal, J. Foy, *Mech. Ageing Dev.* **28**, 23 (1984)
6. L. Guarente, C. Kenyon, *Nature* **408**, 255 (2000)
7. C. E. Finch, G. Ruvkun, *Annu. Rev. Genomics Hum. Genet.* **2**, 435 (2001).
8. J. R. Cypser, P. Tedesco, T. E. Johnson, *Exp. Gerontol.* **41**, 935 (2006).
9. W. Mair, A. Dillin, *Annu. Rev. Biochem.* **77**, 727 (2008)
10. M. Fukuyama, A. E. Rougvie, J. H. Rothman, *Curr. Biol.* **16**, 773 (2006)
11. J. Chen, E. P. Caswell-Chen, *J. Nematol.* **36**, 107 (2004)
12. A corpse is defined as any embryonic material still residing within the eggshell that clearly does not resemble the normal morphology of developing embryos.
13. D. L. Miller, M. B. Roth, *Curr. Biol.* **19**, 1233 (2009)
14. T. L. Kaeberlein *et al.*, *Aging Cell* **5**, 487 (2006)
15. T. L. Gumienny, E. Lambie, E. Hartwieg, H. R. Horvitz, M. O. Hengartner, *Development* **126**, 1011 (1999)
16. S. L. Crittenden, K. A. Leonhard, D. T. Byrd, J. Kimble, *Mol. Biol. Cell* **17**, 3051 (2006)
17. L. S. Salinas, E. Maldonado, R. E. Navarro, *Cell Death Differ.* **13**, 2129 (2006).
18. A. Abaltay, F. M. Ausubel, *Proc. Natl. Acad. Sci. U.S.A.* **98**, 2735 (2001)
19. S. Kersten *et al.*, *J. Clin. Invest.* **103**, 1489 (1999)
20. J. Rhee *et al.*, *Proc. Natl. Acad. Sci. U.S.A.* **100**, 4012 (2003)
21. M. R. Van Gilst, H. Hadjivassiliou, K. R. Yamamoto, *Proc. Natl. Acad. Sci. U.S.A.* **102**, 13496 (2005).
22. M. R. Van Gilst, H. Hadjivassiliou, A. Jolly, K. R. Yamamoto, *PLoS Biol.* **3**, e53 (2005)
23. L. Palanker, J. M. Tennessen, G. Lam, C. S. Thummel, *Cell Metab.* **9**, 228 (2009)
24. M. C. Wang, E. J. O'Rourke, G. Ruvkun, *Science* **322**, 957 (2008)
25. D. Drummond-Barbosa, A. C. Spradling, *Dev. Biol.* **231**, 265 (2001)
26. H. J. Hsu, L. LaFever, D. Drummond-Barbosa, *Dev. Biol.* **313**, 700 (2008).
27. H. F. Huang, W. C. Hembree, *Biol. Reprod.* **21**, 891 (1979).
28. R. T. Tavalue, L. S. Hart, D. T. Dicker, W. S. El-Deiry, *Cell Cycle* **6**, 2554 (2007)
29. K. Selesniemi, H. J. Lee, J. L. Tilly, *Aging Cell* **7**, 622 (2008)

30. We thank J. Priess and B. Edgar for critical reading of the manuscript; J. Kimble and L. Jones for helpful suggestions, the Priess lab for materials and equipment; and the Van Gilst, Priess, and Roth laboratories for helpful discussions and feedback. G.A. is funded by a Ruth Kirchstein postdoctoral fellowship from NIH (GM080895-02). This work was also funded by an American Diabetes Association Junior Investigator Award (ADA 1-07-JF-72) and by a grant from NIH (RDK079273A).

Supporting Online Material

www.sciencemag.org/cgi/content/full/1178343/DC1
Materials and Methods
Figs. S1 to S6
Tables S1 and S2

29 June 2009; accepted 18 August 2009
Published online 27 August 2009;
10.1126/science.1178343
Include this information when citing this paper

Global Observations of the Interstellar Interaction from the Interstellar Boundary Explorer (IBEX)

D. J. McComas,[1,2]* F. Allegrini,[1,2] P. Bochsler,[3] M. Bzowski,[4] E. R. Christian,[5] G. B. Crew,[6] R. DeMajistre,[7] H. Fahr,[8] H. Fichtner,[9] P. C. Frisch,[10] H. O. Funsten,[11] S. A. Fuselier,[12] G. Gloeckler,[13] M. Gruntman,[14] J. Heerikhuisen,[15] V. Izmodenov,[16,17,18] P. Janzen,[19] P. Knappenberger,[20] S. Krimigis,[7,21] H. Kucharek,[22] M. Lee,[22] G. Livadiotis,[1] S. Livi,[1,2] R. J. MacDowall,[5] D. Mitchell,[7] E. Möbius,[22] T. Moore,[5] N. V. Pogorelov,[15] D. Reisenfeld,[19] E. Roelof,[7] L. Saul,[3] N. A. Schwadron,[23] P. W. Valek,[1,2] R. Vanderspek,[6] P. Wurz,[3] G. P. Zank[15]

The Sun moves through the local interstellar medium, continuously emitting ionized, supersonic solar wind plasma and carving out a cavity in interstellar space called the heliosphere. The recently launched Interstellar Boundary Explorer (IBEX) spacecraft has completed its first all-sky maps of the interstellar interaction at the edge of the heliosphere by imaging energetic neutral atoms (ENAs) emanating from this region. We found a bright ribbon of ENA emission, unpredicted by prior models or theories, that may be ordered by the local interstellar magnetic field interacting with the heliosphere. This ribbon is superposed on globally distributed flux variations ordered by both the solar wind structure and the direction of motion through the interstellar medium. Our results indicate that the external galactic environment strongly imprints the heliosphere.

The Sun continuously emits ionized solar wind that flows supersonically outward at ~300 to 800 km s^{-1} until it reaches the termination shock (TS), where it slows and compresses. This flow inflates a bubble in the local interstellar medium (LISM) called the heliosphere. The heliosphere moves through the LISM at ~26 km s^{-1}, so the LISM plasma dynamic pressure pushes the boundary between the solar wind and the LISM (the heliopause) in at the nose and presumably forms a tail in the opposite direction. The solar wind also contains interstellar pickup ions (PUIs) with energies of a few keV/amu, produced by ionization of cold interstellar neutrals that drift into the heliosphere. At the TS, hydrogen PUIs, whose number density is 10 to 20% that of the solar wind, are heated, producing a suprathermal population of ions. These ions dominate the pressure in the inner heliosheath, which lies between the TS and heliopause. Energetic neutral atoms (ENAs) are generated in this region when low-energy [few electron volts (eV)] interstellar neutrals undergo charge exchange with either solar wind ions or PUIs (*1*–*4*). Once produced, the ENAs move freely across magnetic fields that confine the plasma ions, and some small fraction propagate all the way into Earth orbit where they can be detected.

NASA's Interstellar Boundary Explorer (IBEX) (*5*) is dedicated to imaging ENAs propagating in from the far reaches of the outer heliosphere. IBEX was launched 19 October 2008 and subsequently maneuvered into a high-altitude, highly elliptical (~15,000 × 300,000 km), roughly week-long orbit. IBEX carries two high-sensitivity, single-pixel ENA cameras: IBEX-Lo (*6*) measures ENAs from ~10 eV to 2 keV, while IBEX-Hi (*7*) measures them from ~300 eV to 6 keV. Over this broad energy range, IBEX measures H ENAs arising from charge exchange with both the slower solar wind ions (< ~1 keV) and PUIs (~1 to a few keV).

Over the first half of 2009, IBEX built up its first global, energy-resolved maps of ENAs coming in from the outer heliosphere (*5*); these maps generally reflect the solar minimum conditions that have persisted for the past several years. In addition to the all-sky maps and energy spectra, IBEX also made direct observations of interstellar H and O from the LISM (*8*). These observations allow us to differentiate various particle populations, providing information about the interaction of the heliosphere with the LISM and about the interstellar environment itself.

Voyager 1 (*9*) and later Voyager 2 (*10*) crossed the TS and are making in situ measurements along two paths in the inner heliosheath. In contrast, IBEX's energy-resolved maps reveal the global interstellar interaction in all directions. The most striking feature in the IBEX sky maps is an unexpected, bright, narrow ribbon of ENA emissions that snakes between the directions of the Voyagers. This feature was not predicted by any model or theory, so interpreting the IBEX observations will require the development of a new understanding of the heliospheric interaction with the LISM.

The IBEX all-sky maps (Fig. 1) show that ENA fluxes vary over the ribbon, with maxima 2 to 3 times brighter than the surrounding regions. The ribbon is variable in width from <15° to >25° full width at half maximum (*11*), contains fine structure (Fig. 1B), and passes ~25° away from the heliospheric nose. The ribbon has brighter emissions from somewhat broader regions at higher latitudes in both hemispheres (~60°N and ~40°S), with the former having a different spectral shape than the rest of the ribbon (*12*). Although not optimally shown in these projections, the ribbon weakens but also extends back behind the northern pole, nearly closing a loop on the sky (*12*).

IBEX-Lo observations independently confirm the ribbon in the overlapping energy range (Fig. 1H) and extend down to ~200 eV (Fig. 1G). The ribbon is observed from there up to >6 keV, the top of the IBEX-Hi energy range (Fig. 1F), with the highest relative intensity at ~1 keV (*11*). Additional observations from Cassini/INCA (*13*) indicate that some portions of the ribbon may extend to even higher energies. Finally, although observations of the ribbon collected 6 months apart (~0°, ~180° ecliptic longitudes) indicate that it remained a largely stable structure during this period, these observations also suggest the possibility of some temporal evolution.

The power-law spectral slopes of the ENA flux (κ) display broad variations across the sky (Fig. 2) that are ordered by ecliptic latitude and longitude (i.e., the interstellar flow direction). These observations are generally consistent with the concept that ENAs are produced from TS-heated, nonthermal plasma throughout the inner heliosheath. The spectrum is flatter (lower κ) near the poles relative to the equator; this might be caused by the faster solar wind at higher latitudes, which generates and entrains substantially higher-energy PUIs than near the ecliptic. The spectra toward the tail are steeper ($\kappa > 2$) than near the nose ($\kappa \approx 1.5$), possibly owing to longer line-of-sight (LOS) integrations of low-energy ions toward the tail. Remarkably, the ribbon is barely visible in this spectral slope map, even though the fluxes are several times higher.

[1]Southwest Research Institute, San Antonio, TX 78228, USA. [2]University of Texas, San Antonio, TX 78249, USA. [3]Physikalisches Institut, University of Bern, CH-3012 Bern, Switzerland. [4]Space Research Centre of the Polish Academy of Sciences, 00-716 Warsaw, Poland. [5]NASA Goddard Space Flight Center, Greenbelt, MD 20771, USA. [6]Massachusetts Institute of Technology, Cambridge, MA 02139, USA. [7]Applied Physics Laboratory, Johns Hopkins University, Laurel, MD 20723, USA. [8]University of Bonn, 53115 Bonn, Germany. [9]Ruhr-Universität Bochum, 44780 Bochum, Germany. [10]University of Chicago, Chicago, IL 60637, USA. [11]Los Alamos National Laboratory, Los Alamos, NM 87545, USA. [12]Lockheed Martin Advanced Technology Center, Palo Alto, CA 94304, USA. [13]University of Michigan, Ann Arbor, MI 48109, USA. [14]University of Southern California, Los Angeles, CA 90089, USA. [15]University of Alabama, Huntsville, AL 35805, USA. [16]Moscow State University, 119899 Moscow, Russia. [17]Space Research Institute (IKI), Russian Academy of Sciences, 117997 Moscow, Russia. [18]Institute for Problems in Mechanics, Russian Academy of Sciences, 117526 Moscow, Russia. [19]University of Montana, Missoula, MT 59812, USA. [20]Adler Planetarium, Chicago, IL 60605, USA. [21]Office for Space Research and Technology, Academy of Athens, 106 79 Athens, Greece. [22]Space Science Center, University of New Hampshire, Durham, NH 03824, USA. [23]Boston University, Boston, MA 02215, USA.

*To whom correspondence should be addressed. E-mail: dmccomas@swri.org

As an example of the detailed spectral information provided by IBEX, Fig. 3 shows the ENA energy spectra along LOSs toward the two Voyager spacecraft. These spectra are nearly straight power laws with slopes of ~1.5 (Voyager 1) and ~1.6 (Voyager 2). Globally, the spectra generally show simple power laws near the equator with distinct enhancements at several keV at higher latitudes (*12*), again consistent with higher-energy PUIs in the high-latitude, fast solar wind. IBEX observations are consistent with upper bounds on ENA flux based on Ly-α absorption (*14*). Claims of heliospheric ENA measurements from ASPERA-3 (*15*) are inconsistent with IBEX observations.

The discovery of the ribbon, not ordered by ecliptic coordinates or the interstellar flow, requires reconsideration of our fundamental concepts of the heliosphere-LISM interaction. A possible explanation could be based on the idea that the local interstellar magnetic field plays a central role in shaping the outer heliosphere. Figure 4 shows a concept for the interaction where the external dynamic and magnetic forces are comparable. Here we depict the external field (*16*) wrapping around and compressing the heliopause in a way that pushes in the southern hemisphere (*17*) enough to explain why Voyager 2 crossed the TS ~10 AU closer to the Sun (*10*) than did Voyager 1 (*9*), once the effects of the decreasing solar wind dynamic pressure inside the TS (*18*) are included (*19*). The ribbon closely matches locations where a model (*20*) using this external field orientation indicates that just outside the heliopause, the field is transverse to IBEX's radial-viewing LOSs (*21*).

Several factors could contribute to the substantially enhanced emission in the ribbon, including higher energetic ion intensities along the LOS and pitch-angle distributions of ions that preferentially emit radially inward. The combination of the external plasma dynamic (i.e., ram) and magnetic ($\mathbf{J} \times \mathbf{B}$) forces produces a localized band of maximum total pressure around the heliopause, which is substantially offset from the nose for a strong external field (*21*). Because the suprathermal plasma observed in the inner heliosheath is subsonic, information about the enhanced pressure at the heliopause propagates throughout the inner heliosheath, adjusting the plasma properties and bulk flow and potentially affecting the TS. Flows at the Voyager locations appear to be more directed away from the ribbon than away from the nose. At Voyager 2 (*22*), south and offset from the nose meridian (Fig. 1), in radial-tangential-normal (RTN) coordinates, $\langle V_T \rangle \sim +48$ km s^{-1}, whereas $\langle V_N \rangle$ is only ~ -14 km s^{-1}. At Voyager 1, northward of the nose, only V_R and V_T were measured (*23*), but $\langle V_T \rangle \sim -40$ km s^{-1}. Thus, the ribbon might indicate the true region of highest pressure in the inner heliosheath. If so, the location of the ribbon divides inner heliosheath flows down the two sides of the heliotail, analogous to a continental divide; this may explain why V_T is several times V_N at Voyager 2, as well as the large transverse flow at Voyager 1.

If the pressure maximum is aligned with the ribbon and the heliosheath flows are away from it, then this represents the stagnation flow region, where inside the heliopause the radial outflow must go to zero. In this region, the plasma density should maximize, producing copious ENAs that would naturally map the region of maximum pressure. This additional pressure might also extrude a region of the heliopause, forming a spatially limited outward bulge with high density and little bulk flow. Because of the narrow angular extent of the ribbon, it might be expected that the emission region could be radially narrow also, which would require magnetic or some other sort of plasma confinement. Furthermore, the spectral slope of the ribbon is similar to that of the surrounding regions, which suggests that this feature is not dominated by dynamical effects

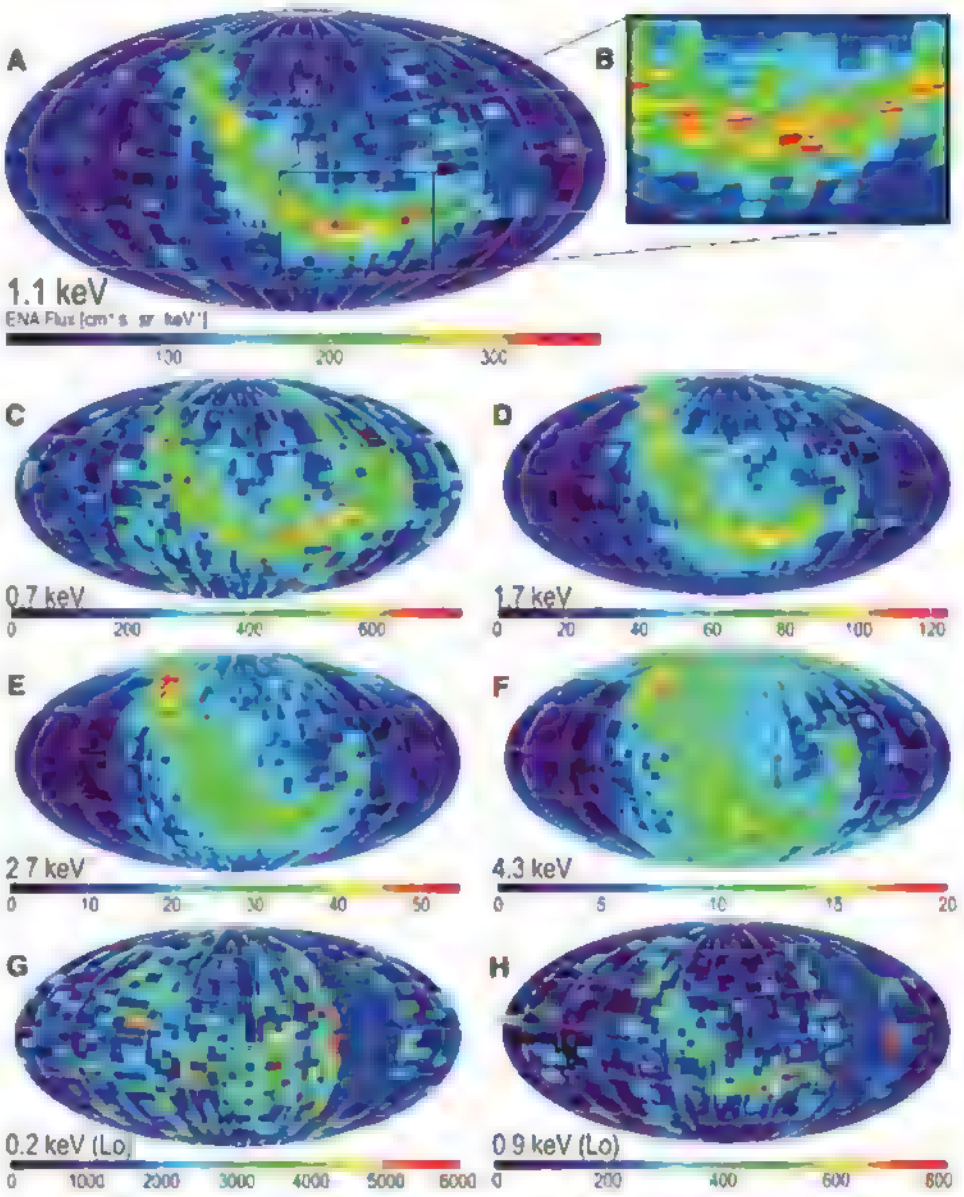

Fig. 1. IBEX all-sky maps of measured ENA fluxes in Mollweide projections in ecliptic coordinates (J2000), where the heliospheric nose is near the middle and the tail extends along both sides. The pixels are 6° in spin phase (latitude), with widths (longitude) determined by the spacecraft pointing for different orbits. Maps are shown in the spacecraft frame for passband central energies from IBEX-Hi of **(A)** 1.1 keV, **(C)** 0.7 keV, **(D)** 1.7 keV, **(E)** 2.7 keV, and **(F)** 4.3 keV, and from IBEX-Lo of **(G)** 0.2 keV and **(H)** 0.9 keV. Also shown in (A) is the galactic plane (red curve), which clearly does not coincide with the ribbon, as well as directions toward Voyager 1 (V1) (35°, 255°), Voyager 2 (V2) (−32°, 289°), and the nose (5°, 255°). **(B)** Magnified section of the ribbon where each 0.5° in spin phase is averaged with nearest neighbors to reach 100 counts (10 counts standard deviation). Because of contamination of ENAs from Earth's magnetosphere, a small region on the right side of each map was not sampled in the first 6 months of data; these regions have been filled in with average values from the adjacent areas and appear unpixelated.

(e.g., different energization processes at the TS or elsewhere) but simply reflects the accumulation of particles. Integration of our measured distributions of ENAs over energy suggests that the pressure in the ribbon is considerably higher than in the rest of the sky (*12*); nonetheless, a region only ~30 to 60 AU thick could still be in rough pressure balance with the combined external dynamic and magnetic forces (*21*).

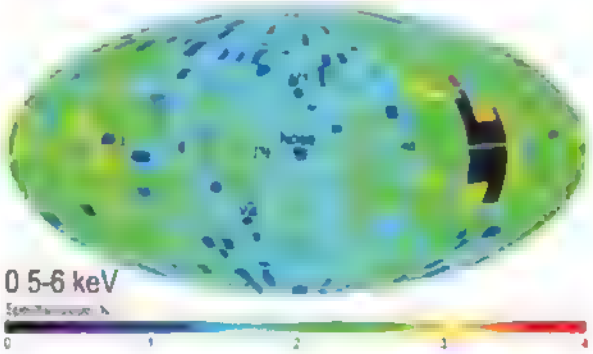

Fig. 2. Sky map, in ecliptic coordinates, of the average power-law spectral slope (κ) from ~0.5 to 6 keV using IBEX-Hi channels 2 to 6. The measurements were transformed into the rest frame of the Sun; unlike Fig. 1, the unsampled region is left black in this image. Although statistical uncertainty remains in individual 6° pixels, global variations are clearly evident.

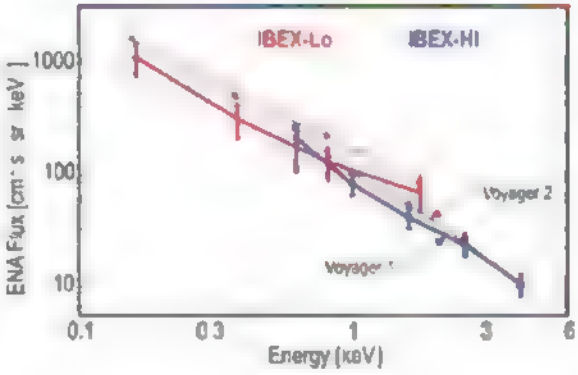

Fig. 3. Energy spectra for 20° × 20° regions centered on the Voyager 1 (thick lines) and Voyager 2 (thin lines) directions. Prelaunch cross-calibration of the IBEX-Lo (red) and -Hi (blue) sensors simultaneously in a single chamber produces quantitative matching between the spectra. Error bars show counting statistics plus likely systematic errors of ±20% for IBEX-Hi and ±30% for IBEX-Lo.

Another way to trap hot, inner-heliosheath plasma in a relatively narrow structure might be via large-scale, Rayleigh-Taylor like instabilities (*24*), which can be driven by neutrals and destabilize the heliopause. Some models show large, semicoherent structures with higher ion densities and sizes greater than tens of AU, moving tailward at <60 km/s along the heliopause (*25*). Magnetic reconnection across the heliopause would also allow suprathermal heliosheath ions out into the cooler, denser outer heliosheath, potentially confining them in narrow structures. For any method that traps hot plasma farther out beyond the heliopause, expected higher densities of interstellar neutrals there would also enhance ENA production.

Another possible ENA source is from outside the heliopause, where compression of the external field would both enhance densities and provide perpendicular heating to produce more perpendicular ion pitch-angle distributions (*21*). Such ions preferentially emit ENAs where the LOS is transverse to the interstellar magnetic field. A possible source of ENAs could be fast neutrals emitted from the inner heliosheath, which become ionized just outside the heliopause and then reneutralize, emitting back inward pref-

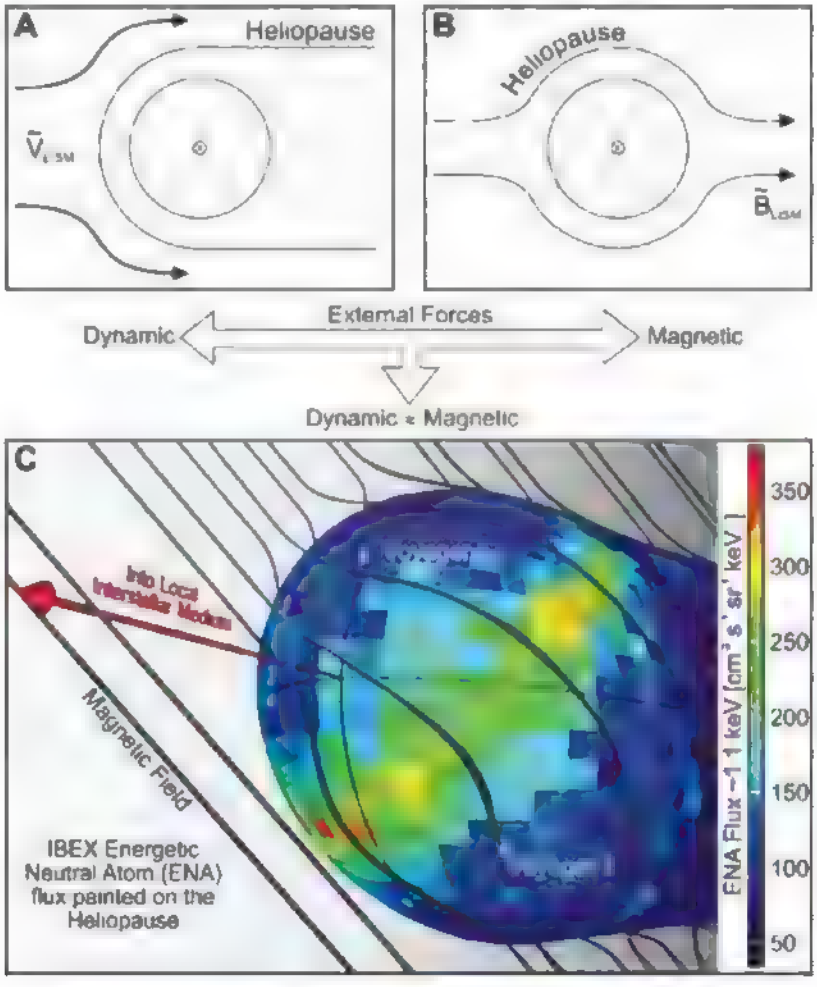

Fig. 4. Schematic diagrams of Parker's limiting cases for the heliospheric interaction (*28*). (**A**) "Hydrodynamic" interaction, where the external dynamic forces >> magnetic forces. (**B**) "Diamagnetic cavity" interaction, where the external magnetic forces >> dynamic forces. (**C**) Schematic showing an intermediate case, where the external magnetic and dynamic forces are comparable. The measured flux at ~1.1 keV is superposed on the heliopause; the ribbon appears to correlate with where the field is most strongly curved around it.

erentially where the field is perpendicular to IBEX's radial LOS. A simulation including this effect but using only isotropic distributions showed a weak ENA signal (*2*). Producing a strong, narrow feature would require the PUIs to remain a ring distribution, in the face of instabilities, long enough for many to neutralize. It is also possible that the ribbon ENAs come from inside the TS, perhaps from shock-accelerated PUIs (*26*) propagating inward through the region where the solar wind decelerates by ~20% over ~10 AU, just inside the shock (*27*).

The brightest regions of the ribbon occur well away from the nose and at latitudes where the slow and fast solar winds interact, forming corotating interaction regions. This suggests that the emissions in the ribbon are at least partially related to the solar wind properties as well as to the external environment. Additionally, although the ribbon appears as a continuous feature, it could be a string of more localized, overlapping "knots" of emission. Certainly other ideas need to be examined, and while our data support some earlier ideas, in other areas a completely new paradigm is needed for understanding the interaction between our heliosphere and the galactic environment.

References and Notes

1. H. Fahr *et al.*, *Rev. Geophys.* **45**, RG4003 (2007).
2. V. V. Izmodenov *et al.*, *Space Sci. Rev.* **146**, 329 (2009).
3. M. A. Lee *et al.*, *Space Sci. Rev.* **146**, 275 (2009).
4. G. P. Zank *et al.*, *Space Sci. Rev.* **146**, 295 (2009).
5. D. J. McComas *et al.*, *Space Sci. Rev.* **146**, 11 (2009).
6. S. A. Fuselier *et al.*, *Space Sci. Rev.* **146**, 117 (2009).
7. H. O. Funsten *et al.*, *Space Sci. Rev.* **146**, 75 (2009).
8. E. Möbius *et al.*, *Science* **326**, 969 (2009); published online 15 October 2009 (10.1126/science.1180971).
9. E. C. Stone *et al.*, *Science* **309**, 2017 (2005).
10. E. C. Stone *et al.*, *Nature* **454**, 71 (2008).
11. S. A. Fuselier *et al.*, *Science* **326**, 962 (2009); published online 15 October 2009 (10.1126/science.1180981).
12. H. O. Funsten *et al.*, *Science* **326**, 964 (2009); published online 15 October 2009 (10.1126/science.1180927).
13. S. M. Krimigis, D. G. Mitchell, E. C. Roelof, K. C. Hsieh, D. J. McComas, *Science* **326**, 972 (2009); published online 15 October 2009 (10.1126/science.1181079).
14. B. E. Wood *et al.*, *Astrophys. J.* **657**, 609 (2007).
15. P. Wurz *et al.*, *Astrophys. J.* **683**, 248 (2008).
16. R. Lallement *et al.*, *Science* **307**, 1447 (2005).
17. M. Opher *et al.*, *Astrophys. J.* **640**, L71 (2006).
18. D. J. McComas *et al.*, *Geophys. Res. Lett.* **35**, L18103 (2008).
19. H. Washimi *et al.*, *Astrophys. J.* **670**, L139 (2007).
20. N. V. Pogorelov *et al.*, *Astrophys. J.* **695**, L31 (2009).
21. N. A. Schwadron *et al.*, *Science* **326**, 966 (2009); published online 15 October 2009 (10.1126/science.1180986).
22. J. D. Richardson *et al.*, *Geophys. Res. Lett.* **36**, L10102 (2009).
23. R. B. Decker *et al.*, *AIP Conf. Proc.* **932**, 197 (2007).
24. V. B. Baranov *et al.*, *Astron. Astrophys.* **261**, 341 (1992).
25. S. N. Borovikov *et al.*, *Astrophys. J.* **682**, 1404 (2008).
26. S. V. Chalov, H. J. Fahr, *Astron. Astrophys.* **311**, 317 (1996).
27. J. D. Richardson *et al.*, *Nature* **454**, 63 (2008).
28. E. N. Parker, *Astrophys. J.* **134**, 20 (1961).

29. We thank all the men and women who made the IBEX mission possible. IBEX was primarily funded by NASA as a part of the Explorers Program (contract NNG05EC85C), foreign investigators were supported by their respective national agencies and institutions.

21 August 2009; accepted 2 October 2009
Published online 15 October 2009
10.1126/science.1180906
Include this information when citing this paper.

Width and Variation of the ENA Flux Ribbon Observed by the Interstellar Boundary Explorer

S. A. Fuselier,[1]* F. Allegrini,[2,3] H. O. Funsten,[4] A. G. Ghielmetti,[1] D. Heirtzler,[5] H. Kucharek,[5] O. W. Lennartsson,[1] D. J. McComas,[2,3] E. Möbius,[5] T. E. Moore,[6] S. M. Petrinec,[1] L. A. Saul,[7] J. A. Scheer,[7] N. Schwadron,[8] P. Wurz[7]

The dominant feature in Interstellar Boundary Explorer (IBEX) sky maps of heliospheric energetic neutral atom (ENA) flux is a ribbon of enhanced flux that extends over a broad range of ecliptic latitudes and longitudes. It is narrow (~20° average width) but long (extending over 300° in the sky) and is observed at energies from 0.2 to 6 kilo–electron volts. We demonstrate that the flux in the ribbon is a factor of 2 to 3 times higher than that of the more diffuse, globally distributed heliospheric ENA flux. The ribbon is most pronounced at ~1 kilo–electron volt. The average width of the ribbon is nearly constant, independent of energy. The ribbon is likely the result of an enhancement in the combined solar wind and pickup ion populations in the heliosheath.

The scientific objective of the Interstellar Boundary Explorer (IBEX) is to discover the global interaction between the Sun's solar wind and the interstellar medium (*1*). This objective is accomplished through the use of two high-sensitivity neutral atom cameras that detect ENAs from 0.01 to 6 keV. Here, the full energy range of the IBEX payload is used to investigate average characteristics of the ribbon of enhanced hydrogen flux (Fig. 1) detected by IBEX across a large fraction of the sky (*2*).

The sky map for 0.2-keV hydrogen [see Fig. 1G in (*2*)] shows evidence of enhanced 0.2-keV hydrogen flux that generally follows the ribbon seen in Fig. 1. In the 0.2-keV sky map, there is also a high-flux region centered approximately on the ecliptic from roughly the nose direction to −150° longitude. A similar region is evident in a sky map of oxygen (*3*). These are interstellar oxygen neutrals originating from the nose. The interstellar oxygen is not observed exactly in the nose direction because neutrals are deflected by the Sun's gravity and IBEX measures them in the Earth's reference frame (*3*). Energetic oxygen neutrals create a hydrogen signature in the IBEX-Lo sensor by knock-off of negative hydrogen ions from the sensor's neutral-to-negative ion conversion surface (*4*). Thus, the high-flux region in the 0.2-keV sky map near the nose is not associated with heliospheric hydrogen. Rather, it is a secondary product in the IBEX-Lo sensor from interstellar oxygen. Indeed, sky maps at $E < 0.2$ keV (*3*) are dominated by the secondary hydrogen flux produced by both interstellar oxygen and helium in the sensor, and it is difficult to identify a ribbon at energies below 0.2 keV. Thus, the ribbon extends from 0.2 to 6 keV [the upper energy of the 4.3-keV sky map in (*2*)].

To investigate average properties of the ribbon, we integrated the maps at each energy parallel to the thick black curve in Fig. 1 in 6°-wide bins. These integrals define the average cross section profile of the ribbon (Fig. 2A). The ribbon is centered near −3° for all energies, except at 0.2 keV. It is not symmetric about 0° because there is structure in the ribbon at higher angular resolution than shown here (*2*). The ribbon is a flux enhancement above a more diffuse, globally distributed heliospheric ENA flux (*2*, *5*) (the fluxes at [−30, −24°] and [24, 30°] define the distributed flux). It is most pronounced at 0.9 keV, where it is a factor of 2.3 times more intense than the distributed flux. At both higher and lower energies, the average intensity of the ribbon decreases so that at 0.2 and 2.7 keV, the ribbon flux is only ~25% more intense than the distributed flux. The ribbon is centered in the same location up to 6 keV [the highest IBEX energy; see Fig. 1F in (*2*)].

At 0.2 keV, the influence of the interstellar neutrals is seen from 12° to 30°. In addition, the ribbon appears to be wider and somewhat displaced from the location at all other energies. Below 0.2 keV, it is difficult to identify a ribbon because hydrogen created in the sensor from

[1]Lockheed Martin Advanced Technology Center, Palo Alto, CA 94304, USA. [2]University of Texas at San Antonio, San Antonio, TX 78249, USA. [3]Southwest Research Institute, San Antonio, TX 78228, USA. [4]Los Alamos National Laboratory, Los Alamos, NM 87545, USA. [5]University of New Hampshire, Durham, NH 03824, USA. [6]Goddard Space Flight Center, Greenbelt, MD 20771, USA. [7]University of Bern, Physikalisches Institut, 3012 Bern, Switzerland. [8]Boston University, Boston, MA 02215, USA.

*To whom correspondence should be addressed. E-mail: stephen.a.fuselier@lmco.com

interstellar neutral helium and oxygen overlaps the ribbon signal (*3*).

Figure 2A seems to suggest that the width of the ribbon increases at energies both above and below 0.9 keV. However, the real effect is a decrease in the intensity of the ribbon relative to the distributed ENA flux both above and below 0.9 keV. To remove this energy-dependent distributed component, a very shallow parabola was fitted to the distributed components in Fig. 2A (at [−30, −24°] and [24, 30°]), this curve was subtracted, and the results were renormalized to the flux at 0° (Fig. 2B).

From 0.7 to 2.7 keV, the width of the ribbon is independent of energy, and the full width at half maximum of the ribbon is 20°. At 0.2 keV, the ribbon width is larger and shifted from its location at −3° (and the presence of a secondary hydrogen signal created from interstellar neutral helium and oxygen in the sensor is still evident at angles >12°).

There are statistically significant variations in both the width of the ribbon and its intensity relative to the distributed flux. For example, the ribbon flux at 1.1 keV varies by about a factor of 2 along its length, and the width varies from about 15° to 25°. Furthermore, there are statistically significant variations in the ribbon profile across the width at angular resolution <6° (*2*). These variations are manifested in the asymmetric ribbon location in Fig. 2, A and B.

Heliospheric ENAs are created by charge exchange of solar wind and pickup ions with interstellar neutrals that penetrate the heliopause. The observed ENA flux in any given direction in the sky is the integral of the neutral flux along the line of sight (LOS). Thus, a flux enhancement like the ribbon indicates that there is either a corresponding enhancement in the parent ion flux along the LOS, or a longer LOS for ion charge exchange. The neutral flux is enhanced over a broad energy range and is greatest at 0.9 keV. These two features indicate that the parent ion population of the ribbon is the combined solar wind and pickup ions as they propagate into the heliosheath. Because the enhancement occurs over a broad energy range, ion fluxes of several origins (i.e., decelerated solar wind, pickup ions, and accelerated pickup ions) must be enhanced along the LOS.

Such a narrow (20° wide) but very long, coherent structure in the sky suggests that magnetic fields play an important role (*2*). Indeed, the ribbon appears to be oriented in the sky along the curve where the predicted interstellar magnetic field (external to the heliopause) is normal to the radial direction from the Sun (*6*).

At the solar wind termination shock [assumed to be at 100 astronomical units (AU); 1 AU = 1.5×10^{10} km], the 20° width of the ribbon translates to a spatial width of ~35 AU. At the heliopause (assumed to be at 150 AU), the width increases to ~50 AU. These widths are small compared to the dimensions of these respective boundaries, but are very large compared to scale lengths like the gyroradius of a 1-keV proton.

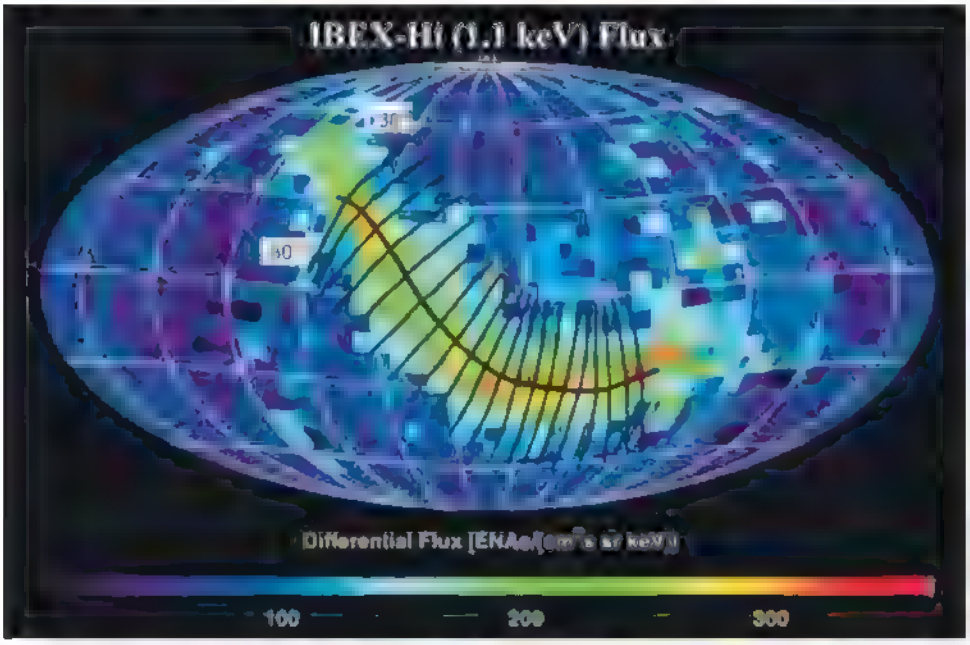

Fig. 1. Sky map of 1.1-keV neutral hydrogen flux [in $(cm^2\ s\ sr\ keV)^{-1}$] from the IBEX-Hi sensor from the first 6 months of the IBEX mission. This standard IBEX sky map is an oblique Mollweide projection in ecliptic coordinates. The nose direction (the direction of motion of the Sun with respect to the local interstellar medium) is in the center and the tail direction (opposite the nose) is on both the left- and right-hand sides. The map is tilted by ~5° so that the nose direction is exactly in the middle, with north (south) nearly at the top (bottom). The pixel size is ~6°. The dominant feature in this sky map is a ribbon of enhanced ENA flux stretching from −30° to −180° ecliptic longitude. The thick, black line traces this ribbon. The short lines show the directions perpendicular to the ribbon out to ±30° and are used to determine the average width of the ribbon.

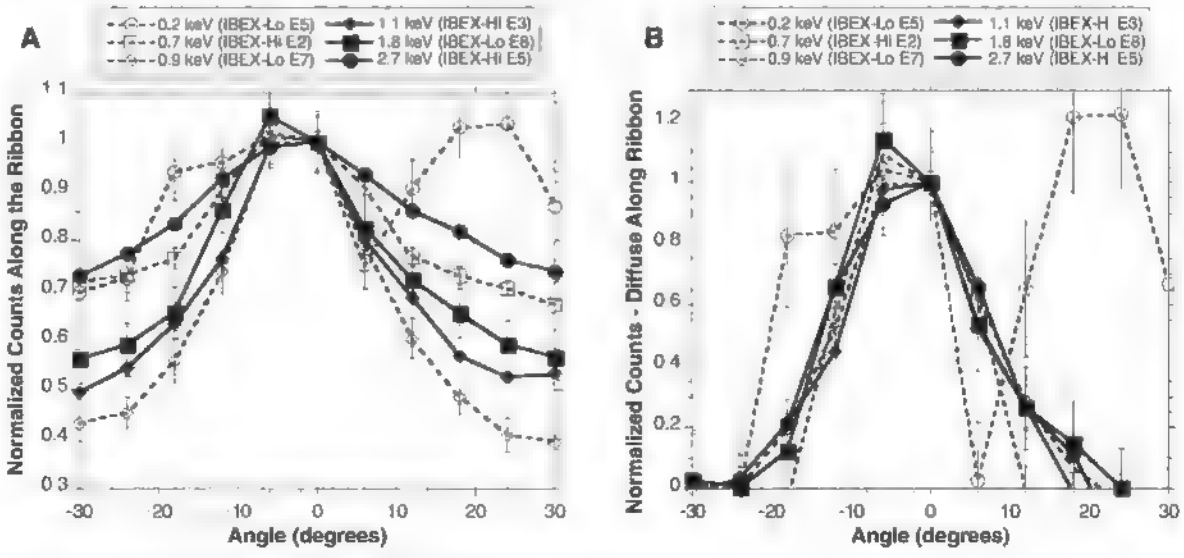

Fig. 2. (**A**) Average profile of the ribbon for energies from 0.2 to 2.7 keV. These average profiles were obtained by integrating parallel curves that follow the peak flux in the ribbon (Fig. 1) and then normalized by the peak (at 0°). Dashed lines with open symbols show energies up to 1 keV. Solid lines with filled symbols show energies above 1 keV. Error bars are 1 SD from the mean. The ribbon is most pronounced above the globally distributed heliospheric flux at energies near 1 keV. (**B**) Average profile of the ribbon for energies above and below 1 keV with the distributed flux from Fig. 2A removed. The width of the ribbon is the same for energies from 0.7 to 2.7 keV.

Identifying the ribbon over a broad energy range has implications for its stability. ENAs with energies of 1 keV take ~1.1 years to propagate from 100 AU to Earth, whereas ENAs with energies of 0.2 keV take ~2.4 years to make the same journey. Thus, the ribbon must exist over at least ~1 year.

References and Notes

1. D. J. McComas *et al.*, *Space Sci. Rev.* 10.1007/s11214-009-9499-4 (2009).
2. D. J. McComas *et al.*, *Science* 326, 959 (2009); published online 15 October 2009 (10.1126/science.1180906).
3. E. Möbius *et al.*, *Science* 326, xxx (2009); published online 15 October 2009 (10.1126/science.1180971).
4. S. A. Fuselier *et al.*, *Space Sci. Rev.* 10.1007/s11214-009-9495-8 (2009).
5. H. O. Funsten *et al.*, *Science* 326, 964 (2009); published online 15 October 2009 (10.1126/science.1180927).
6. N. A. Schwadron *et al.*, *Science* 326, 966 (2009); published online 15 October 2009 (10.1126/science.1180986).
7. These results from the IBEX mission are a tribute to the hard work of many scientists and engineers. Work at Lockheed Martin was funded by NASA through sub-contract from Southwest Research Institute.

24 August 2009; accepted 2 October 2009
Published online 15 October 2009;
10.1126/science.1180981
Include this information when citing this paper

Structures and Spectral Variations of the Outer Heliosphere in IBEX Energetic Neutral Atom Maps

H. O. Funsten,[1]* F. Allegrini,[2,3] G. B. Crew,[4] R. DeMajistre,[5] P. C. Frisch,[6] S. A. Fuselier,[7] M. Gruntman,[8] P. Janzen,[9] D. J. McComas,[2,3] E. Möbius,[10] B. Randol,[3,2] D. B. Reisenfeld,[9] E. C. Roelof,[5] N. A. Schwadron[11]

The Interstellar Boundary Explorer (IBEX) has obtained all-sky images of energetic neutral atoms emitted from the heliosheath, located between the solar wind termination shock and the local interstellar medium (LISM). These flux maps reveal distinct nonthermal (0.2 to 6 kilo–electron volts) heliosheath proton populations with spectral signatures ordered predominantly by ecliptic latitude. The maps show a globally distributed population of termination-shock–heated protons and a superimposed ribbonlike feature that forms a circular arc in the sky centered on ecliptic coordinate (longitude λ, latitude β) = (221°, 39°), probably near the direction of the LISM magnetic field. Over the IBEX energy range, the ribbon's nonthermal ion pressure multiplied by its radial thickness is in the range of 70 to 100 picodynes per square centimeter AU (AU, astronomical unit), which is significantly larger than the 30 to 60 picodynes per square centimeter AU of the globally distributed population.

Energetic neutral atoms (ENAs) are formed when energetic ions in the heliosheath, predominantly H^+, are neutralized by charge exchange with the neutral component of the interstellar gas, predominantly H^0. Imaging and spectroscopy of these ENAs are used to remotely survey the structure and dynamics of heliosheath plasmas (*1*, *2*). The IBEX-Lo (*3*) and IBEX-Hi imagers (*4*) on the Interstellar Boundary Explorer (IBEX) mission (*5*) measure heliosheath ENAs over the energy range from ~0.2 to 6 keV. The IBEX-Hi and IBEX-Lo all-sky maps show a ribbon (*6*, *7*) that was not anticipated by current models of the structure and dynamics of the interaction region (*8*). The ribbon is superimposed on a globally distributed ENA flux that varies slowly over the sky (*6*). Here we characterize the underlying plasma structures in the heliosheath by analyzing the spectral index derived from the ENA flux maps (*6*) both inside and outside the ribbon.

The ENA spectra show two distinct spectral shapes independent of ecliptic longitude λ (Fig. 1, A to C). The blue (north) and red (south) spectra are similar in shape, even though their corresponding intensities vary over a factor of ~2 to 3, with higher intensities in the ribbon. They all exhibit a conspicuous flattening of their slopes for energies >1 keV, which is the characteristic energy range for pickup ions in the fast solar wind that are further heated at the termination shock (*9*). At each energy passband, the ENA fluxes of all north and south spectra of Fig. 1, A to C (except for the northern tail, which contains the ribbon), are similar, with average fluxes of 192, 79, 30, 17, and 8.7 $cm^{-2}\ s^{-1}\ sr^{-1}\ keV^{-1}$ at energy passbands centered at 0.7, 1.1, 1.7, 2.7, and 4.3 keV, respectively, and standard deviations within 10% of the average flux values at each energy.

In contrast to the high-latitude spectra, the smooth low-latitude (green) spectra can be approximated as a power law spectrum with a single spectral index κ (*8*). This applies even in the ribbon, which exhibits a larger overall intensity but a similar single slope as compared to nonribbon spectra (Fig. 2, A and C). The value of κ at low latitudes shows a weak trend with longitude (Fig. 1D), with fits of the data over the nine energy channels yielding κ = 1.5 for the nose and κ = 2.1 for the tail. The nose and tail spectral shapes are also slightly but consistently different, possibly resulting from longer line-of-sight (LOS) integrations of low-energy ions toward the tail. Another exception is the spectrum in the direction of Voyager 1 (*6*), which is more characteristic of high-latitude spectra.

The spectral index κ at higher energies is predominantly ordered by ecliptic latitude β (Fig. 2, A and B). The spectral indexes within the ribbon nearly overlap with and show the same strong latitude dependence as the globally distributed flux outside the ribbon. For the globally distributed flux that does not include the ribbon, the average spectral index at low latitudes ($-30° \le \beta \le 30°$) is $\kappa = 1.95 \pm 0.09$ at 1.7 keV and $\kappa = 1.91 \pm 0.07$ at 2.7 keV, and at high latitudes ($\beta \le -54°$, $\beta \ge 54°$) is $\kappa = 1.49 \pm 0.05$ and $\kappa = 1.36 \pm 0.08$, respectively, revealing a distinctly different higher-energy ion population at high latitude.

These observations show that the global characteristics of nonthermal heliosheath ions are ordered predominantly by ecliptic latitude, regardless of whether they reside inside or outside of the ribbon. Because ecliptic latitude is almost indistinguishable from heliographic latitude, this spectral signature is probably imposed by the latitude dependence of the solar wind, whose transition from slow (equatorial) to fast (polar) solar wind in the outer heliosphere occurs at mid-latitudes throughout the present minimum phase of the solar cycle (*10*). It also suggests that the intensity features of the ribbon are not produced by local heliosheath acceleration processes that would presumably impose a different spectral signature associated only with these higher fluxes. If the solar wind orders the spectral characteristics of heliosheath plasma, we expect temporal variation of the globally distributed flux, and possibly structures such as the ribbon, caused by the changing solar wind pattern throughout the 11-year (and possibly 22-year) solar cycle.

We divided the ribbon into three regions based on differences in spectral signature (Fig. 2, C and D). The spectra of regions 1 and 3 are consistent with the spectral signatures of low- and high-latitude regions, respectively (Fig. 1, A

[1]Los Alamos National Laboratory, Los Alamos, NM 87545, USA. [2]Southwest Research Institute, San Antonio, TX 78228, USA. [3]University of Texas at San Antonio, San Antonio, TX 78249, USA. [4]Massachusetts Institute of Technology, Cambridge, MA 02139, USA. [5]Applied Physics Laboratory, Johns Hopkins University, Laurel, MD 20723, USA. [6]University of Chicago, Chicago, IL 60637, USA. [7]Lockheed Martin Advanced Technology Center, Palo Alto, CA 94304, USA. [8]University of Southern California, Los Angeles, CA 90089–1192, USA. [9]University of Montana, Missoula, MT 59812, USA. [10]University of New Hampshire, Morse Hall, Durham, NH 03824, USA. [11]Boston University, Boston, MA, 02215, USA.

*To whom correspondence should be addressed. E-mail: hfunsten@lanl.gov

to C). However, region 2 is a highly localized knot of ENA emission that is apparent in the ENA flux maps and lies within ~30° to 12° longitude and 38° to 72° latitude. The flux is enhanced relative to region 3 at 1.7 and 2.7 keV and is highly variable over small spatial scales. By 4.3 keV, the fluxes converge to the values of region 3. These observations suggest the presence of a dynamic process whose characteristic signature lies in the energy range from ~1 to 2.7 keV. Region 2 lies toward the northern extent of the interaction region of fast and slow solar wind and might, for example, arise from preferential ion acceleration near the termination shock (*11*).

The ribbon is probably associated with an enhanced plasma pressure, consistent with plasma flow away from the ribbon measured at the Voyager spacecraft, whose locations straddle the ribbon (*6*). Along a single LOS, heliospheric ENAs are emitted from a source region with average thickness L. The energetic ions over this emission region exert an average nonthermal partial pressure ΔP_{ion}. We estimate the product $\Delta P_{ion}L$ by assuming an isotropic ion distribution of intensity $j_{ion}(E)$. The average ENA flux along the LOS as measured by IBEX is $j_{ENA}(E) = \sigma_{10}(E) n_H\, j_{ion}(E) L$, where $\sigma_{10}(E)$ is the charge exchange cross section for $H^+ + H^0 \rightarrow H^+ + H^0$ (*12*) and $n_H \cong 0.1$ cm^{-3} is the lower-bound density of H^0 from the local interstellar medium (LISM) along the LOS (*13*). The ion partial pressure over an energy range ΔE (such as an IBEX energy passband) is $\Delta P_{ion} = (4\pi/3) j_{ion}(E) p_{ion} \Delta E$, where p_{ion} is the ion momentum.

Over the energy range from 0.2 to 6.0 keV, the ribbon dominates $\Delta P_{ion}L$, ranging from 70 to 110 pdynes cm^{-2} AU as compared to 30 to 60 pdynes cm^{-2} AU for the globally distributed flux (Fig. 3). The larger $\Delta P_{ion}L$ in the ribbon could be from higher ion pressure, a thicker plasma source region, or a combination of both. Using $\Delta P_{ion}L \approx$ 100 pdynes cm^{-2} AU and assuming that the ribbon radial thickness $L \approx 50$ AU is similar to its apparent 20° width (*9*) at 150 AU, the average IBEX partial pressure in the ribbon is $\Delta P_{ion} \approx$ 2 pdynes cm^{-2} (~0.2 pPa), which is comparable to the estimated external forces exerted by the LISM (*8*).

The pressure produced by the nonthermal ion distribution probably governs the structure, dynamics, and geometry of the heliosheath. The region of highest $\Delta P_{ion}L$ (~100 pdynes cm^{-2} AU) follows a circular arc whose center is the likely direction of the LISM magnetic field direction. The arc center, derived by linear regression using the latitude of the 6° × 6° pixel having maximum $\Delta P_{ion}L$ at each longitude, lies along a LOS through ecliptic $(\lambda, \beta) = (221°, 39°)$, which is ~46° from the heliospheric nose. The mean angle between the LOS of the arc center and the LOS of the $\Delta P_{ion}L$ maxima is 71.6° ± 3.9°. The three-dimensional geometry of the regions of enhanced $\Delta P_{ion}L$ is therefore a cone through the heliosheath with the Sun as its apex. The ribbon's arc of high $\Delta P_{ion}L$ is con-

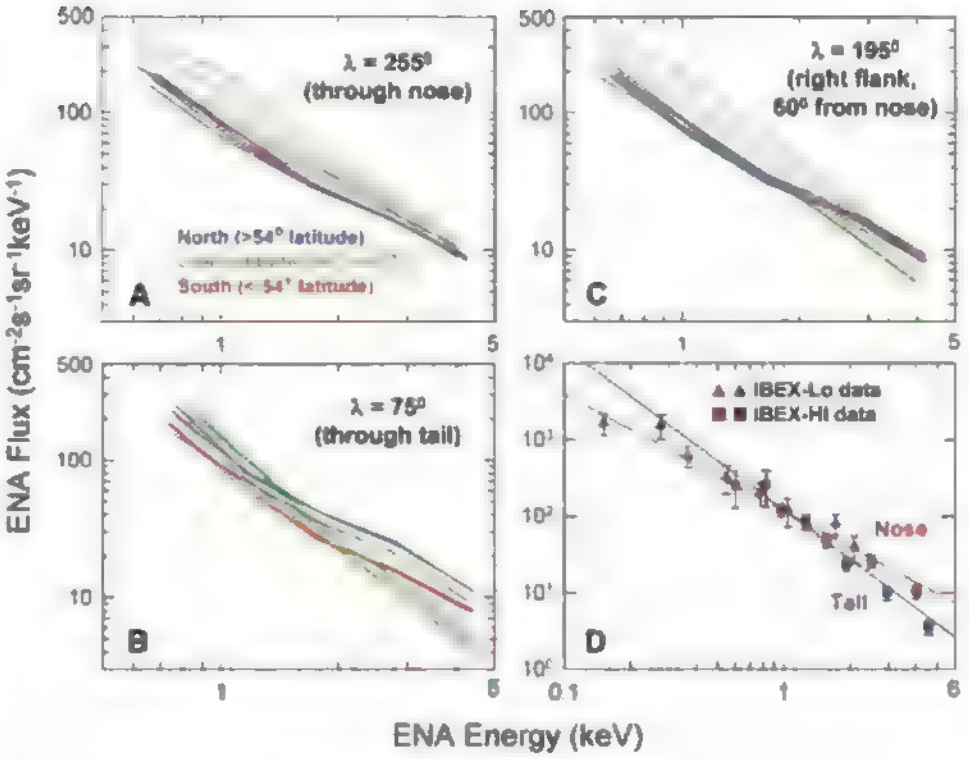

Fig. 1. ENA spectra from several regions. Measurements were transformed into the rest frame of the Sun. Average fluxes from 24° longitude × 12° latitude areas in longitudinal slices centered on the heliospheric **(A)** nose (λ = 255°), **(B)** tail, and **(C)** right flank (60° from the nose) are shown. The green spectra are from low ecliptic latitudes (−30° ≤ β ≤ 30°), and the blue and red spectra are from northern (β ≥ 54°) and southern (β ≤ −54°) polar regions, respectively. The low-latitude spectra with the highest flux in (A) and (C) are from latitudes centered on −12° and −24° and contain the ribbon. The north latitude spectra with the highest flux in (B) also contain the ribbon. **(D)** Spectra from 20° × 20° regions centered on the nose (red) and tail (blue) and fit over nine energy passbands of IBEX. Typical error bars in (D) represent counting statistics and systematic errors of ±20% for IBEX-Hi and ±30% for IBEX-Lo.

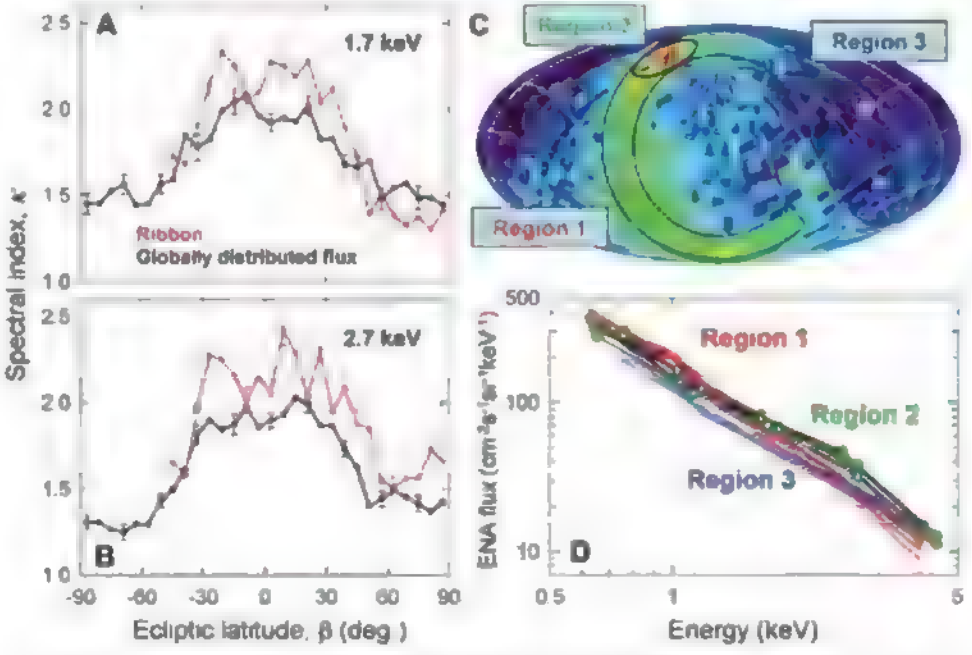

Fig. 2. Global spectral variation with latitude and within the ribbon. The variance-weighted mean of κ for the ribbon (red) and globally distributed flux outside the ribbon (black) are calculated using three adjacent IBEX-Hi energy passbands centered on **(A)** 1.7 keV and **(B)** 2.7 keV. Error bars represent errors in the weighted mean. The 2.7 keV ENA flux map **(C)** is centered on ecliptic $(\lambda, \beta) = (221°, 39°)$ and shows three regions of the ribbon. **(D)** Spectra from these three regions are derived from the average ENA flux in areas 6° in longitude by 18° in latitude centered on the ribbon.

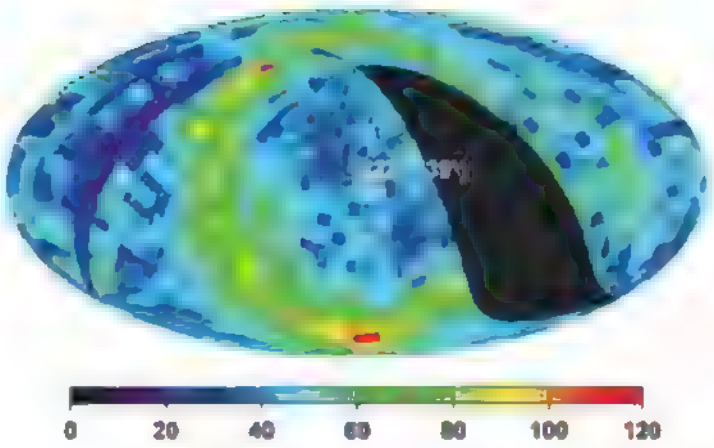

Fig. 3. The product of the ion pressure ΔP_{ion} in the heliosheath and the radial thickness L of the ENA emission in units of pdynes cm^{-2} AU over the energy range from 0.2 to 6 keV that includes the 0.44-keV passband of IBEX-Lo and the 0.7-, 1.1-, 1.7-, 2.7-, and 4.3-keV passbands of IBEX-Hi. The black swath is data removed because of poor statistics in the IBEX-Lo energy passband.

sistent with the locus of points for which the external LISM magnetic field vector lies transverse to the IBEX LOS, a region of comparably strong dynamic and magnetic force exerted by the LISM (*6*, *8*). The likely LOS direction (λ, β) = (221°, 39°) parallel to the interstellar magnetic field derived here lies within the range $210° \leq \lambda \leq 240°$ and $30° \leq \beta \leq 60°$, obtained using the offset in flow directions between interstellar H^0 and He^0 (*14*), and is consistent with the direction inferred from 2- to 3-kHz radio emissions measured at the Voyager spacecraft (*15*).

References and Notes

1. M. Gruntman, *Rev. Sci. Instrum.* **68**, 3617 (1997)
2. M. Gruntman *et al.*, *J. Geophys. Res.* **106**, 15767 (2001)
3. S. A. Fuselier *et al.*, *Space Sci. Rev.*, 10.1007/s11214-009-9495-8 (2009)
4. H. O. Funsten *et al.*, *Space Sci. Rev.*, 10.1007/s11214-009-9504-y (2009)
5. D. J. McComas *et al.*, *Space Sci. Rev.*, 10.1007/s11214-009-9499-4 (2009)
6. D. J. McComas *et al.*, *Science* **326**, 959 (2009); published online 15 October 2009 (10.1126/science.1180906)
7. S. A. Fuselier *et al.*, *Science* **326**, 962 (2009); published online 15 October 2009 (10.1126/science.1180981)
8. N. A. Schwadron *et al.*, *Science* **326**, 966 (2009); published online 15 October 2009 (10.1126/science.1180986)
9. R. B. Decker *et al.*, *Nature* **454**, 67 (2008)
10. D. J. McComas *et al.*, *Geophys. Res. Lett.* **25**, 1 (1998)
11. N. A. Schwadron, D. J. McComas, *Geophys. Res. Lett.* **30**, 1587 (2003)
12. B. G. Lindsay, R. F. Stebbings, *J. Geophys. Res.* **110**, A12213 (2005).
13. H. R. Muller, G. P. Zank, *J. Geophys. Res.* **109**, A07104 (2004)
14. R. Lallement *et al.*, *Science* **307**, 1447 (2005)
15. D. A. Gurnett, W. S. Kurth, I. H. Cairns, J. Mitchell, *AIP Conf. Proc.* **858**, 129 (2006)

16. We thank all the IBEX team members, who enabled the success of IBEX through their individual talents, dedication, and hard work. This work was funded by the NASA Explorer Program. Work at Los Alamos was performed under the auspices of the U.S. Department of Energy.

21 August 2009; accepted 2 October 2009
Published online 15 October 2009;
10.1126/science.1180927
Include this information when citing this paper

Comparison of Interstellar Boundary Explorer Observations with 3D Global Heliospheric Models

N. A. Schwadron,[1,13]* M. Bzowski,[2] G. B. Crew,[3] M. Gruntman,[4] H. Fahr,[5] H. Fichtner,[6] P. C. Frisch,[7] H. O. Funsten,[8] S. Fuselier,[9] J. Heerikhuisen,[10] V. Izmodenov,[11] H. Kucharek,[12] M. Lee,[12] G. Livadiotis,[13] D. J. McComas,[13,14] E. Moebius,[12] T. Moore,[15] J. Mukherjee,[13] N.V. Pogorelov,[10] C. Prested,[1] D. Reisenfeld,[16] E. Roelof,[17] G.P. Zank[10]

Simulations of energetic neutral atom (ENA) maps predict flux magnitudes that are, in some cases, similar to those observed by the Interstellar Boundary Explorer (IBEX) spacecraft, but they miss the ribbon. Our model of the heliosphere indicates that the local interstellar medium (LISM) magnetic field (B_{LISM}) is transverse to the line of sight (LOS) along the ribbon, suggesting that the ribbon may carry its imprint. The force-per-unit area on the heliopause from field line draping and the LISM ram pressure is comparable with the ribbon pressure if the LOS ~ 30 to 60 astronomical units and B_{LISM} ~ 2.5 microgauss. Although various models have advantages in accounting for some of the observations, no model can explain all the dominant features, which probably requires a substantial change in our understanding of the processes that shape our heliosphere.

Previous models of energetic neutral atom (ENA) maps (*1*) provide limits on possible emission patterns depending on the assumed proton distributions in the heliosheath. Models with assumed Maxwellian distributions in the heliosheath show a broad enhanced emission region near the nose where the flow stagnates, whereas highly nonthermal distributions dominated by pickup ions (PUIs) show higher intensities in the sidewind direction and toward the tail where the line-of-sight (LOS) integrations across the heliosheath extended over large distances [hundreds of astronomical units (AU)]. Three-dimensional (3D) models incorporating a κ distribution, defined in (*2*), as a distribution with a Gaussian-like core and a power-law tail, manifest structure influenced by the local interstellar medium (LISM) magnetic field (B_{LISM}) (*3*). The observed difference inside the termination shock (TS) between interstellar helium flow and the hydrogen flow (*4*), which interacts more strongly with the outer heliosheath plasma (beyond the heliopause), suggests that B_{LISM} lies in the plane of the two flow vectors (the hydrogen deflection plane), which can push the TS closer to the Sun in the Southern Hemisphere, helping to explain why Voyager 2 (V2; −29° latitude) crossed the TS ~10 AU closer to the Sun than

[1]Department of Astronomy, Boston University, Boston, MA 02215, USA. [2]Space Research Centre of the Polish Academy of Sciences, 00-716 Warsaw, Poland. [3]Kavli Institute, Massachusetts Institute of Technology, Cambridge, MA 02139, USA. [4]Astronomical Engineering Division, University of Southern California, Los Angeles, CA 90089, USA. [5]Institut für Astrophysik und Extraterrestrische Forschung, University of Bonn, 53115 Bonn, Germany. [6]Institut für Theoretische Physik IV, Ruhr-Universitaet Bochum, 44780 Bochum, Germany. [7]Department of Astronomy and Astrophysics, University of Chicago, Chicago, IL 60637, USA. [8]Los Alamos National Laboratory, Los Alamos, NM 87545, USA. [9]Lockheed Martin Advanced Technology Center, Palo Alto, CA 94304, USA. [10]Department of Physics, University of Alabama, Huntsville, Alabama 35805, USA. [11]Department of Aeromechanics and Gas Dynamics, Moscow State University, and Space Research Institute (IKI) and Institute for Problems in Mechanics Russian Academy of Sciences, 117997 Moscow, Russia. [12]Department of Physics, University of New Hampshire, Space Science Center, Durham, NH 03824, USA. [13]Department of Space Science and Engineering, Southwest Research Institute, San Antonio, TX 78228, USA. [14]Department of Physics, University of Texas at San Antonio, San Antonio, TX 78249, USA. [15]NASA Goddard Space Flight Center, Greenbelt, MD 20771, USA. [16]Department of Physics, University of Montana, Missoula, MT 59812, USA. [17]Applied Physics Laboratory, Johns Hopkins University, Laurel, MD 20723, USA.

*To whom correspondence should be addressed. E-mail: nathanas@bu.edu

did Voyager 1 (V1; 34° latitude) (*5*–*8*). Here, we compare Interstellar Boundary Explorer (IBEX) observations (*9*–*11*) with sophisticated models of the heliosphere and outline considerations in the development of new concepts to understand the ribbon.

The ENA flux observed by IBEX derives from the LOS integral over the charge-exchange probability for the differential intensity of protons that move radially inward toward the Earth as they gyrate about the field. ENAs experience charge-exchange and photo-ionization losses as they propagate through the supersonic solar wind and are deflected and shifted in energy by the Sun's gravity and radiation pressure. At the energies considered here (~0.4 to 4 keV), these are small effects (at 0.4 keV, the ionization loss is ~40%, deflection is ~0.5°, and energy shift is ~2%) that decrease with energy. The ENA distribution at 1 AU is sensitive to the LOS path along which emission occurs, the density and bulk motion of the heliosheath plasma, and the energy and pitch-angle distributions of the source proton population.

We simulated ENA maps using different models with different assumptions for the local interstellar conditions. Model 1 (*3*) uses a magnetohydrodynamic (MHD) model (B_{LISM} = 1.8 μG) (*8*) incorporating a κdistribution (with κ =1.6) throughout the heliosheath with the derived MHD plasma parameters, but assumes a uniform density of interstellar hydrogen (0.1 cm^{-3}) a posterion to generate ENAs and does not treat the interaction between the plasma and neutrals self-consistently. Model 2 (Fig. 1) (*12*) uses an MHD model that self-consistently treats the charge-exchange interaction between neutral atoms from the LISM and protons that have a κ-function distribution of κ =1.6 inside the heliopause but a Maxwellian distribution outside. The model assumes a 450 km/s solar wind emitted inside the TS and a 3 μG B_{LISM} in the hydrogen deflection plane, tilted by 30° to the LISM flow. There are few structural differences at 1.1 and 4.4 keV (Fig. 1, A and B), indicating that global heliospheric structure, rather than energy-dependent heating, determines the modeled maps. Other sophisticated models incorporating the self-consistent interactions between the heliosheath plasma and LISM neutrals have been run for a range of LISM and solar wind conditions, revealing considerable variability in global structure and dynamics (*13*).

The features detected by IBEX may be separated into two parts: the ribbon and distributed emissions outside the ribbon. Models currently miss the ribbon. We compared observations (*9*–*11*) with simulated fluxes (Table 1) in ~20° regions outside the ribbon. The IBEX fluxes were interpolated to 0.44, 1, and 4 keV in the Sun-centered inertial reference frame. The model fluxes differ substantially from observations by ~6 to 200%. Models also show that the time-varying latitudinal structure of the solar wind may cause 11-year quasi-periodic variations of

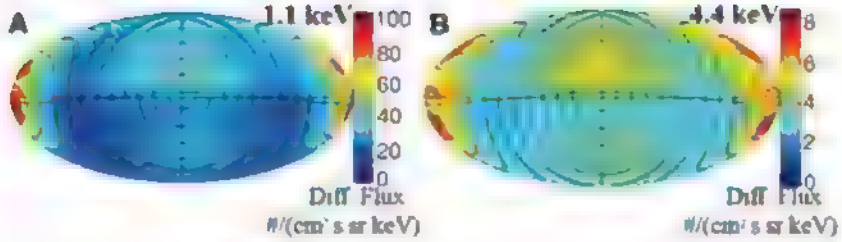

Fig. 1. Simulated ENA maps (Mollweide projection) using Model 2 show incident 1 AU ENA fluxes at 1.1 keV (**A**) and 4.4 keV (**B**).

Table 1. Observed and simulated ENA Fluxes at 0.44, 1 and 4 keV, respectively.

Source	IBEX	Model 1 (*3*)	Model 2 (*12*)
	ENAs/(cm2 s sr keV)	ENAs/(cm2 s sr keV) (percent relative to IBEX observations)	
Nose	470	230 (49%)	150 (31%)
	96	60 (63%)	43 (45%)
	9	6 (67%)	5.6 (62%)
Tail	530	30 (6%)	360 (68%)
	120	17 (14%)	100 (83%)
	4	4 (100%)	8 (200%)
North Pole	410	150 (37%)	110 (28%)
	76	45 (59%)	34 (45%)
	9	5 (56%)	4 (48%)
South Pole	360	130 (36%)	89 (25%)
	70	40 (57%)	30 (43%)
	9	5 (56%)	4 (44%)
Right flank (longitude = −165°)	230	190 (83%)	110 (48%)
	70	50 (71%)	35 (50%)
	6	5 (83%)	4.3 (72%)
Left flank (longitude = −45°)	380	170 (45%)	110 (30%)
	86	46 (53%)	33 (38%)
	7	5 (71%)	4.3 (61%)

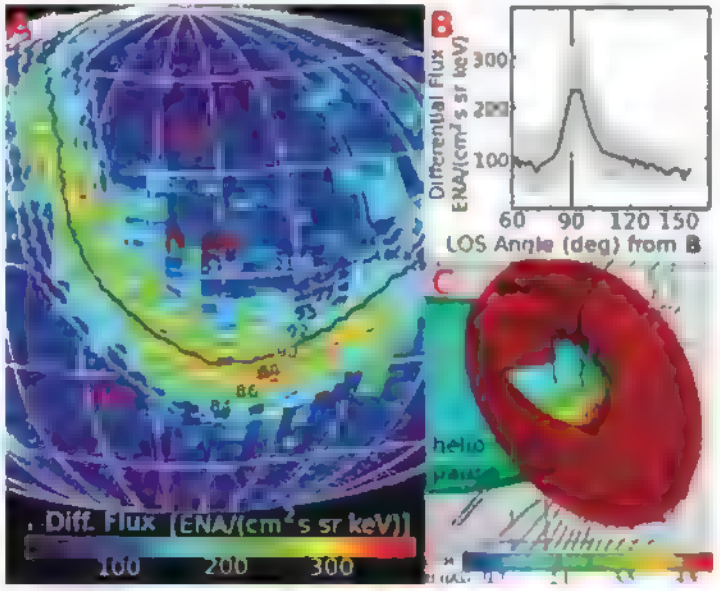

Fig. 2. (**A**) The observed ENA map at 1.1 keV superimposed with contours of the *B*•*r* angle (from 82° to 99°, black contour at 90°) between the simulated *B* (from Model 2 in Table 1) and the LOS, *r*, averaged over a 10-AU region just outside the heliopause (taken where the modeled plasma temperature is <80,000 K). (**B**) The overall correlation between ENA fluxes (−180° to 0° ecliptic longitude) and the *B*•*r* angle. (**C**) Global configuration of field lines draped over the heliopause, and the surface where *B*•*r* = 0. The black contour in (A) corresponds to the red 3D surface outside the heliopause in (C) where the LISM field is most stressed by draping about the heliopause and *B*•*r* = 0. The assumed B_{LISM} direction (ecliptic longitude = −120°, latitude = 31°) is consistent with indirect observational inferences (*5*, *13*, *16*).

ENA fluxes (*14*) with a local maximum around 60° latitude for 1 keV ENAs (*15*).

Model 2 shows correlation between the ribbon and the locus of $B \cdot r = 0$, where B denotes the draped field outside the heliopause and r is the radial vector along the LOS (Fig. 2). Notwithstanding the assumed direction and strength of B_{LISM}, the correlation with the $B \cdot r = 0$ locus suggests that the ribbon may carry the imprint of B_{LISM} via physical processes not identified in current models.

To quantify the implications of the ribbon for global models, we computed the plasma pressure (P) in the ribbon. Direct analysis of the observed fluxes yields $P \cdot LOS \sim 100$ AU-pdyne/cm^2 (*11*). The ribbon's observed width (*10*) of ~50 AU for a heliopause distance 150 AU from the Sun yields LOS ~ 50 AU, assuming comparable width and depth. This 50 AU LOS suggests $P \sim 2$ pdyne/cm^2, 2.5 times the LISM ram pressure (*16*). We computed a crude model to estimate the increase in pressure ahead of the heliopause caused by the external $J \times B$ force (where J is the current density) and thermal pressure [approximated by the dynamical pressure for a LISM proton density of 0.07 cm^{-3} and a flow speed of 26 km/s (*16*)] (Fig. 3). We approximated the heliopause as a perfectly conducting sphere with a slightly flared external magnetic field, conceptually similar to (*17*) and figure 4C in (*9*). The crude model compressed $|B|$ to ~4 μG outside the heliopause for $B_{LISM} = 2.5$ μG. The analytic approach was validated against MHD simulations in other applications (*18*) and provides the net MHD forces acting on the surface by collapsing current onto the conducting sphere. A ring of high pressure centered on B_{LISM} is associated with magnetic field line draping. If P is comparably high, then the LOS is approximately 60 to 30 AU.

Field-draping around the heliopause also compresses the heliosheath plasma, which could enhance ENA emission because of density enhancement (the plasma density, n, scales with the field strength, B) and first adiabatic invariance ($v_\perp^2/B = \text{const}$, where $v_\perp$ is the velocity of plasma protons perpendicular to the field), provided that some mechanism creates a large suprathermal population beyond the heliopause and there is limited scattering. We assumed a κ distribution (κ = 1.6) in the unperturbed LISM, applied n/B and $v_\perp^2/B$ conservation, and integrated along the LOS from the heliopause to 40 AU beyond it in order to estimate ENA emission (Fig. 3). The structure of the map is preserved at different energies with only the absolute fluxes changing. If distributions are isotropic because of scattering, adiabatic heating and density compression could still enhance fluxes, but the emission band broadens because of the lack of pitch-angle dependence.

Our crude model does not explain the origin of the ribbon but supports the notion that the draped LISM magnetic field influences the heliosheath pressures and ENA emission. Our crude model suggests that the flow may stagnate along the ribbon (*9*). However, the $J \times B$ forces that we isolated are present in all MHD models, and stagnation along the $B \cdot r = 0$ locus is not seen. Therefore, if the $J \times B$ forces lead to an enhanced ribbon pressure, they must do so via mechanisms not currently present in global models. For example, elevated $J \times B$ forces could induce an interchange instability near the heliopause, causing the higher-pressure plasma inside the heliopause to displace field lines longitudinally and protrude beyond the heliopause and elevating ENA emission through charge-exchange with the higher neutral density beyond the heliopause (*16*) and the lengthened LOS. This instability could depend critically on highly mobile ions, effectively enhancing the pressure along the protruding plasma fingers and highlighting the importance of ion-kinetic effects that are not self-consistently included in current models.

Model predictions provide mixed agreement with observations, and the ribbon is not predicted. The ribbon suggests a high-pressure region in the heliosheath possibly imprinted by the influence of the LISM magnetic field. However, current models are unable to translate the influence of LISM magnetic field into enhanced ENA fluxes along the ribbon, indicating that an important physical ingredient is missing.

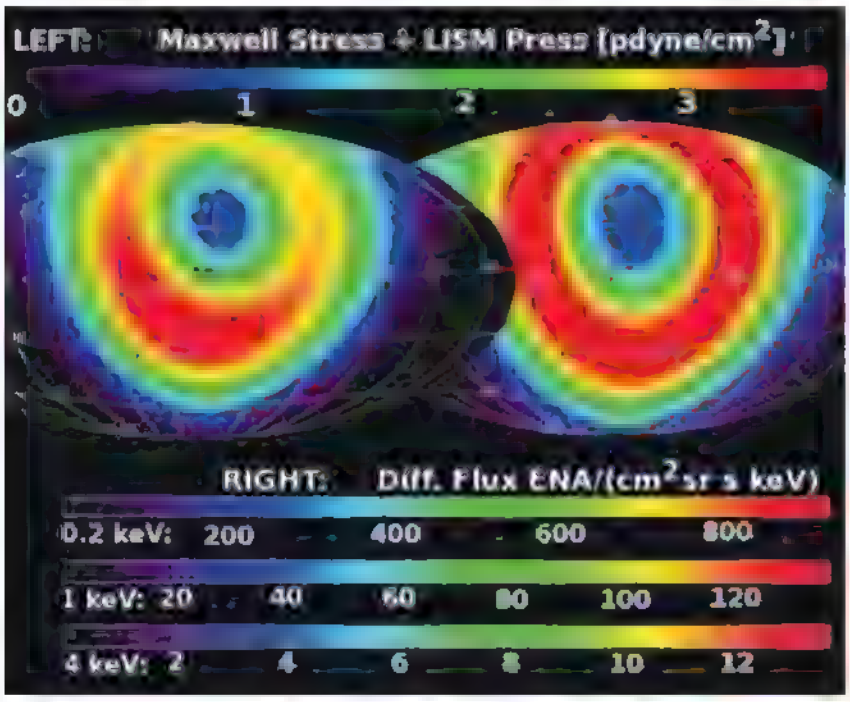

Fig. 3. (Left) Results of a crude model for the combined force-per-unit area on the heliopause from external $J \times B$ forces (Maxwell stress). **(Right)** Estimated ENA emission from beyond the heliopause using a crude model of plasma compression.

References and Notes

1. M. Gruntman *et al.*, *J. Geophys. Res.* **106**, 15767 (2001).
2. V. M. Vasyliunas *et al.*, *J. Geophys. Res.* **73**, 2839 (1968).
3. C. Prested *et al.*, *J. Geophys. Res.* **113**, 6102 (2008).
4. R. Lallement *et al.*, *Science* **307**, 1447 (2005).
5. E. C. Stone *et al.*, *Science* **309**, 2017 (2005).
6. J. D. Richardson *et al.*, *Nature* **454**, 63 (2008).
7. M. Opher *et al.*, *Astrophys. J.* **640**, L71 (2006).
8. M. Opher, E. C. Stone, T. I. Gombosi, *Science* **316**, 875 (2007).
9. D. J. McComas *et al.*, *Science* **326**, 959 (2009); published online 15 October 2009 (10.1126/science.1180906).
10. S. A. Fuselier *et al.*, *Science* **326**, 962 (2009); published online 15 October 2009 (10.1126/science.1180981).
11. H. O. Funsten *et al.*, *Science* **326**, 964 (2009); published online 15 October 2009 (10.1126/science.1180927).
12. N. V. Pogorelov *et al.*, *Astrophys. J.* **695**, 31 (2009).
13. V. Izmodenov, D. Alexashov, A. Myasnikov, *Astron. Astrophys.* **437**, 35 (2005).
14. K. Scherer, H. J. Fahr, *Geophys. Res. Lett.* **30**, 1045 (2003).
15. O. Sternal, H. Fichtner, K. Scherer, *Astron. Astrophys.* **477**, 365 (2008).
16. P. C. Frisch *et al.*, in *The IBEX Mission*, D. J. McComas, N. A. Schwadron, G. Zank, Eds. (Springer, Dordrecht, Netherlands, 2009), chap. 9, pp. 28–66 (2009).
17. E. N. Parker, *Astrophys. J.* **134**, 20 (1961).
18. P. Wu *et al.*, *J. Geophys. Res.* **113**, A00B05 (2008).

19. We thank the many dedicated people who have made IBEX a success. Special thanks to K. Goodrich, J. Siegel, K. Maynard, and M. Schwadron for their help. This work was primarily supported by the IBEX program.

24 August 2009; accepted 2 October 2009
Published online 15 October 2009;
10.1126/science.1180986
Include this information when citing this paper.

Direct Observations of Interstellar H, He, and O by the Interstellar Boundary Explorer

E. Möbius,[1]* P. Bochsler,[1,2] M. Bzowski,[3] G. B. Crew,[4] H. O. Funsten,[5] S. A. Fuselier,[6] A. Ghielmetti,[6] D. Heirtzler,[1] V. V. Izmodenov,[7,8] M. Kubiak,[3] H. Kucharek,[1] M. A. Lee,[1] T. Leonard,[1] D. J. McComas,[9,10] L. Petersen,[1] L. Saul,[2] J. A. Scheer,[2] N. Schwadron,[11] M. Witte,[12] P. Wurz[2]

Neutral gas of the local interstellar medium flows through the inner solar system while being deflected by solar gravity and depleted by ionization. The dominating feature in the energetic neutral atom Interstellar Boundary Explorer (IBEX) all-sky maps at low energies is the hydrogen, helium, and oxygen interstellar gas flow. The He and O flow peaked around 8 February 2009 in accordance with gravitational deflection, whereas H dominated after 26 March 2009, consistent with approximate balance of gravitational attraction by solar radiation pressure. The flow distributions arrive from a few degrees above the ecliptic plane and show the same temperature for He and O. An asymmetric O distribution in ecliptic latitude points to a secondary component from the outer heliosheath.

Interstellar neutral gas flows through the inner heliosphere due to the Sun's motion relative to the local interstellar medium (LISM), thus making interstellar gas measurements possible from Earth's orbit. Ionization of neutral atoms approaching the Sun and the Sun's gravitational field result in a characteristic flow pattern and density structure in the inner heliosphere with a cavity close to the Sun and gravitational focusing on the downwind side (Fig. 1A). For H this pattern is distinctly modified by radiation pressure, eliminating the downwind focusing. Previous LISM H and He diagnostic studies used ultraviolet backscatter observations (*1*, *2*), pickup ion studies (*3*, *4*), and a combination of methods for He (*5*). Making use of the Sun's gravitational deflection, the velocity distributions of various species can be studied in detail using neutral atom imagers (*6*, *7*) to derive interstellar gas parameters, filtering of the species in the outer heliosheath, and their deflection by interstellar magnetic field effects on the plasma. Previously, only neutral He had been observed, first by Ulysses outside 1.5 astronomical units (AU) (*8*, *9*) and then by IMAGE at 1 AU (*10*). Here, we present Interstellar Boundary Explorer (IBEX) observations of the interstellar neutral H, He, and O flow from January through April 2009. With the IBEX sensors pointing radially outward on a spacecraft whose spin axis points Sunward (*11*), the LISM flow is in the IBEX-Lo sensor field of view (FOV) in the spring, when Earth (and IBEX) move into the flow, and in the fall, when Earth recedes from the flow (*7*) (Fig. 1A).

The LISM flow dominates the IBEX-Lo all-sky maps at 15 and 110 eV with rates that exceed those of the diffuse energetic neutral atom (ENA) distributions (*12*–*14*) by up to four orders of magnitude (Fig. 1, B and C). The intense flow started with orbit 9 (mid-December 2008), peaked in orbit 16 (about −135° ecliptic longitude), and was seen through orbit 26 (April 2009) at 15 eV (Fig. 1B), but only through orbit 22 at 110 eV (Fig. 1C). A much narrower peak, maximized in orbit 16, showed up in the O maps for 280 eV and 600 eV (600 eV shown in Fig. 1D), with a tail extending from this peak toward higher latitude (up to about 20°) and smaller longitude (about 165°). The peak flux in all three maps arrives from slightly above the ecliptic plane. Based on the expected interstellar bulk flow energies at 1 AU for an observer that moves into flow with Earth's velocity, the distribution observed at 280 and 600 eV is largely interstellar O (529 eV bulk flow energy in the observer frame), the distribution seen up to 110 eV stems from interstellar He (132 eV), and the extended distribution seen into April at 15 eV is interstellar H (16 eV if radiation pressure cancels gravitational attraction).

With its time-of-flight (TOF) mass spectrometer, IBEX-Lo directly determines incoming neutral gas species after their conversion into negative ions on a diamond-like carbon conversion surface for H and O (*15*). However, He only produces a few metastable negative ions at higher energies (*16*). Therefore, it is identified in the TOF system through a well-characterized mixture of H, C, and

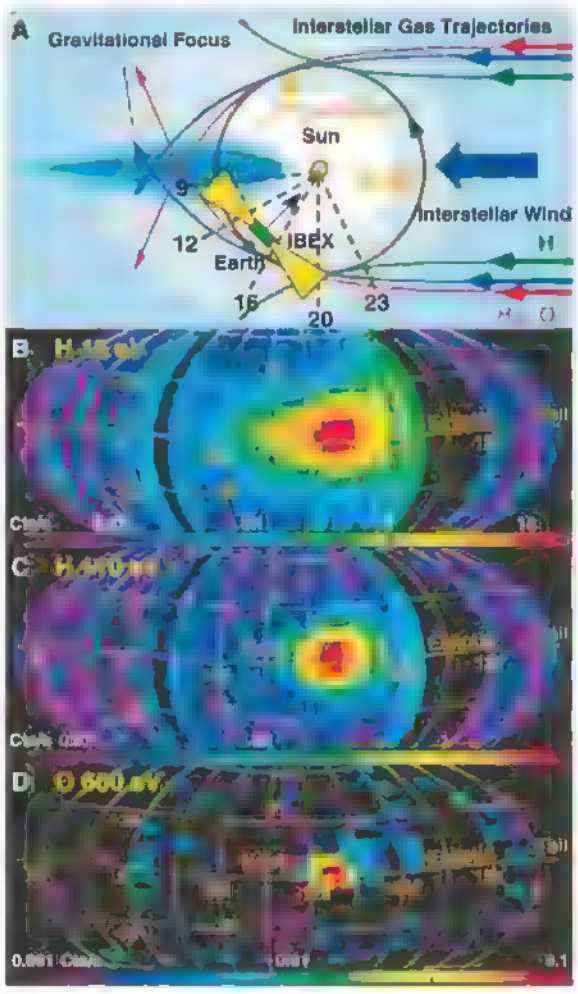

Fig. 1. (**A**) Schematic diagram of the interstellar gas flow through the inner heliosphere as deflected by the Sun's gravitational field. He and O trajectories are bent toward the Sun, stronger for slower atoms (red) than for faster ones (blue), making the bulk of them tangential to Earth's orbit for IBEX orbit 16, whereas H trajectories (green) are diverted outward by the Sun's radiation pressure. The color shading indicates the density pattern of He with its focusing cone. Also shown are Earth's positions for IBEX orbits 9 to 23 and the IBEX FOV for orbit 14. (**B**) H all-sky map (viewing direction) at 15 eV in a Mollweide projection (*12*) with color-coding of the count rate on a logarithmic scale after culling times with background from the magnetosphere and upstream particles (*12*). Black pixels either have zero counts or are culled for foreground from the magnetosphere (in particular in orbits 27 to 30, looking backward relative to Earth's motion, and all around in orbit 31). An intense flow is seen from −180° (orbit 9) to −50° (orbit 26) ecliptic longitude, that is, looking forward, with wide spread in latitude, and well away from potential magnetospheric interference. (**C**) H map at 110 eV with intense flow from −180° to −100° ecliptic longitude. (**D**) O map at 600 eV with intense flow from −165° to −110° ecliptic longitude.

[1]Space Science Center and Department of Physics, University of New Hampshire, Durham, NH 03824, USA. [2]Physikalisches Institut, Universität Bern, 3012 Bern, Switzerland. [3]Space Research Centre, Polish Academy of Sciences, 00-716 Warsaw, Poland. [4]Massachusetts Institute of Technology, Cambridge, MA 02139, USA. [5]Los Alamos National Laboratory, Los Alamos, NM 87545, USA. [6]Lockheed Martin Advanced Technology Lab, Palo Alto, CA, USA. [7]Moscow State University, 119899 Moscow, Russia. [8]Space Research Institute, Russian Academy of Sciences, 117997 Moscow, Russia. [9]Southwest Research Institute, San Antonio, TX 78228, USA. [10]University of Texas at San Antonio, San Antonio, TX 78249, USA. [11]Department of Astronomy, Boston University, Boston, MA 02215, USA. [12]Max Planck-Institute for Solar System Research, 37191 Katlenburg-Lindau, Germany

*To whom correspondence should be addressed. E-mail: Eberhard.moebius@unh.edu

Table 1. Observed species branching ratios. Shown in the first two rows are the C+O percentages of the total number of counts observed in the TOF spectra at 15, 29, 55, and 110 eV, after subtracting underlying H from diffuse ENAs (*12*–*14*), and in the third row (in italics) the C+O percentage found during calibration with a He beam at 110 eV and close to the actual LISM energy at 135 eV. The fourth row shows the observed C+O percentages for H at 15 eV and for O at 600 eV; the corresponding values from calibration are shown in the last row (in italics).

	E(eV)	%C+O	E(eV)	%C+O	E(eV)	%C+O	E(eV)	%C+O
Orbits 10 & 11	15	7	29	6	55	8	110	14
Orbits 13–19	15	14	29	18	55	16	110	11
110 & 135 eV He	*15*	*11 & 14*	*29*	*13 & 20*	*55*	*11 & 19*	*110*	*8 & 13*
Orbit 23	15	1			Orbits 16–18		600	100
15 & 29 eV H	*15*	*0–1*			*600 eV O*		*600*	*99*

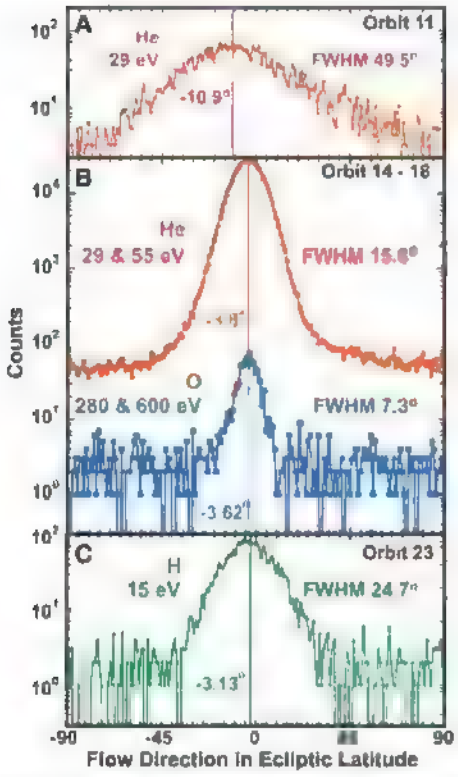

Fig. 2. Observed flow distributions as counts per 1° bin in ecliptic latitude for He [red, orbits 11 (**A**) and 14 to 18 (**B**)], O [blue, orbits 14 to 18 (**B**)], and H [green, orbit 23 (**C**)]. LISM H was seen only at 15 eV, sputter products of He at 15 to 110 eV (29 to 55 eV shown here), and O at 280 to 600 eV. The center position and FWHM of each distribution is shown, obtained with a Gaussian fit for the incoming flow convoluted with the IBEX-Lo angular response function

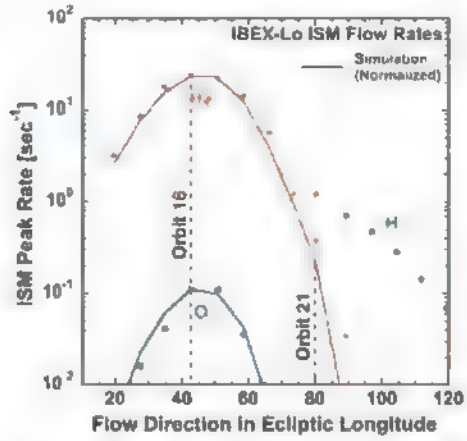

Fig. 3. Orbit-averaged count rates at the peak of the angular distributions (compare Fig. 2) for He, O, and H as a function of observed flow direction (after gravitational deflection at 1 AU) for orbits 13 (IBEX spin axis orientation finalized) through 26, together with the simulated rate for He and O, normalized to the observed rates at the maximum in orbit 16. These observed rates correspond to peak fluxes of 4.6×10^5 s^{-1} cm^{-2} sr^{-1} for He and 1.3×10^3 s^{-1} cm^{-2} sr^{-1} for O, based on the IBEX-Lo calibration. The LISM flow simulations use a hot interstellar gas model (*21*) with a flow speed of 26.3 km s^{-1} and temperature of 6300 K (*9*) for both He and O. The simulated distributions were accumulated for each orbit over the IBEX-Lo FOV in the actual spin axis orientation. The H rates in orbits 21 and 22 may contain small contaminations (25% and 4%) from He sputter products.

O that are sputtered from the conversion surface at energies below that of the incoming He.

For orbits 13 to 19, the observed composition reflected that from calibration (Table 1). At slightly lower energy, He produced substantially less C+O. This explains the generally lower amount seen in orbits 10 and 11, where lower He energies are visible because of their stronger gravitational deflection. Starting with orbit 20, we saw a transition to H at 15 eV, which was complete in orbit 23 (lower left in Table 1). In orbits 16 to 18 at 600 eV, we observed almost 100% of C+O, consistent with O calibration results (lower right in Table 1). The visibility of the interstellar neutral flow as a function of energy and longitude, together with the composition, shows that we observed interstellar He from orbit 9 through orbit 22, O simultaneously with He in orbits 14 to 18, and H after orbit 23, when the He flow vanished.

With the spin axis always in the ecliptic plane, IBEX records detailed angular distributions of the LISM flow in ecliptic latitude (Fig. 2). The interstellar flow observations started with a relatively wide distribution of He (shown for orbit 11 in Fig. 2A), with the flow pointing at about 11° into the ecliptic plane. During the passage of the main interstellar flow (orbits 14 to 18 in Fig. 2B), He showed a much narrower peak, with O about half the width of He. Their flows point at somewhat less than 4° ecliptic latitude. The H flow distribution from orbit 23 peaks about 3° in latitude and is substantially wider than the He distribution (Fig. 2C). Thus, all interstellar species flow at small negative latitude angles, consistent with the primary interstellar flow pointing at 5.3° in latitude, based on a recent analysis of several interstellar He observations (*5*).

The O peak flow appears slightly asymmetric, with a foot toward negative latitude, consistent with the average latitude of the entire distribution being 0.3° more negative than the center of the Gaussian. Also consistent with such a foot, O exhibits a tail toward higher latitude and lower longitude in viewing direction in the O sky map at 600 eV (Fig. 1D). This tantalizing finding, which warrants further investigation, points to a secondary component from charge exchange in the heliosheath, beyond the heliopause (*7*). The direction of the asymmetry is consistent with the observed deflection of the interstellar H flow toward lower latitudes compared with the primary He flow (*17*) that was interpreted as an effect of the interstellar magnetic field (*18*) and with the heliospheric asymmetry indicated by the Voyager termination shock crossings (*19*).

The width [Gaussian full width half-maximum (FWHM)] of the latitudinal He flow distribution when IBEX is looking into the flow (orbits 14 to 18) is about twice that of O. Using a convected Maxwellian with 6300 K (LISM temperature) for both species and a gravitational free-fall speed of 49.9 km s^{-1} at 1 AU, consistent with an original flow velocity of 26.3 km s^{-1} (*9*), the resulting width of the angular distributions in the moving frame of Earth is consistent with the observed He and O distributions. Because the strong radiation pressure on H mostly compensates the Sun's gravity (*20*), such a simple flow model may not be valid for H.

Simulated count rates (*21*) follow closely the observed count rates taken at the peak of the latitudinal distributions (Fig. 3). This comparison indicates that both the He and O observations by IBEX are consistent with physical He LISM flow parameters from recent studies (*5*, *9*) and with the two species having the same temperature. The interstellar H flow was seen only after He disappeared, and thus the peak in H was likely masked by the much stronger He signal. The continuing observation of H in late spring when Earth's motion pointed beyond the interstellar upwind direction and when trajectories fall into the IBEX FOV that appear deflected away from the Sun point to a strong effect of solar radiation pressure on H, as reported in previous studies (*20*).

IBEX observed the interstellar neutral gas flow distribution of three key species, H, He, and O, over a wide angular range in ecliptic longitude and latitude. A He flow distribution is presented that extends from right after Earth intercepts the gravitational focusing cone of He in December 2008 through March 2009. These combined observations provide a snapshot of the interstellar

flow conditions for three species during the current extended solar minimum. Any temporal variations of these conditions are of a much longer time scale than the observation period presented here. These observations provide constraints on the interstellar flow parameters and the interaction of the interstellar flow with the heliospheric boundary. Together with future observations during different solar activity, they also constrain the ionization rates of these species and the solar radiation pressure for H.

References and Notes

1. J. L. Bertaux, J. E. Blamont, *Astron. Astrophys.* **11**, 200 (1971).
2. C. S. Weller, R. R. Meier, *Astrophys. J.* **193**, 471 (1974).
3. E. Möbius *et al.*, *Nature* **318**, 426 (1985).
4. G. Gloeckler *et al.*, *Science* **261**, 70 (1993).
5. E. Möbius *et al.*, *Astron. Astrophys.* **426**, 897 (2004).
6. M. Gruntman, *Planet. Space Sci.* **41**, 307 (1993).
7. E. Möbius *et al.*, *Space Sci. Rev.* 10.1007/s11214-009-9498-5 (2009).
8. M. Witte, M. Banaszkiewicz, H. Rosenbauer, *Space Sci. Rev.* **78**, 289 (1996).
9. M. Witte, *Astron. Astrophys.* **426**, 835 (2004).
10. P. Wurz *et al.*, *AIP Conf. Proc.* **719**, 195 (2004).
11. D. J. McComas *et al.*, *Space Sci. Rev.* 10.1007/s11214-009-9499 (2009).
12. D. J. McComas *et al.*, *Science* **326**, 959 (2009); published online 15 October 2009 (10.1126/science.1180906).
13. H. Funsten *et al.*, *Science* **326**, 964 (2009); published online 15 October 2009 (10.1126/science.1180927).
14. S. A. Fuselier *et al.*, *Science* **326**, 962 (2009); published online 15 October 2009 (10.1126/science.1180981).
15. S. A. Fuselier *et al.*, *Space Sci. Rev.* 10.1007/s11214-009-9495 (2009).
16. P. Wurz *et al.*, *J. Appl. Phys.* **103**, 10.1063/1.2842398 (2008).
17. R. Lallement *et al.*, *Science* **307**, 1447 (2005).
18. V. V. Izmodenov, D. B. Alexashov, A. V. Myasnikov, *Astron. Astrophys.* **437**, L35 (2005).
19. E. C. Stone *et al.*, *Nature* **454**, 71 (2008).
20. E. Quemerais *et al.*, *Astron. Astrophys.* **455**, 1135 (2006).
21. M. Bzowski *et al.*, *Astron. Astrophys.* **491**, 7 (2008).

22. We thank the many individuals who made this mission possible. This work is supported by NASA under contract NNG05EC85C, by the Swiss National Science Foundation, the Programme de Développement d'Expériences Scientifiques (PRODEX) the Space Research Centre of the Polish Academy of Sciences, and the Russian Federation.

24 August 2009; accepted 2 October 2009
Published online 15 October 2009;
10.1126/science.1180971
Include this information when citing this paper.

Imaging the Interaction of the Heliosphere with the Interstellar Medium from Saturn with Cassini

S. M. Krimigis,[1,2]* D. G. Mitchell,[1] E. C. Roelof,[1] K. C. Hsieh,[3] D. J. McComas[4,5]

We report an all-sky image of energetic neutral atoms (ENAs) >6 kilo–electron volts produced by energetic protons occupying the region (heliosheath) between the boundary of the extended solar atmosphere and the local interstellar medium (LISM). The map obtained by the Ion and Neutral Camera (INCA) onboard Cassini reveals a broad belt of energetic protons whose nonthermal pressure is comparable to that of the local interstellar magnetic field. The belt, centered at ~260° ecliptic longitude extending from north to south and looping back through ~80°, appears to be ordered by the local interstellar magnetic field. The shape revealed by the ENA image does not conform to current models, wherein the heliosphere resembles a cometlike figure aligned in the direction of Sun's travel through the LISM.

The quest for the dimensions and shape of the bubble of plasma called the heliosphere, created by the continuously flowing solar wind as the Sun travels through the LISM, is older than the space age (*1*). Estimates of the distance to the boundary in the general direction of the solar apex have ranged from a few astronomical units (1 AU equals the distance between Earth and Sun, 150 million km) to tens of AU (*2*–*4*). Voyager 1 and 2 (V1 and V2) crossed the termination shock (TS) at distances of 94 and 84 AU in 2004 and 2007 at +35° and −26° ecliptic latitudes, respectively [e.g., (*5*–*7*)], implying that the radial dimensions of the TS are different in time and/or location. More surprisingly, the shocked thermal plasma in the heliosheath remained supersonic because only 20% of the upstream energy density went into heating the downstream thermal plasma, while most of the rest went into heating pickup ions (PUI), including a substantial part (≥15%) going into protons >28 keV (*6*, *7*). PUI are interstellar neutrals that are ionized in the solar wind and picked up and accelerated to energies >1 keV by the flow (*8*).

The prevailing models of the shape of the heliosphere suggest a cometary-type interaction (Fig. 1) with a possible bow shock and/or heliopause, heliosheath, and TS, all foreshortened in the direction of motion of the solar system through the LISM (*3*, *9*). Energetic singly charged particles in the heliosheath will charge-exchange with interstellar neutral hydrogen and enter the heliosphere as ENAs unimpeded by the interplanetary magnetic field [e.g., (*10*, *11*)].

Launch of the ENA imager on the Cassini-Huygens mission to Saturn occurred in October 1997. The Cassini spacecraft spent nearly 7 years in interplanetary cruise with sporadic data coverage before insertion into orbit at Saturn on 1 July 2004. Because the principal objective of the Ion and Neutral Camera (INCA) instrument (*12*) (fig. S1) is to image the energetic plasma ions trapped in Saturn's magnetosphere through ENAs, it took several years to obtain a nearly full image of the heliosphere in directions away from Saturn, with a minor gap in the direction of the Sun. In October 2008, Interstellar Boundary Explorer (IBEX) was launched with ENA cameras specifically designed to map the heliospheric boundary at lower (<6 keV) energies (*13*, *14*).

Here, we present the INCA map of the sky in ~6 to 13 keV ENAs (Fig. 2A). The ENA map reveals an intensity ratio ≥ 10 between low intensities in the middle of the image and a bright, broad, latitude-dependent belt of higher intensities. The minimum reappears beyond the belt at ≥120° to about −170° at the respective edges of the image. The belt that makes a rough circle in the sky about the interstellar field direction as it extends from north to south is ~100° full width at half maximum (FWHM) at the ecliptic equator in

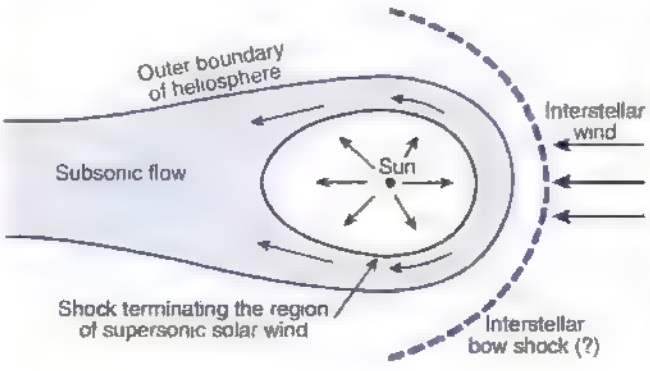

Fig. 1. Conventional concept of the heliosphere [(adapted from (*3*)]: The Sun is at the center, the region of the supersonic solar wind being asymmetric and compressed in the direction facing the interstellar wind flow (nose). Beyond the TS, the solar wind is expected to become subsonic and flow into the wake of the solar system, forming a cometlike tail.

[1]Applied Physics Laboratory, Johns Hopkins University, Laurel, MD 20723, USA. [2]Office for Space Research and Technology, Academy of Athens, 106 79 Athens, Greece. [3]Department of Physics, University of Arizona, Tucson, AZ 85721, USA. [4]Southwest Research Institute, San Antonio, TX 78228, USA. [5]University of Texas, San Antonio, TX 78249, USA.

*To whom correspondence should be addressed. E-mail: tom.krimigis@jhuapl.edu.

the range 30° to 150° and then loops back to recross the equator again at longitudes ~50° to ~110°, albeit at a lower intensity. Also, there are statistically significant enhancements in the intensity as the belt loops toward both north and south ecliptic poles. It is similar to, but broader than, the ribbon seen at lower (<6-keV) energies in the IBEX images (*14*). However, there is no maximum in the direction of the local interstellar flow (nose) at about 100°, as anticipated from the model shown in Fig. 1. The lower intensities in the direction of the anticipated tail at ~90° longitude are less organized. The intensities in the directions of V1 and V2 are slightly lower than those at the belt maximum.

Plotted in galactic coordinates (Fig. 2B), the belt of higher intensities now lies within ±60° of the galactic equator, being tilted ~30° toward north and south at positive and negative longitudes, respectively. The two intensity minima discussed earlier are now identified with the galactic north and south poles, although their boundaries are also tilted ~30° to the galactic equator. Although most x-ray, ultraviolet, and extreme ultraviolet radiation sources reside close to the galactic plane, a detailed study of the most intense of these proves that they are not correlated with the INCA ENA emissions [supporting online material (SOM) text and fig. S1]. It is clear from Fig. 2B that, contrary to theoretical expectations (compare with Fig. 1), the ENA emissions are at least partially ordered by galactic rather than ecliptic coordinates.

We evaluated the role that the nonthermal energetic ion pressure in the heliosheath (estimated from the observed ENAs) plays in the dynamics of the interaction with the LISM. The intensity (j_{ENA}) measured by INCA for ENAs with velocity (v) is given by the line-of-sight (LOS) integral beyond the TS ($\mathbf{r}_0$) through the heliosheath of the product of interstellar H-atom density (n_H) and the energetic ion intensity (j_{ion}) multiplied by the charge-exchange cross section (σ^{10})

$$j_{ENA}(\mathbf{v},t+\mathbf{r}_0/v) = \sigma^{10}\int_{r_0}^{\infty} d\mathbf{r} n_H(\mathbf{r}-\mathbf{v}t) j_{ion}(\mathbf{r}-\mathbf{v}t,t) \quad t \geq 0 \qquad (1)$$

We could rewrite the integral as

$$j_{ENA} = (\sigma^{10} n_0 j_0) L_{ion} \qquad (2)$$

where $n_0 j_0$ is the average value of the product of the density and intensity ($n_H\ j_{ion}$) over some radial interval ($\mathbf{r}_0$, $\mathbf{r}_0 + L_{ion}$), presumably beyond the TS that contains the bulk of the energetic ion population. This allows us to convert the measured j_{ENA} into a proton intensity averaged over a radial interval L_{ion} beyond the TS.

$$j_0 = j_{ENA}/(\sigma^{10} n_0 L_{ion}) \qquad (3)$$

Figure 2C shows ENA spectra at key locations identified in Fig. 2, A and B. Proton spectra (Eq. 3) are derived by normalizing the intensity of the highest ENA energy channel (~45 keV) to the overlapping Voyager 1 proton channel (~46 keV), making in situ measurements in the heliosheath at 110 AU. We find that $j_0 \approx 80\ j_{ENA}$ at V1. By assuming that $n_H \sim 0.1$ cm^{-3} and using the known value of σ^{10} (~2.32×10^{-16} cm^2) at that energy, we find that $L_{ion} \sim 36$ AU or $n_H L_{ion} = 3.6$ AU cm^{-3} for any other choice of n_H. The value for L_{ion} may well be different at other locations along the belt, and various assumptions on averaging can change it by up to ~40%; we adopt a representative value of 50 AU. The ENA spectra have a power-law slope of ~E^{-4} where E is particle energy, whereas the resulting ion spectrum is substantially less steep because of the energy dependence of the cross sections, and it joins smoothly with the V1 slope of ~$E^{-1.5}$ at >40 keV. The ENA spectrum overall has the same slope, irrespective of locations marked on the map shown in Fig. 2A. A calculation of the spectral index over every pixel in the entire map gives the same slope throughout to within ~5%.

Having converted the ENA intensities into equivalent ion intensities beyond the TS, we computed the partial plasma pressure at ≥6 keV, a range where many of the PUIs associated with the TS and heliosheath are expected to reside. The partial pressure ΔP is given by

$$\Delta P = (4\pi p/3) j_{ion} \Delta E$$

where p is proton momentum and ΔE is the energy width of each INCA channel. This becomes

$$\Delta P(\text{pPa}) = (7.47 \times 10^{-8}) v(\text{km s}^{-1}) \times j_{ENA} \Delta E(\text{cm}^2 \text{sr s})^{-1} / \sigma^{10} n_0 L_{ion}$$

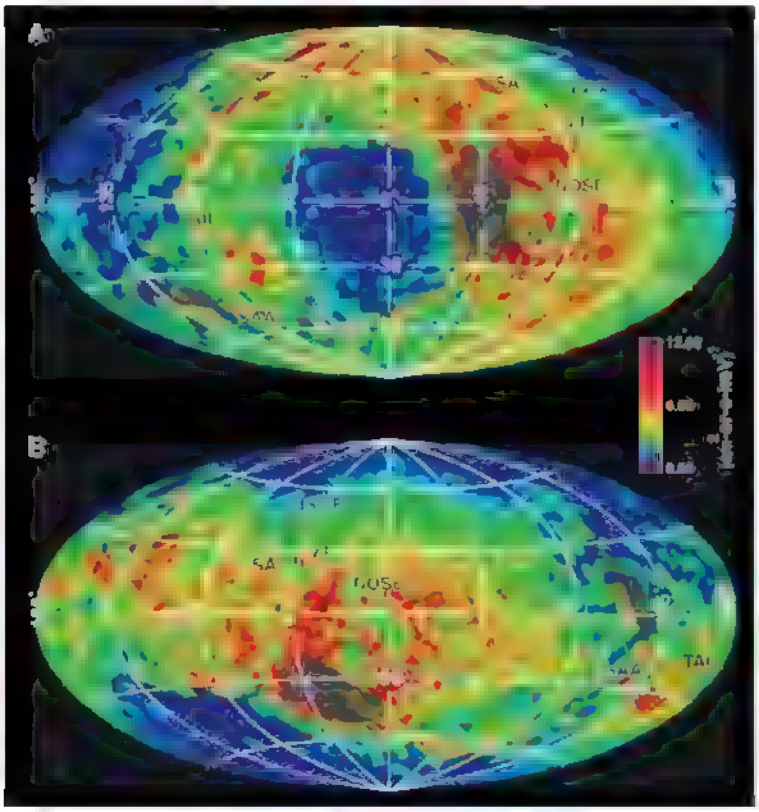

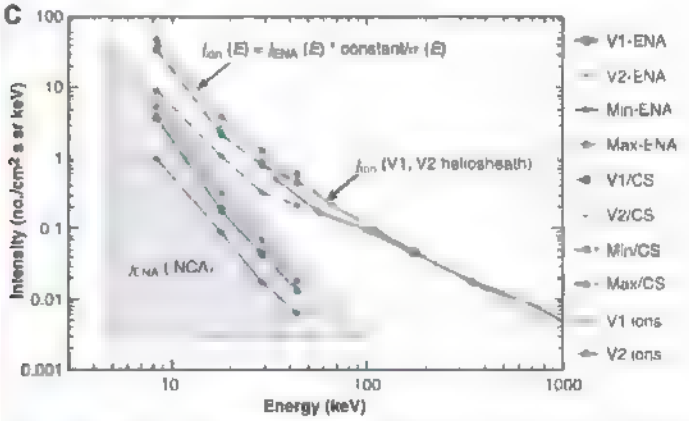

Fig. 2. **(A)** Image of heliospheric ENAs in the range of 5.2 to 13.5 keV (data from day 265, 2003, to day 184, 2009) plotted in ecliptic coordinates. The location of local interstellar flow (nose), its opposite (tail), solar apex (SA), and anti-apex (SAA), as well as the positions of Voyager 1 and 2 in the heliosheath are marked; the local ISMF direction (*16*, *17*) is indicated. Gray-shaded areas centered at about −70° longitude, 0° latitude and at ~120° longitude, −40° latitude are regions of incomplete coverage in the directions of the Sun and Saturn, respectively. **(B)** The same data plotted in galactic coordinates. **(C)** ENA spectra of INCA data over the energy range 5.2 to 55 keV (lower grouping) and deduced proton spectra (upper grouping) from selected locations shown in (A). Horizontal bars indicate the INCA energy channel limits for hydrogen ENAs. Laboratory charge exchange (CS) cross sections for protons on hydrogen (Eq. 3) were used for each channel.

with the pressure expressed in picopascals. Thus, our measurable quantity is the product $n_0 L_{ion} \Delta P$ for each channel: its sum over all INCA channels is shown in Fig. 3 in ecliptic coordinates (Mercator projection). Its distribution is similar to the ENA intensity profile shown in Fig. 2A, as would be expected. The total INCA partial pressure (assuming L_{ion} ~ 50 AU) ranges from 0.02 to 0.09 pPa. The in situ measurements (40 keV to 4 Mev) from Voyager 1 near the brightest part of the belt add another ~0.02 pPa (*6*). When the IBEX-derived pressure (*14*) of protons 0.2 to 6 keV (0.2 pPa) is added in, the total nonthermal pressure above 0.2 keV becomes larger than 0.31 pPa, exceeding the hydrostatic pressure ($B^2/2\mu_0$ = 0.25 pPa) for a 0.25-nT interstellar magnetic field (ISMF).

The ram pressure of the interstellar flow (with a proton density of 0.1 cm^{-3}) is 0.11 pPa. This is less than half of the pressure of the ISMF, which is why the signature of the ISMF shows up as the dominant one in the ENA images; the interstellar flow produces secondary effects in terms of dynamics compared with the nonthermal pressure of the energetic protons in the heliosheath interacting with the ISMF. Thus implies that the nonthermal pressure of >0.2-keV protons dominates the configuration of the heliopause through their interaction with the local ISMF.

There was an alternative model to the one shown in Fig. 1, where the termination-shocked plasma generates a partially closed diamagnetic "bubble" in which a strong local ISMF interacts directly and dynamically with the subsonic outflow (*15*). This model neglects the ram pressure of the interstellar plasma in favor of the thermal pressure of the heated plasma downstream of the heliospheric TS. The particle pressure interacts directly with the Maxwell stresses ($\mathbf{J} \times \mathbf{B}$) of the interstellar field to produce the diamagnetic bubble. We have modified this model by replacing the shock-heated thermal plasma pressure at the TS with the ENA-inferred nonthermal proton pressure that fills the heliosheath from the TS to the heliopause, thus moving the interaction with the ISMF from the TS to the heliopause (Fig. 4). The directions to the belt correspond approximately to the locations where the ISMF is normal (**N**) to the heliopause ($\mathbf{B} \cdot \mathbf{N} \cong 0$) (*16*). This simple concept of the dominant interaction provides an immediate quantitative explanation of the dominant topological feature (the ribbon or belt) in the ENA images obtained from both IBEX and INCA.

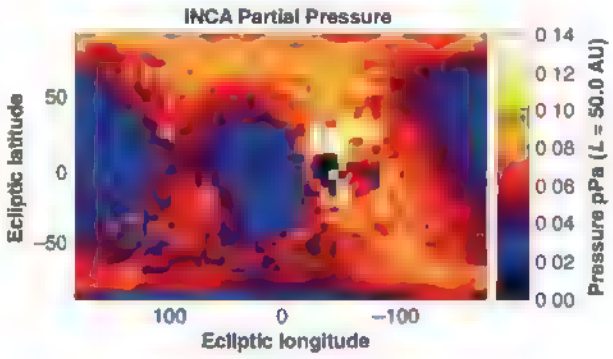

Fig. 3. Pressure contributed by protons beyond the TS computed from spectra deduced from the ENA observations in pPa (1 pPa = 10^{-11} dynes cm^{-2}). The thickness of the heliosheath is estimated to be ~50 AU.

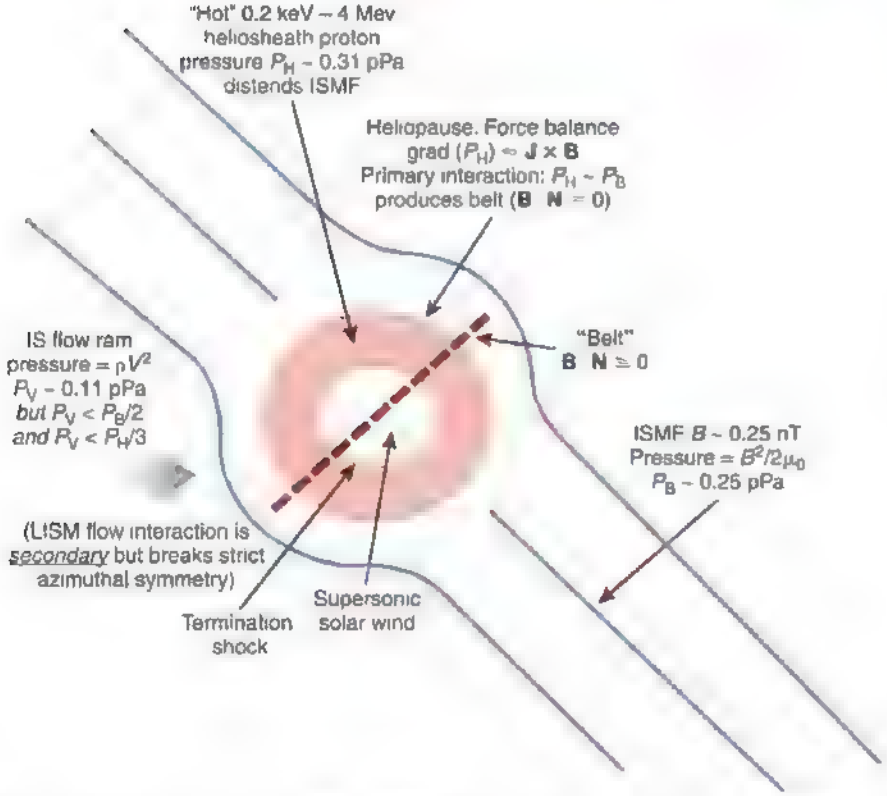

Fig. 4. Annotated summary of basic findings from the ENA maps of the heliosheath; the dominant interaction between the nonthermal heliosheath pressure with the ISMF tends to produce a diamagnetic bubble, as envisioned by Parker (*15*), who neglected the effects of the ram pressure of the interstellar plasma. It is very different from the contemporary paradigm (Fig. 1).

References and Notes

1. L. Davis Jr., *Phys. Rev.* **100**, 1440 (1955).
2. J. A. Simpson, J. R. Wang, *Astrophys. J.* **149**, L73 (1967).
3. W. I. Axford, *Space Sci. Rev.* **14**, 582 (1973).
4. H. Fichtner *et al.*, *AIP Conf. Proc.* **528**, 345 (2000).
5. R. B. Decker *et al.*, *Science* **309**, 2020 (2005).
6. R. B. Decker *et al.*, *Nature* **454**, 67 (2008).
7. J. D. Richardson *et al.*, *Nature* **454**, 63 (2008).
8. L. A. Fisk, B. Kozlovsky, R. Ramaty, *Astrophys. J.* **190**, L35 (1974).
9. V. Izmodnov, V. B. Baranov, in *The Physics of the Heliospheric Boundaries*, V. V. Izmodenov, R. Kallenbach, Eds. (The International Space Science Institute, Bern, Switzerland, 2006), pp. 67–136.
10. K. C. Hsieh, K. L. Shih, J. R. Jokipii, S. Grzedzielski, *Astrophys. J.* **393**, 756 (1992).
11. M. A. Gruntman *et al.*, *J. Geophys. Res.* **106**, 15767 (2001).
12. S. M. Krimigis *et al.*, *Space Sci. Rev.* **114**, 233 (2004).
13. D. J. McComas *et al.*, *Space Sci. Rev.* **146**, 11 10.1007/s11214-009-9499-4 (2009).
14. H. O. Funsten *et al.*, *Science* **326**, 964 (2009); published online 15 October 2009 (10.1126/science.1180927).
15. E. N. Parker, *Astrophys. J.* **134**, 20 (1961).
16. D. A. Gurnett, W. S. Kurth, I. H. Cairns, J. Mitchell, *AIP Conf. Proc.* **858**, 129 (2006).
17. R. Lallement *et al.*, *Science* **307**, 1447 (2005).
18. We are grateful to M. Kusterer, S. Turner, J. Allello, and R. DeMajistre for assistance in the data reduction and analyses efforts of Cassini and the Magnetospheric Imaging Instrument in general and this work in particular. Discussions with R. B. Decker are most appreciated. The work at the Johns Hopkins University Applied Physics Laboratory was supported by NASA under contracts NAS5-97271 and NNX07AJ69G and by subcontract at University of Arizona; the work at the Southwest Research Institute was supported by the NASA IBEX contract.

Supporting Online Material

www.sciencemag.org/cgi/content/full/1181079/DC1
SOM Text
Fig. S1
References

25 August 2009; accepted 5 October 2009
Published online 15 October 2009;
10.1126/science.1181079
Include this information when citing this paper

Observation of Half-Quantum Vortices in an Exciton-Polariton Condensate

K. G. Lagoudakis,[1]* T. Ostatnický,[2] A. V. Kavokin,[2,3] Y. G. Rubo,[4] R. André,[5] B. Deveaud-Plédran[1]

Singly quantized vortices have already been observed in many systems, including the superfluid helium, Bose-Einstein condensates of dilute atomic gases, and condensates of exciton-polaritons in the solid state. Two-dimensional superfluids carrying spin are expected to demonstrate a different type of elementary excitations referred to as half-quantum vortices, characterized by a π rotation of the phase and a π rotation of the polarization vector when circumventing the vortex core. We detect half-quantum vortices in an exciton-polariton condensate by means of polarization-resolved interferometry, real-space spectroscopy, and phase imaging. Half-quantum vortices coexist with single-quantum vortices in our sample.

Quantized vorticity is a property of quantum fluids that has been widely studied in various types of superfluids, either with or without spin (*1*–*4*). Superfluids with a two-component (spinor) order parameter are characterized by a different type of vortices than those found in conventional scalar superfluids (*5*–*8*). This new type of vortices is the so-called half-quantum vortices (HQV). They have lower energy with respect to full vortices and constitute the elementary excitations of spinor superfluids. When circumventing their core, the phase and the polarization vector experience a $\pm\pi$ rotation. In this sense, HQV can be understood as a half-phase vortex combined with a half-polarization vortex (*5*). In ^{3}He superfluids, the HQV cannot be formed because the spin degree of freedom is absent. However, in ^{3}He (*5*, *6*) or in triplet superconductors (*7*, *8*), the order parameter has two or more components, so the formation of HQV is possible. So far, experiments have not presented unambiguous evidence for HQV in ^{3}He (*9*), although more reliable indications of the existence of HQV have been reported in cuprate superconductors (*10*, *11*). Recently, HQV have been proposed as a smoking gun for the superfluid of exciton-polaritons in semiconductor microcavities (*12*). We report on a direct observation of HQVs in a high-temperature quantum fluid: microcavity exciton-polaritons. Exciton-polaritons are composite bosons carrying spin. They can occur in semiconductor microcavities in the strong coupling regime and are partly excitons and partly photons. The energy, wave vector, polarization, and statistics of cavity polaritons are directly transferred to light emitted by the microcavity due to photon tunneling through the mirrors of the cavity (*13*). Because of their photonic component, the cavity polaritons have an extremely low effective mass on the order of 10^{-4} of the free electron mass. This allows for their Bose-Einstein condensation (BEC) at temperatures achievable by cryogenic means. BEC of exciton-polaritons has been demonstrated in various types of microcavities composed either of II-VI (*14*) or III-V compounds (*15*). The most prominent effects found in these systems are the bosonic stimulation, the appearance of long-range spatial coherence, and the buildup of the vector polarization (*13*). Several indications of the polariton superfluidity have been reported, including the Bogoliubov-like dispersion (*16*), the appearance of phase vortices (*4*), and diffusionless motion of coherent polariton fluids in the presence of obstacles (*17*). In this work, HQVs are reported in a II-VI microcavity where BEC of the exciton-polaritons and formation of the integer phase vortices have been reported recently (*4*, *14*). Coexistence of HQV and integer vortices in the same sample is possible because of the spatially inhomogeneous

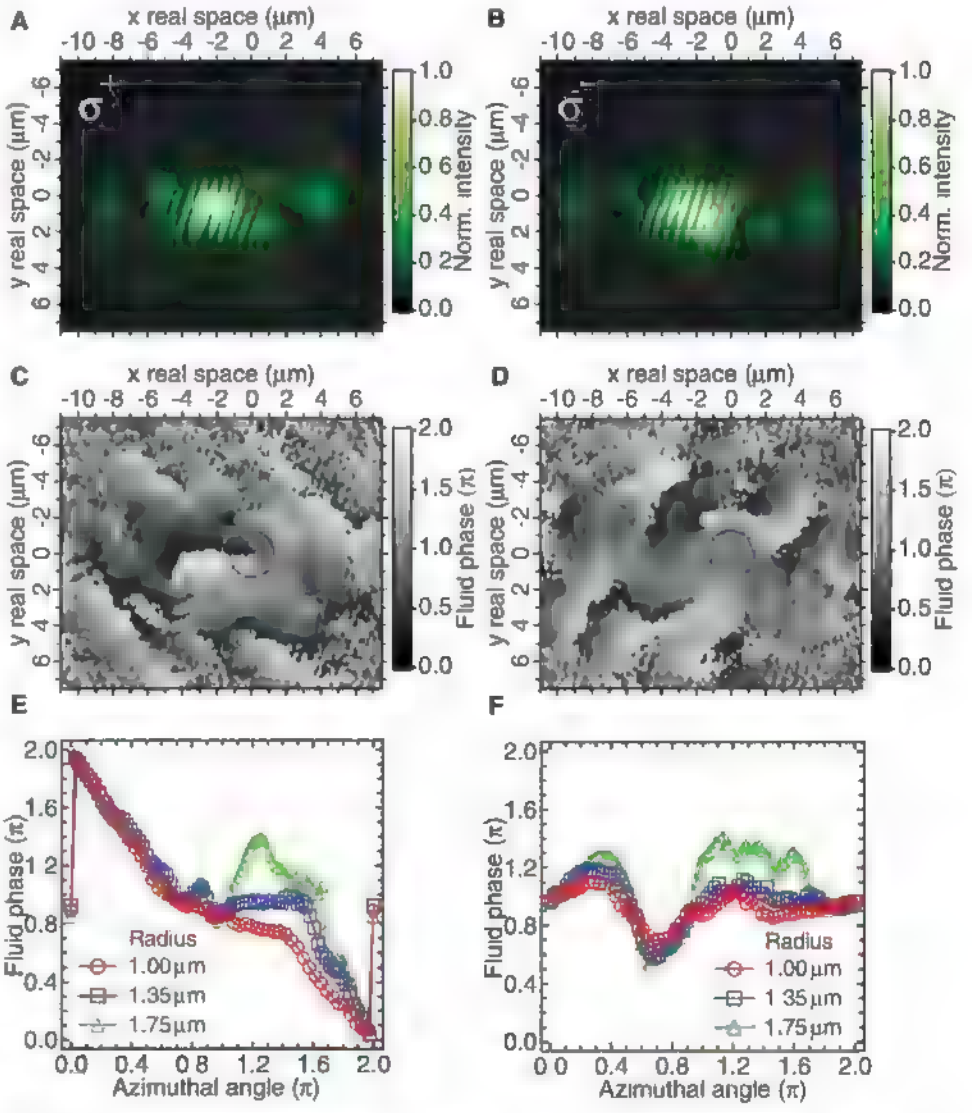

Fig. 1. (**A** and **B**) Reconstructed interferograms for σ^+ and σ^- polarizations at the energy of the condensate. (**C** and **D**) Real space phase map extracted from the interferograms (**A**) and (**B**) for polarizations σ^+ and σ^-, respectively. The three circles with different colors denote the real space paths over which we have plotted the phase as a function of the azimuthal angle in panels (**E** and **F**). The phase profiles in σ^+ polarization (**E**) show that the phase changes by -2π when circumventing the vortex core, which is the signature of the singularity. In contrast, for the σ^- polarization (**F**), we see a quasi-flat phase profile with zero overall phase shift as one goes around the core. The farther we probe the phase away from the vortex core, the more the phase diverges from the linear behavior versus angle.

[1]Institut de Photonique et d'Electronique Quantique (IPEQ), Ecole Polytechnique Fédérale de Lausanne (EPFL), 1015 Lausanne, Switzerland. [2]School of Physics and Astronomy, University of Southampton, Highfield, Southampton SO17 1BJ, UK. [3]Marie-Curie Chair of Excellence, University of Rome II, Via della Ricerca Scientifica 1, 00133 Rome, Italy. [4]Centro de Investigación en Energía, Universidad Nacional Autónoma de México, Temixco, 62580 Morelos, Mexico. [5]Institut Néel, Centre National de la Recherche Scientifique (CNRS), 38042 Grenoble, France.

*To whom correspondence should be addressed. E-mail: konstantinos.lagoudakis@epfl.ch

polarization splitting in microcavities, which is responsible for the suppression of HQV in certain areas of the sample. Thus, in different parts of the sample the polariton fluid has a different topology.

To fully characterize a vortex in a polariton condensate, one needs two winding numbers, (k,m), one for the polarization angle and one for the phase. One can express the order parameter of the condensate in the linear xy basis as

$$\Psi_{lin}(r) = \sqrt{n}e^{i\theta(r)}\begin{pmatrix}\cos\eta(r)\\ \sin\eta(r)\end{pmatrix} \quad (1)$$

where $\theta(\mathbf{r})$ is the phase of the coherent polariton fluid and $\eta(\mathbf{r})$ is the polar angle that characterizes the orientation of the electric field of polaritons, i.e., the polarization angle. Vortices are described in this notation by rotation of the phase and the polarization as $\eta(\mathbf{r}) \rightarrow \eta(\mathbf{r}) + 2\pi k$ and $\theta(r) \rightarrow \theta(r) + 2\pi m$ where k,m can take integer or half-integer values with $(k+m) \in \mathbb{Z}$. Four types of half vortices are described by winding numbers $(k,m) = (\pm\frac{1}{2},\pm\frac{1}{2})$. To reveal the specific phenomenology of HQVs with respect to the integer vortices, it is convenient to analyze the circularly polarized components of the order parameter, which can be expressed as

$$\Psi_{lin}(\mathbf{r}) = \frac{\sqrt{n}}{2}\left[e^{i(\theta(\mathbf{r})-\eta(\mathbf{r}))}\begin{pmatrix}1\\ i\end{pmatrix} + e^{i(\theta(\mathbf{r})+\eta(\mathbf{r}))}\begin{pmatrix}1\\ -i\end{pmatrix}\right] \quad (2)$$

One can see that for $\eta(\mathbf{r}) \rightarrow \eta(\mathbf{r}) + \pi$ and $\theta(\mathbf{r}) \rightarrow \theta(\mathbf{r}) + \pi$ a zero rotation takes place for one circular polarization and a full 2π rotation is achieved for the other circular polarization. This means that if one were to detect a half vortex, it would be easiest when looking in σ^- and σ^+ polarizations simultaneously. Then HQV would be observed as a full vortex in one polarization and no vortex in the other one. A signature for the phase vortex is a forklike dislocation in the interference pattern (*4*, *18*). In the case of full phase vortices, the forklike dislocations are expected to be seen in the same place in both circular polarizations, whereas in the case of HQV the fork appears only in one of the circular polarizations. In the circular basis, one can write the order parameter of HQV in cylindrical coordinates as

$$\Psi_{k,m}(\rho,\phi) = \sqrt{\frac{n}{2}}e^{im\phi}\begin{Bmatrix}[f(\rho)+\mathrm{sgn}(km)\,g(\rho)]\cdot e^{-ik\phi}\\ [f(\rho)-\mathrm{sgn}(km)\,g(\rho)]\cdot e^{ik\phi}\end{Bmatrix} \quad (3)$$

with $\rho = \frac{r}{a}$ being the relative distance from the vortex core in vortex radii and ϕ being the angular coordinate. The form of the two radial density functions f and g is known (*12*) and will give zero density for one circular polarization ($f - g$) and a finite density for the other polarization ($f + g$), as it is expected for the simplistic image of a full vortex in one circular polarization and no singularities for the other circular polarization.

An important feature of polariton condensates is the presence of polarization splitting induced by the structural anisotropy and stationary disorder. This splitting pins the polarization vector of the condensate to a given crystal axis. It is theoretically predicted that HQVs still exist in this case but the spatial distribution of the polariton vector field is modified. Similarly to the vortices in multicomponent quantum Hall systems (*19*), the polariton half vortices acquire "strings" [or solitons; figure 16.1 in (*6*)], whereby the polarization angle rotates by π (*20*). The width of the string is given by $\hbar/\sqrt{2m^*\varepsilon}$, where m^* is the effective mass of polaritons and ε is the energy of the polarization splitting. HQVs remain the lowest-energy topological defects if this width is greater than or comparable to the excitation spot radius. However, when this length becomes comparable to the vortex core size ($a \approx \hbar/\sqrt{2m^*\mu}$, where μ is the chemical potential), the excitation of HQVs would require too much energy, and the integer phase vortices $(0, \pm 1)$ become elementary topological excitations. For a realistic vortex core size on the order of ~2 μm and the polariton mass $m^* \approx 10^{-4}\, m_e$, pairs of HQVs will be replaced by integer phase vortices for polarization splittings $\varepsilon \geq 100$ μeV. [Two close pairs of HQVs are shown in (*21*), figs. S2 and S3].

The situation in real microcavity samples is additionally complicated by the fact that the polarization splitting ε fluctuates as a function of the coordinate in the plane of the cavity. This is why the HQV and integer phase vortices may coexist within the same condensate. The underlying mechanisms for the polarization splitting are thought to be the different penetration depths in the distributed Bragg reflectors (microcavity mirrors) for transverse electric and transverse magnetic polarizations (*22*) and the intrinsic anisotropy of the microcavity (*23*, *24*). The anisotropy is expected to be the product of a number of parameters, including the alloy concentrations, the wedge, quantum well width fluctuations, and the built-in strain. Splittings vary from zero to several tenths of μeVs. All HQVs that we observed in this sample were at regions where the splitting was less than our experimental resolution (≈ 20 μeV).

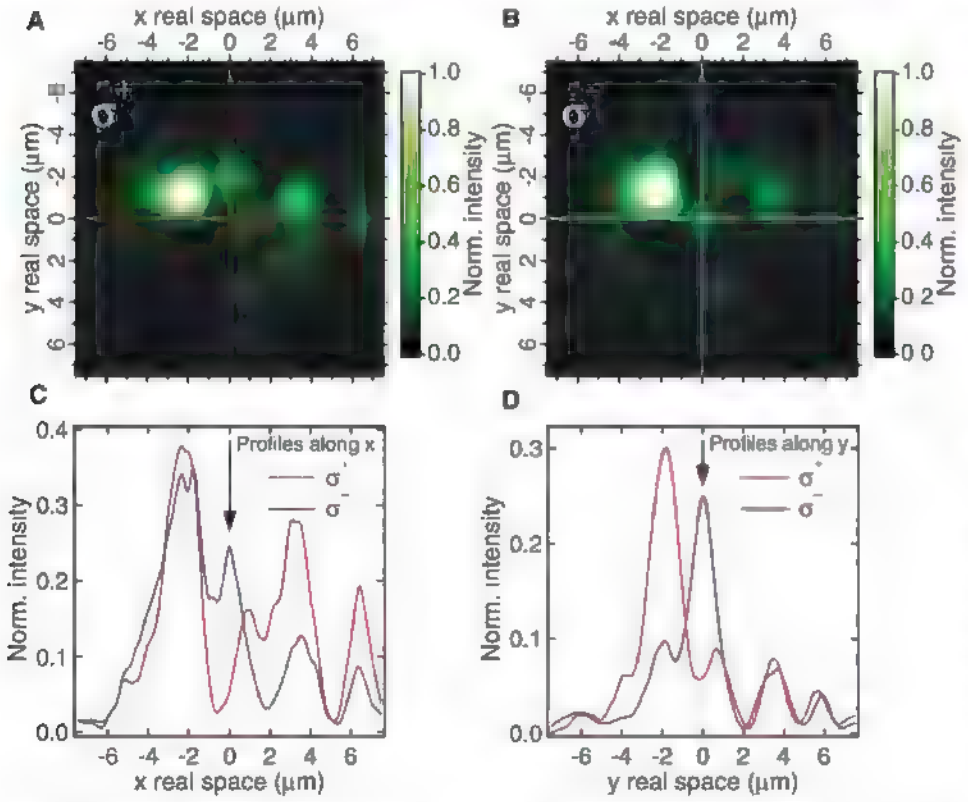

Fig. 2. (**A** and **B**) Polariton densities in real space at the frequency of the condensate for σ^+ and σ^- polarizations, respectively. It is easily seen that at the position of the vortex core (0,0), which is indicated by the red cross for σ^+ polarization and the blue cross for the σ^- polarization, there is a local minimum for σ^+ polariton density and a local maximum for the σ^- density. (**C**) Density profiles along the x direction for the two polarizations and (**D**) the corresponding density profiles along the y direction. Experimentally measured polariton density behaves in excellent agreement with the theoretical prediction [Eq. 3 and (*21*)]. This behavior is also evident from the fact that half vortices must be fully circularly polarized at the centers of their cores.

The sample we studied is the same CdTe/CdMgTe microcavity that was used in our previous experiments cooled down to ~10 K by a liquid helium flow cryostat (*4*). We used continuous-wave monomode nonresonant optical excitation. Detection was performed by means of the modified Michelson interferometer in the mirror-retroflector configuration with active stabilization (*4*) completed by a lambda quarter and a Wollaston prism. This allowed for polarization-resolved interferometry in σ^+ and σ^- polarizations simultaneously, which facilitated the identification of half vortices (*21*). All spectral studies were performed using a monochromator with ≈ 20 μeV resolution. The output of the interferometer could be sent to the entrance slits of the spectrometer through a polarizer, allowing for spectrally and polarization-resolved interferometry images to be acquired. The HQV were observed only at the excitation powers exceeding the condensation threshold. Once a good candidate was found, we performed a number of preliminary "test experiments" to verify unambiguously the persistence of the vortex for all possible detection configurations. The two most reliable tests were to change the overlap conditions at the output of the interferometer by shifting the mirror arm image with respect to one reflected from the retroreflector and to rotate by π the orientation of the fringes, making sure that for all orientations the singularity of the vortex is always clearly observable (*4*). We took care to verify the mutual coherence of the two cross-circular polarization components by means of polarization mixing interferometry in order to eliminate the possibility of having two independent condensates in the two polarizations. In all cases, we observed excellent mutual coherence properties with good contrast in the interference fringes between the two circular polarization components (*21*). The appearance of half vortices was quite rare; that is, one out of six regions with no polarization splitting was exhibiting a HQV.

Once the HQV was identified, the interferometric image was being sent on the entrance slits of the spectrometer. Then we performed an optical tomography experiment (*25*) for σ^+ and σ^- polarized images, which provided us with the full set of polarization-resolved interferograms in real space for all frequencies within the observable spectral window. Figure 1, A and B, shows the reconstructed interferogram coming from the frequency of the polariton condensate for the polarizations σ^+ and σ^-, on which we have added a red circle centered at the vortex core to help the reader locate the singularity. The singularity (forklike dislocation) is clearly visible for the σ^+ polarization, whereas on the same position in real space for the σ^- polarization we observe straight fringes. The interference patterns gave us access to the phase of the coherent polariton fluid. To extract the phase, we assumed that the reference field coming from a region of the condensate without a vortex has a flat phase profile. Figure 1, C and D, shows the phase of the polariton fluid in real space calculated from the interferograms. The phase has distinguishable characteristics only where there is enough signal intensity, whereas at the regions with no signal we get a noisy phase with no distinguishable features. The position of the HQV in the phase map is highlighted by circles. In σ^+ polarization, the phase rotates by 2π as one goes around the core. This behavior of the phase is clearly seen within an area of a few micrometers' size. In the same region for the σ^- polarization, there are no observable singularities and the phase is homogeneous. Figure 1, E and F, shows the phase as a function of the azimuthal angle as one goes around the core along the circles of different radii (shown by color). For the radius of 1μm, the phase changes monotonously in σ^+ polarization, decreasing by 2π as one makes a full round. Contrary to this, for the same radius in σ^- polarization, we observe a quasi-flat phase profile indicating the lack of any singularity. For larger radii, the phase dependence on the azimuthal angle becomes strongly nonlinear, whereas the total phase shift as one goes around the core remains -2π for one and 0 for the other polarization. Distortion of the phase profile at the large radii may be indicative of the existence of nearby regions with substantial vorticity but can also be indicative of formation of a string.

We note that the specific HQV shown in Fig. 1 is characterized by the winding numbers $(k,m) = \left(+\frac{1}{2},-\frac{1}{2}\right)$, while we have observed also the three remaining types of HQVs in different locations on the sample (*21*). On the basis of measurements we have done, we believe that four possible types of HQV are realized with approximately the same probability in our sample.

Using the same tomographic technique of spectrally resolved real space imaging as before, we then probed only the density of polaritons in the condensate state (Fig. 2, A and B). Locating the vortex in real space and looking at the density close to its core, we observed that a local minimum for one polarization coincides with a maximum for the other one, as Fig. 2, C and D shows. The widths of these minima-maxima coincide with the theoretical vortex core size a. This behavior is another signature of HQVs, as one can see from Eq. 3. The theory (*12*) predicted that at the center of the HQV the condensate should be fully circularly polarized, and this is exactly what we observe in Fig. 2, C and D).

The HQV we observed here are pinned by the disorder to specific locations on the sample. This is confirmed by the behavior of the interferometric images as a function of the pumping power. Increasing the excitation intensity, we modify the effective disorder potential acting upon the polariton condensate by changing the polariton-polariton repulsion strength. When the pumping is strong, we screen the disorder potential so that HQV get unpinned and disappear from the interferometry image of a specific spot on the sample. This is what we observed at the excitation power exceeding the threshold pumping by a factor of 4.5. Above this power, the forklike dislocation in σ^+ polarization disappears (*21*).

The stationary disorder fixes the winding numbers of the pinned vortices, so that repeating the experiment we find HQVs with the same winding numbers in the same locations. This is also true for the integer vortices. Handedness of each pinned vortex is dependent on the direction of polariton fluxes propagating in the disorder landscape during formation of the condensate, as the modeling based on the Gross-Pitaevskii equation showed (*4*, *26*).

This experimental work provides direct evidence of half-quantum vortices in a spinor condensate, by means of polarization-resolved interferometry, phase imaging, and spectrally resolved real space density imaging.

References and Notes

1. L. P. Pitaevskii, S. Stringari, *Bose-Einstein Condensation* (Clarendon Press, Oxford, 2003)
2. R. J. Donnelly, *Quantized Vortices in Helium II* (Cambridge Univ. Press, Cambridge, England, 1991).
3. M. R. Matthews *et al.*, *Phys. Rev. Lett.* **83**, 2498 (1999).
4. K. G. Lagoudakis *et al.*, *Nat. Physics* **4**, 706 (2008)
5. M. M. Salomaa, G. E. Volovik, *Rev. Mod. Phys.* **59**, 533 (1987).
6. G. E. Volovik, *The Universe in a Helium Droplet* (Clarendon Press, Oxford, 2003)
7. I. A. Luk'yanchuk, M. E. Zhitomirsky, *Supercond. Rev* **1**, 207 (1995)
8. M. Kato, Y. Niwa, K. Maki, *J. Phys. Conf. Ser.* **150**, 052103 (2009)
9. M. Yamashita *et al.*, *Phys. Rev. Lett.* **101**, 025302 (2008)
10. J. R. Kirtley *et al.*, *Phys. Rev. Lett.* **76**, 1336 (1996)
11. C. C. Tsuei, J. R. Kirtley, *Physica C* **367**, 1 (2002)
12. Y. G. Rubo, *Phys. Rev. Lett.* **99**, 106401 (2007)
13. A. V. Kavokin, J. J. Baumberg, G. Malpuech, F. P. Laussy, *Microcavities* (Oxford Univ. Press, Oxford 2007)
14. J. Kasprzak *et al.*, *Nature* **443**, 409 (2006)
15. R. Balili *et al.*, *Science* **316**, 1007 (2007).
16. S. Utsunomiya *et al.*, *Nat. Physics* **4**, 700 (2008)
17. A. Amo *et al.*, *Nature* **457**, 291 (2009)
18. M. R. Matthews *et al.*, *Phys. Rev. Lett.* **83**, 2498 (1999)
19. S. M. Girvin, A. H. MacDonald, in *Perspectives in Quantum Hall Effects*, S. Das Sarma, A. Pinczuk, Eds. (Wiley, New York, 1997), chap. 5.
20. H. A. Fertig, *Phys. Rev. Lett.* **89**, 035703 (2002)
21. Materials and methods are available as supporting material on *Science* Online
22. G. Panzarini *et al.*, *Phys. Rev. B* **59**, 5082 (1999)
23. J. Kasprzak *et al.*, *Phys. Rev. B* **75**, 045326 (2007)
24. Ł. Kłopotowski *et al.*, *Sol. St. Com.* **139**, 511 (2006)
25. G. Nardin *et al.*, *Appl. Phys. Lett.* **94**, 181103 (2009)
26. T. C. H. Liew, Y. G. Rubo, A. V. Kavokin, *Phys. Rev. Lett.* **101**, 187401 (2008)

27. We thank Le Si Dang for crucial remarks and detailed proofreading of this manuscript. We also thank T. C. H. Liew, M. Toledo Solano, M. Wouters, B. Pietka, Y. Leger, M. Richard, A. Baas, G. Nardin, D. N. Krizhanovskii, D. Sanvitto, P. G. Lagoudakis, and V. Savona for enlightening discussions. K.G.L. and B.D.-P. thank the Quantum Photonics–National Centre of Competence in Research for financial support through the Swiss National Science Foundation. A.V.K. and Y.G.R. thank the Engineering and Physical Sciences Research Council and the Dirección General de Asuntos del Personal Academico de la Universidad Nacional Autónoma de Mexico for support.

Supporting Online Material

www.sciencemag.org/cgi/content/full/326/5955/974/DC1
Materials and Methods
Figs. S1 to S9
References

19 June 2009; accepted 8 September 2009
10.1126/science.1177980

A Strain-Driven Morphotropic Phase Boundary in $BiFeO_3$

R. J. Zeches,[1]* M. D. Rossell,[2] J. X. Zhang,[1] A. J. Hatt,[3] Q. He,[4] C.-H. Yang,[4] A. Kumar,[5] C. H. Wang,[7] A. Melville,[5,6] C. Adamo,[5,6] G. Sheng,[5] Y.-H. Chu,[7] J. F. Ihlefeld,[5,6] R. Erni,[2] C. Ederer,[8] V. Gopalan,[5] L. Q. Chen,[5] D. G. Schlom,[6] N. A. Spaldin,[3] L. W. Martin,[9,10] R. Ramesh[1,4,9]

Piezoelectric materials, which convert mechanical to electrical energy and vice versa, are typically characterized by the intimate coexistence of two phases across a morphotropic phase boundary. Electrically switching one to the other yields large electromechanical coupling coefficients. Driven by global environmental concerns, there is currently a strong push to discover practical lead-free piezoelectrics for device engineering. Using a combination of epitaxial growth techniques in conjunction with theoretical approaches, we show the formation of a morphotropic phase boundary through epitaxial constraint in lead-free piezoelectric bismuth ferrite ($BiFeO_3$) films. Electric field–dependent studies show that a tetragonal-like phase can be reversibly converted into a rhombohedral-like phase, accompanied by measurable displacements of the surface, making this new lead-free system of interest for probe-based data storage and actuator applications.

Modern functional materials, for example ferromagnets and piezoelectrics, are typically chemically complex and exhibit the coexistence of multiple phases that evolve as a consequence of chemical alloying (*1*, *2*). In such materials, huge responses to external stimuli are often found at phase boundaries (*3*). In the past two decades, examples of the discovery of such behavior include the emergence of colossal magnetoresistance in doped manganites, high-temperature superconductivity in doped cuprates, and large piezoelectric responses in relaxor ferroelectrics (*4*). The large piezoelectric coefficients in $Pb(Zr_xTi_{1-x})O_3$ (PZT), $Pb(Mg_{0.33}Nb_{0.67})O_3$-$PbTiO_3$ (PMN-PT), and $Pb(Zn_{0.33}Nb_{0.67})O_3$-$PbTiO_3$ (PZN-PT) systems, for example, occur in compositions that lie at the boundary between two crystal structures, for example, a rhombohedral-to-tetragonal phase boundary (*5*–*8*). These giant piezoelectric responses have made PZT, PMN-PT, and PZN-PT the materials of choice for a variety of applications ranging from micropositioners to acoustic sensing in sonar. Notwithstanding the dramatic progress in the development of functional piezoelectric devices from these lead-based perovskites, two broad questions remain: (i) are there lead-free alternatives to the above-mentioned systems, and (ii) are there viable alternative pathways that are fundamentally different from the chemical alloying approaches (such as that seen in the PZT and PMN-PT systems) to achieve large piezoelectric responses? In this report, we demonstrate that epitaxial strain can be used to drive the formation of a morphotropic phase boundary and create large piezoelectric responses in lead-free ferroelectric materials.

$BiFeO_3$ (BFO) is a multiferroic perovskite that exhibits antiferromagnetism coupled with ferroelectric order (*9*, *10*). The structural stability of the parent rhombohedral phase of this material has been the focus of a number of theoretical studies (*11*, *12*). Although the parent ground state is a rhombohedrally distorted perovskite (*R3c*), a tetragonally distorted perovskite phase (*P4mm* symmetry, with in-plane lattice parameter a ~ 3.665 Å and out-of-plane lattice parameter c ~ 4.655 Å) with a large spontaneous polarization has been identified (*11*, *13*, *14*). We use the "T" notation in reference to a parent tetragonal phase with *P4mm* symmetry that has a c axis lattice parameter of ~4.65 Å and encompasses small monoclinic distortions from this tetragonal symmetry. Similarly, we use the "R" notation in reference to a distorted form of the *R3c* parent phase that has a c axis lattice parameter of ~4.0 Å. It has been established that that strain is particularly effective in altering the stable crystal structure of thin films where strains of several percent can be imparted through commensurate epitaxial growth on an underlying substrate (*15*). We show that epitaxial strain can be used to stabilize a tetragonal polymorph of BFO and that intermediate strains position BFO on a morphotropic phase transition between its T and R polymorphs.

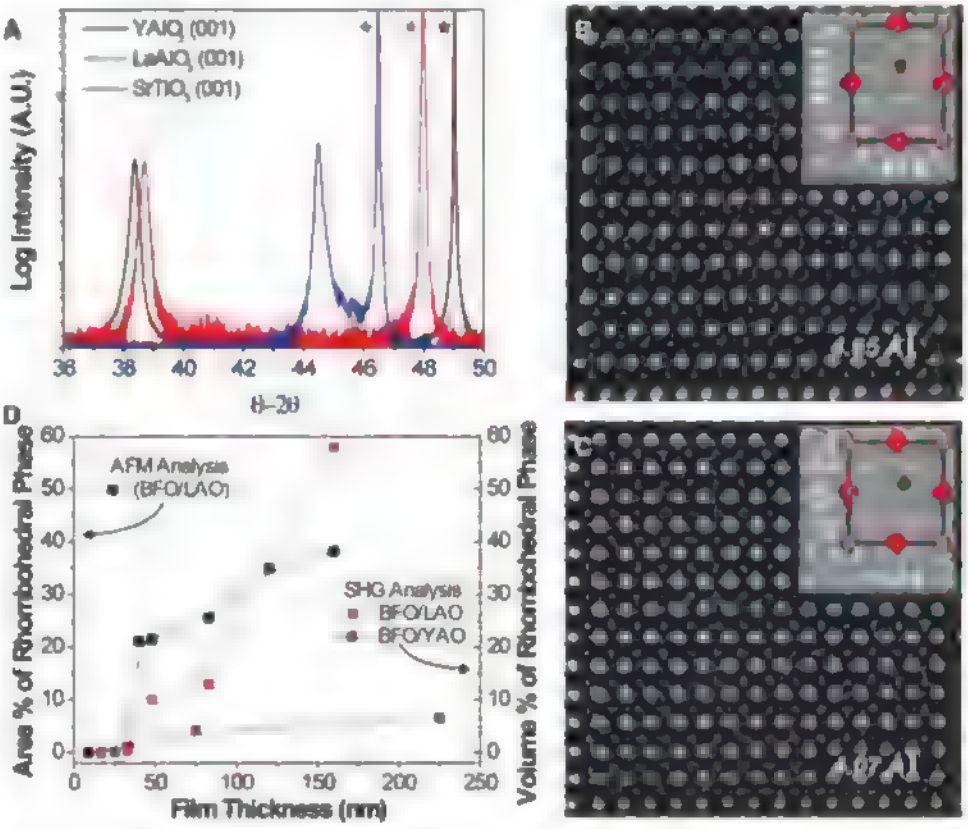

Fig. 1. (**A**) X-ray diffraction of the pseudocubic 002-diffraction peak of BFO/STO (001), BFO/LAO(001), and BFO/YAO(110) shows the presence of a long-axis T phase on both LAO and YAO substrates. Substrate peaks are marked with a star. (**B** and **C**) Atomic resolution STEM images of the T phase and the R phase, respectively. Insets show schematic illustration of the unit cell. (**D**) The evolution of the structure with thickness, including the area fraction (left axis) and the volume fraction of the R phase.

[1]Department of Materials Science and Engineering, University of California, Berkeley, Berkeley, CA 94720, USA. [2]National Center for Electron Microscopy, Lawrence Berkeley National Laboratory, Berkeley, CA 94720, USA. [3]Materials Department, University of California, Santa Barbara, Santa Barbara, CA 93106, USA. [4]Department of Physics, University of California, Berkeley, Berkeley, CA 94720, USA. [5]Department of Materials Science and Engineering, Pennsylvania State University, State College, PA 16802, USA. [6]Department of Materials Science and Engineering, Cornell University, Ithaca, NY 14853, USA. [7]Department of Materials Science and Engineering, National Chiao Tung University, HsinChu, Taiwan 30010. [8]School of Physics, Trinity College Dublin, College Green, Dublin 2, Ireland. [9]Materials Science Division, Lawrence Berkeley National Laboratory, Berkeley, CA 94720, USA. [10]Department of Materials Science and Engineering, University of Illinois, Urbana-Champaign, Urbana, IL 61822, USA.

*To whom correspondence should be addressed. E-mail: rzeches@berkeley.edu

After establishing the characteristics of the pure T polymorph, we show that the T and R phases can coexist on a length scale of tens of nanometers in films grown with intermediate strain and have huge piezoelectric responses.

We grew epitaxial BFO films using conventional molecular beam epitaxy (MBE) and laser-MBE on single-crystal substrates of (001) $LaAlO_3$ (LAO) (rhombohedral with a pseudocubic lattice parameter $a = 3.79$ Å) and (110) $YAlO_3$ (YAO) (orthorhombic with a pseudocubic lattice parameter $a = 3.69$ Å). Reference rhombohedral polymorphs of BFO were grown on (001) $SrTiO_3$ (STO) (cubic with lattice parameter $a = 3.905$ Å) substrates. For electrical and piezoresponse force microscopy (PFM) studies only, a 3- to 50-nm layer of epitaxial $La_{0.5}Sr_{0.5}CoO_3$ (LSCO) (a = 3.82 Å) or $La_{0.7}Sr_{0.3}MnO_3$ (LSMO) ($a = 3.85$ Å) was used as a bottom electrode. Detailed structural characterization was completed by a combination of x-ray diffraction, reciprocal space mapping, and scanning transmission electron microscopy based atomic imaging (TEAM 0.5 at the National Center for Electron Microscopy). Ferroelectric domains were imaged and switched using PFM as described previously (*16*). Local surface displacements were measured using high-resolution atomic force microscopy (AFM) as a function of applied DC field.

These measurements of the structural aspects of the T phase and its evolution with thickness were completed without a bottom electrode in order to understand the direct influence of epitaxial constraint on the phase evolution. Figure 1A shows a typical θ–2θ scan of BFO films grown on LAO, YAO, and STO substrates. The films grown on the reference STO substrate show the same monoclinically distorted rhombohedral structure that is established in the literature (*17*–*20*). In contrast, the films grown on LAO and YAO exhibit strong reflections at 2θ values corresponding to an out-of-plane lattice parameter of ~4.65 Å. Detailed reciprocal space mapping scans as a function of film thickness reveal a number of interesting aspects (*21*). First, for thinner films on LAO substrates (less than ~50 nm), we measure the in-plane lattice parameters to be $a \sim 3.84$ Å and $b \sim 3.76$ Å, respectively. (See fig. S1 for reciprocal space map data used to determine these lattice constants.) Second, we observe a monoclinic tilt of the structure with $\beta \sim 88.6°$. On the other hand, for thicker films (>50 nm) we observe the coexistence of the two phases. The insets of Fig. 1, B and C schematically describe the T and R phases discussed throughout this report.

The atomic structure of these two phases was imaged directly using the TEAM 0.5 transmission electron microscope (*21*). Atomic resolution high-angle annular dark-field scanning transmission electron microscopy (HAADF-STEM) images, also referred to as *Z*-contrast images, of these two different phases are shown in Fig. 1, B and C, respectively. Both images were acquired along the perovskite pseudocubic direction and exhibit atomic columns with two distinct intensities, with the Bi atom columns appearing brighter than the Fe atom columns. The strong atomic-number contrast of HAADF-STEM prevents the observation of the oxygen atomic columns next to the cation-containing columns (*22*). It is interesting to note that the small size of the aberration-corrected electron probe (~0.6 Å) used for the HAADF-STEM imaging and the high mechanical and electrical stability of the microscope employed allowed for resolving the displacement of the Fe atoms from the center of the unit cell defined by Bi rectangles. The electron diffraction patterns and the Fourier transforms in fig. S2, obtained from the images in Fig. 1, B and C, reveal clear differences between the symmetries of the T and R phases.

As the films are made thicker, we observe the emergence of the R phase that coexists with the T phase. The relative areal and volume fractions of these two phases as a function of film thickness are shown for films on both LAO and YAO substrates in Fig. 1D. Areal fractions were calculated from detailed high-resolution AFM studies of the surface, shown in fig. S3, while second harmonic generation (SHG) studies shown in fig. S4 give volumetric fractions (*21*). As expected, in the case of films grown on YAO (the substrate with the smallest lattice mismatch with the T phase), we observe that the film remains essentially tetragonal-like for the range of thicknesses studied. In contrast, films grown on LAO show a distinct evolution of the phase mixture due to relaxation of the epitaxial strain with increased thickness.

Let us now turn our attention to understanding the atomic structure of this morphotropic phase boundary-like interface in the mixed phase. High-resolution AFM images (Fig. 2A) show a characteristic striped contrast that we attribute to the mixed phase. From such images, the spacing of the stripes is measured to be ~30 to 50 nm, with a peak-to-valley height difference of 1 to 2 nm (Fig. 2B). We then carried out low- and high-resolution transmission electron microscopy (TEM) studies of this mixed phase region. Figure 2C shows a typical low-magnification TEM image of the portion of the sample that exhibits the striped contrast. The spacing of the stripes in this image is commensurate with that obtained in the AFM image, that is, 30 to 50 nm. Higher-resolution atomic imaging (carried out on the TEAM 0.5 microscope) reveals the structural details of this mixed phase (Fig. 2D), in which the T phase is inter-

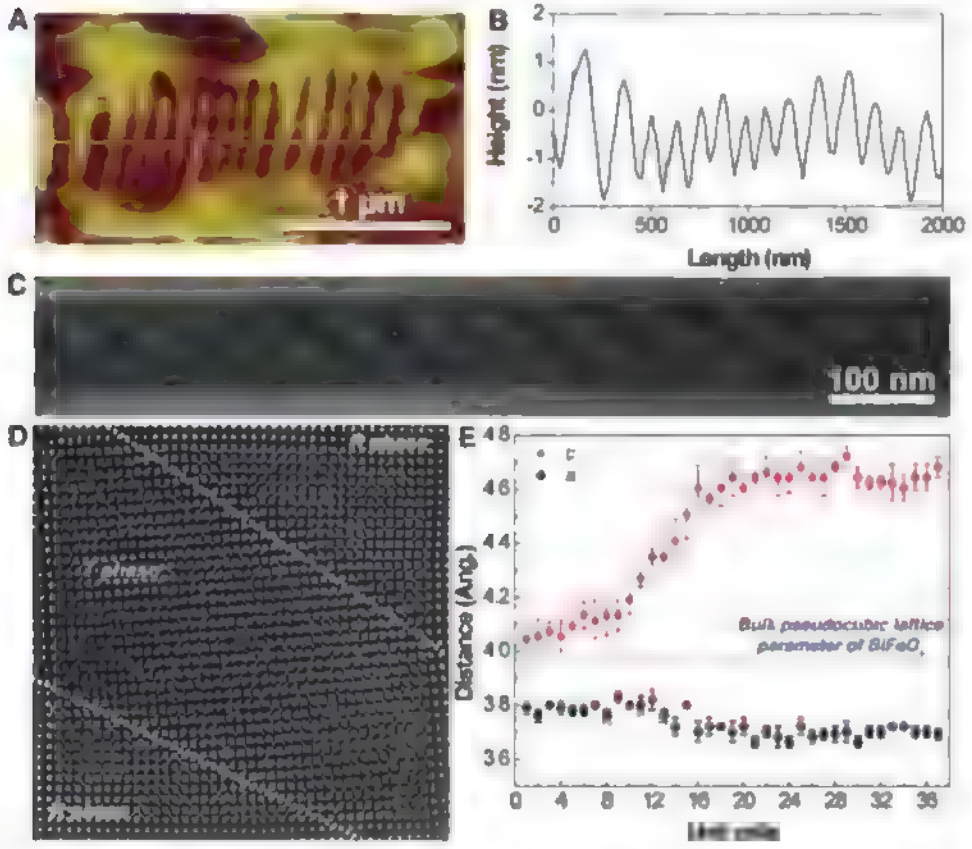

Fig. 2. (**A**) High-resolution AFM image of a mixed phase region. (**B**) Corresponding line trace at white line in (A) demonstrates ~2- to 3-nm height changes going from the T (bright) to R (dark) phase. (**C**) Low-resolution cross-sectional TEM image of a mixed phase region in an 85-nm-thick BFO/LAO film. Here, the light areas correspond to the T phase and the dark areas to the R phase. (**D**) High-resolution TEM image of the boundaries between R and T regions, indicated by dashed lines. A smooth transition between phases is observed; no dislocations or defects are found at the interface. (**E**) Corresponding in-plane (*a*, black) and out-of-plane (*c*, red) lattice parameters (mean ± SD) demonstrate nearly a 13% change in the out-of-plane lattice parameter in just under 10 unit cells.

spersed between two R phase regions. The structure changes smoothly from the T phase to the R phase over a distance of ~10 unit cells, as shown in Fig. 2E. Specifically, the out-of-plane lattice parameter changes from 4.06 Å in the R phase to 4.65 Å in the T phase without the insertion of misfit dislocations. The in-plane lattice parameter is constrained by the substrate lattice parameter and changes slightly (from ~3.8 Å in the R phase to ~3.7 Å in the T phase). Thus, the *c*/*a* ratio changes from 1.07 for the R phase to 1.27 in the T phase in just over 10 unit cells.

To understand the observed coexistence of T and R phases, we performed density functional calculations within the local density approximation plus the Hubbard parameter U (LDA+U) approximation ($U_{eff} = U - J = 2$ eV), using the projector augmented wave (PAW) method as implemented in the Vienna ab initio simulation package (VASP) (*23*, *24*). We use a monoclinic 10-atom unit cell, which allows the structure to continuously change from the rhombohedral *R3c* symmetry of bulk BFO to the *P4mm* tetragonal symmetry studied in earlier theoretical work (*11*). We employ a 5 by 5 by 5 k-point sampling and a plane wave energy cut-off of 550 eV, and assume the G-type antiferromagnetic ordering of bulk BFO. To simulate the effect of epitaxial strain, we constrain the unit cell lattice vectors in the pseudocubic (001) plane and relax the out-of-plane cell parameter and all internal coordinates by minimizing the Hellman-Feynman forces to a tolerance of 0.005 eV/Å. The internal coordinates are initialized corresponding to monoclinic *Cc* symmetry. The results for compressive strain are shown in Fig. 3, A and B. Strains are given relative to the LDA+U equilibrium lattice parameter $a = 3.89$ Å of bulk *R3c* BFO.

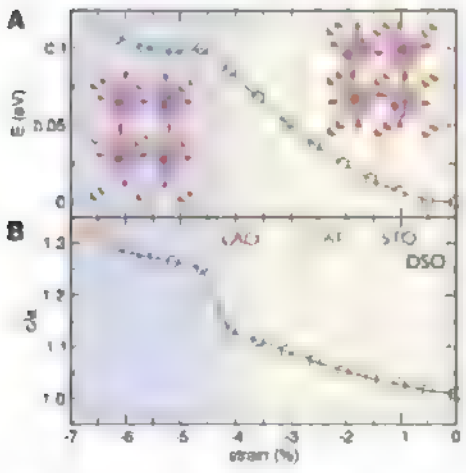

Fig. 3. (**A**) Evolution of the energy of the BFO structure as a function of in-plane strain. (**B**) Evolution of the *c*/*a* lattice parameter ratio as a function of strain for BFO. These data show the presence of two phases—both with monoclinic symmetry—the long-axis T phase (left) and the short-axis R phase. The lattice mismatches between a number of commonly used and tested oxide substrates are shown as dashed lines.

We find that for a compressive strain, around 4.5% BFO undergoes a strain-induced iso-symmetric structural transformation (*25*) that is accompanied by an abrupt increase in *c*/*a* ratio (Fig. 3B). Although the structures on both sides of this transition have the same monoclinic symmetry (*Cc*), there is a distinct change in the ionic coordinates from a distorted version of the rhombohedral bulk structure (with octahedral coordination of the Fe^{3+} cation) to a structure with essentially five-fold coordination of the Fe cation, resembling the "super-tetragonal" structure observed for $PbVO_3$ and $BiCoO_3$ (*26*, *27*) but with additional tilting of the oxygen polyhedra (see insets in Fig. 3A). The energy versus strain curve (Fig. 3A) shows a maximum separating the two lower-energy phases at around 4.5% strain, suggesting that films strained to this critical value may lower their energy by spontaneously phase-separating into the T and R phases. In this case, the two phases have in-plane lattice parameters that are smaller and larger, respectively, than that of the substrate, allowing for phase-separation without an overall change of in-plane film dimensions. Films grown at higher strain values will be in the metastable tetragonal-like phase energy minimum and are not expected to phase separate. We have investigated this experimentally by studying the evolution of the BFO films on a wide range of substrates, including (110) $DyScO_3$ (DSO) ($a = 3.94$ Å), STO ($a = 3.905$ Å), (001) $(LaAlO_3)_{0.3}(SrAl_{0.5}Ta_{0.5}O_3)_{0.7}$ (LSAT) ($a = 3.87$ Å), LAO ($a = 3.79$ Å), and YAO ($a = 3.69$ Å) (all lattice parameters reported here are the cubic or pseudocubic values, and the lattice mismatch of the various substrates relative to bulk BFO is shown in Fig. 3, A and B). These studies show that BFO films on YAO consist entirely of the T phase for film thicknesses up to ~220 nm, whereas films on LAO are mixed T and R phases, and films on LSAT, STO, and DSO are rhombohedral-like in nature, consistent with the theoretical predictions in Fig. 3. Phase field calculations of the strain-driven morphotropic phase boundary, shown in fig. S5, confirm the conclusions from ab initio calculations. They also reveal the existence of the two-phase region between the tetragonal-like and rhombohedral-like phases and show the persistence of this two-phase region at finite temperature.

We probe the surface displacements and piezoelectric properties on a local scale using AFM and PFM, and we focus here on samples that exhibit a mixed T and R phase structure. An overview of the piezoelectric switching behavior for such a sample is shown in fig. S6. The AFM image (fig. S6A) shows two major topographical features: bright plateaus that we interpret to arise from the T phase and areas of stripe-like contrast that we interpret to arise from mixed T and R regions. The corresponding out-of-plane (fig. S6B) and in-plane (fig. S6C) PFM images show that there is an out-of-plane switching of the polarization upon application of an electric field, and the in-plane image shows no change in contrast, consistent with the idea that the polarization vector is primarily perpendicular to the sample surface.

We now focus on the details of the piezoelectric behavior of an 85-nm-thick mixed T and R phase sample. We have measured the normalized relative surface displacement of a local poled area as a function of electric field applied to the scanning probe tip (Fig. 4A). (Fig. S8 shows in-plane and out-of-plane PFM data corresponding to Fig. 4, B to E.) These measurements were repeated at five locations on each of five different samples to ensure repeatability. The relative displacements were measured by comparing the average height within the switched area to the entire scanned area outside the switched area. These relative displacements were then converted to strain values. The data in this figure present several interesting features: first is the observation of a "butterfly-loop," which is typical of the strain versus field behavior that is commonly observed in piezoelectrics. At the highest fields (both positive and negative polarity), the relative deformation

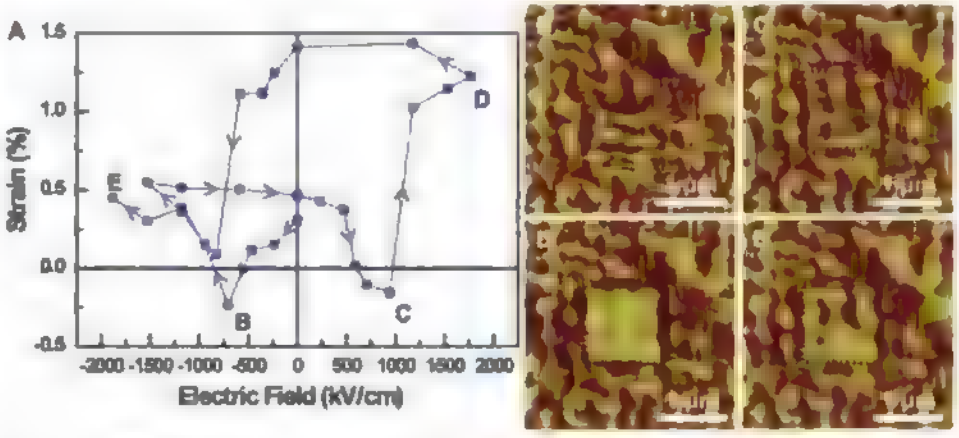

Fig. 4. (**A**) Electric field induced changes in surface displacement, here represented as strains, show a classic "butterfly" loop structure. Corresponding AFM images at (**B**) −1880 kV/cm, (**C**) −705 kV/cm, (**D**) 1760 kV/cm, and (**E**) 941 kV/cm are shown. At the extremes of applied voltage, a clear, single contrast is observed in the switched box corresponding to the presence of the tetragonal phase. A dashed line indicates the area that was subjected to the electric field.

is the highest; this corresponds to an essentially single-domain, tetragonal-like state of the sample, as exemplified by the uniform image contrast in the AFM images (Fig. 4, D and E). In contrast, at the lowest value of relative displacement, the AFM images (Fig. 4, B and C) show clear signatures of stripe-like image contrast, indicative of a mixed state. As shown in fig. S7, we have been able to reversibly switch it through the states shown in Fig. 4, B to D. We note that the absolute value of the local surface displacement is ~1 to 2 nm per 85 nm of film thickness. This corresponds to an effective strain of 1.2 to 2.4%, which is of the same order of magnitude as the highest strains reported for the relaxor ferroelectrics. These relatively large and nonvolatile changes in surface displacements make this an attractive system for use in nanoscale data storage elements (such as probe-based data storage) and microscale actuators (*28*).

Our experimental and theoretical studies have revealed the ability of the BFO system to morph into allotropic modifications. These forms are stabilized through the epitaxial strain imposed by the substrate. Of particular interest from the piezoelectrics point of view is the mixed phase state of the films. The ability to reversibly convert the T phase to a mixture of T and R phases through the application of an electric field suggests a close resemblance to other well-known piezoelectrics such as the morphotropic phase boundary compositions in the PZT family and the PMN-PT family. Our observations support the notion that such strain-driven phase evolution is a generic feature, akin to chemically driven phase changes that are now well established in the manganites, cuprates, and relaxors. Furthermore, the observation of the strain-driven phase changes in BFO should motivate a search for similar control in other related perovskite systems. Furthermore, this reversible interconversion is accompanied by substantial changes in the height of the sample surface (a few nanometers), thus making this potentially attractive for AFM probe-based data storage applications.

References and Notes

1. P. Groth, *Ann. Phys. Chem.* **217**, 31 (1870)
2. V. M. Goldschmidt, *Trans. Faraday Soc.* **25**, 253 (1929)
3. R. E. Newnham, *Mater. Res. Soc. Bull.* **22**, 20 (1997)
4. E. Dagotto, *Nanoscale Phase Separation and Colossal Magnetoresistance*, (Springer Verlag, New York, 2003)
5. S. E. Park, T. R. Shrout, *J. Appl. Phys.* **82**, 1804 (1997)
6. R. Guo *et al.*, *Phys. Rev. Lett.* **84**, 5423 (2000)
7. H. Fu, R. E. Cohen, *Nature* **403**, 281 (2000)
8. M. Ahart *et al.*, *Nature* **451**, 545 (2008)
9. W. Eerenstein, N. D. Mathur, J. F. Scott, *Nature* **442**, 759 (2006)
10. R. Ramesh, N. A. Spaldin, *Nat. Mater.* **6**, 21 (2007)
11. C. Ederer, N. A. Spaldin, *Phys. Rev. Lett.* **95**, 257601 (2005)
12. P. Ravindran, R. Vidya, A. Kjekshus, H. Fjellvåg, *Phys. Rev. B* **74**, 224412 (2006)
13. D. Rioński, K.-Y. Yun, M. Okuyama, *J. Phys. Condens. Matter* **18**, 197 (2006)
14. H. Béa *et al.*, *Phys. Rev. Lett.* **102**, 217603 (2009)
15. D. G. Schlom *et al.*, *Annu. Rev. Mater. Res.* **37**, 589 (2007)
16. F. Zavaliche *et al.*, *Phase Transit.* **79**, 991 (2006)
17. G. Xu *et al.*, *Appl. Phys. Lett.* **86**, 182905 (2005)
18. Y. H. Chu *et al.*, *Appl. Phys. Lett.* **90**, 252906 (2007)
19. H. Béa *et al.*, *Phys. Rev. B* **74**, 020101 (2006)
20. K. Y. Yun *et al.*, *J. Appl. Phys.* **96**, 3399 (2004)
21. Materials and methods are available as supporting material on *Science* Online
22. M. F. Chisholm *et al.*, *Microsc. Microanal.* **10**, 256 (2004)
23. G. Kresse, J. Furthmüller, *Phys. Rev. B* **54**, 11169 (1996)
24. V. I. Anisimov, F. Aryasetiawan, A. I. Liechtenstein, *J. Phys. Condens. Matter* **9**, 767 (1997)
25. A. G. Christy, *Acta Crystallogr. B* **51**, 753 (1995)
26. R. V. Shpanchenko *et al.*, *Chem. Mater.* **16**, 3267 (2004)
27. A. A. Belik *et al.*, *Chem. Mater.* **18**, 798 (2006)
28. S. Hong, Ed., *Nanoscale Phenomena in Ferroelectric Thin Films* (Kluwer Academic Publishing, Boston, MA, 2004)

29. The work at Berkeley is supported by the Director, Office of Science, Office of Basic Energy Sciences, Materials Sciences Division of the U.S. Department of Energy under contract DE-AC02-05CH11231. The authors from Berkeley acknowledge the support of the National Center for Electron Microscopy, Lawrence Berkeley National Laboratory. Y.H.C. also acknowledges the support of the National Science Council, R.O.C., under contract NSC 98-2119-M-009-016. V.G. and D.G.S. acknowledge support from National Science Foundation grants DMR-0820404 and DMR-0507146. A.H. and N.S. acknowledge support from the National Science Foundation under DMR-0820404 and NIRT-0609377. Theoretical work used the SGI Altix [Cobalt] system and the TeraGrid Linux Cluster [Mercury] at the National Center for Supercomputing Applications under grant DMR-090420. C.E. acknowledges support from the Science Foundation of Ireland (grant SFI-07/YI2/I051). The work of G.S. and L.Q.C. is supported by Department of Energy Basic Sciences under contract DE-FG02-07ER46417

Supporting Online Material

www.sciencemag.org/cgi/content/full/326/5955/977/DC1
Materials and Methods
Figs. S1 to S8
References

29 May 2009; accepted 1 September 2009
10.1126/science.1177046

Observation of the Role of Subcritical Nuclei in Crystallization of a Glassy Solid

Bong-Sub Lee,[1,2] Geoffrey W. Burr,[3] Robert M. Shelby,[3] Simone Raoux,[3]* Charles T. Rettner,[3] Stephanie N. Bogle,[1,2] Kristof Darmawikarta,[1,2] Stephen G. Bishop,[2,4] John R. Abelson[1,2]†

Phase transformation generally begins with nucleation, in which a small aggregate of atoms organizes into a different structural symmetry. The thermodynamic driving forces and kinetic rates have been predicted by classical nucleation theory, but observation of nanometer-scale nuclei has not been possible, except on exposed surfaces. We used a statistical technique called fluctuation transmission electron microscopy to detect nuclei embedded in a glassy solid, and we used a laser pump-probe technique to determine the role of these nuclei in crystallization. This study provides a convincing proof of the time- and temperature-dependent development of nuclei, information that will play a critical role in the development of advanced materials for phase-change memories.

The phase transformation of a material often starts with the formation of nanometer-sized volumes of the new phase, nuclei, which then grow in size. The nucleation process has been described by classical theory (*1*–*3*), in which the thermodynamic free energy is reduced by the phase transformation, whereas the formation of a nucleus involves an energy penalty associated with the boundary region between the phases, particularly when atomic bonds are broken or strained. This interplay between volume and surface effects results in a critical nucleus size. For a subcritical nucleus, the energy rises as atoms are added to the new configuration; for a supercritical nucleus, the energy falls, because the energy reduction by phase transformation is now greater than the surface penalty. As thermal fluctuations induce atoms to join or leave each subcritical nucleus, a size distribution of subcritical nuclei develops in the material. Only a minute fraction of subcritical nuclei achieve the critical size (n_c) and continue to grow into a crystalline grain that is large enough to be detected by conventional analyses.

However, very few experimental studies have provided quantitative information on the distribution of nanoscale subcritical nuclei that develops before the observable phase transformation. Data are available only in very special cases, such as heteroepitaxial film growth where the nuclei are exposed on a flat surface (*4*, *5*). On the micron length scale, nuclei and their behaviors can be observed in the agglomeration of colloidal particles in liquids (*6*, *7*). The general case, such as crystallization from nanometer-scale nuclei that are embedded in the parent glassy phase,

[1]Department of Materials Science and Engineering, University of Illinois at Urbana-Champaign (UIUC), Urbana, IL 61801, USA. [2]Coordinated Science Laboratory, University of Illinois at Urbana-Champaign, Urbana, IL 61801, USA. [3]IBM/Macronix Phase Change Random Access Memory Joint Project, IBM Almaden Research Center, San Jose, CA 95120, USA. [4]Department of Electrical and Computer Engineering, University of Illinois at Urbana-Champaign, Urbana, IL 61801, USA.

*Present address: IBM T. J. Watson Research Center, Yorktown Heights, NY 10598, USA.
†To whom correspondence should be addressed. E-mail: abelson@illinois.edu.

offers substantial experimental challenges. X-ray diffraction fails to show the presence of these nuclei in the amorphous material, and the interpretation of image contrast in high-resolution transmission electron microscopy (TEM) has been shown to be unreliable for embedded objects smaller than ~3 nm (*8*, *9*).

This study combines a kinetic measurement, structural probe, and numerical simulation to reveal the presence of nanoscale subcritical nuclei in a glassy solid and their role in crystallization. For the detection of nuclei, we discover that a statistical technique, fluctuation TEM (FTEM), is a powerful tool. FTEM was originally devised to analyze topological order on the length scale of 1 to 4 nm, with spatial correlations beyond the nearest neighbor often called medium range order (*10*). In FTEM, hundreds of nanodiffraction patterns are obtained in a scanning transmission electron microscope and analyzed in terms of the scattering variance $V(k)$, where k is the scattering vector (*11*). It has been proven that this variance is mathematically related to a sum over three- and four-atom correlations in the material (*9*, *12*), enabling the study of medium range order. Simulations with computational model structures (*9*, *12*–*14*) have shown that one way to generate a realistic variance signal is by mixing ordered regions (e.g., crystalline nuclei) of a specified size and volume fraction in the parent random-network matrix. No alternative models have been identified yet, and the present study experimentally confirms the validity of the interpretation based on subcritical nuclei.

We find that Ag/In-incorporated Sb_2Te [known as AIST, technologically important for phase-change data storage (*15*, *16*)] provides a nearly ideal system for the purpose of this study. We can systematically modify the population of subcritical nuclei embedded in amorphous AIST with the use of low-temperature thermal annealing or short laser pulses. The effect of such a pretreatment is not detectable in conventional diffraction measurements but is evidenced as follows: (i) We use a laser pump-probe technique to measure the time required for nucleation (the formation of a supercritical nucleus) and find significant enhancement or suppression of this nucleation time by pretreatment. (ii) We use FTEM to measure changes in the nanoscale structural order within the sample, and we show that these changes are consistent with the laser data. Finally, (iii) we simulate the kinetic process by which the size distribution of subcritical nuclei evolves, and we show that it is in good agreement with (i) and (ii).

To induce and monitor the crystallization process, we used a laser pump-probe technique (*11*, *17*, *18*). A focused pump laser heats a thin-film sample of amorphous AIST with specified power and duration, whereas a low-power probe laser monitors the optical reflectivity in real time during the process (Fig. 1A). Thermal simulations show that any particular portion of the irradiated area reaches a constant temperature in only ~10 ns and also that the area cools in ~10 ns after the laser is turned off (fig. S1A). Because the beam intensity has a Gaussian spatial profile, the temperature is substantially higher at the center than at the edges of the spot. When held at an intermediate temperature for a sufficient length of time, in this case under a pump laser of 40 to 60 mW ($1/e^2$ diameter = 2 μm) for more than 80 μs, the amorphous state crystallizes. This crystallization process can be detected in real time with the use of the probe laser, because

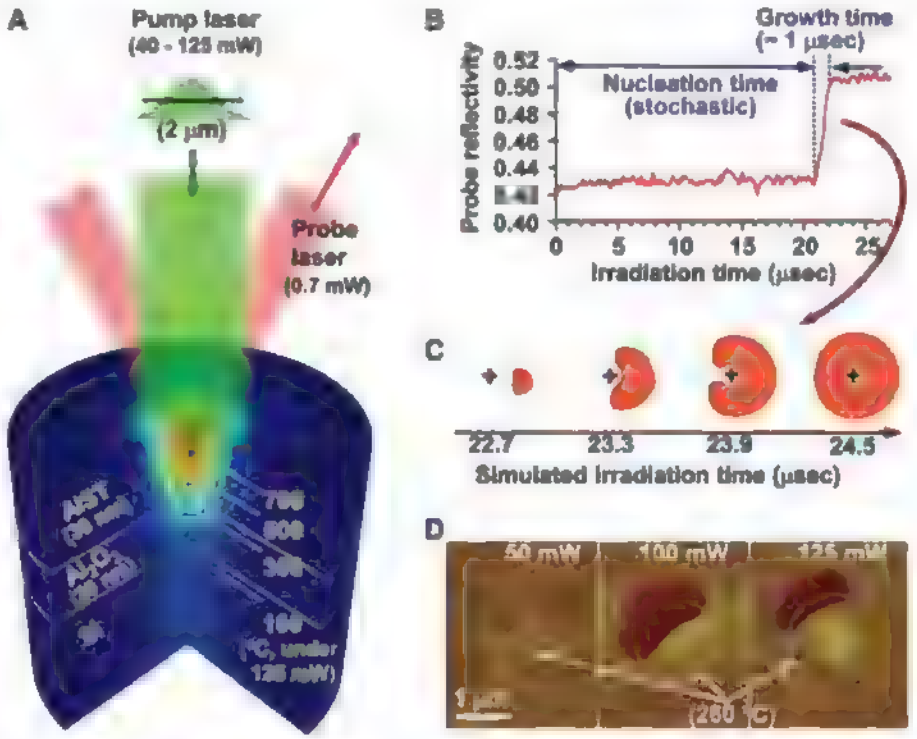

Fig. 1. Pump-probe laser analysis of nucleation in amorphous AIST (Ag/In-incorporated Sb_2Te). (**A**) Experimental setup with a pump laser for heating and a probe laser (normal incidence in the real setup) for monitoring reflectivity in situ. The simulated steady-state temperature distribution under a Gaussian pump laser of 125 mW is inscribed. (**B**) Typical change in reflectivity that accompanies the laser crystallization of AIST, showing the time before a single supercritical nucleus appears, followed by rapid growth across the irradiated area, which increases the reflectivity. (**C**) Plan-view snapshots of simulated laser crystallization, in which the center temperature is near the melting point. (**D**) AFM images obtained after interrupted crystallization (dark contrast), where the pump laser was turned off after nucleation but before full crystallization. Laser crystallization of AIST proceeds from a single nucleus, which develops near an optimal temperature $T_0 \sim 260$°C (dotted circles).

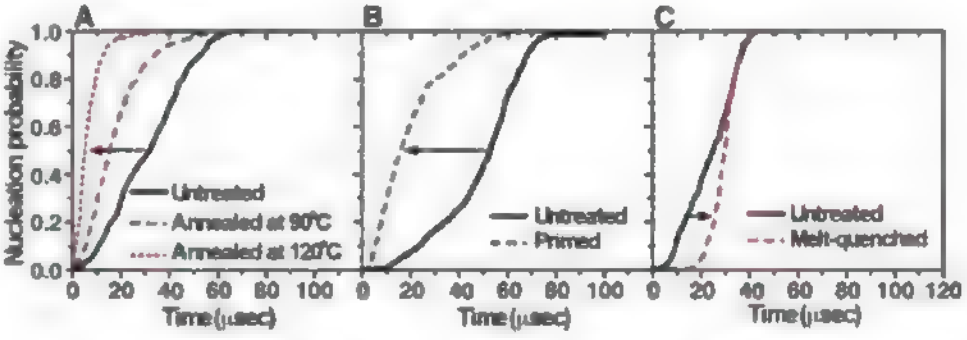

Fig. 2. Cumulative probability that nucleation occurs within a given time in AIST under pump laser. (**A**) Effect of low-temperature annealing. The nucleation time from a pre-annealed amorphous state is shorter than that from an untreated state (pump-laser power = 50 mW in these cases; the result was nearly insensitive to the choice of laser power between 40 and 60 mW). (**B**) Effect of laser priming. A short prepulse (1 μs, 60 mW) does not induce crystallization, but, from such a primed area, nucleation generally occurs in a shorter time under the next pulse with the same power. (**C**) Effect of melt quenching. From a melt-quenched amorphous area produced by an intense prepulse (122 mW), nucleation occurs in a slightly longer time under the next pulse (40 mW) (*11*). The change in nucleation time originates from the modification of subcritical nuclei population by pretreatment, as proven by FTEM (Fig. 4) and supported by simulation (Fig. 3).

the crystalline phase has a higher optical reflectivity (by ~20% in the layered structure used here). Under a high laser power (~120 mW), the center of the spot exceeds the AIST melting temperature of 544°C (*19*). When the laser is turned off, the cooling time is sufficiently short to transform the liquid into the melt-quenched amorphous state.

The laser-induced crystallization of an irradiated area typically results from the formation—after an incubation delay (nucleation time)—of a single supercritical nucleus, which then rapidly grows across the entire hot zone (*17*). The nucleation time is measured via the reflectivity (Fig. 1B). The solid amorphous state attempts to create the first supercritical nucleus for many microseconds (constant reflectivity) and, after one supercritical nucleus forms, the crystallization front spreads across the irradiated area in only ~1 μs (rapid increase in reflectivity). The nucleation time may range from 5 to 60 μs in laser spots obtained on a single sample, which demonstrates the stochastic nature of nucleation. Figure 1C shows simulated plan-view snapshots (*11*) that illustrate the growth of a supercritical nucleus from an irradiated area; the center temperature is near the melting point in this case. Images similar to those in Fig. 1C can be experimentally obtained. Crystallization results in a ~5% volume contraction, and a crystallized area (if larger than tens of nanometers in lateral extent) can be detected via the associated thickness change in an atomic force microscopy (AFM) image [(*20*, *21*), also see fig. S2A]. If the pump beam happens to terminate after nucleation but before full crystallization, then the transformation process comes to a halt and leaves a partly crystallized region (interrupted crystallization). Figure 1D presents examples of such regions (dark contrast), which are approximately centered on the location of the single nucleus.

The location at which nucleation occurs within an irradiated spot demonstrates the existence of an optimal nucleation temperature T_0, as predicted by classical theory. At low temperatures, the thermodynamic driving force for crystallization (the free energy difference between the two phases) is large, but the kinetic rate of atomic rearrangements is small. At high temperatures, the rate of rearrangements is large, but the driving force is small (that is, the critical nucleus size is large and difficult to attain). The nucleation rate reaches a sharp maximum at an intermediate temperature T_0 (*2*, *22*). Our numerical simulation of the nucleation process in AIST (*11*) suggests a maximum rate at ~260°C. In every case where interrupted crystallization was observed, the originating nucleus was located not far from the annulus where the temperature was 260°C [shown as dotted circles on Fig. 1D according to our temperature calculations (*11*), also see fig. S1B].

Statistical analysis reveals that the nucleation time of AIST can be systematically modified by a thermal pretreatment. Figure 2 presents the cumulative probability that nucleation occurs within a given time. Each curve was obtained from 500 identical laser shots for ~100 μs applied to a set of neighboring areas on one sample (*11*) and represents the distribution of stochastic nucleation times measured, as in Fig. 1B. Thermal annealing in a furnace for 30 min at 90° or at 120°C does not induce crystallization, but the laser-crystallization time in such a pre-annealed sample is statistically shorter (Fig. 2A) (*17*). The time for 50% nucleation probability was reduced from 32 (untreated) to 5 μs (annealed at 120°C). Alternatively, the sample can be treated by a laser prepulse of the same power (e.g., 60 mW) that would eventually initiate crystallization, but of a duration (1 μs) shorter than the time required for the onset of crystallization. This pretreatment, referred to as laser priming (*23*), also reduces the crystallization time [from 53 to 16 μs (Fig. 2B)]. Thus, either long furnace annealing at low temperatures or short laser annealing at intermediate temperatures shortens the nucleation time. [In extreme cases where nucleation time was very much shortened, multiple supercritical nuclei could occur before full crystallization (fig. S2B).] On the other hand, a high-power (122-mW) prepulse can induce melt quenching. Figure 2C shows that the nucleation time from a melt-quenched amorphous region (30 μs for 50%) is somewhat longer than that from untreated regions on the same sample (25 μs). The nucleation time from the initial untreated states varies in different samples as shown by the continuous curves in Fig. 2, A to C (between 25 and 53 μs for 50%), due to variations in the sample preparation conditions. Regardless, the effects of pre-annealing, laser priming, and melt quenching have been confirmed in a consistent manner from at least four samples in each case.

The observation that nucleation times can be shortened or lengthened by a thermal pretreatment indicates the presence of metastable configurations in the amorphous material. Nucleation theory predicts that a size distribution of subcritical nuclei will develop and evolve according to the thermal history of the sample. To evaluate this, we employed a customized finite-difference simulation program (*24*), which models the stochastic evolution of subcritical nuclei via rate equations (*18*, *22*), as well as the propagation of crystalline growth fronts as a function of time and temperature distribution over a three-dimensional Cartesian mesh with more than 370,000 simulation grid-cells (*11*). This simulation models a collection of identical atoms, each representative of the weighted average constituent atom in $Ag_{5.5}In_{6.5}Sb_{65}Te_{29}$ (*19*); this is a reasonable approximation considering that the reported crystal structure of AIST is nearly identical to that of elemental antimony and also that the constituent atoms randomly occupy the atomic sites (*25*). A typical simulation (Fig. 1C) shows a satisfactory match to the experimental results. A supercritical nucleus forms after ~22 μs, then grows in ~2 μs. The distributions at 125°C (Fig. 3) report the total number of nuclei within the simulation volume of 3.5 μm by 3.5 μm by 30 nm. From a quasi-equilibrium state at 25°C, the distribution slowly shifts to a larger size, with the upper end (the maximum nucleus size) fluctuating by random attachment or detachment of atoms; the apparent small peaks at the upper end of the distribution are noise from this stochastic process. Supercritical nuclei may appear after tens of hours; they will then grow in size but at an extremely low rate. At high temperature under laser heating, the development of nuclei can occur in as little as 1 μs (priming), followed by nucleation and growth (crystallization of the spot). In phase-change memory devices, the difference between a stored "1" and "0" data bit is the presence (or absence) of a small amorphous region. Therefore, the development of nuclei as in Fig. 3 and subsequent crystallization of the amorphous region is a possible mechanism to lose the stored data (*26*); the kinetics is highly

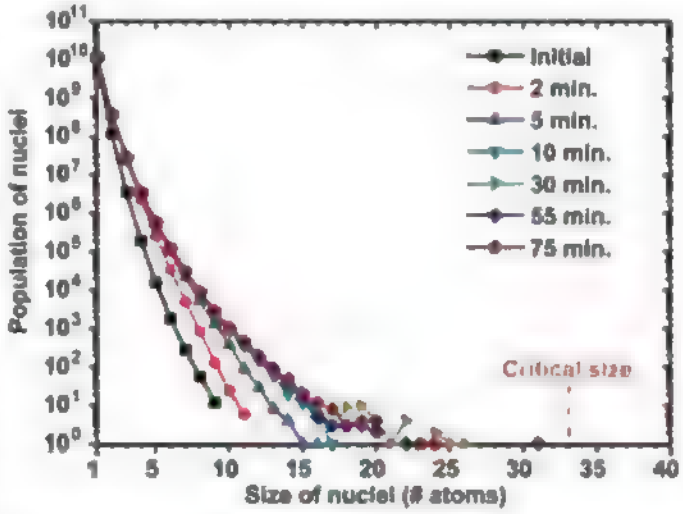

Fig. 3. Simulated evolution of nuclei size distribution in amorphous AIST at 125°C, which illustrates the effect of thermal pretreatment. The distribution of nuclei across a 3.5 μm by 3.5 μm by 30 nm volume of AIST is shown at various times after the simulated volume is instantaneously brought to 125°C. The initial nuclei distribution corresponds to the steady-state condition at 25°C. The total population of atoms not associated with clusters ($n = 1$) decreases slightly over time, from 1.20×10^{10} to 1.14×10^{10} after 5 min. At higher temperatures (e.g., by laser priming), such evolution occurs on a shorter time scale. From a pretreated sample, the time to generate a supercritical nucleus under laser irradiation is shorter.

dependent on the temperature at the working environment.

The experimentally measured distributions of nucleation time (Figs. 1B and 2, A to C) reveal the time necessary for the upper end of the initial distribution of subcritical nuclei to fluctuate until at least one nucleus exceeds n_c at the temperature established by the pump laser. The average nucleation time is shorter after pre-annealing or priming (Fig. 2, A and B), because the upper end of the size distribution has already been moved up from the room-temperature distribution. When the sample is melted, all nuclei are dissolved. During a short cooling time (~10 ns), a distribution of subcritical nuclei again forms but only reaches small sizes before it is kinetically frozen at room temperature. Thus, the nucleation time from the melt-quenched state of AIST may be similar to or even longer than that from the untreated state (Fig. 2C). It is reasonable that a distribution of subcritical nuclei forms in the untreated state as a result of fast particle bombardment or energy dissipation during the sputter-deposition process (*27*). [If the development of nuclei is substantial during cooling from melt, the melt-quenched state may exhibit a shorter nucleation time. Such a reduced nucleation time is observed for the composition $Ge_2Sb_2Te_5$ (*17*, *28*). In the extreme case of a bad glass-former, the material will fully crystallize during cooling.]

Although the average electron diffraction intensity is unaltered by the pretreatments (fig. S3), FTEM clearly demonstrates the structural differences between pretreated states. A membrane structure was designed to allow both laser pretreatment and FTEM analysis (*11*); an area showing interrupted crystallization (Fig. 4A) allows a precise comparison between different amorphous states. The center is in the melt-quenched amorphous state, the uncrystallized portion of the perimeter is in the primed (irradiated but not crystallized) state, and the regions well outside the laser irradiation remain in the untreated amorphous state. The FTEM data (Fig. 4B, obtained by statistical analysis of nanodiffraction patterns as in fig. S4) reveal substantially higher peak intensity (i.e., higher structural order) for the primed state. Similar trends of smaller magnitude are found when samples are subjected to furnace annealing (Fig. 4C). On the other hand, the signal (most importantly, the first peak at $k \sim 0.32$ Å^{-1}) is similar or slightly lower in the melt-quenched state. It is clear that the increase and decrease of FTEM peaks are consistent with the expected change of nuclei distribution. Annealing or priming shifts the distribution to larger sizes, whereas melt quenching leaves the material in a glassy state with a smaller or similar size distribution. [We previously observed similar annealing effects with $Ge_2Sb_2Te_5$ and AIST (*17*, *29*) but did not systematically relate them to nucleation theory.]

Although quantitative interpretation of FTEM data is complex, general principles are given by our simulation of the FTEM peak structure from a family of amorphous silicon models (*13*). The number of ordered regions mainly controls the magnitude of the FTEM peaks, whereas the mean size is related to the ratio in heights of the second and first peaks. The data in Fig. 4C then indicate mostly an increase in the number of such clusters, and the data from the primed state in Fig. 4B indicate a larger size of clusters in addition to the number. This interpretation is also supported by the data from the primed state, which is an extreme case: ~5% of the nanodiffraction patterns contain disc-type diffraction spots, which are produced by nuclei that are large enough to detect but did not grow under the laser irradiation (fig. S5). Patterns from all other amorphous states do not have such spots, and differences in the structural order can only be distinguished by FTEM. [The substrates of the samples shown in Figs. 2 and 4 are optimized for different purposes; consequently, they have different thermal and interfacial characteristics. The longer priming time (4.4 μs) and cooling time (~100 ns) of the sample in Fig. 4 may induce a higher density of nuclei in the laser-treated state.] Overall, FTEM provides direct evidence that the subcritical nuclei in amorphous AIST increase in size and number after either laser priming or furnace annealing, and they decrease slightly (or maintain) upon melt quenching.

The agreement shown in this work among laser crystallization time, theoretical modeling, and FTEM provides a strong form of proof for the predicted development of subcritical nuclei and their role in the crystallization process. This study establishes FTEM as a powerful method to detect the existence of nanometer-scale nuclei within glassy solids. Such a capability will be an important tool in the further study of the crystallization dynamics in a wide variety of glassy materials. For example, continued development of phase-change memory devices requires the materials to be neither too difficult to crystallize, because this would require excessive transformation power or time, nor too easy to crystallize, because this would compromise long-term data retention by the onset of unwanted crystallization.

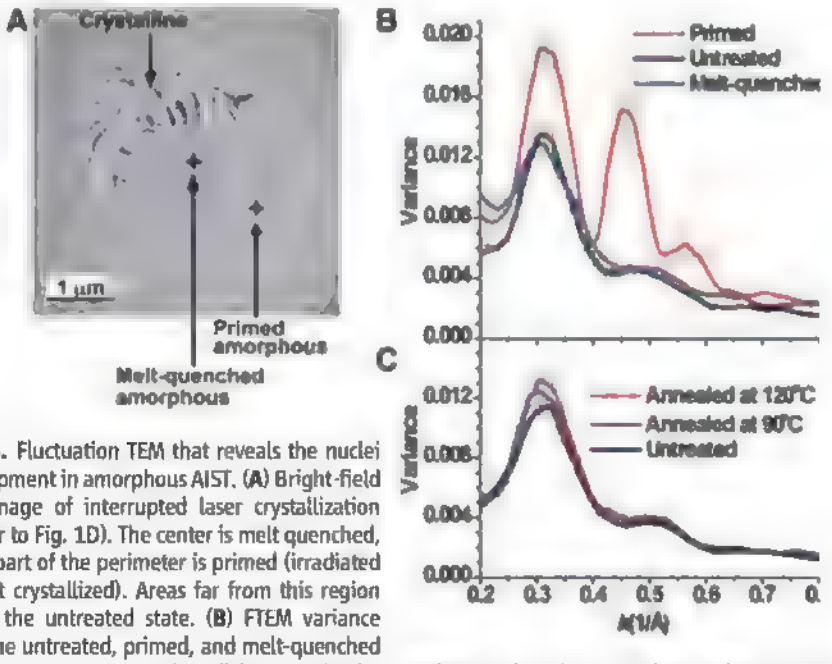

Fig. 4. Fluctuation TEM that reveals the nuclei development in amorphous AIST. (**A**) Bright-field TEM image of interrupted laser crystallization (similar to Fig. 1D). The center is melt quenched, and a part of the perimeter is primed (irradiated but not crystallized). Areas far from this region are in the untreated state. (**B**) FTEM variance from the untreated, primed, and melt-quenched amorphous states, revealing differences in the population of nuclei; error bars indicate 1 SD of the average (fig. S4). (**C**) FTEM variance showing the gradual change in nuclei concentration upon low-temperature annealing. Conventional diffraction techniques that use average diffraction intensity cannot distinguish these amorphous states.

References and Notes

1. J. W. Christian, *The Theory of Transformations in Metals and Alloys: An Advanced Textbook in Physical Metallurgy* (Pergamon, Oxford, ed. 2, 1975).
2. K. F. Kelton, in *Solid State Physics*, vol. 45, H. Ehrenreich, D. Turnbull., Eds. (Academic Press, New York, 1991), pp. 75–177.
3. D. Kashchiev, *Nucleation: Basic Theory with Applications* (Butterworth Heinemann, Oxford, 2000).
4. D. E. Jesson, M. Kastner, B. Voigtlander, *Phys. Rev. Lett.* **84**, 330 (2000).
5. I. Goldfarb, *Phys. Rev. Lett.* **95**, 025501 (2005).
6. U. Gasser, E. R. Weeks, A. Schofield, P. N. Pusey, D. A. Weitz, *Science* **292**, 258 (2001).
7. K.-Q. Zhang, X. Y. Liu, *Nature* **429**, 739 (2004).
8. O. L. Krivanek, P. H. Gaskell, A. Howie, *Nature* **262**, 454 (1976).
9. M. M. J. Treacy, J. M. Gibson, L. Fan, D. J. Paterson, I. McNulty, *Rep. Prog. Phys.* **68**, 2899 (2005).
10. M. M. J. Treacy, J. M. Gibson, *Acta Crystallogr. A* **52**, 212 (1996).
11. Materials and methods are available as supporting material on *Science* Online.
12. P. M. Voyles, J. R. Abelson, *Sol. Energy Mater. Sol. Cells* **78**, 85 (2003).
13. S. N. Bogle, P. M. Voyles, S. V. Khare, J. R. Abelson, *J. Phys. Condens. Matter* **19**, 455204 (2007).
14. J. Wen, Y. Q. Cheng, J. Q. Wang, E. Ma, *J. Appl. Phys.* **105**, 043519 (2009).
15. A. L. Greer, N. Mathur, *Nature* **437**, 1246 (2005).
16. M. Wuttig, N. Yamada, *Nat. Mater.* **6**, 824 (2007).
17. B.-S. Lee, thesis, University of Illinois at Urbana-Champaign (2006).
18. M. Salinga, thesis, RWTH, Aachen, Germany (2008).

19. J. Kalb, F. Spaepen, M. Wuttig, *J. Appl. Phys.* **93**, 2389 (2003).
20. J. Kalb, F. Spaepen, M. Wuttig, *Appl. Phys. Lett.* **84**, 5240 (2004).
21. S. Ziegler, M. Wuttig, *J. Appl. Phys.* **99**, 064907 (2006).
22. S. Senkader, C. D. Wright, *J. Appl. Phys.* **95**, 504 (2004).
23. J. H. Coombs, A. P. J. M. Jongenelis, W. van Es-Spiekman, B. A. J. Jacobs, *J. Appl. Phys.* **78**, 4906 (1995).
24. S. Raoux *et al.*, *IBM J. Res. Dev.* **52**, 465 (2008).
25. T. Matsunaga, Y. Umetani, N. Yamada, *Phys. Rev. B* **64**, 184116 (2001).
26. R. Bez, R. J. Gleixner, F. Pellizzer, A. Pirovano, G. Atwood, in *Phase Change Materials: Science and Applications*, S. Raoux, M. Wuttig, Eds. (Springer, New York, 2009), pp. 355–380.
27. A. N. Pargellis, *J. Vac. Sci. Technol. A* **7**, 27 (1989).
28. V. Weidenhof, I. Friedrich, S. Ziegler, M. Wuttig, *J. Appl. Phys.* **89**, 3168 (2001).
29. M. H. Kwon *et al.*, *Appl. Phys. Lett.* **90**, 021923 (2007).
30. We thank Y. Xiao, M. Jurich, Y.-C. Chen, M. Salinga, and M. Hitzbleck for their help with thin-film growth and thermal treatments. This material is based on work conducted under IBM-UIUC joint study agreement and is supported by NSF under awards DMR 04-12939 and DMR 07-06267. The FTEM technique was available thanks to collaborative support under award DMR 06-05890. FTEM, AFM, and thermal treatments were carried out, in part, in the Frederick Seitz Materials Research Laboratory Central Facilities, University of Illinois, which are partially supported by the U.S. Department of Energy under grants DE-FG02-07ER46453 and DE-FG02-07ER46471.

Supporting Online Material
www.sciencemag.org/cgi/content/full/326/5955/980/DC1
Materials and Methods
Figs. S1 to S5
References

9 June 2009; accepted 11 September 2009
10.1126/science.1177483

Partitioning Recent Greenland Mass Loss

Michiel van den Broeke,[1]* Jonathan Bamber,[2] Janneke Ettema,[1] Eric Rignot,[3,4] Ernst Schrama,[5] Willem Jan van de Berg,[1] Erik van Meijgaard,[6] Isabella Velicogna,[3,4] Bert Wouters[5,6]

Mass budget calculations, validated with satellite gravity observations [from the Gravity Recovery and Climate Experiment (GRACE) satellites], enable us to quantify the individual components of recent Greenland mass loss. The total 2000–2008 mass loss of ~1500 gigatons, equivalent to 0.46 millimeters per year of global sea level rise, is equally split between surface processes (runoff and precipitation) and ice dynamics. Without the moderating effects of increased snowfall and refreezing, post-1996 Greenland ice sheet mass losses would have been 100% higher. Since 2006, high summer melt rates have increased Greenland ice sheet mass loss to 273 gigatons per year (0.75 millimeters per year of equivalent sea level rise). The seasonal cycle in surface mass balance fully accounts for detrended GRACE mass variations, confirming insignificant subannual variation in ice sheet discharge.

There are strong indications that mass loss from the Greenland ice sheet (GrIS) has recently accelerated (*1*–*3*) after atmospheric warming and increased runoff (*4*, *5*) and increased ice discharge through the acceleration of outlet glaciers in the west (*6*, *7*) and east (*8*–*11*). Recently reported GrIS mass balance (*12*) varies from near-balance (*13*) to modest mass losses [47 to 97 gigatons (Gt) year^{-1}] (*14*) in the 1990s, increasing to a mass loss of 267 ± 38 Gt year^{-1} in 2007 (*15*). These mass losses are equivalent to a global sea level rise (SLR) of 0.13 to 0.74 mm year^{-1} or 4 to 23% of the SLR of 3.1 ± 0.7 mm year^{-1} reported for the period 1993–2005 (*16*).

Here we present consistent 2003–2008 GrIS mass loss rates produced by two fully independent methods: The mass budget method, which quantifies the individual components of ice sheet mass balance [surface mass balance (SMB) and ice discharge (D)], is validated with data from the Gravity Recovery and Climate Experiment (GRACE) satellites, which observe ice sheet mass anomalies by repeat satellite gravimetry. This combination of results enables us to resolve the individual components of recent GrIS mass loss in space and time.

For SMB, we used the monthly output of a 51-year climate simulation (1958–2008) with the Regional Atmospheric Climate Model (RACMO2/GR) at high horizontal resolution (~11 km) (fig. S1). The modeled SMB from RACMO2/GR agrees very well with in situ observations [N = 265, correlation coefficient (r) = 0.95], without need for post-calibration (*17*). For D, we used ice flux data from 38 glacier drainage basins (*15*), covering 90% of the ice sheet (fig. S2), corrected for SMB between flux gate and grounding line and updated to include 2008. To compare SMB-D with GRACE requires the calculation of cumulative SMB-D anomalies. The temporal evolution of the cumulative SMB-D anomaly was evaluated using monthly GRACE mass changes (*18*). The spatial distribution of GrIS mass changes was compared to a regionally distributed GRACE solution (*19*), updated to include 2008. For more details on data and methods, see the supporting online material.

Figure 1 compares the time series of the cumulative SMB-D anomaly with GRACE data (*18*) in the epoch during which both are available (2003–2008). The high correlation (r = 0.99) between the two fully independent time series and the similarity in trends support the consistency of the mass balance reconstruction. A linear regression on the SMB-D time series yields a 2003–2008 GrIS mass loss rate of -237 ± 20 Gt year^{-1}.

A potential source of error is that the GRACE signal includes the seasonal cycles of supraglacial/englacial water storage and ice discharge (*20*–*22*). Because only a single discharge data point per year is available, we assume slow-

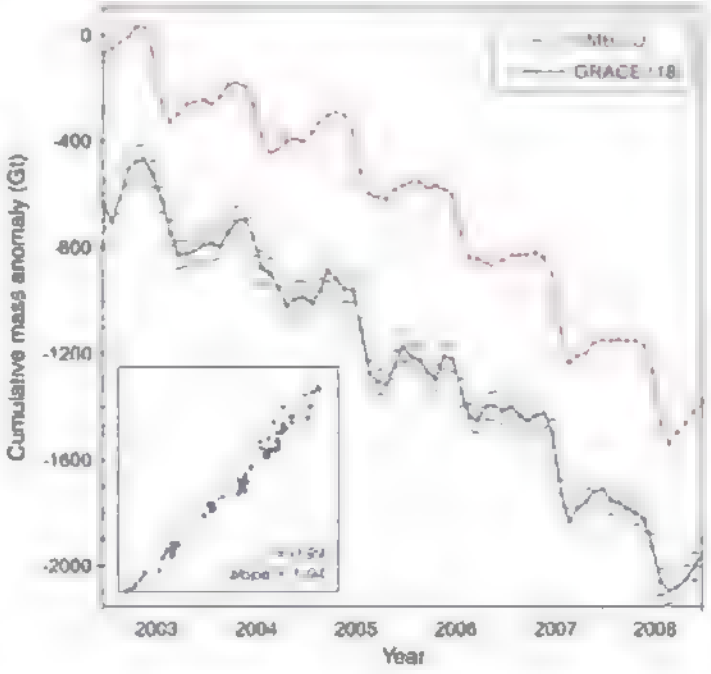

Fig. 1. Cumulative SMB-D anomaly (2003–2008) and comparison with GRACE data (*18*). Short horizontal lines indicate GRACE uncertainty, dashed lines the linear trends. GRACE values are not absolute numbers, and the curve has been vertically shifted for clarity. The scatter plot in the inset shows a direct linear regression between the monthly GRACE values as a function of the cumulative SMB-D anomaly, together with the linear regression coefficients.

[1]Institute for Marine and Atmospheric Research, Utrecht University, Netherlands. [2]Bristol Glaciology Centre, School of Geographical Sciences, University of Bristol, Bristol, UK. [3]Department of Earth System Science, University of California, Irvine, CA, USA. [4]Jet Propulsion Laboratory, Pasadena, CA, USA. [5]Delft Institute of Earth Observation and Space Systems, Delft University of Technology, Delft, Netherlands. [6]Royal Netherlands Meteorological Institute, De Bilt, Netherlands.

*To whom correspondence should be addressed. E-mail: m.r.vandenbroeke@uu.nl

ly changing ice flow without a seasonal cycle. The difference between the detrended GRACE and SMB time series, which represents these effects, shows no significant seasonal cycle. We confirm, therefore, that the influence of seasonal modulation of ice velocity on the ice sheet mass balance is insignificant (*2*, *7*).

A principal result is GrIS annual mass balance SMB-D (fig. S3 and eq. S1). Since 2000, GrIS mass balance has been persistently negative, caused by a simultaneous decrease in SMB and an increase in D. In total, the GrIS lost 1492 Gt between 2000 and 2008, or 166 Gt year^{-1}, equivalent to 0.46 mm year^{-1} of global SLR. Mass loss rate increased to 273 Gt year^{-1} in the period 2006–2008, equivalent to 0.75 mm year^{-1} of global SLR.

An important feature in fig. S3 is the large interannual variability of SMB, which may change by up to 400 Gt year^{-1} between consecutive years (standard deviation 107 Gt year^{-1}). Apart from the uncertainties involved in estimating mass balance components, this offers a partial explanation for the wide range of recently reported values of GrIS mass balance (*12*) and emphasizes the need for long-term observations.

The three main budgets that determine GrIS mass balance are ice sheet mass balance, SMB, and liquid water balance (eqs. S1 to S3). Our results show that both mass balance components, SMB and D (eq. S1), contributed equally to the post-1996 cumulative GrIS mass loss (Fig. 2A). Previous results (*15*) showed that discharge anomalies contributed 61% to recent GrIS mass loss; the shift to 50% can be fully explained by the larger interannual variability and the stronger downward trend in our updated SMB time series as compared to earlier estimates (*17*).

A quadratic decrease ($r^2 = 0.97$) explains the 2000–2008 cumulative mass anomaly better than a linear fit ($r^2 = 0.90$). Equation S1 implies that when SMB-D is negative but constant in time, ice sheet mass will decrease linearly in time. If, however, SMB-D decreases linearly in time, as has been approximately the case since 2000 (fig. S3), ice sheet mass is indeed expected to decrease quadratically in time.

The surface effects are further partitioned in Fig. 2B, detailing the contributions of the SMB components precipitation, sublimation, and runoff (eq. S2). Before 1996, decadal precipitation variability fully explained SMB anomalies. Between 1996 and 2004, large positive (~800 Gt) runoff and precipitation anomalies developed simultaneously. Because these approximately cancelled each other out, the SMB anomaly remained small during this period. After 2004, the cumulative precipitation anomaly no longer increased, but runoff remained high, resulting in an acceleration of GrIS mass loss, which was also detected by GRACE (*3*).

To further partition the runoff anomaly, Fig. 2C shows the main components of the liquid water balance: rain, melt, refreezing, and retention (eq. S3). After regional atmospheric warming (*4*, *5*), a cumulative meltwater anomaly of ~1900 Gt developed between 1996 and 2008, to which increased rainfall added another ~200 Gt. Only ~70% (1500 Gt) of this excess liquid water left the ice sheet as runoff, the remainder (~600 Gt) being refrozen in the firn layer. Since 1996, this refreezing anomaly has released ~2.0×10^{20} J of energy into the GrIS firn layer. Assuming the firn layer to be 100 m thick, to have an average density of 600 kg m^{-3}, and to cover 90% of the ice sheet surface, this is sufficient to heat up the entire firn column by 1 K. However, the refreezing anomaly

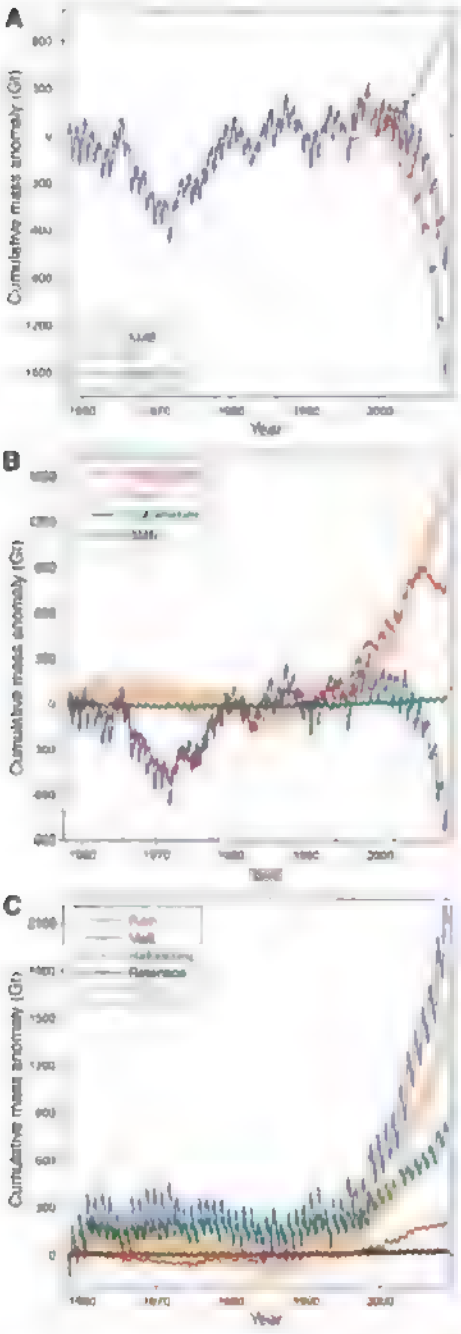

Fig. 2. Cumulative anomalies of the three main ice sheet mass budgets. (**A**) Mass balance and its components SMB and D (eq. S1). Before 1996, D and hence SMB-D, are poorly constrained and therefore not shown. (**B**) SMB and its components precipitation, runoff, and sublimation (eq. S2). (**C**) Liquid water balance and its main components rain, melt, refreezing, retention, and runoff (eq. S3).

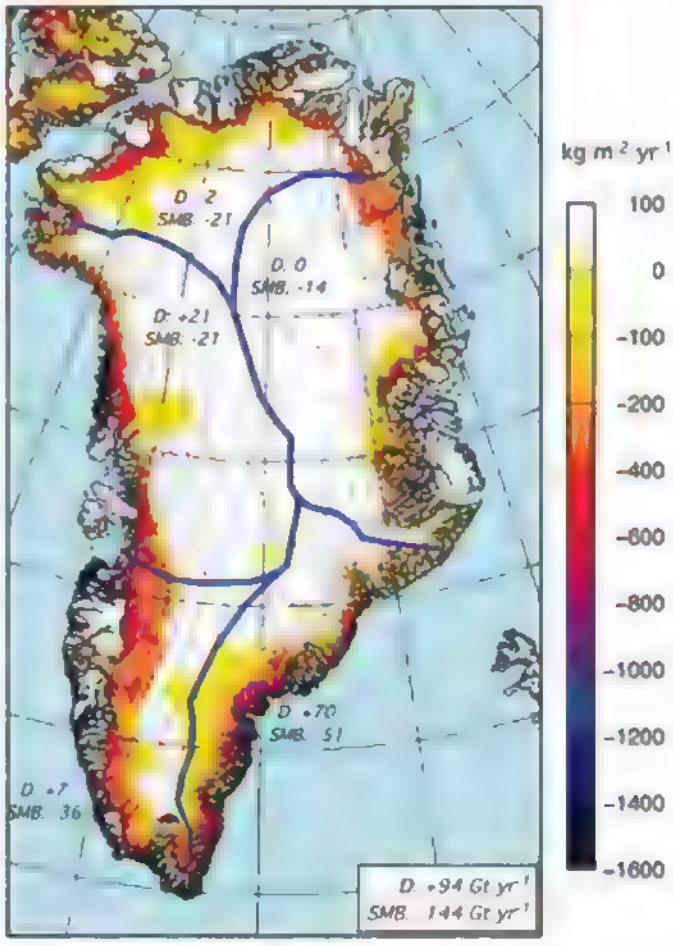

Fig. 3. Distribution of 2003–2008 mass changes across the ice sheet. The period (2003–2008) was chosen to coincide with the GRACE and IceSAT epochs. Numbers indicate basin-integrated mass loss rates due to SMB and D (in Gt year^{-1}). Numbers in the lower right corner represent the values for the whole ice sheet, indicating the dominant surface contribution to GrIS mass loss during 2003–2008. Colors represent the rate of surface mass change.

is not equally distributed over the GrIS, but concentrated in the lower accumulation zone. Our model data suggest that over the period 1990–2008, the first 15 m of the firn column in these areas has locally warmed by 5° to >10°. From Fig. 2, B and C, we conclude that, without the moderating effects of increased precipitation and refreezing, the post-1996 cumulative mass anomaly and associated SLR from the GrIS would have been 100% greater than actually observed.

The results also shed light on the relative timing of changes in surface conditions and ice dynamics. In central Greenland, enhanced surface melting started around 1996, several years before marine-terminating glaciers started to accelerate and retreat in the west (~1998) (*6*, *7*) and east (~2002) (*2*, *8*, *10*). In south Greenland, enhanced melting started in the early 1990s, but dynamic thinning was already active south of Helheim glacier in southeast Greenland (*23*, *24*).

To mimic the spatial distribution of GrIS mass loss during the GRACE and ICESat (Ice, Cloud, and Land Elevation Satellite) operational period, we performed a linear regression on 2003–2008 cumulative anomalies of D and SMB components, integrated over five major drainage basins (north, northeast, southeast, southwest, and northwest; fig. S2). The contributions from D and SMB to the basin-integrated mass change are given as numbers in Fig. 3, whereas the contributions from individual SMB components are listed in table S1.

In the north and northeast, which are regions with low accumulation and hence low rates of ice discharge, the discharge anomaly is small, and above-normal runoff dominated 2003–2008 mass loss. In the southwest, the ablation area is relatively large, with few marine-terminating glaciers; here, meltwater production and ice flow strongly interact (*20*–*22*), and increased discharge also contributed to the mass loss. In the northwest, which harbors numerous tidewater glaciers, mass loss is equally distributed between surface processes and ice discharge. In these four basins, surface mass losses represent increased runoff, moderated by above-normal snowfall (table S1).

The greatest 2003–2008 basin mass loss, representing about half of the ice sheet total, is found in the very wet southeast. Here, ice discharge dominates the signal. This is the only basin where the trend in the cumulative precipitation anomaly is negative, after anomalously high snowfall in this region from September 2002 to April 2003 (*25*), just at the onset of the GRACE period. As a result, the surface mass loss in the southeast is equally split between above-normal runoff and below-normal precipitation (table S1). Without the precipitation anomaly, the 2003–2008 mass loss rate in the southeast would have been ~20% smaller.

The colors in Fig. 3 represent surface mass loss rate (2003–2008). Because surface mass loss is dominated by runoff, it is heavily concentrated in the ablation zone of the ice sheet, roughly below 2000 m above sea level (asl). Surface mass loss rates range from 200 to 600 kg m^{-2} $year^{-1}$ in the northern and western ablation zones, and locally exceed 600 kg m^{-2} $year^{-1}$ in the southeast, owing to the effect of decreased precipitation. Assuming (conservatively) the surface mass loss to occur at the density of ice (910 kg m^{-3}), they account for >60 cm $year^{-1}$ of surface lowering locally in the southeast and 20 to 60 cm $year^{-1}$ elsewhere in the GrIS ablation zone. This explains part of the 2003–2008 thinning pattern as observed by the IceSAT and ASTER (Advanced Spaceborne Thermal Emission and Reflection Radiometer) satellites (*26*, *27*), noting that the strong thinning of the fastest-flowing parts of many outlet glaciers, up to several meters per year, remains dominated by dynamic processes. Figure 3 resembles the spatial GrIS mass loss pattern observed by GRACE (*19*), with mass losses concentrated in the southeast, northwest, and southwest at elevations below 2000 m asl.

The good agreement between mass budget calculations and the GRACE data enables us to make a detailed interpretation of the GRACE signal in terms of its individual components. Examining the period with well-constrained discharge data (1996–2008, fig. S4), we see that the ice sheet integrated GRACE signal primarily consists of (i) the slowly changing ice discharge anomaly, (ii) the asymmetric yet regular sawtooth shape of the seasonal runoff anomaly, and (iii) noise from precipitation variability on monthly to decadal time scales.

References and Notes

1. R. Thomas, E. Frederick, W. Krabill, S. Manizade, C. Martin, *Geophys. Res. Lett.* **33**, L10503 (2006)
2. E. Rignot, P. Kanagaratnam, *Science* **311**, 986 (2006)
3. I. Velicogna, J. Wahr, *Nature* **443**, 329 (2006)
4. J. E. Box, A. E. Cohen, *Geophys. Res. Lett.* **33**, L12706 (2006)
5. E. Hanna *et al.*, *J. Clim.* **21**, 331 (2008)
6. I. Joughin, W. Abdalati, M. Fahnestock, *Nature* **432**, 608 (2004)
7. A. Luckman, T. Murray, *Geophys. Res. Lett.* **32**, L08501 (2005)
8. A. Luckman, T. Murray, R. de Lange, E. Hanna, *Geophys. Res. Lett.* **33**, L03503 (2006)
9. L. A. Stearns, G. S. Hamilton, *Geophys. Res. Lett.* **34**, L05503 (2007)
10. I. M. Howat, I. Joughin, S. Tulaczyk, S. Gogineni, *Geophys. Res. Lett.* **32**, L22502 (2005)
11. I. M. Howat, I. Joughin, T. Scambos, *Science* **315**, 1559 (2007).
12. A. Cazenave, *Science* **314**, 1250 (2006)
13. H. J. Zwally *et al.*, *J. Glaciol.* **51**, 509 (2005)
14. W. Krabill *et al.*, *Science* **289**, 428 (2000)
15. E. Rignot, J. E. Box, E. Burgess, E. Hanna, *Geophys. Res. Lett.* **35**, L20502 (2008)
16. N. L. Bindoff *et al.*, in *Climate Change 2007: The Physical Science Basis* (Cambridge Univ. Press, Cambridge, 2007), pp. 385–432
17. J. Ettema *et al.*, *Geophys. Res. Lett.* **36**, L12501 (2009)
18. I. Velicogna, *Geophys. Res. Lett.* **36**, L19503
19. B. Wouters, D. Chambers, E. J. O. Schrama, *Geophys. Res. Lett.* **35**, L20501 (2008)
20. H. J. Zwally *et al.*, *Science* **297**, 218 (2002)
21. R. S. W. van de Wal *et al.*, *Science* **321**, 111 (2008)
22. I. Joughin *et al.*, *Science* **320**, 781 (2008).
23. W. Krabill *et al.*, *Science* **283**, 1522 (1999)
24. E. Rignot, D. Braaten, S. P. Gogineni, W. B. Krabill, J. R. McConnel., *Geophys. Res. Lett.* **31**, L10401 (2004).
25. J. E. Box *et al.*, paper presented at the 8th International Conference on Polar Meteorology and Oceanography, San Diego, CA, 9 to 13 January 2005
26. D. C. Slobbe, R. C. Lindenbergh, P. Ditmar, *Remote Sens. Environ.* **112**, 4204 (2008)
27. I. M. Howat, B. E. Smith, I. Joughin, T. A. Scambos, *Geophys. Res. Lett.* **35**, L17505 (2008)

28. This work is funded by Utrecht University (M.v.d.B. and W.J.v.d.B.) and the Netherlands Polar Program of the Netherlands Organization of Scientific Research (NWO/ALW) through the international RAPID project (J.E.), UK Natural Environment Research Council grant NE/C509474/1 (J.L.B.), the Royal Netherlands Meteorological Institute (E.v.M.), and Netherlands Institute for Space Research grant SRON/EO-076 (B.W.). E.R. and I.V. performed their work at the University of California, Irvine, and Caltech's Jet Propulsion Laboratory under a contract with NASA's Cryosphere Science Program. Climate data are available from the RAPID data repository at the British Atmospheric Data Centre (badc.nerc.ac.uk)

Supporting Online Material

www.sciencemag.org/cgi/content/full/326/5955/984/DC1
Data and Methods
Figs. S1 to S4
Table S1
References

24 June 2009; accepted 8 September 2009
10.1126/science.1178176

$CD4^+$ Regulatory T Cells Control T_H17 Responses in a Stat3-Dependent Manner

Ashutosh Chaudhry,[1,2] Dipayan Rudra,[1,2] Piper Treuting,[3] Robert M. Samstein,[1] Yuqiong Liang,[1] Arnold Kas,[2] Alexander Y. Rudensky[1,2]*

Distinct classes of protective immunity are guided by activation of STAT transcription factor family members in response to environmental cues. $CD4^+$ regulatory T cells (T_{regs}) suppress excessive immune responses, and their deficiency results in a lethal, multi-organ autoimmune syndrome characterized by T helper 1 (T_H1) and T helper 2 (T_H2) $CD4^+$ T cell–dominated lesions. Here we show that pathogenic T_H17 responses in mice are also restrained by T_{regs}. This suppression was lost upon T_{reg}-specific ablation of Stat3, a transcription factor critical for T_H17 differentiation, and resulted in the development of a fatal intestinal inflammation. These findings suggest that T_{regs} adapt to their environment by engaging distinct effector response–specific suppression modalities upon activation of STAT proteins that direct the corresponding class of the immune response.

The vertebrate immune system affords defense against different classes of pathogens by activation of a particular type of immune response. Intracellular pathogens induce protective T_H1 responses, whereas parasitic helminthes induce T_H2 cytokine production. In contrast, pathogenic yeast, fungi, and extracellular bacteria elicit highly inflammatory T_H17

responses associated with the production of interleukin-17 (IL-17), IL-22, IL-23, and granulocyte recruitment. Commitment of naïve T cells to these effector lineages is influenced by the cues derived from their microenvironment, particularly cytokines. Cytokine receptor signaling results in activation of the STAT (signal transducers and activators of transcription) family of transcription factors. Uncontrolled STAT activation can result in a variety of immune-mediated disease states. For instance, activation of Stat3 in response to the proinflammatory cytokine IL-6 in combination with transforming growth factor–β (TGF-β) leads to increased expression of orphan nuclear receptors RORγ and RORα, signature transcription factors for T_H17 cells (*1*–*4*). Deregulated Stat3-dependent T_H17 responses have been implicated in the pathogenesis of inflammatory bowel disease (IBD), psoriasis, multiple sclerosis, and arthritis (*5*).

T_{reg} cells act "in trans" to suppress immune responses to self and to commensal microbiota, and to limit pathology associated with the immune responses to infection. The differentiation and maintenance of suppressive T_{regs} require expression of the X-chromosome–encoded forkhead transcription factor Foxp3 (*6*, *7*). In both humans and mice, mutations in Foxp3 result in a fatal immune disorder characterized by uncontrolled T cell proliferation and drastically elevated production of T_H1 and T_H2 cytokines, suggesting that T_{reg}-elaborated suppression is involved in controlling these responses (*7*). In contrast, T_{reg}-mediated control of T_H17 responses remains an open question. Recent reports suggest that T_H17 and peripherally induced T_{regs} represent competing fates of naïve T cell differentiation, and the lineage choice is determined by relative amounts of IL-6 and TGF-β (*8*–*10*). Therefore, T_{regs} might limit T_H17 differentiation by "stealing" common precursors. Accordingly, a block in T_H17 differentiation in IL-6–deficient mice correlates with an increase in T_{reg} numbers (*11*). We hypothesized that analogous to effector T cell differentiation, T_{regs} suppress a particular type of immune response by activating a distinct STAT family member in response to its cytokine microenvironment. We explored whether activation of Stat3 endows T_{regs} with the ability to suppress T_H17 responses because Stat3 is a key factor in the initiation of T_H17 differentiation.

Using coimmunoprecipitation and Western blot analysis, we found that in T_{regs}, Foxp3 was associated with the transcriptionally active, phosphorylated form of Stat3 (Fig. 1A). Stat3 association with Foxp3 was markedly diminished in cytokine-stimulated T_{regs} cultured in the presence of Stat3 dimerization or phosphorylation inhibitors (fig. S1). These data suggest that Stat3 association with Foxp3 is phosphorylation dependent. In contrast, Stat5, a related STAT family member activated downstream of the IL-2 receptor, did not coimmunoprecipitate with Foxp3 (Fig. 1A).

To assess the role of Stat3 in T_{regs} in vivo, we induced deletion of a conditional *Stat3* allele by crossing $Stat3^{fl/fl}$ mice to $Foxp3^{Cre}$ mice that express a yellow fluorescent protein (YFP)–Cre recombinase fusion protein under the control of the *Foxp3* locus (*12*). We determined that the deletion was efficient and specific to T_{regs} (fig. S2). Male $Foxp3^{Cre}Stat3^{fl/fl}$ and female $Foxp3^{Cre/Cre}Stat3^{fl/fl}$ were born at expected Mendelian ratios and initially appeared healthy. At 6 weeks of age, however, these mice displayed splenomegaly and a pronounced enlargement of the mesenteric lymph nodes (Fig. 1B). In contrast to T_{reg}-deficient mice, we did not observe generalized lymphadenopathy characteristic of a systemic lymphoproliferative disorder. Instead, the size of lymph nodes, except for those draining the gastrointestinal tract, was reduced (Fig. 1B). Over time, $Foxp3^{Cre}Stat3^{fl/fl}$ mice developed anemia, weight loss, rectal prolapse, and colon thickening and succumbed to the disease by 12 to 14 weeks of age (Fig. 1, C and D). These manifestations are hallmarks of IBD, which was further confirmed by histological examination of the intestinal tissue, with the cecum and the colon of the diseased mice exhibiting massive lymphoid and neutrophilic infiltration (Fig. 1, E and F). In addition, hepatitis and liver lipidosis, which are thought to

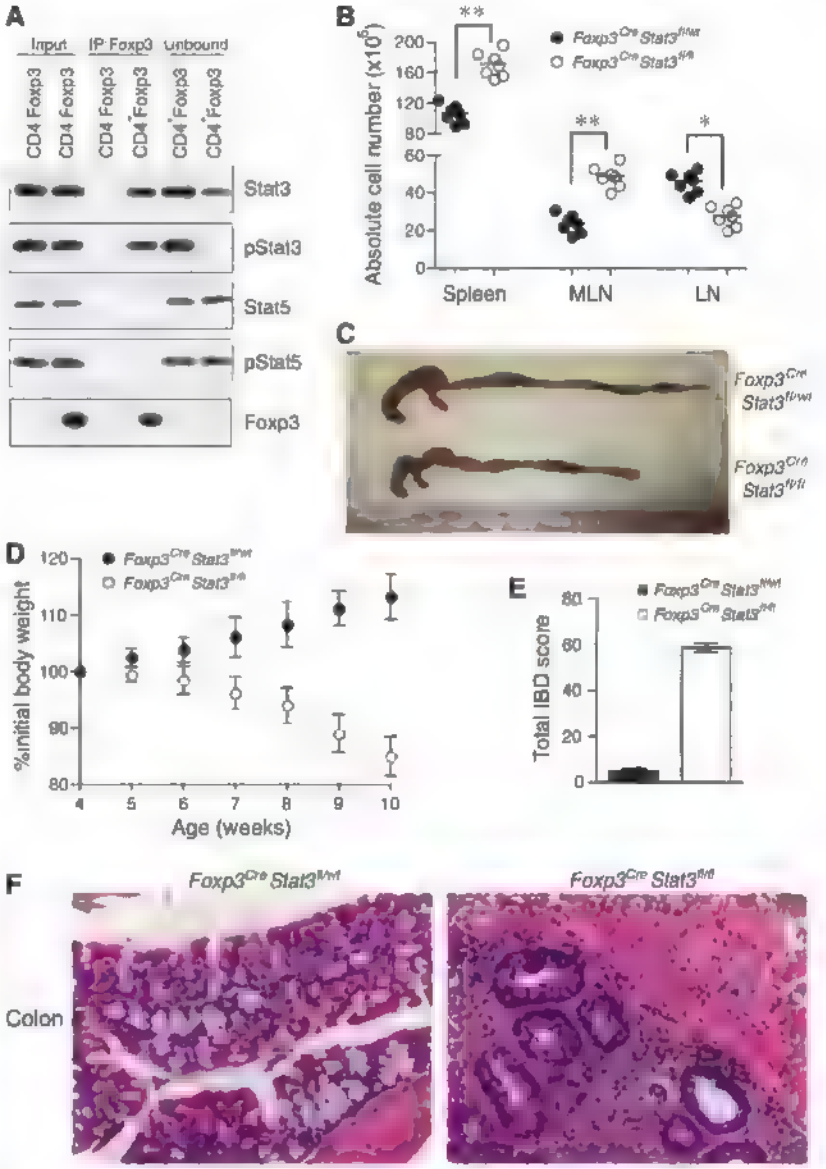

Fig. 1. Phosphorylated Stat3 interacts with Foxp3, and its expression in T_{reg} cells is required for suppression of fatal colitis. (**A**) Foxp3 immunoprecipitation from nuclear lysates of sorted $CD4^+Foxp3^-$ and $CD4^+Foxp3^+$ cells followed by Western blot analysis for the indicated proteins. The input lanes represent 3 to 5% of cell equivalents used for Foxp3 immunoprecipitation. (**B**) Spleen and lymph node cellularity. $^{**}P < 0.001$; $^{*}P < 0.01$. (**C**) Examples of colon thickening. (**D**) Weight loss over time ($n = 7$). (**E**) IBD scores derived from histopathologic evaluation of colon and cecum from 8- to 9-week-old mice. Formalin-fixed sections were stained with hematoxylin and eosin (H&E) before examination ($n = 4$ mice per group). The data in (D) and (E) represent the mean ± SE. (**F**) Representative H&E-stained colon sections from 8- to 9-week-old mice (original magnification, ×20).

[1]Howard Hughes Medical Institute and Immunology Program, Memorial Sloan-Kettering Cancer Center, New York, NY 10065, USA. [2]Department of Immunology, University of Washington, Seattle, WA 98195, USA. [3]Department of Comparative Medicine, University of Washington, Seattle, WA 98195, USA.

*To whom correspondence should be addressed. E-mail: rudenska@mskcc.org

Fig. 2. Stat3 ablation in T_{reg} cells does not affect their numbers, yet leads to $CD4^+$ T cell activation and selective increase in T_H17 responses. (**A**) $CD4^+$ and $CD8^+$ T cell numbers in the spleen and lymph nodes. $^{**}P < 0.001$; $^{*}P < 0.01$. (**B**) Flow cytometric analysis of CD44 and CD62L expression on $CD4^+Foxp3^-$ T cells in 6- to 8-week-old mice. A representative of five independent experiments is shown. (**C**) Frequency and numbers of $CD4^+Foxp3^+$ T cells. $^{**}P < 0.001$; $^{*}P < 0.01$. (**D**) Cytokine production by splenic $CD4^+Foxp3^-$ T cells as determined by flow cytometric analysis. A representative of four independent experiments is shown.

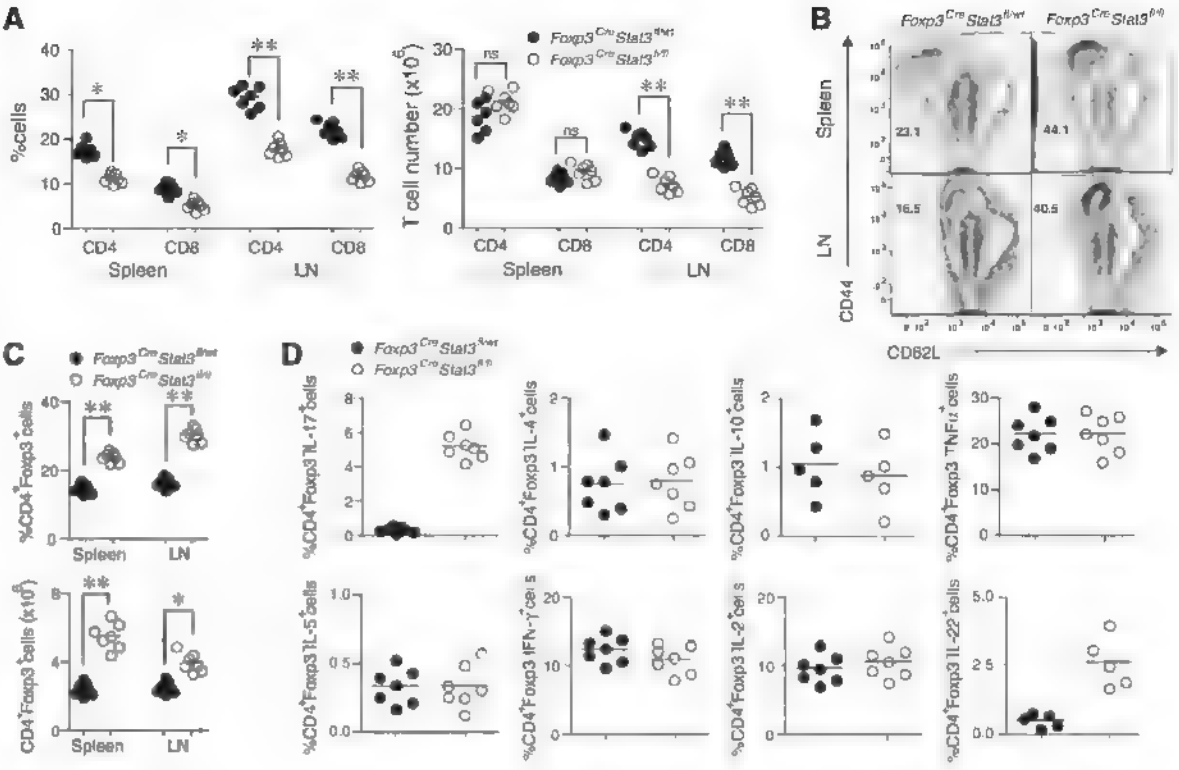

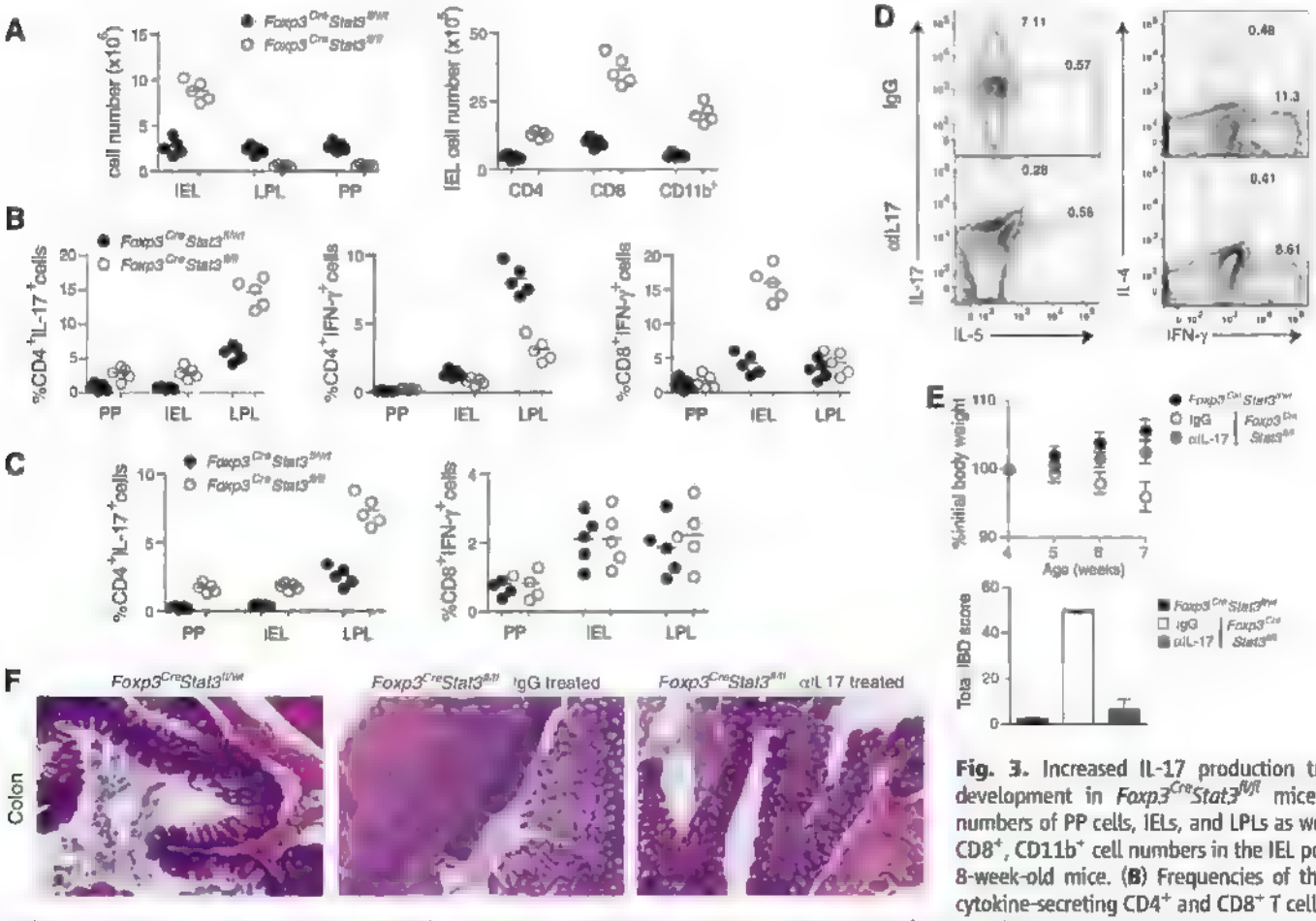

Fig. 3. Increased IL-17 production triggers IBD development in $Foxp3^{Cre}Stat3^{fl/fl}$ mice. (**A**) Total numbers of PP cells, IELs, and LPLs as well as $CD4^+$, $CD8^+$, $CD11b^+$ cell numbers in the IEL population in 8-week-old mice. (**B**) Frequencies of the indicated cytokine-secreting $CD4^+$ and $CD8^+$ T cells in PP, IEL, and LPL populations in 7- to 8-week-old mice. (**C**) Frequencies of the indicated cytokine-producing $CD4^+$ and $CD8^+$ T cells in PP, IELs, and LPLs in 3- to 4-week-old mice. (**D**) Flow cytometric analysis of cytokine production by splenic $CD4^+Foxp3^-$ T cells in $Foxp3^{Cre}Stat3^{fl/fl}$ mice treated with isotype-matched immunoglobulin G (IgG) or IL-17 neutralizing antibody. A representative of three independent experiments is shown. (**E**) Weight loss and IBD scores and (**F**) representative H&E-stained colon sections from 7- to 8-week-old $Foxp3^{Cre}Stat3^{fl/fl}$ mice treated with isotype-matched IgG control or neutralizing IL-17 antibody (original magnification, ×10). The data in (E) represent the mean ± SE.

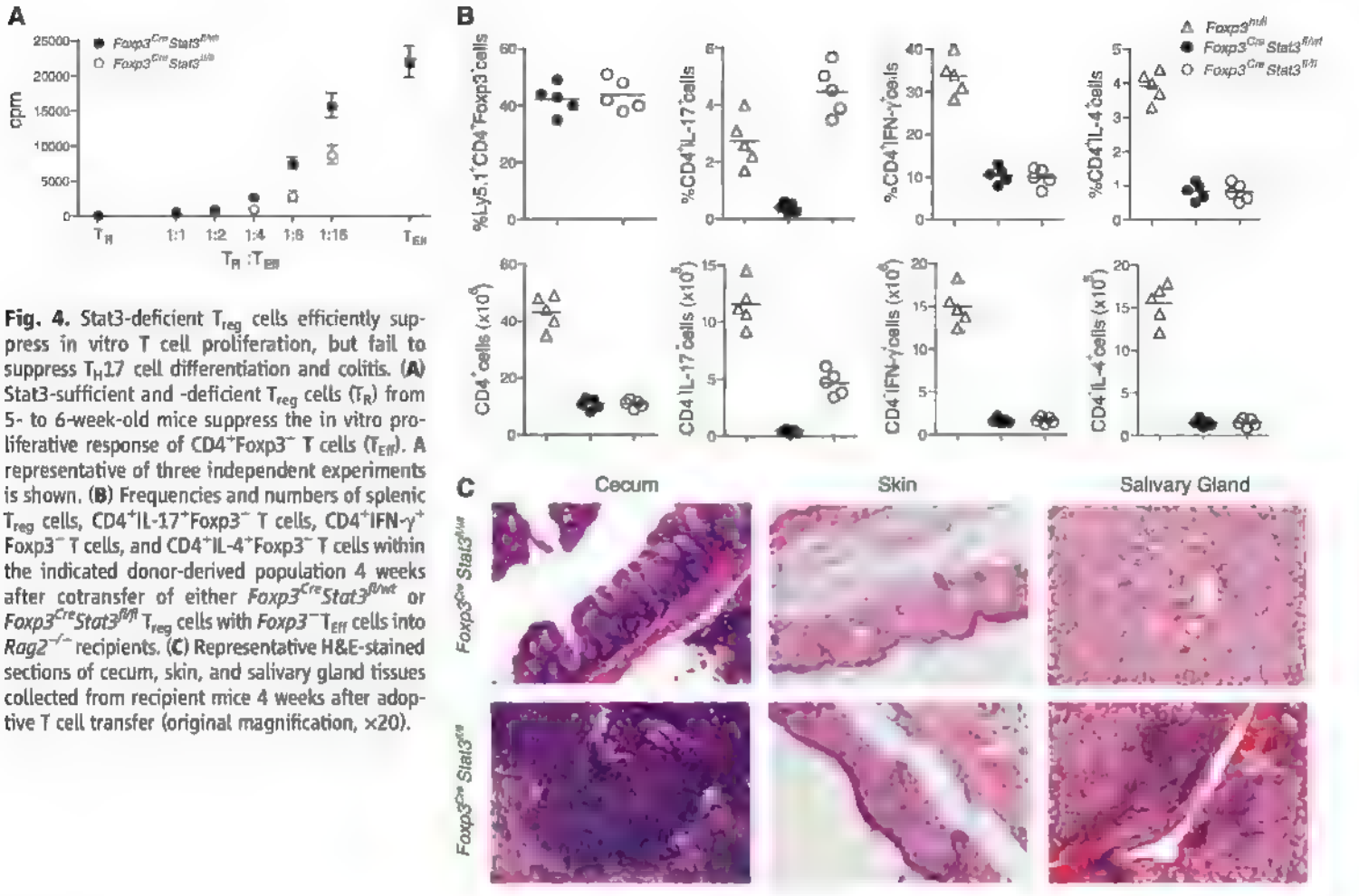

Fig. 4. Stat3-deficient T_{reg} cells efficiently suppress in vitro T cell proliferation, but fail to suppress T_H17 cell differentiation and colitis. (**A**) Stat3-sufficient and -deficient T_{reg} cells (T_R) from 5- to 6-week-old mice suppress the in vitro proliferative response of $CD4^+Foxp3^-$ T cells (T_{Eff}). A representative of three independent experiments is shown. (**B**) Frequencies and numbers of splenic T_{reg} cells, $CD4^+IL\text{-}17^+Foxp3^-$ T cells, $CD4^+IFN\text{-}\gamma^+$ $Foxp3^-$ T cells, and $CD4^+IL\text{-}4^+Foxp3^-$ T cells within the indicated donor-derived population 4 weeks after cotransfer of either *Foxp3*^{Cre}*Stat3*$^{fl/wt}$ or *Foxp3*^{Cre}*Stat3*$^{fl/fl}$ T_{reg} cells with *Foxp3*$^{-/-}$ T_{Eff} cells into *Rag2*$^{-/-}$ recipients. (**C**) Representative H&E-stained sections of cecum, skin, and salivary gland tissues collected from recipient mice 4 weeks after adoptive T cell transfer (original magnification, ×20).

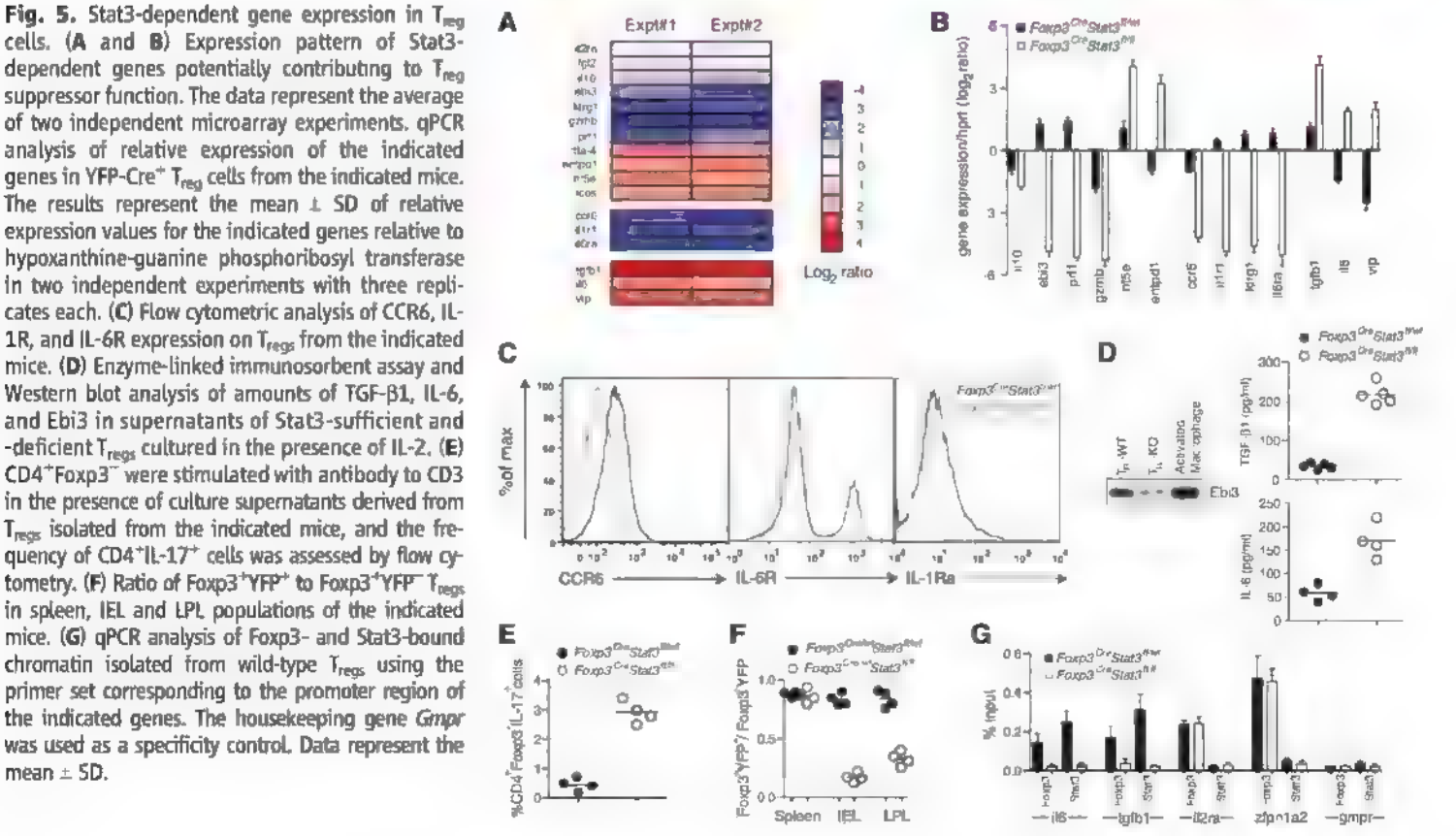

Fig. 5. Stat3-dependent gene expression in T_{reg} cells. (**A** and **B**) Expression pattern of Stat3-dependent genes potentially contributing to T_{reg} suppressor function. The data represent the average of two independent microarray experiments. qPCR analysis of relative expression of the indicated genes in YFP-Cre^+ T_{reg} cells from the indicated mice. The results represent the mean ± SD of relative expression values for the indicated genes relative to hypoxanthine-guanine phosphoribosyl transferase in two independent experiments with three replicates each. (**C**) Flow cytometric analysis of CCR6, IL-1R, and IL-6R expression on T_{regs} from the indicated mice. (**D**) Enzyme-linked immunosorbent assay and Western blot analysis of amounts of TGF-β1, IL-6, and Ebi3 in supernatants of Stat3-sufficient and -deficient T_{regs} cultured in the presence of IL-2. (**E**) $CD4^+Foxp3^-$ were stimulated with antibody to CD3 in the presence of culture supernatants derived from T_{regs} isolated from the indicated mice, and the frequency of $CD4^+IL\text{-}17^+$ cells was assessed by flow cytometry. (**F**) Ratio of $Foxp3^+YFP^+$ to $Foxp3^+YFP^-$ T_{regs} in spleen, IEL and LPL populations of the indicated mice. (**G**) qPCR analysis of Foxp3- and Stat3-bound chromatin isolated from wild-type T_{regs} using the primer set corresponding to the promoter region of the indicated genes. The housekeeping gene *Gmpr* was used as a specificity control. Data represent the mean ± SD.

be secondary to colitis, were also observed (fig. S3). In contrast to the massive widespread tissue lesions observed in *Foxp3*$^{-}$ mice, in *Foxp3*^{Cre}*Stat3*$^{fl/fl}$ mice pathology limited to the intestinal mucosa suggested that the absence of Stat3 only affects a particular subset of T_{reg} functions (fig. S3).

As opposed to the systemic T cell expansion observed in T_{reg}-ablated mice (*13*), we observed reduced splenic and lymph node T cell frequencies in *Foxp3*^{Cre}*Stat3*$^{fl/fl}$ mice, whereas the numbers of B cells, macrophages, and dendritic cells were increased (Fig. 2A and fig. S4). Despite reduced or unchanged numbers of T cells in the lymph node and spleen, we observed a marked increase in activated CD44^{high}CD62^{low}CD4^{+} T cells in these mice as compared to control littermates (Fig. 2B). Increased T_{reg} frequencies suggested, however, that the elevation in activated CD4^{+} T cell numbers was not due to reduced numbers of Stat3-deficient T_{regs} (Fig. 2C). Moreover, examination of the surface phenotype of T_{regs} upon Stat3 ablation indicated the heightened activation of T_{regs} in these mice (fig. S5). Furthermore, we found that Stat3-sufficient and -deficient T_{regs} expressed similar amounts of Foxp3, thus excluding altered Foxp3 expression as an explanation for the pathology in *Foxp3*^{Cre}*Stat3*$^{fl/fl}$ mice (fig. S6).

Recent work suggests that proinflammatory T_H17- and T_H1-associated cytokines have a major impact on colitis development and progression (*14*, *15*). Therefore, we assessed T_H1-, T_H17- and T_H2- associated cytokine production in *Foxp3*^{Cre}*Stat3*$^{fl/fl}$ mice. We observed increased production of T_H17-associated cytokines, IL-17 and IL-22, by splenic CD4^{+}Foxp3^{-} T cells in *Foxp3*^{Cre}*Stat3*$^{fl/fl}$ mice (Fig. 2D and fig. S7). In contrast, T_H1- and T_H2-associated cytokine production was kept in check by Stat3-deficient T_{regs}, as demonstrated by the comparable secretion of interferon-γ (IFN-γ), IL-4, and IL-5 in *Foxp3*^{Cre}*Stat3*$^{fl/fl}$ and littermate control mice. Production of IL-2, tumor necrosis factor–α (TNF-α), and IL-10 was also unaffected (Fig. 2D). Notably, Stat3-deficient Foxp3^{+} T_{regs} did not produce any of these cytokines (fig. S8). These results demonstrate a selective dysregulation of T_H17 responses upon Stat3 ablation in T_{regs} and identify T_{reg}-dependent control of T_H17 responses as an essential component of immune homeostasis.

We further analyzed Peyer's patch (PP), intraepithelial lymphocytes (IELs), and lamina propria lymphocytes (LPLs) because most T_H17 cells in normal mice are induced in the gut-associated lymphoid tissue (GALT) in response to intestinal flora (*16*) and because we observed that the intestinal tract was the major site of inflammation in *Foxp3*^{Cre}*Stat3*$^{fl/fl}$ mice. Whereas the numbers of LPLs and PP cells were diminished, we observed increased numbers of IELs, particularly CD8^{+} T cells and mononuclear cells, in agreement with the massive colonic infiltration revealed by the histopathological evaluation (Fig. 3A). Analysis of cytokine production by PP, LPL, and IEL T cells revealed an increased frequency of IL-17 producing CD4^{+}Foxp3^{-} T cells in *Foxp3*^{Cre}*Stat3*$^{fl/fl}$ mice in comparison to controls, whereas IFN-γ production was reduced (Fig. 3B). Stat3 deficiency did not affect the frequencies of IL-2-, IL-4-, and IL-10-producing cells (fig. S9). We also observed elevated frequencies of IFN-γ producing CD8^{+} T cells among IELs (Fig. 3B).

We next sought to determine whether IL-17 produced by CD4^{+} T cells or IFN-γ produced by CD8^{+} IELs instigated the disease in *Foxp3*^{Cre}*Stat3*$^{fl/fl}$ mice because both cytokines have been implicated in IBD development (*14*, *15*). We observed clinical symptoms of colitis in *Foxp3*^{Cre}*Stat3*$^{fl/fl}$ mice at about 7 to 8 weeks of age, whereas younger mice were disease-free (fig. S10). Assuming that the cytokine skewing should precede IBD development, we analyzed IL-17 and IFN-γ production in 3- to 4-week-old mice. We observed significantly higher frequencies of IL-17 producing CD4^{+}Foxp3^{-} T cells in the PP, LPL and IEL populations in *Foxp3*^{Cre}*Stat3*$^{fl/fl}$ mice, whereas the frequency of IFN-γ producing CD8^{+} and CD4^{+} T cells was similar in mutant and control mice (Fig. 3C). These results suggested that IL-17 responses act as the initial trigger of the disease. This was further supported by our finding that antibody-mediated IL-17 blockade in disease-free 3- to 4-week-old *Foxp3*^{Cre}*Stat3*$^{fl/fl}$ resulted in the alleviation of colitis and a reduction in T_H17 frequencies similar to those found in *Foxp3*^{Cre}*Stat3*$^{fl/wt}$ controls (Fig. 3, D to F). In contrast, IFN-γ neutralization failed to prevent or delay colitis in *Foxp3*^{Cre}*Stat3*$^{fl/fl}$ mice (fig. S11). Together, these data suggest that dysregulated T_H17 responses drive colitis induction in *Foxp3*^{Cre}*Stat3*$^{fl/fl}$ mice. Unrestricted T_H17 responses are likely to facilitate the activation or recruitment of IFN-γ producing CD8^{+} T cells at a later stage of disease progression. This phenomenon mirrors an initial requirement for a T_H17 response to bring T_H1 cells to infected or inflamed tissues (*17*, *18*).

The selective dysregulation of T_H17 responses and aggressive colitis observed in *Foxp3*^{Cre}*Stat3*$^{fl/fl}$ mice suggested that only a distinct aspect of the suppressor program was impaired in Stat3-deficient T_{regs}. Consistent with this assumption, their in vitro suppressor capacity was unaffected (Fig. 4A). To examine suppressor function of these cells in vivo, we cotransferred sorted Stat3-deficient or -sufficient Ly5.2^{+} T_{regs} and effector Ly5.1^{+} CD4 T cells from *Foxp3*$^{-}$ mice into *Rag2*$^{-/-}$ (recombination activating gene 2) recipients. Before transfer, the effector CD4 T cell population was heavily T_H1-skewed and contained ~40% of IFN-γ–producing cells, but few IL-17–producing cells (fig. S12). Similar to unmanipulated *Foxp3*$^{-}$ mice, after 4 to 6 weeks, recipients of *Foxp3*$^{-}$ T cells developed a systemic multi-organ autoimmune syndrome, which was completely abrogated upon cotransfer of Stat3-sufficient T_{regs}. Recipient mice that only received Ly5.1^{+} *Foxp3*$^{-}$ CD4 T cells contained 3- to 5-fold higher frequencies and 15- to 20-fold higher numbers of IFN-γ– and IL-4–producing cells as compared to recipient mice transferred with Ly5.1^{+} *Foxp3*$^{-}$ CD4 T cells mixed with either Stat3-deficient or -sufficient T_{regs} (Fig. 4B). In contrast, cotransfer of Stat3-deficient T_{regs} resulted in increased frequencies and absolute numbers of only IL-17 producing Ly5.1^{+} *Foxp3*$^{-}$ CD4 T cells (Fig. 4B). A similar trend was observed among LPLs in the recipient mice (fig. S13). These mice also developed a fulminant colitis similar to that seen in *Foxp3*^{Cre}*Stat3*$^{fl/fl}$ mice, as well as pronounced dermatitis and sialoadenitis, whereas other organs remained largely unaffected (Fig. 4C and fig. S13). In control mice, cotransfer of Stat3-sufficient T_{regs} prevented all autoimmune manifestations and tissue pathology. It is noteworthy that all three affected tissues are known targets of T_H17-mediated inflammation. Thus, Stat3-deficient T_{regs} are selectively impaired in their ability to control T_H17 responses in vivo, and this impairment leads to fatal colitis.

To gain insight into the potential mechanisms of Stat3-dependent regulation of T_{reg} function, we compared gene expression patterns in Stat3-deficient and -sufficient YFP^{+} T_{regs} isolated from healthy heterozygous *Foxp3*$^{Cre/wt}$*Stat3*$^{fl/fl}$ and *Foxp3*$^{Cre/wt}$*Stat3*$^{fl/wt}$ female mice. Cross-referencing of the resulting data sets with the previously identified set of Foxp3-dependent genes (*19*) showed that 20% of these genes are also dependent on Stat3 expression in T_{regs} (fig. S14). Within this group, we found decreased expression of *Il10*, *Ebi3*, *Gzmb*, and *Prf1*, genes implicated in T_{reg} suppressor function (Fig. 5, A and B). In particular, T_{reg} production of IL-10 and the Ebi3-containing cytokine, IL-35, is important for preventing colitis (*12*, *20*). In contrast, expression of other genes encoding proteins related to T_{reg} suppressor function was unaltered (*Il2ra*, *Fgl2*) or markedly increased (*Ctla4*, *Nt5e*, *Entpd1*, *Tgfb1*).

Substantially reduced expression of *Ccr6* in Stat3-deficient T_{regs} (Fig. 5, A to C) may also contribute to failure of Stat3-deficient T_{regs} to suppress T_H17-mediated inflammation. CCR6 is expressed by both T_H17 and T_{regs} and plays an important role in migration of T_H17 cells to inflammatory sites and in T_{reg}-mediated suppression thereof (*21*, *22*). We therefore compared relative distribution of YFP-Cre^{+} Stat3-deficient and YFP-Cre^{+} Stat3-sufficient Foxp3^{+} T_{regs} in the colon, secondary lymphoid organs, and GALT in the absence of any inflammation in female heterozygous *Foxp3*$^{Cre/wt}$Stat3$^{fl/fl}$ mice. These cells were present at a ~1:1 ratio in spleen; however, we observed a diminished proportion of Stat3-deficient T_{regs} in the gut (Fig. 5E). These results are consistent with the idea that Stat3-deficient T_{reg} cells are impaired in their ability to migrate to the gut tissue before establishment of colitis because Stat3-deficient and -sufficient T_{reg} cell populations had similar proportions of cycling and apoptotic cells (fig. S15). In contrast to healthy *Foxp3*$^{Cre/wt}$Stat3$^{fl/fl}$ mice, increased numbers of Foxp3^{+} T cells were observed in the inflamed colon of *Foxp3*^{Cre}Stat3$^{fl/fl}$ mice, in agreement with a recent report that CCR6-deficient T cells enter the central nervous system at late, but not at early, stages in the progression of experimental autoimmune encephalomyelitis (*18*).

Additionally, a low level of IL-1 receptor and IL-6 receptor expression in Stat3-deficient T_{regs}

(Fig. 5C) can potentially reduce the ability of these receptors to compete with effector T cells and other immune cell types for IL-1 and IL-6, cytokines that enhance T_H17 differentiation (*3*, *10*, *23*). In this regard, IL-2 receptor expressed on T_{regs} can deprive effector T cells of IL-2, thereby, effectively limiting the immune response (*24*). Consistent with this idea, Stat3-sufficient, but not Stat3-deficient, T_{regs} depleted IL-1 and IL-6 from the culture medium (fig. S17).

Unexpectedly, Stat3 deficiency in T_{regs} resulted in increased expression of *Il6*, *Tgfb1*, and *Vip*. Although T_{reg}-produced TGF-β1 can mediate suppression (*25*), TGF-β1 in combination with IL-6 also facilitates the generation of T_H17 cells. Similarly, *Vip*-encoded vasoactive intestinal peptide (VIP) promotes T_H17 differentiation (*26*). Indeed, soluble factors produced by Stat3-deficient T_{regs} facilitated differentiation of IL-17 producing T cells in vitro in the absence of exogenously supplied IL-6 and TGF-β1 (Fig. 5F). Increased expression of IL-6 and TGF-β1 in Stat3-deficient T_{regs} (Fig. 5, B and D) might amplify, but cannot fully account for, the observed increase in IL-17 production in diseased $Foxp3^{Cre}Stat3^{fl/fl}$ mice because heterozygous $Foxp3^{Cre/wt}Stat3^{fl/fl}$ female mice cohabited by Stat3-deficient and -sufficient T_{regs} do not exhibit augmented T_H17 responses.

To test whether Stat3 facilitates recruitment of Foxp3 to regulatory elements of *Il6* and *Tgfb1* genes, we used chromatin immunoprecipitation combined with quantitative polymerase chain reaction (qPCR) to examine Foxp3 binding to promoter regions of these genes in Stat3-sufficient and -deficient T_{reg} cells. Indeed, we found that Foxp3 was bound to *Il6* and *Tgfb1* promoters in a Stat3-dependent manner. In contrast, Foxp3 binding to *Zfpn1a2* (Helios) and *Il2ra*, well-known Foxp3-binding genes expressed in a Stat3-independent manner, was unaffected by the absence of Stat3 (Fig. 5G). These results suggest that Stat3 activation dependent association with Foxp3 transcriptional complexes may result in modulation of Stat3-dependent gene expression partly through Stat3-dependent recruitment of Foxp3.

Thus, the activation of Stat3 in T_{regs} endows them with the ability to suppress T_H17 responses plausibly through increased expression of a subset of suppressor molecules, as well as cytokine and chemokine receptors, which may deprive immune effector cells of essential activation cues and facilitate the spatial proximity of T_{regs} and T_H17 cells. Furthermore, Stat3 in T_{regs} limits the expression of soluble mediators of T_H17 differentiation. We suggest that altered expression of a combination of genes, but not changes in any one of them, can account for the inability of Stat3-deficient T_{regs} to restrain T_H17 responses.

Our findings support the idea that the same transcription factors integrate environmental cues that guide a particular immune response type and facilitate T_{reg} cells' ability to suppress the corresponding type of immune response. Consistent with this notion, Irf4 (interferon regulatory factor 4), an IRF transcription factor family member essential for T_H2 differentiation, is required for T_{reg} cells to suppress T_H2 responses (*27*). Furthermore, T_{reg} expression of T-bet, a T_H1-specific transcription factor, is required for T_{reg} homeostasis under conditions of induced T_H1 inflammation (*28*). We propose that the STAT-IRF axis of transcriptional regulation allows T_{regs} to adapt to a particular environment and ensures appropriate "class"-specific control of immune-mediated inflammation.

References and Notes

1. P. R. Mangan *et al.*, *Nature* **441**, 231 (2006)
2. M. Veldhoen, R. J. Hocking, C. J. Atkins, R. M. Locksley, B. Stockinger, *Immunity* **24**, 179 (2006)
3. L. Zhou *et al.*, *Nat. Immunol.* **8**, 967 (2007)
4. X. O. Yang *et al.*, *Immunity* **28**, 29 (2008)
5. E. Bettelli, T. Korn, M. Oukka, V. K. Kuchroo, *Nature* **453**, 1051 (2008)
6. S. Hori, T. Nomura, S. Sakaguchi, *Science* **299**, 1057 (2003)
7. J. D. Fontenot, M. A. Gavin, A. Y. Rudensky, *Nat. Immunol.* **4**, 330 (2003)
8. I. I. Ivanov *et al.*, *Cell* **126**, 1121 (2006)
9. E. Bettelli *et al.*, *Nature* **441**, 235 (2006)
10. L. Zhou *et al.*, *Nature* **453**, 236 (2008)
11. T. Korn *et al.*, *Nature* **448**, 484 (2007)
12. Y. P. Ruhtsov *et al.*, *Immunity* **28**, 546 (2008)
13. J. M. Kim, J. P. Rasmussen, A. Y. Rudensky, *Nat. Immunol.* **8**, 191 (2007)
14. W. Strober, I. J. Fuss, R. S. Blumberg, *Annu. Rev. Immunol.* **20**, 495 (2002)
15. K. J. Maloy, M. C. Kullberg, *Mucosal Immunol.* **1**, 339 (2008)
16. I. I. Ivanov *et al.*, *Cell Host Microbe* **4**, 337 (2008)
17. S. A. Khader *et al.*, *Nat. Immunol.* **8**, 369 (2007)
18. A. Reboldi *et al.*, *Nat. Immunol.* **10**, 514 (2009)
19. M. A. Gavin *et al.*, *Nature* **445**, 771 (2007)
20. D. A. Vignali, L. W. Collison, C. J. Workman, *Nat. Rev. Immunol.* **8**, 523 (2008)
21. M. Klemewetfeld *et al.*, *Blood* **105** 2877 (2005)
22. T. Yamazaki *et al.*, *J. Immunol.* **181**, 8391 (2008)
23. C. Sutton, C. Brereton, B. Keogh, K. H. Mills, E. C. Lavelle, *J. Exp. Med.* **203**, 1685 (2006)
24. P. Pandiyan, L. Zheng, S. Ishihara, J. Reed, M. J. Lenardo, *Nat. Immunol.* **8**, 1353 (2007)
25. M. O. Li, Y. Y. Wan, R. A. Flavell, *Immunity* **26**, 579 (2007)
26. M. Yadav, J. Rosenbaum, E. J. Goetzl, *J. Immunol.* **180**, 2772 (2008)
27. Y. Zheng *et al.*, *Nature* **458**, 351 (2009)
28. M. A. Koch *et al.*, *Nat. Immunol.* **10**, 595 (2009)

29. We thank K. Forbush, T. Chu, L. Karpik, and A. Bravo for assistance with the mouse colony management; S. Akira for *Stat3*$^{fl/fl}$ mice; and J. Renauld for antibody to IL-22. This work was supported by NIH grants AI-061816 and AI-034206. A.C. is supported by the Cancer Research Institute, and D.R. is supported by the Arthritis Foundation. A.Y.R. is an investigator with the Howard Hughes Medical Institute. Gene expression microarray data have been deposited in the NCBI Gene Expression Omnibus repository with the accession code GSE17962.

Supporting Online Material

www.sciencemag.org/cgi/content/full/1172702/DC1
Methods
Figs. S1 to S17
References

24 February 2009; accepted 2 September 2009
Published online 1 October 2009;
10.1126/science.1172702
Include this information when citing this paper

A Spindle Assembly Checkpoint Protein Functions in Prophase I Arrest and Prometaphase Progression

Hayden Homer,* Liming Gui, John Carroll

Two critical stages of mammalian oocyte regulation are prophase I arrest, which is important for sustaining the oocyte pool, and the progression through meiosis I (MI) to produce fertilizable eggs. We have found that the spindle assembly checkpoint protein BubR1 regulates both stages in mouse oocytes. We show that oocytes depleted of BubR1 cannot sustain prophase I arrest and readily undergo germinal vesicle breakdown, a marker for reentry into MI. BubR1-depleted oocytes then arrest before completing MI, marked by failure of polar body extrusion. Both meiotic defects in BubR1-depleted oocytes are due to reduced activity of the master regulator known as the anaphase-promoting complex (APC), brought about through diminished levels of the APC coactivator Cdh1.

Mammalian oocytes arrest at prophase I from birth until puberty when hormonal signals induce the resumption of meiosis I (MI) and progression to meiosis II (MII), the stage at which fertilization occurs. Prophase I–arrested oocytes possess an intact nucleus referred to as the germinal vesicle (GV), with GV breakdown (GVBD) and first polar body extrusion (PBE) signifying the resumption and conclusion of MI, respectively (Fig. 1A). Cell-cycle progression is driven by a proteolytic machinery known as the anaphase-promoting complex (APC) acting in concert with one of two coactivators, Cdc20 or Cdh1 (*1*). Unlike mitotic prometaphase—in which APC-Cdc20 is the principal APC species (*1*)—in mammalian oocytes, APC-Cdh1 is active during prophase I (*2*, *3*) and early prometaphase I before APC-Cdc20, which acts in late MI (*4*) (Fig. 1A). In both systems, however, the anaphase-trigger is APC-Cdc20–mediated securin and cyclin B1 degradation (*1*, *4*, *5*). The key inhibitor of APC-Cdc20–dependent anaphase onset is the spindle assembly checkpoint (SAC), the core compo-

Oocyte and Embryo Research Laboratory, Department of Cell and Developmental Biology, Division of Biosciences and Institute for Women's Health, University College London, London, UK.

*To whom correspondence should be addressed. E-mail: h.homer@ucl.ac.uk

nents of which are drawn from the Mad and Bub protein families (*6*). Mitotic arrest deficient 2 (Mad2) and Bub1 have predicted APC-Cdc20 directed SAC roles in mouse oocytes and consequently regulate late MI coincident with APC-Cdc20 activity (*7*, *8*). Here, we examine the role of another key SAC protein, BubR1, in mouse oocytes where APC-Cdh1 is active before activation of APC-Cdc20.

We employed a morpholino-based gene-silencing approach (*9*) to deplete BubR1 in oocytes (*2*, *7*). Using a *BubR1*-targeting morpholino (termed BubR1MO) (*9*), we depleted ~80% of endogenous BubR1 (fig. S1). During the course of evaluating BubR1MO, we found that 25% of BubR1-depleted oocytes spontaneously underwent GVBD in 3-isobutyl-1-methylxanthine (IBMX), a drug that maintains prophase I arrest in almost 98% of control and Mad2-depleted oocytes (Fig. 1B) (*2*, *9*). This indicated that BubR1-depleted oocytes have reduced capacity for sustaining prophase I arrest. In mouse oocytes, the prophase I arrest state is dependent upon APC-Cdh1 activity (*2*, *3*). We therefore examined Cdh1 in BubR1-depleted oocytes and found that it was reduced by ~60% (Fig. 1C). This reduction in Cdh1 levels was specific to BubR1 depletion, because Cdh1 was unaffected by Mad2-depletion (Fig. 1C), and Cdh1 levels could be restored in BubR1MO-injected oocytes by coexpressing human BubR1 (hBubR1) from *hBubR1* complementary RNA (cRNA) (Fig. 1D). This suggested that the fragility of prophase I arrest after BubR1 depletion was due to reduced APC-Cdh1 activity. In support of this, GVBD rates in BubR1-depleted oocytes declined considerably after restoring Cdh1 levels by injecting either *Cdh1* cRNA or *hBubR1* cRNA (Fig. 1B). Thus, by maintaining APC-Cdh1 activity, BubR1 is important for prophase I arrest in mouse oocytes, consistent with a prophase I role for homologs of BubR1 in yeast and flies (*10*, *11*).

Although BubR1-depleted oocytes readily resumed MI, there was a marked reduction in PBE rates. By 10 hours after GVBD, 80% of control oocytes undergo PBE, contrasting sharply with only 6% of BubR1-depleted oocytes (Fig. 2, A and B). This effect was not anticipated, because BubR1, like Mad2, is known to inhibit APC-Cdc20 (*1*, *6*). Indeed, we find that in oocytes, BubR1 exhibits properties typical of an SAC protein, including the capacity for APC-Cdc20 inhibition (fig. S2). Hence, BubR1 depletion would be expected to prematurely activate APC-Cdc20 and to advance MI exit, as occurs after Mad2 depletion (Fig. 2A) (*7*). Instead, BubR1-depleted oocytes undergo an MI arrest (Fig. 2, A and B), which implies that BubR1 has additional functions during MI separate from its SAC role.

To explore the mechanism of MI arrest in BubR1-depleted oocytes, we examined the levels of securin and cyclin B1. We observed that after BubR1 depletion, securin and cyclin B1 levels remained stable by 8 hours after GVBD, whereas both proteins had been destroyed in controls (Fig. 2C and fig. S3). Given that securin and cyclin B1 destruction are required for anaphase I (*4*, *5*), this indicated that BubR1-depleted oocytes arrest before anaphase I. We confirmed this by immunostaining spindles and chromosomes. By 10 hours after GVBD and beyond, BubR1-depleted oocytes show no evidence of anaphase I, telophase I, or MII configurations, all of which are apparent in controls between 8 and 10 hours after GVBD (Fig. 2, D and E). Together, these data show that BubR1-depleted oocytes arrest in prometaphase I.

APC-Cdh1 is active during prometaphase I (Fig. 1A), the stage at which BubR1-depleted oocytes arrest. Given that we have found BubR1 to be important for Cdh1 stability in prophase I (Fig. 1, C and D), a similar BubR1-dependent effect on APC-Cdh1 in prometaphase I could plausibly underpin prometaphase I arrest after BubR1 depletion. This prompted us to examine Cdh1 levels during MI. As with prophase I, after BubR1 depletion, Cdh1 was again reduced by 50 to 70% throughout prometaphase I, whereas Cdc20 was unaffected (Fig. 3, A to C). In the reverse experiment, BubR1 overexpression stabilized Cdh1 (fig. S4, A and B). This supported our hypothesis that deregulated APC-Cdh1 is central to prometaphase I arrest after BubR1 depletion. Moreover, because Mad2 does not share BubR1's influence on Cdh1 levels (Fig. 1C), this explains why BubR1 and Mad2 depletion produce contrasting phenotypes.

We therefore focused on the first 6 hours of MI when APC-Cdh1 is active (Fig. 1A) and examined securin and cyclin B1, two recognized APC-Cdh1 substrates that must be meticulously regulated for proper M phase progression (*1*). We observed that during early prometaphase I, securin was twice as high as in BubR1-depleted oocytes compared with controls, whereas cyclin B1 was unaffected (Fig. 3, D to F). Thus, after BubR1 depletion, Cdh1 is reduced and securin is increased. The inverse relationship between Cdh1 and securin was consistent with securin being a preferential APC-Cdh1 substrate during early prometaphase I, as is the case during prophase I (*2*) and in mitosis (*12*). In support of this, we found that securin, but not cyclin B1, was stabilized during early prometaphase I in oocytes depleted of Cdh1 (Fig. 3, D to F, fig. S5, and fig. S11). The converse was also true, because Cdh1 overexpression led to a reduction in securin (fig. S6). Hence, these data show that low-level APC-Cdh1 mediated securin destruction occurs during prometaphase I and is BubR1-dependent. As further confirmation of BubR1 dependency, we found that the extent of the Cdh1 decrease and securin increase was proportional to the severity of BubR1 depletion (fig. S7). Moreover, BubR1 overexpression increased Cdh1 and decreased securin (fig. S4, A to C), changes that were exactly opposite to those induced by BubR1 depletion. Thus, APC-Cdh1 mediated securin destruction during early prometaphase I is BubR1-dependent and is required for preventing overaccumulation of securin.

Next, we asked whether failure of anaphase I in BubR1-depleted oocytes (Fig. 2) might be attributable to high securin levels. We now turned our attention to APC-Cdc20, because anaphase I

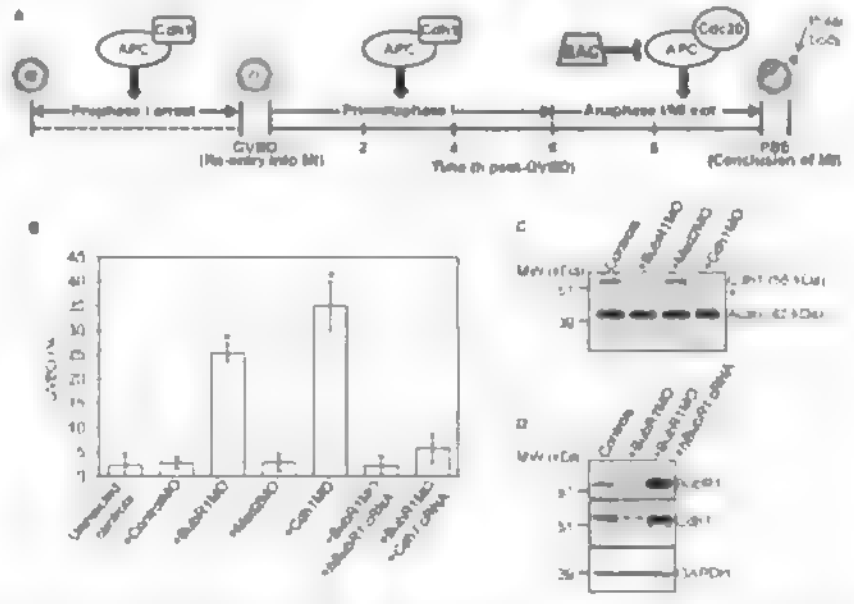

Fig. 1. Prophase I arrest is compromised after BubR1 depletion. (**A**) Schematic of MI. (**B**) Mock-depleted (+ControlMO), BubR1-depleted (+BubR1MO), Mad2-depleted (+Mad2MO) (*7*), Cdh1-depleted (+Cdh1MO), (*9*) and uninjected oocytes were scored for GVBD after 24 hours in IBMX. Cdh1-depleted oocytes escape prophase I arrest as shown previously (*2*). Increased GVBD after BubR1 depletion could be prevented by expressing either BubR1 from an *hBubR1* cRNA (+BubR1MO+*hBubR1* cRNA) or Cdh1 from a *Cdh1* cRNA (+BubR1MO+*Cdh1* cRNA) (*9*). Error bars, mean ± SEM; $N \geq 3$ experiments. Asterisks denote a significant difference from uninjected controls ($P < 0.0001$; Student's *t*-test). (**C** and **D**) Samples (50 oocytes) of GV-stage oocytes from each of the groups depicted were immunoblotted either for Cdh1 and actin (C) or for BubR1, Cdh1, and glyceraldehyde phosphate dehydrogenase (GAPDH) (D) ($N = 2$ experiments). *, Nonspecific band.

is mediated by late-acting APC-Cdc20 and not by APC-Cdh1 (*4*) (Fig. 1A). Anaphase I is vulnerable to any perturbation of the natural balance between APC-Cdc20 and either securin or cyclin B1. For instance, overexpression of securin from an exogenous *Securin-GFP* cRNA invokes a prometaphase I arrest (*5*) by overwhelming APC-Cdc20. Similarly, prometaphase I arrest after BubR1 depletion could arise if APC-Cdc20 was being outstripped by elevated securin. If this were so, one clear prediction is that redressing the presumed APC-Cdc20/securin mismatch should enable BubR1-depleted oocytes to undergo anaphase I and to exit MI. Consistent with this notion, PBE rates were significantly increased in BubR1-depleted oocytes either by overexpressing Cdc20 or by restraining securin expression (from 6% to 40% and 66%, respectively) (fig. S8).

Notably, however, PBE rates in BubR1-depleted oocytes were not fully restored to wild-type levels after reinstating a favorable APC-Cdc20/securin balance (fig. S8). This suggested that other deficits after BubR1 knockdown, such as kinetochore-microtubule attachment defects, known to be BubR1-dependent in mitosis (*13*), might also hinder meiotic progression. To address this possibility, we investigated two readouts of kinetochore-microtubule attachment status: Mad2, which localizes to unattached kinetochores (*14*); and the presence of cold-stable microtubules, because microtubules are unstable at 4°C unless attached to kinetochores (*13*). At 4 hours after GVBD, kinetochore-microtubule attachments have not yet formed in control oocytes (*15*), which consequently exhibit strong Mad2 staining (fig. S2B) and virtually no cold-stable microtubules (Fig. 4D). By 8 hours after GVBD, when kinetochores become fully attached, chromosomes are well aligned, Mad2 becomes undetectable (Fig. 4A and fig. S2C), and a metaphase I spindle persists after cold treatment (Fig. 4E). In stark contrast, by 8 hours after GVBD in BubR1-depleted oocytes, chromosomes are misaligned, remain strongly positive for Mad2 (Fig. 4, B and C), and have very few cold-stable microtubules (Fig. 4F). Kinetochore-microtubule attachment defects are not a consequence of the Cdc20/securin imbalance brought about by BubR1 depletion because they persist when securin expression is restrained or Cdc20 is coexpressed in BubR1-depleted oocytes (fig. S9). Thus, microtubule attachments form less efficiently after BubR1 depletion and likely explain previous observations of chromosome alignment defects in MII oocytes from BubR1-deficient mutant mice (*16*).

We show here that BubR1 sustains Cdh1 levels in prophase I and prometaphase I before inhibiting APC-Cdc20 in late MI. Cdh1 is also required for sustaining BubR1 levels, revealing a codependency between BubR1 and Cdh1 that could be relevant to the mechanism by which BubR1 stabilizes Cdh1 (fig. S10). In prophase I, BubR1-dependent Cdh1 stabilization is important for preventing unscheduled reentry into MI. After GVBD, BubR1 promotes prometaphase I progression by preventing indiscriminate securin accumulation and by contributing to the establishment of kinetochore-microtubule attachments. As part of its SAC role, BubR1 then modulates the metaphase I–to–anaphase I transition. BubR1's Cdh1-directed role appears to predominate as

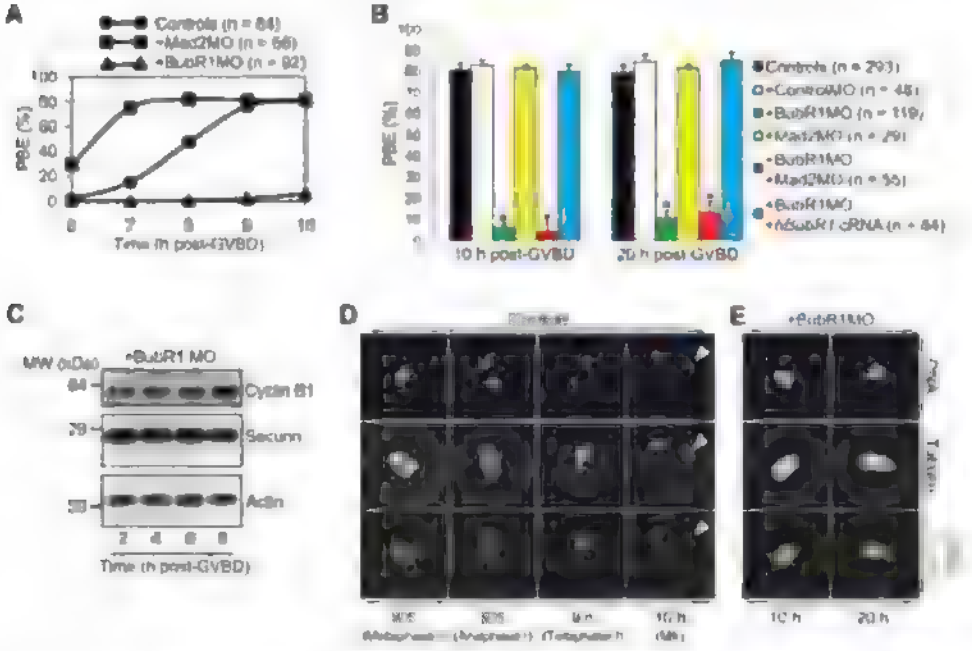

Fig. 2. BubR1 depletion induces a prometaphase I arrest. (**A**) Timeline of PBE for uninjected controls, Mad2-depleted, and BubR1-depleted oocytes. Oocytes were scored for the presence of polar bodies at 6, 7, 8, 9, and 10 hours after GVBD. Note the contrasting effects of Mad2 and BubR1 depletion on PBE. (**B**) PBE is inhibited after BubR1 depletion. PBE rates were determined at 10 and 20 hours after GVBD. Prometaphase I arrest is robust after BubR1 depletion so that PBE increases only modestly (from 6% to 11%) during an additional 10 hours of culture (from 10 to 20 hours after GVBD). Furthermore, codepletion of Mad2 does not restore PBE rates, indicating that MI arrest is not SAC-mediated. Error bars, mean + SEM; $N \geq 3$ experiments. Asterisks denote a significant difference from uninjected controls ($P < 0.0001$; Student's t test). (**C**) Samples (50 oocytes) of BubR1-depleted oocytes at 2, 4, 6, and 8 hours after GVBD were blotted for cyclin B1, securin, and actin. (**D** and **E**) Control and BubR1-depleted oocytes were immunostained for tubulin and DNA at the times after GVBD indicated in the figure ($N \geq 15$ oocytes per time point). By 10 hours after GVBD in controls, a polar body (white arrowhead) with associated chromosomes is present.

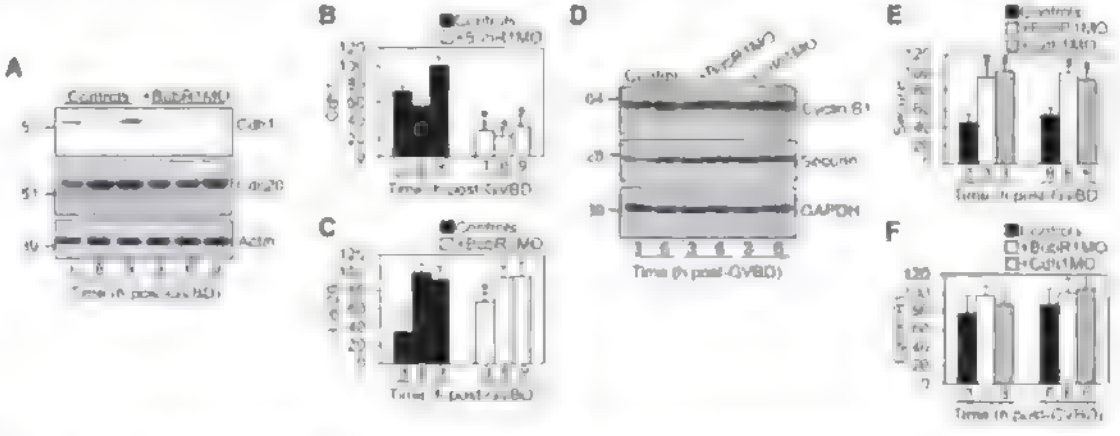

Fig. 3. (**A** to **C**) Cdh1 is reduced after BubR1 depletion. Samples (30 oocytes) of BubR1-depleted oocytes were immunoblotted along with uninjected controls at 3, 6, and 9 hours after GVBD for Cdh1, Cdc20, and actin (A). Band intensities of (B) Cdh1 and (C) Cdc20 on blots were quantified and normalized to values found in controls. (**D** to **F**) Securin is preferentially stabilized after either BubR1 or Cdh1 depletion. Samples (30 oocytes) of BubR1-depleted and Cdh1-depleted oocytes were immunoblotted along with uninjected controls at 3 and 6 hours after GVBD for securin, cyclin B1, and GAPDH (D). Band intensities of (E) securin and (F) cyclin B1 on blots were quantified and normalized to values found in controls. Error bars, mean + SEM; $N = 3$ experiments. Asterisks [(B), (C), and (E)] denote a significant difference from uninjected controls ($P < 0.0001$; Student's t test).

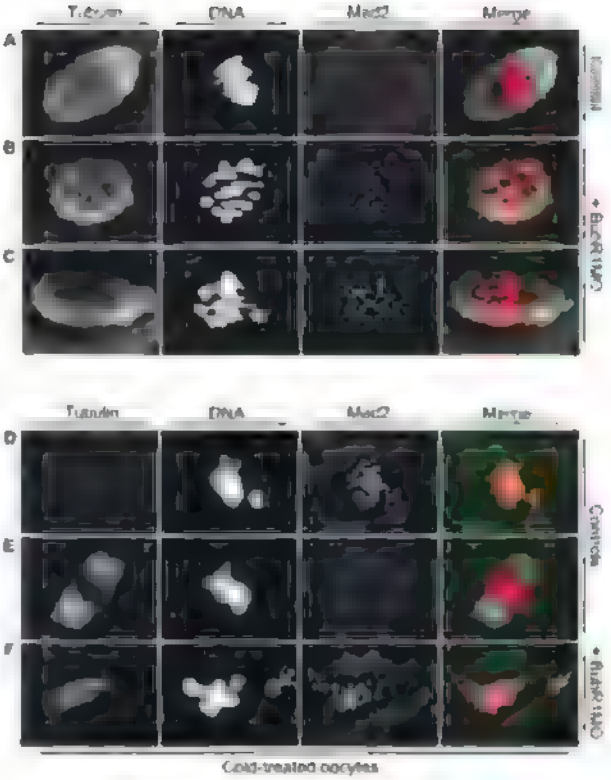

Fig. 4. BubR1 depletion impairs kinetochore-microtubule attachments. (**A** to **C**) At 8 hours after GVBD, control oocytes (A) and BubR1-depleted oocytes [(B) and (C)] were immunostained for tubulin, DNA, and Mad2. (**D** to **F**) Control oocytes were cold-treated (*9*) and immunostained at 4 (D) and 8 (E) hours after GVBD. Note the change in spindle morphology after cold treatment [compare (A) and (E)]. BubR1-depleted oocytes were cold-treated and immunostained at 8 hours after GVBD (F) ($N \geq 20$ oocytes per group). Chromosomes are extended, although kinetochore-microtubule attachments are lacking [(B) and (C)], implicating direct contacts between microtubules and chromatin as demonstrated previously (*15*). Conversely, chromosomes become compacted when microtubules are lacking (F, white arrow).

BubR1-depleted oocytes experience MI arrest while BubR1 overexpression accelerates MI (fig. S4D).

These data uncover a contrast between somatic cells and oocytes: during APC-Cdh1 dominated prometaphase I in oocytes, BubR1 promotes M-phase progression by stabilizing Cdh1, whereas in mitotic prometaphase, where APC-Cdc20 predominates, BubR1 delays anaphase onset by inhibiting APC-Cdc20. Moreover, cyclin B1 is the APC substrate that is preferentially regulated by BubR1 during mitosis (*12*), whereas during MI, it is securin. BubR1 deficiency could have grave consequences for fertility by reducing the prophase I–arrested oocyte reservoir and compromising the yield of fertilizable eggs.

References and Notes

1. J. Peters, *Nat. Rev. Mol. Cell Biol.* **7**, 644 (2006).
2. P. Marangos, J. Carroll, *Nat. Cell Biol.* **10**, 445 (2008).
3. A. Reis, H. Chang, M. Levasseur, K. Jones, *Nat. Cell Biol.* **8**, 539 (2006).
4. A. Reis *et al.*, *Nat. Cell Biol.* **9**, 1192 (2007).
5. M. Herbert *et al.*, *Nat. Cell Biol.* **5**, 1023 (2003).
6. A. Musacchio, E. D. Salmon, *Nat. Rev. Mol. Cell Biol.* **8**, 379 (2007).
7. H. Homer *et al.*, *Genes Dev.* **19**, 202 (2005).
8. B. E. McGuinness *et al.*, *Curr. Biol.* **19**, 369 (2009).
9. Materials and methods are available as supporting material on *Science* Online.
10. P. Cheslock, B. Kemp, R. Boumil, D. Dawson, *Nat. Genet.* **37**, 756 (2005).
11. N. Malmanche *et al.*, *Curr. Biol.* **17**, 1489 (2007).
12. K. B. Jeganathan, L. Malureanu, J. M. van Deursen, *Nature* **438**, 1036 (2005).
13. M. Lampson, T. Kapoor, *Nat. Cell Biol.* **7**, 93 (2005).
14. J. C. Waters, R. H. Chen, A. W. Murray, E. D. Salmon, *J. Cell Biol.* **141**, 1181 (1998).
15. S. Brunet *et al.*, *J. Cell Biol.* **146**, 1 (1999).
16. D. Baker *et al.*, *Nat. Genet.* **36**, 744 (2004).

17. This work was supported by a Wellcome Trust Clinical Fellowship (082587/Z/07/Z) to H.H. J.C. is funded by a Medical Research Council grant. We thank S. Taylor, W. Earnshaw, and K. Wassmann for reagents.

Supporting Online Material

www.sciencemag.org/cgi/content/full/326/5955/991/DC1
Materials and Methods
Figs. S1 to S11
References

22 April 2009; accepted 24 September 2009
10.1126/science.1175326

Two Chemoreceptors Mediate Developmental Effects of Dauer Pheromone in *C. elegans*

Kyuhyung Kim,[1] Koji Sato,[2] Mayumi Shibuya,[1] Danna M. Zeiger,[1] Rebecca A. Butcher,[3] Justin R. Ragains,[3] Jon Clardy,[3] Kazushige Touhara,[2] Piali Sengupta[1]*

Intraspecific chemical communication is mediated by signals called pheromones. *Caenorhabditis elegans* secretes a mixture of small molecules (collectively termed dauer pheromone) that regulates entry into the alternate dauer larval stage and also modulates adult behavior via as yet unknown receptors. Here, we identify two heterotrimeric GTP-binding protein (G protein)–coupled receptors (GPCRs) that mediate dauer formation in response to a subset of dauer pheromone components. The SRBC-64 and SRBC-66 GPCRs are members of the large *Caenorhabditis*-specific SRBC subfamily and are expressed in the ASK chemosensory neurons, which are required for pheromone-induced dauer formation. Expression of both, but not each receptor alone, confers pheromone-mediated effects on heterologous cells. Identification of dauer pheromone receptors will allow a better understanding of the signaling cascades that transduce the context-dependent effects of ecologically important chemical signals.

Pheromones are molecules secreted by an individual that induce behavioral or developmental changes in other animals of the same species (*1*). Pheromone signals can trigger long-term changes in development or physiology (primer effects) by modulating endocrine signaling and gene expression, or short-term changes in behaviors (releaser effects) via acute effects on neuronal responses (*2*). The mechanisms by which the same molecule (or molecules) can elicit these markedly distinct effects are not well understood. The nematode *C. elegans* secretes a complex mixture of chemicals that are collectively termed dauer pheromone. Dauer pheromone concentrations are assessed before the first larval molt and regulate the decision either to proceed through the reproductive cycle or to enter into the alternate, developmentally arrested dauer developmental stage (*3*, *4*). Dauer pheromone also modulates adult behaviors (*5*, *6*), indicating that it can evoke both primer and releaser effects in *C. elegans*. The active components of dauer pheromone have recently been shown to be structurally related derivatives of the dideoxysugar ascarylose (*7*–*9*), including the ascarosides C6, C9, C7, and C3 (these molecules are referred to based on the numbers of carbons in their side chains) (fig. S1). However, pheromone receptors are as yet unidentified.

In the course of searching for mutants that exhibit altered responses to dauer pheromone (*10*), we found that mutations in the predicted GTP-binding protein (G protein)–coupled receptor (GPCR) gene *srbc-64* resulted in defects in dauer formation. Loss-of-function mutations in both *srbc-64* and the closely related *srbc-66* gene (fig. S2) (*11*) resulted in similar strong defects in the ability to form dauers in response to C6, C9, and C7, with weaker defects in response to C3 (Fig. 1, A to D). These defects could be rescued upon expression of wild-type

[1]Department of Biology and National Center for Behavioral Genomics, Brandeis University, Waltham, MA 02454, USA. [2]Department of Integrated Biosciences, University of Tokyo, Chiba 277-8562, Japan. [3]Department of Biological Chemistry and Molecular Pharmacology, Harvard Medical School, Boston, MA 02115, USA.

*To whom correspondence should be addressed. E-mail: sengupta@brandeis.edu

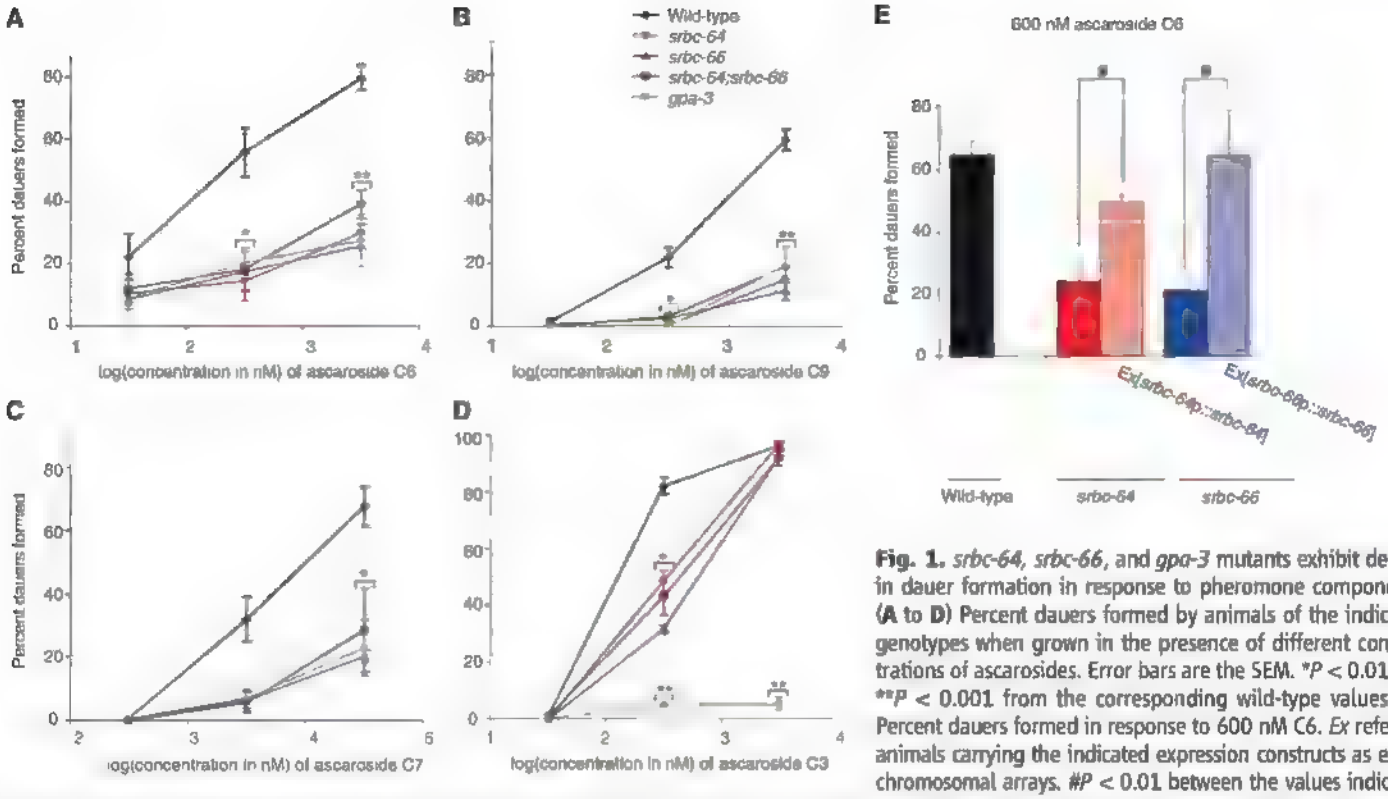

Fig. 1. *srbc-64*, *srbc-66*, and *gpa-3* mutants exhibit defects in dauer formation in response to pheromone components. (**A** to **D**) Percent dauers formed by animals of the indicated genotypes when grown in the presence of different concentrations of ascarosides. Error bars are the SEM. $^{*}P < 0.01$ and $^{**}P < 0.001$ from the corresponding wild-type values. (**E**) Percent dauers formed in response to 600 nM C6. *Ex* refers to animals carrying the indicated expression constructs as extrachromosomal arrays. $\#P < 0.01$ between the values indicated by brackets. Shown are the averages from at least four independent experiments with 50 to 100 animals each. For each experiment, all strains were assayed in parallel.

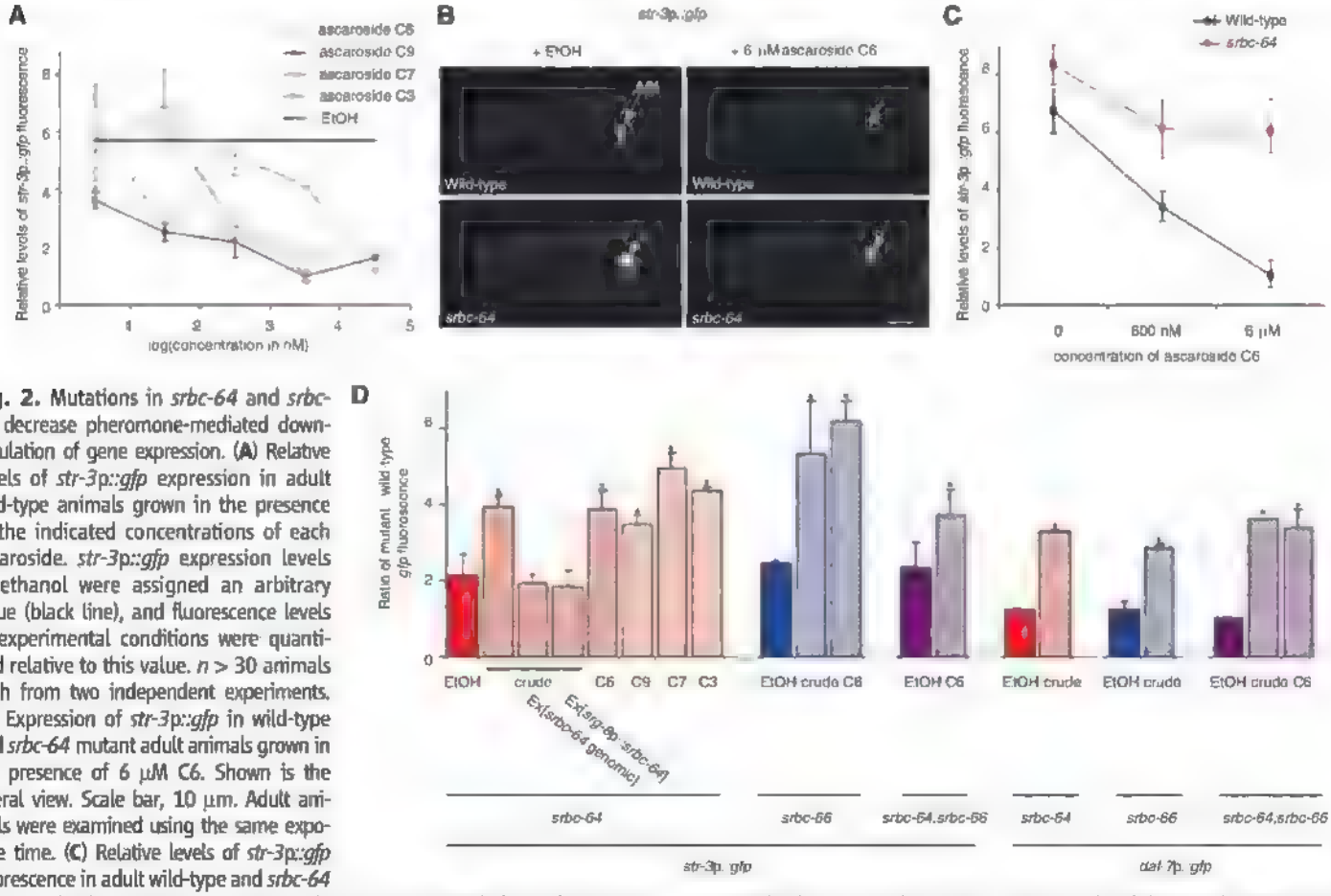

Fig. 2. Mutations in *srbc-64* and *srbc-66* decrease pheromone-mediated downregulation of gene expression. (**A**) Relative levels of *str-3p::gfp* expression in adult wild-type animals grown in the presence of the indicated concentrations of each ascaroside. *str-3p::gfp* expression levels in ethanol were assigned an arbitrary value (black line), and fluorescence levels in experimental conditions were quantified relative to this value. $n > 30$ animals each from two independent experiments. (**B**) Expression of *str-3p::gfp* in wild-type and *srbc-64* mutant adult animals grown in the presence of 6 μM C6. Shown is the lateral view. Scale bar, 10 μm. Adult animals were examined using the same exposure time. (**C**) Relative levels of *str-3p::gfp* fluorescence in adult wild-type and *srbc-64* mutant animals, grown in the presence of C6. $n > 50$ animals for each from two independent experiments. (**D**) Shown is the ratio of *gfp* fluorescence in animals of the indicated genotypes to *gfp* levels in wild-type animals grown on the same plates in the presence of ethanol, crude pheromone (1 μl/ml), or ascarosides (C3, C6, and C9, 6 μM; C7, 60 μM). Adult animals were examined in all cases. $n > 30$ animals each from two independent experiments. Error bars are the SEM. $^{*}P < 0.05$ from wild type [with the exception of (D), in which values are compared with those of animals grown in ethanol].

srbc-64 and *srbc-66* cDNAs driven under their respective upstream regulatory sequences (Fig. 1E) but not by the related *srbc-65* gene (fig. S3). *srbc-64; srbc-66* double mutants exhibited phenotypes similar to those of either single mutant alone (Fig. 1, A to D). Single and double mutants retained the ability to form dauers at high concentrations of C6, C7, and C9 and showed wild-type responses to high concentrations of C3 (Fig. 1, A to D), suggesting that additional receptors, perhaps of the SRBC subfamily, are also likely to play a role. These findings are consistent with previous observations that suggested that C6, C9, and C7 may act in the same pathway to promote dauer formation (*8*), whereas C3 may target a distinct pathway (*8*).

Pheromone regulates dauer formation in part via repression of *daf-7* transforming growth factor β (TGF-β) expression in the bilateral ASI chemosensory neuron pair (*12*, *13*) and also represses expression of the candidate *str-3* chemoreceptor gene in the ASI neurons (*14*, *15*). The four examined ascarosides also down-regulated expression of the *green fluorescent protein* (*gfp*) reporter gene driven under *str-3* or *daf-7* regulatory sequences (Fig. 2, A and B, and fig. S4), with C3, C6, and C9 being more potent than C7. Repression of pheromone-mediated gene expression was affected in *srbc-64*, *srbc-66*, and *srbc-64; srbc-66* mutants (Fig. 2, B to D, and fig. S4) and could be rescued upon expression of genomic receptor sequences (Fig. 2D). These observations were further validated by examining the effects of pheromone on endogenous *str-3* message levels via quantitative reverse transcription polymerase chain reaction (RT-PCR) (fig. S4). The placement of SRBC-66 upstream of *daf-7* TGF-β signaling in dauer formation was also verified by means of epistasis analysis (table S1). These results indicate that SRBC-64 and SRBC-66 partly mediate the effects of all examined ascarosides on both dauer formation and gene expression.

We next determined the site (or sites) of action of SRBC-64 and SRBC-66 in the regulation of dauer formation and gene expression. We found that full-length GFP-tagged SRBC-64 and SRBC-66 proteins were expressed in and localized to the sensory cilia of the ASK chemosensory neurons (Fig. 3A and fig. S5). The expression levels and subcellular localization of each chemoreceptor were not altered in the absence of the other chemoreceptor (fig. S5), suggesting that these proteins are not dependent on each other for correct expression or localization. Expression of *srbc-64* or *srbc-66* specifically in the ASK neurons, but not in the ASI neurons, was sufficient to rescue the dauer formation defects (Fig. 1E and fig. S6). Expression of *srbc-64* under the ASK-specific *srg-8* promoter (*16*) also rescued the gene expression defects of *srbc-64* mutants (Fig. 2D), further indicating that SRBC-64 and SRBC-66 act in the ASK neurons.

Previous work showed that ablation of the ASK neurons, particularly in combination with ablation of other chemosensory neuron types, decreases the efficacy of dauer formation by crude pheromone extracts (*12*). To further examine the contribution of the ASK neurons to dauer formation, we examined dauer formation in animals in which the ASK neurons have been genetically ablated via expression of the mouse caspase-1 gene expressed under an ASK-specific promoter (the animals were a gift from Dr. R. Shingai) (fig. S7). Animals lacking the ASK neurons exhibited strong defects in dauer formation in response to C6 and weaker defects in response to C3 (Fig. 3, B and C). The dauer formation defect of ASK-ablated animals was significantly stronger than that of *srbc-64, srbc-66* double mutants (Fig. 3, B and C), suggesting that additional ASK-expressed chemoreceptors probably contribute to the response.

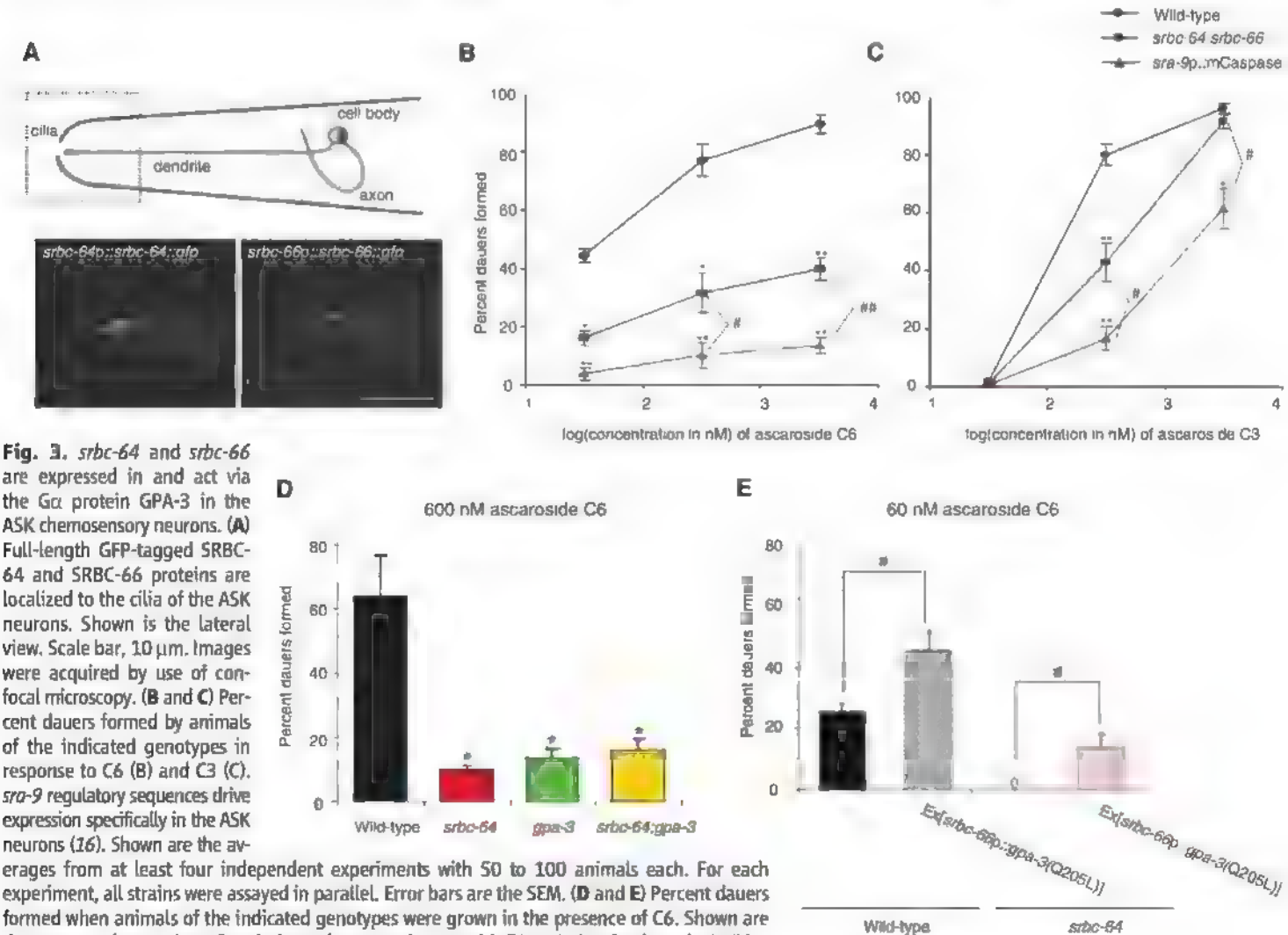

Fig. 3. *srbc-64* and *srbc-66* are expressed in and act via the Gα protein GPA-3 in the ASK chemosensory neurons. (**A**) Full-length GFP-tagged SRBC-64 and SRBC-66 proteins are localized to the cilia of the ASK neurons. Shown is the lateral view. Scale bar, 10 μm. Images were acquired by use of confocal microscopy. (**B** and **C**) Percent dauers formed by animals of the indicated genotypes in response to C6 (B) and C3 (C). *sra-9* regulatory sequences drive expression specifically in the ASK neurons (*16*). Shown are the averages from at least four independent experiments with 50 to 100 animals each. For each experiment, all strains were assayed in parallel. Error bars are the SEM. (**D** and **E**) Percent dauers formed when animals of the indicated genotypes were grown in the presence of C6. Shown are the averages from at least four independent experiments with 50 to 100 animals each. ###$P <$ 0.01 and ##$P < 0.001$, between the values indicated by brackets. *$P < 0.01$ and **$P < 0.001$ from corresponding values of wild type animals.

We next investigated the intracellular mechanisms mediating the dauer pheromone response in the ASK neurons. Down-regulation of intracellular cyclic guanosine monophosphate (cGMP) levels has previously been implicated in pheromone-regulated dauer formation. Addition of 8-bromo cyclic guanosine monophosphate (8-Br-cGMP) suppresses pheromone-induced dauer formation (*17*), and loss-of-function mutations in the *daf-11* receptor guanylyl cyclase result in constitutive dauer formation as well as the down-regulation of *daf-7p*::*gfp* expression (*17*, *18*). DAF-11 appears to act in multiple cell types, including the ASK neurons, to regulate dauer formation (*12*, *18*). We confirmed that mutations in *daf-11* also strongly down-regulate *str-3p*::*gfp* expression (fig. S8), suggesting that addition of pheromone decreases intracellular cyclic nucleotide levels to both promote dauer formation and down-regulate gene expression.

The Gα proteins GPA-2 and GPA-3 have been proposed to mediate pheromone signal transduction, although their sites of action are unknown (*19*). Loss-of-function mutations in *gpa-3* resulted in defects in dauer formation and *str-3p*::*gfp* repression in response to ascarosides (Figs. 1, A to D, and 3D and fig. S9). *srbc-64; gpa-3* and *srbc-66 gpa-3* double mutants exhibited dauer formation defects similar to those of either single mutant alone (Fig. 3D and fig. S9), and expression of constitutively activated GPA-3[Q205L] specifically in the ASK neurons resulted in increased dauer formation and partly bypassed the dauer formation defects of *srbc-64* and *srbc-66* mutants (Fig. 3E and fig. S9). Taken together, these observations are consistent with a model in which pheromone signals via SRBC-64 and SRBC-66 chemoreceptors and the GPA-3 Gα protein in larval ASK neurons to inhibit DAF-11 guanylyl cyclase activity and promote dauer formation (fig. S10).

To investigate whether expression of SRBC-64 and SRBC-66 was sufficient to confer pheromone responses in a heterologous context, we expressed one or both receptors in human embryonic kidney (HEK) 293 cells and monitored intracellular second messenger levels upon the addition of ascarosides. Coexpression of SRBC-64 and SRBC-66, but not each receptor alone, enhanced forskolin-mediated increases in cyclic adenosine monophosphate (cAMP) levels (Fig. 4, A and B), and this increase was significantly inhibited upon addition of C6 and C9 at different concentrations (Fig. 4, A to C). Similar inhibition was not observed in cells transfected with the control construct, SRBC-64 or SRBC-66 alone, or upon addition of the structurally unrelated odorants diacetyl that is attractive to *C. elegans* or a mouse pheromone 2-heptanone (Fig. 4, A and B). Moreover, ascarosides did not affect the increase in cAMP levels resulting from the activation of adenylyl cyclase by the mouse eugenol olfactory receptor in the presence of eugenol (fig. S11). Receptors that exhibit constitutive basal activity such as histamine H_2 receptors similarly enhance forskolin-mediated cAMP production in transfected cells, and this increased response is inhibited by inverse agonists (*20*). Thus, it is conceivable that ascarosides act as inverse agonists of SRBC-64 and SRBC-66 receptors. These results indicate that coexpression of SRBC-64 and SRBC-66 is sufficient to confer ascaroside-dependent responses in HEK293 cells. Moreover, pheromone acts via SRBC-64 and SRBC-66 to decrease intracellular cyclic nucleotide levels both in vivo and in vitro.

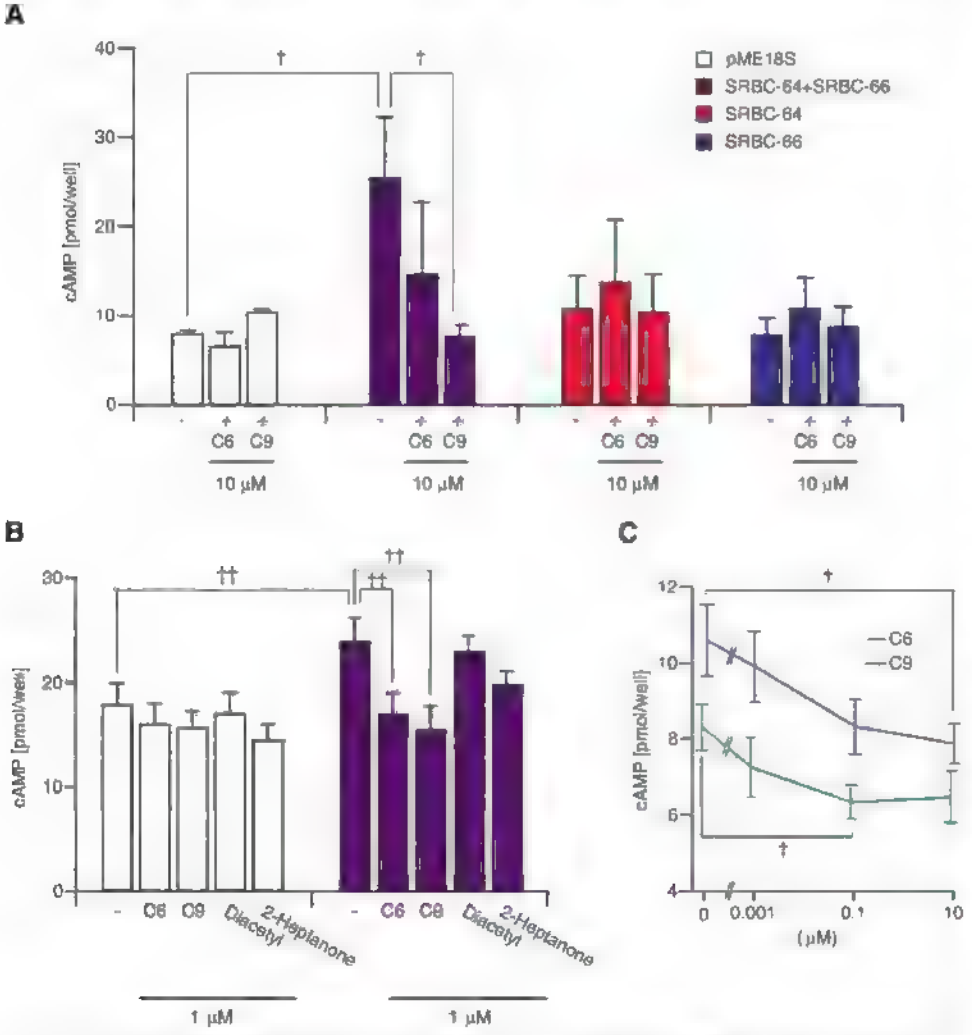

Fig. 4. Ascarosides inhibit forskolin-induced cAMP production in HEK293 cells coexpressing SRBC-64 and SRBC-66. (**A** to **C**) HEK293 cells were transiently transfected with the indicated expression constructs and stimulated with 5 μM forskolin in the absence or presence of the indicated compounds. pME18S is a control vector. (**C**) Cells were cotransfected with SRBC 64 and SRBC 66. Representative data from one of four independent experiments are shown. Each data point is the average of three to 11 trials. †$P < 0.05$ and ††$P < 0.01$ between the values indicated by brackets.

We next asked whether in addition to mediating the developmental effects, SRBC-64 and SRBC-66 also mediate the adult acute effects of dauer pheromone (*5*, *6*). Recently, ASK neurons in adult hermaphrodites have been shown to respond to a mixture of C3, C6, and C9 with a decrease in intracellular calcium levels, and this calcium response has been associated with a behavioral response of aggregation and related behaviors (*5*). We found that calcium dynamics in adult ASK neurons in response to C3 and C6 were unaffected in *srbc-64; srbc-66* or *gpa-3* mutant animals (fig. S12), despite the fact that mutations in each strongly affected pheromone-induced dauer formation (Fig. 1, A to D). We were unable to monitor intracellular calcium levels in larval ASK neurons because of low calcium sensor expression levels. These results indicate that the long- and short-term effects of dauer pheromone may be mediated via distinct receptors and signaling cascades at different developmental stages.

Taken together, our findings are consistent with the hypothesis that SRBC-64 and SRBC-66 are receptors for subsets of dauer pheromone components in the dauer formation pathway and that alternate receptors and signaling cascades mediate adult pheromone responses. Whereas short-term releaser effects of pheromones appear to be mediated by fast neuronal and synaptic responses (*5*, *21*), long-term primer effects of pheromones occur on a slower developmental time scale, involving long-term changes in gene expression and modulation of neurohormonal signaling (*22*, *23*). The *C. elegans* genome encodes 86 predicted members of the *srbc* subfamily (*11*), which has undergone extensive expansion in *C. elegans*. Large lineage-specific gains and losses in gene numbers have been noted in other chemoreceptor families that are proposed to mediate responses to niche- and species-specific signals such as pheromones (*24*). A particular characteristic of

the SRBC subfamily is the presence of four invariant Cys residues in the third extracellular loop (*11*), which may bind structurally related ligands such as ascarosides. Expression of additional SRBC chemoreceptors, coupled to distinct downstream signaling proteins, may account for the distinct effects of pheromone at different developmental stages or in different sexes (*5*, *6*). Expansion of the SRBC subfamily may therefore contribute to the fidelity and diversity of the pheromone response in *C. elegans*.

Our results imply that after pheromone binding, the ASK neurons communicate with the ASI neurons via as-yet unknown signaling pathways to regulate critical developmental decisions. Integration of multiple environmental cues such as pheromone, food, and temperature signals, as well as information regarding internal state, may allow for the precise regulation of neurohormone signaling and dauer entry by the ASI neurons (*12*, *13*, *25*, *26*). This integration resembles the monitoring of external and internal signals such as nutritional status and temperature cues by the hypothalamus to regulate metabolism and behavior via neuroendocrine and autonomic mechanisms (*27*). Identification of members of the SRBC subfamily as receptors for a subset of pheromone components will now allow us to begin to explore the mechanisms by which complex species-specific chemical cues elicit the appropriate stage- and sex-specific developmental and behavioral responses and may provide insights into related processes in other animals.

References and Notes

1. P. Karlson, M. Lüscher, *Nature* **183**, 55 (1959).
2. T. S. Wyatt, *Pheromones and Animal Behavior: Communication by Smell and Taste* (Cambridge Univ. Press, Cambridge, 2003).
3. J. W. Golden, D. L. Riddle, *Dev. Biol.* **102**, 368 (1984).
4. J. W. Golden, D. L. Riddle, *Science* **218**, 578 (1982).
5. E. Z. Macosko *et al.*, *Nature* **458**, 1171 (2009).
6. J. Srinivasan *et al.*, *Nature* **454**, 1115 (2008).
7. P.-Y. Jeong *et al.*, *Nature* **433**, 541 (2005).
8. R. A. Butcher, J. R. Ragains, E. Kim, J. Clardy, *Proc. Natl. Acad. Sci. U.S.A.* **105**, 14288 (2008).
9. R. A. Butcher, M. Fujita, F. C. Schroeder, J. Clardy, *Nat. Chem. Biol.* **3**, 420 (2007).
10. Materials and methods are available as supporting material on *Science* Online.
11. J. H. Thomas, H. R. Robertson, *BMC Biol.* **6**, 42 (2008).
12. W. S. Schackwitz, T. Inoue, J. H. Thomas, *Neuron* **17**, 719 (1996).
13. P. Ren *et al.*, *Science* **274**, 1389 (1996).
14. E. L. Peckol, E. R. Troemel, C. I. Bargmann, *Proc. Natl. Acad. Sci. U.S.A.* **98**, 11032 (2001).
15. K. M. Nolan, T. R. Sarafi-Reinach, J. G. Horne, A. M. Saffer, P. Sengupta, *Genes Dev.* **16**, 3061 (2002).
16. E. R. Troemel, J. H. Chou, N. D. Dwyer, H. A. Colbert, C. I. Bargmann, *Cell* **83**, 207 (1995).
17. D. A. Birnby *et al.*, *Genetics* **155**, 85 (2000).
18. M. Murakami, M. Koga, Y. Ohshima, *Mech. Dev.* **109**, 27 (2001).
19. R. R. Zwaal, J. E. Mendel, P. W. Sternberg, R. H. Plasterk, *Genetics* **145**, 715 (1997).
20. A. F. Alewijnse *et al.*, *FEBS Lett.* **419**, 171 (1997).
21. A. Kurtovic, A. Widmer, B. J. Dickson, *Nature* **446**, 542 (2007).
22. C. M. Grozinger, N. M. Sharabash, C. W. Whitfield, G. E. Robinson, *Proc. Natl. Acad. Sci. U.S.A.* **100**, (suppl. 2), 14519 (2003).
23. C. Alaux *et al.*, *Genes Brain Behav.* **8**, 309 (2009).
24. W. E. Grus, J. Zhang, *Mol. Biol. Evol.* **25**, 1593 (2008).
25. W. Li, S. G. Kennedy, G. Ruvkun, *Genes Dev.* **17**, 844 (2003).
26. N. A. Bishop, L. Guarente, *Nature* **447**, 545 (2007).
27. P. Dowell, Z. Hu, M. D. Lane, *Annu. Rev. Biochem.* **74**, 515 (2005).

28. We are grateful to E. Macosko, C. Bargmann, J. Thomas, and R. Shingai for advice, assistance, and reagents. We thank the *Caenorhabditis* Genetics Center and S. Mitani for strains, members of the Sengupta lab and P. Garrity for discussion, and C. Li for critical comments. This work was supported by NSF (IOS 0542372 to P.S.), NIH (R01 GM56223 to P.S., P30 NS45713, R01 CA24487 to J.C., and F32 GM077943 to R.A.B.), and the Ministry of Education, Science, Sports, and Culture, Japan (K.T.).

Supporting Online Material

www.sciencemag.org/cgi/content/full/1176331/DC1
Materials and Methods
Figs. S1 to S12
Table S1
References

15 May 2009; accepted 21 August 2009
Published online 1 October 2009;
10.1126/science.1176331
Include this information when citing this paper

Sexual Conflict Resolved by Invasion of a Novel Sex Determiner in Lake Malawi Cichlid Fishes

Reade B. Roberts, Jennifer R. Ser, Thomas D. Kocher*

Sex determination mechanisms differ among animal species, but it is not clear how these differences evolve. New sex determiners may arise in response to sexual conflicts, which occur when traits benefit one sex but hinder the other. We identified the genetic basis for the orange-blotch (OB) color pattern, a trait under sexually antagonistic selection in the cichlid fish of Lake Malawi, East Africa. The OB phenotype is due to a cis-regulatory mutation in the *Pax7* gene. OB provides benefits of camouflage to females but disrupts the species-specific male color patterns used for mate recognition. We suggest that the resulting sexual conflict over the *OB* allele has been resolved by selection for a novel female sex determination locus that has invaded populations with an ancestral male sex determination system.

When an autosomal mutation modulates a trait to the benefit of one sex and the detriment of the other, the resulting sexually antagonistic selection creates a genetic conflict. This conflict can be resolved if expression of the phenotype is limited to the sex that gains a fitness benefit from the mutation (*1*, *2*). Sexually dimorphic pigmentation is a hallmark of the radiation of cichlid fishes in Lake Malawi, one of the three major East African Great Lakes (Malawi, Tanganyika, and Victoria). Competition for females has resulted in sexual selection for brightly colored, conspicuous males (Fig. 1B). In contrast, female coloration is generally drab and brown, making females inconspicuous to predators (*3*) (Fig. 1A).

An exception to uniformly brown pigmentation in female rock-dwelling cichlids in Lake Malawi is the orange-blotch (OB) phenotype (*4*). OB is found almost exclusively in females and usually cosegregates with the more widespread brown barred (BB) female phenotype in local populations (*3*). The OB phenotype is characterized by dark melanophore blotches of variable

Department of Biology, University of Maryland, College Park, MD 20742, USA.

*To whom correspondence should be addressed. E-mail: tdk@umd.edu

Fig. 1. OB pigmentation affects different aspects of fitness in females and males. (**A**) Typical female BB (top) and OB (bottom) morphs, represented by *Tropheops* "orange chest." (**B**) Common BB male nuptial coloration (top) and rare OB male (bottom) of *Labeotropheus fuelleborni*. (**C**) OB (white arrow) and BB (black arrow) *L. fuelleborni* females are differently cryptic over the boulder reef habitat at Nankoma Island (13°53′30″S, 34°36′43″E; frame from movie S1).

number and size on a background of orange xanthophores (Fig. 1A and fig. S1). The blotching provides an alternative form of crypsis by background-matching the mottled rock substrate that the cichlids inhabit (Fig. 1C and movie S1). The variable high-contrast blotching may also provide camouflage by disruptive coloration, independent of background matching (*5*). OB males are rare and their characteristic nuptial colors are highly disrupted (Fig. 1B) (*4*). Given the strong reliance on specific male nuptial color cues for mate recognition and attraction (*6*), the disruption of pattern is predicted to lower the fitness of OB males. The OB phenotype has been observed in more than 20 species in four genera in Lake Malawi. Similar sex-associated blotched phenotypes are found in cichlids from Lake Victoria, but the cichlids of Lake Tanganyika appear to lack comparable phenotypes (*7*).

The *OB* locus was previously localized to a 5-cM region of Malawi cichlid linkage group 5 (LG5) (*8*). In the absence of a cichlid genome sequence, we took a comparative mapping approach to refine the map interval, using the *Tetraodon* genome as a guide (Fig. 2A and fig. S2B). We identified additional markers in the region by aligning cichlid genome survey sequences to the *Tetraodon* genome (*9*, *10*) and resequencing a panel of cichlid DNA to identify polymorphisms. Genotyping these new markers confirmed the broad-scale synteny among these species.

Pedigreed families from several species of the genera *Labeotropheus* and *Metriaclima* were genotyped for newly identified microsatellite markers on LG5 (46 families, 678 individuals, 349 OB individuals; table S1). Breakpoint analysis localized *OB* to an interval of less than 1 cM, corresponding to a region from 3.9 to 4.0 Mb on *Tetraodon* chromosome 11 (Fig. 2A). We then used association mapping in natural populations to pinpoint the causative locus. Single-nucleotide polymorphism (SNP) markers were developed spanning the region, including an intronic SNP marker for each annotated gene within the *OB* interval. We measured linkage disequilibrium (LD) between OB and SNPs within natural populations of *Labeotropheus*, *Metriaclima*, and *Tropheops* from the northern and southern parts of Lake Malawi (Fig. 2B). Within each population, a peak of LD was found in a region overlapping the interval defined by breakpoint analysis (Fig. 2, C to G). Given the shared pattern of association across study populations, we created a lake-wide mapping panel to increase the effective size of the mapping population. This lake-wide panel contains BB and OB individuals from 36 distinct populations of 12 species segregating OB (table S2). Analysis of marker data across these populations increased the resolution and statistical significance of LD beyond that available from any single population (Fig. 2H).

The maintenance of strong LD in the lake-wide mapping panel suggests the presence of a single, shared haplotype of SNP genotypes across the flock. Indeed, we identified a common hap-

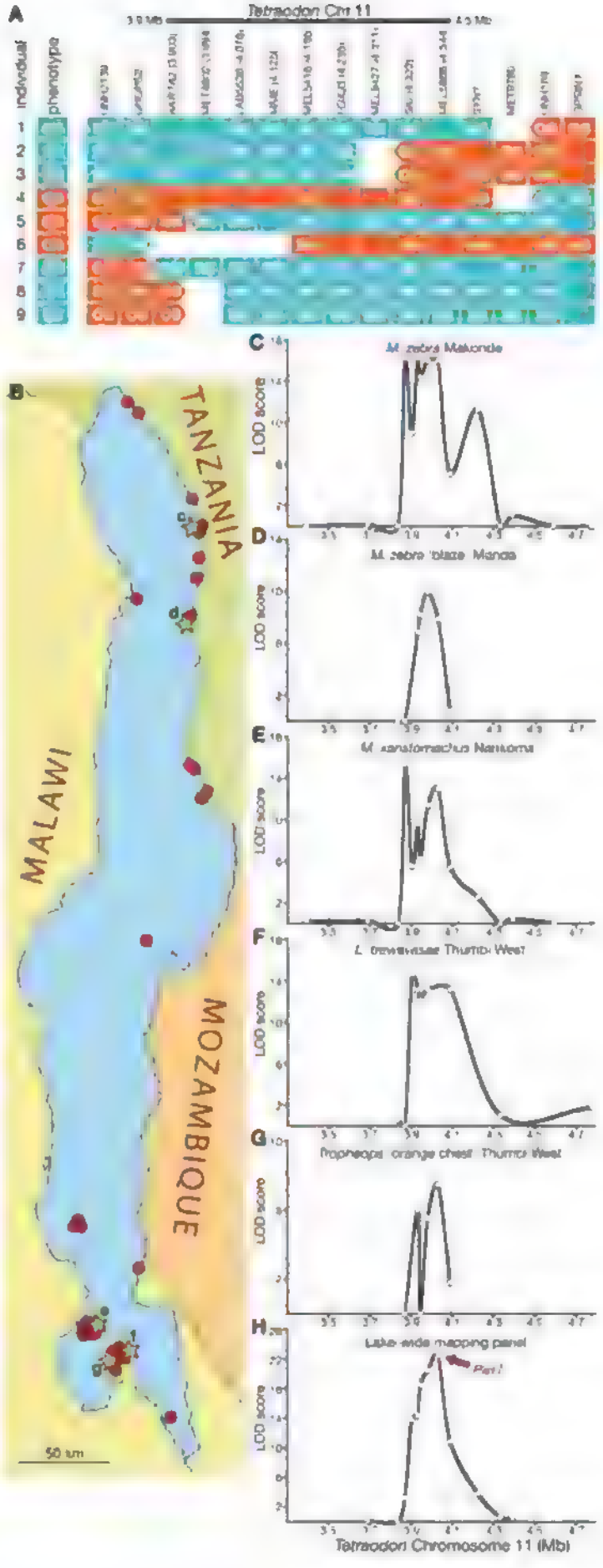

Fig. 2. Genetic mapping in families and natural populations. (**A**) Individual recombinant chromosomes (rows) at the *OB* locus from pedigreed families; "OB" and "BB" indicate genotypes of inherited maternal alleles, and empty blocks indicate noninformative markers. Marker names and Mb position on *Tetraodon* chromosome 11 are indicated at top of marker columns. Breakpoint analysis across multiple recombinants defines an *OB* interval between markers *AKR7A2* and *SKI*; one recombinant refines the interval to *AKR7A2* and MET4802. Italics indicate gene-associated markers. (**B**) Collecting sites in Lake Malawi. The populations analyzed in (C) to (G) are marked with orange stars (c to g). Localities combined for the lake-wide mapping panel (H) are marked with red dots. (**C** to **G**) Association of markers with OB and OB-like phenotypes in populations, graphed as lod scores (logarithm of the odds ratio for linkage) of association versus position on *Tetraodon* chromosome 11. (C) *M. zebra* Makonde (24 BB, 24 WhB & Wh); (D) *M. zebra* "blaze" Manda (24 BB, 16 OB & O); (E) *M. xanstomachus* Nankoma (26 BB, 22 OB); (F) *L. trewavasae* Thumbi West (24 BB, 24 OB & O); (G) *Tropheops* "orange chest" Thumbi West (32 BB, 18 OB). (**H**) Multispecies lake-wide mapping panel (34 BB, 44 OB class; table S2).

lotype signature found largely intact in OB individuals of all species, indicating a single origin of the causative *OB* mutation in Lake Malawi (Table 1). The *OB* haplotype block extends from *Akr7A2* to *Pax7* in most individuals, and comparative genomic information indicates that this block includes at least five genes (fig. S2). Comparison to outgroup species suggests that BB chromosomes represent the ancestral haplotypes across this interval (table S3). The single blotched cichlid examined from Lake Victoria also carries an ancestral haplotype, suggesting an indepen-

Table 1. The most prevalent SNP genotypes at the *OB* locus in the four genera segregating OB and in outgroup genera. The most frequent OB and BB haplotypes are indicated separately at the bottom. SNP genotypes indicating the OB-specific haplotype signature are in orange type.

Genus*	Lake	*n* (pop)	Morph	Marker†										
				HRH1	*PPARG*	*AKR7A2*	*MEGF6*	*KCNAB2*	*DJ1*	*PAX7*	*TAS1R3*	*FOXJ3*	*SKI*	*PTK9L*
Metriaclima Ob/Ob	Malawi (mbuna)	1	OB	G	A	C	T	G	G	T	T	C	C	C
Genyochromis	Malawi (mbuna)	1	OB	G	C/A	C/T	T/C	G/A	G/T	T/C	G/T	C/T	C	A/C
Metriaclima	Malawi (mbuna)	19	OB *M. zebra*	G	C/A	C/T	T/C	G/A	G/T	T/C	G/T	C/T	C	A/C
Labeotropheus	Malawi (mbuna)	13	OB *L. fuelleborni*	G/T	A	C/T	T/C	G/A	C/T	T/C	G/T	C/T	C/T	C
Tropheops	Malawi (mbuna)	3	OB	G/T	A	C/T	T/C	G/A	G/T	T/C	G/T	C/T	C	C
Genyochromis	Malawi (mbuna)	1	BB	G	A	T	C	A	T	C	G	T	C	A/C
Metriaclima	Malawi (mbuna)	22	BB	G	A	T	C	A	T	C	G/T	C/T	C	A/C
Labeotropheus	Malawi (mbuna)	12	BB	G/T	A	T	C	A	T	C	G	C/T	C/T	C
Tropheops	Malawi (mbuna)	3	BB	G/T	A	T	C	A/G	T	C	T	C/T	C	C
Melanochromis	Malawi (mbuna)	2	-	T	A	T	C	A	T	C	G/T	T	-	C
Cynotilapia	Malawi (mbuna)	1	-	G	A	-	C	A	T	C	T	C	-	-
Aulonocara	Malawi (non-mbuna)	1	-	G	A	T	C	A	T	C	T	-	-	-
Copadichromis	Malawi (non-mbuna)	1	-	G	A	T	C	A	T	C	G/T	T	C	C
Rhamphochromis	Malawi (non-mbuna)	1	-	G	A	T	C	A	T	C	T	C	-	C
Astatotilapia	Tanganyika	1	-	G	A	-	C	A	T	C	G	-	-	C
Neolamprologus	Tanganyika	1	-	G	A	-	C	A	T	C	G	-	-	-
Pundamilia	Victoria	1	-	G	A	-	C	A	T	-	T	-	-	C
Neochromis	Victoria	1	"blotch"	G	A	-	C	A	T	C	T	-	-	-
Oreochromis	Riverine	1	-	G	-	-	C	-	-	I/D	G/T	C	-	-
	Most frequent Malawi mbuna OB haplotype			G	A	C	T	G	T	T	T	C	C	C
	Most frequent Malawi mbuna BB haplotype			G	A	T	C	A	T	C	G	C/T	C	C

*See tables S2 and S3 for details of species and localities †Intronic SNP markers labeled by gene are a subset of those used in LD analysis (Fig. 2, C to H)

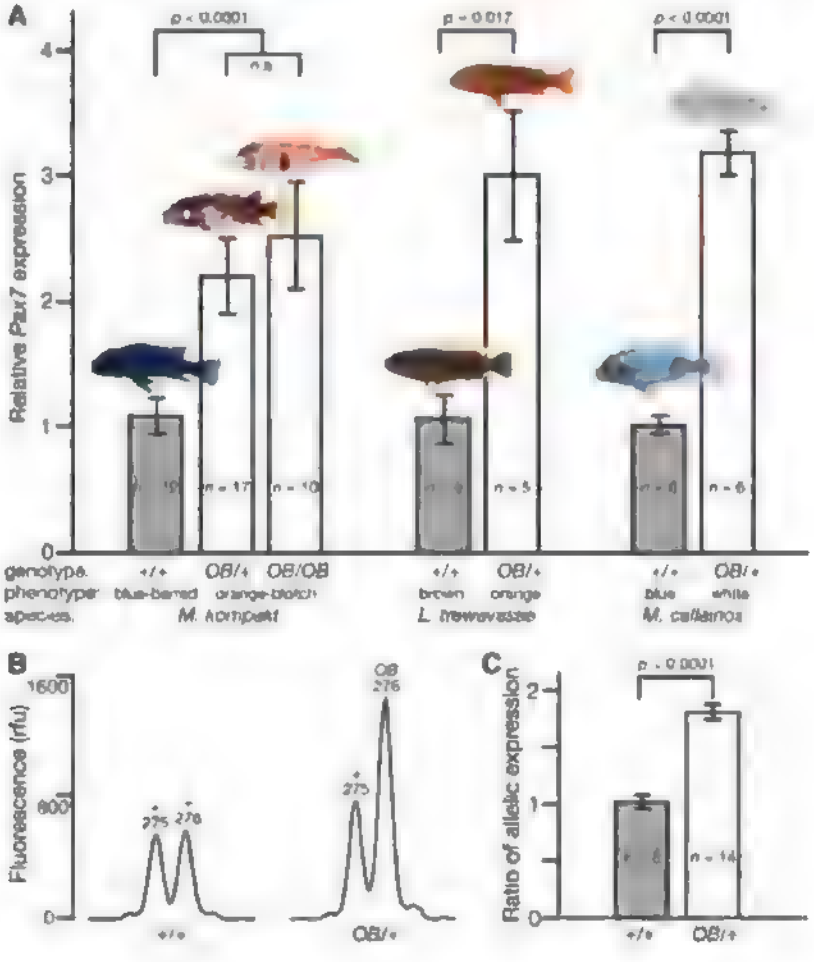

Fig. 3. *Pax7* expression is increased in OB individuals independent of species and morph. (**A**) *Pax7* expression relative to BB expression level within each species, measured by quantitative real-time polymerase chain reaction (PCR) of juvenile tailfin RNA and normalized to β-*actin* expression. *OB* genotypes and expressed phenotypes are indicated along the *x* axis. (**B** and **C**) Allele-specific expression using reverse transcription PCR of a size polymorphism in the 5′ untranslated region of *Pax7*. (B) Representative size separation traces of products from +/+ and *OB*/+ individuals, with allele type and size indicated above peaks. (C) Ratio of *OB*-sized to non–*OB*-sized allele expression. All *P* values are from pairwise *t* tests.

dent evolutionary origin for the Victorian OB-like phenotype (Table 1, *Neochromis* "blotch" morph). Our finding of a single origin of *OB* in Lake Malawi cichlids contrasts with a previous phylogenetic analysis that suggested multiple origins (*11*).

The *OB* haplotype is a genetic marker allowing us to make additional conclusions about the relationship between genotype and phenotype. Individuals in some populations are heavily pigmented with melanophore blotches, whereas individuals in other populations lack blotches almost entirely (the orange or "O" morph). Sex-linked white-blotch and white morphs ("WhB" and "Wh"), similar to OB and O morphs but lacking orange background coloration, also exist in the Malawi flock (fig. S1). Individuals of these morphs also carry the *OB* haplotype and can be definitively attributed to the *OB* locus (Table 1). Discrete morphs with different degrees of blotching sometimes segregate within a population, covering a phenotypic range similar to that found across species. OB individuals from the three study populations segregating multiple blotch phenotypes are all heterozygous for the same SNP haplotype block (Fig. 2, C, D, and F), which suggests that differences between morphs are not due to gene dosage. Discrete morphs may result from allelic variants within the *OB* haplotype or from genetic modifiers of *OB* segregating in some populations.

The peak of LD in the lake-wide mapping panel corresponds to a noncoding SNP within a *Pax3/7* subfamily gene. These transcription factors play key roles in specifying pigment cell lineages from neural crest precursors (*12*, *13*). Gene phylogeny and conserved synteny identify the OB-associated gene as cichlid *Pax7* (fig. S2). OB individuals have significantly higher expression of *Pax7* in tailfin, regardless of the degree of melanophore blotching or relative numbers of other pigment cell populations (Fig. 3A). Allele-specific expression analysis demonstrates that the *OB* allele of *Pax7* is specifically up-regulated (Fig. 3, B and C). Because no OB-associated differences were found in *Pax7* coding sequence from the species used for expression analysis, we suggest that cis-regulatory differences in *Pax7* account for the OB pigmentation phenotype (*14*).

In addition to overt pigmentation differences between BB and OB individuals, close examination reveals cell-level differences in tailfin melanophores. Melanophore number is reduced in 3-month-old *M. kompakt OB/+* individuals relative to BB broodmates [BB ($n = 7$), 414 ± 173; *OB/+* ($n = 10$), 118 ± 77; Welch's t test: $P = 0.0032$]. In contrast, contracted melanophore size is larger in *OB/+* individuals [BB ($n = 7$), 26.5 ± 8.6 pixels^2; *OB/+* ($n = 10$), 50.6 ± 14.3 pixels^2; t test: $P = 0.0013$]. The finding that up-regulation of *Pax7* in cichlids is correlated with a fewer-but-larger melanophore phenotype is particularly interesting given that down-regulation of *Pax3* in zebrafish produces a more-but-smaller melanophore phenotype (*13*). In both cichlids and zebrafish, higher *Pax3/7* dosage correlates with development of fewer, larger melanophores.

In our analysis of families and natural populations, we have been unable to genetically separate *OB* from the female sex determiner (W) known to be in the same region of LG5. Only one species in our laboratory stocks, *M. kompakt*, occasionally produces *OB/+* males. However, these OB males inherit the maternal *OB* haplotype intact, and when bred, their *OB*-carrying chromosome determines female sex in offspring (table S4) (*14*). We conclude that these OB males are genetically female at the W locus and are sex-reversed by another mechanism. Mating of *M. kompakt OB/+* males to *OB/+* females produces viable *OB/OB* homozygotes in expected Mendelian ratios (21 of 89 individuals from five broods, $\chi^2 = 1.36$, $P = 0.5067$). Thus, *OB* homozygotes are fully viable, at least on some genetic backgrounds. However, we have not observed *OB* homozygous individuals in natural populations (0 of 199 wild OB individuals), which suggests that OB males have low mating success.

The maintenance of the *OB* haplotype over evolutionary time scales might be explained by selection for tight linkage between *OB* (*Pax7*) and the W sex determiner (*15*). Linkage and suppression of recombination between *OB* and W might be further increased by a W-specific inversion encompassing both genes, a rearrangement of the kind hypothesized to be an early stage of sex chromosome evolution (*16*). However, no obvious candidate gene for sex determination is within the interval (*14*), and we found no evidence of structural rearrangements.

We suggest that *OB* originated once as a novel allele up-regulating *Pax7* expression, and was then incorporated into multiple species across four genera of the Malawi cichlid flock by sorting of an ancestral polymorphism and/or hybridization events after the radiation of species. The OB phenotype positively affects the fitness of females by providing an alternative form of crypsis against the mottled background of their habitat. Conversely, OB reduces males' fitness by disrupting their nuptial pigmentation patterns. The genetic conflict created by sexually antagonistic selection on the OB phenotype may be resolved by sexually dimorphic expression of the trait. In the case of the *OB* locus, the sexual conflict has been resolved by tight genetic linkage with a dominant female sex determiner, rather than by evolution of modifier genes to sex-limit expression of the phenotype during development. Thus, the *OB*-W haplotype has invaded populations in a manner consistent with a model of sex chromosome evolution by sexual conflict (*17*).

The OB-associated ZW sex-determining system is epistatically dominant to a putatively ancestral XY locus on LG7, which is responsible for sex determination in several other Malawi cichlids (tables S5 and S6) (*14*). We propose that sexually antagonistic selection at *OB* (*Pax7*) provided conditions facilitating the invasion of a tightly linked female sex determiner on LG5 to resolve the genetic conflict. Alternatively, the *OB* polymorphism may have arisen near a nascent female sex determiner, providing conditions for the *OB*-W allele to rise in frequency and persist in multiple lineages along with the ancestral XY sex determination system. In either case, the evolutionary success of the allele is a result of the interaction of the pigmentation and sex determination traits.

The *OB*-W locus is a nascent sex chromosome, and its existence demonstrates the interactive evolution of sexual dimorphism and sex determination resulting from the resolution of sexual conflicts. Sexually antagonistic selection is usually thought to arise from processes of sexual selection (*18*). Our results show that a novel trait increasing fitness under natural selection can readily create strong sexual conflicts, especially if the trait has a negative impact on sexually selected characters in the opposite sex. Phenotypes rarely fall into a simple dichotomy of sexually and naturally selected traits, nor do they affect overall male and female fitness equally. Thus, multiple aspects of a phenotype can trigger sexual conflicts and, ultimately, the evolution of new sex determiners. We suspect that similar genetic conflicts are important in the evolution of many other traits and likely contributed to the extraordinary rates of diversification and speciation in African cichlid fishes.

References and Notes

1. R. A. Fisher, *Biol. Rev. Camb. Philos. Soc.* **6**, 345 (1931).
2. W. R. Rice, *Evolution* **38**, 735 (1984).
3. A. Konings, *Malawi Cichlids in Their Natural Habitat* (Cichlid Press, El Paso, TX, ed. 4, 2007).
4. S. Holzberg, *J. Zool. Syst. Evol. Res.* **16**, 171 (1978).
5. H. M. Schaefer, N. Stobbe, *Proc. R. Soc. London Ser. B* **273**, 2427 (2006).
6. M. J. H. van Oppen *et al.*, *Mol. Ecol.* **7**, 991 (1998).
7. R. Lande, O. Seehausen, J. J. van Alphen, *Genetica* **112–113**, 435 (2001).
8. J. T. Streelman, R. C. Albertson, T. D. Kocher, *Mol. Ecol.* **12**, 2465 (2003).
9. Y. H. Loh *et al.*, *Genome Biol.* **9**, R113 (2008).
10. S. Kurtz *et al.*, *Genome Biol.* **5**, R12 (2004).
11. C. J. Allender, O. Seehausen, M. E. Knight, G. F. Turner, N. Maclean, *Proc. Natl. Acad. Sci. U.S.A.* **100**, 14074 (2003).
12. A. M. Lacosta, P. Mumesa, J. Ruberte, M. Sarasa, L. Domínguez, *Pigment Cell Res.* **18**, 243 (2005).
13. J. E. N. Minchin, S. M. Hughes, *Dev. Biol.* **317**, 508 (2008).
14. See supporting material on *Science* Online.
15. W. R. Rice, *Evolution* **41**, 911 (1987).
16. D. Charlesworth, B. Charlesworth, G. Marais, *Heredity* **95**, 118 (2005).
17. G. S. van Doorn, M. Kirkpatrick, *Nature* **449**, 909 (2007).
18. G. Arnqvist, L. Rowe, *Sexual Conflict* (Princeton Univ. Press, Princeton, NJ, 2005).

19. We thank O. Seehausen for providing cichlid tissues from Lake Victoria, and S. Salzberg for assistance in aligning cichlid genome sequences to the *Tetraodon* genome. Supported by NIH fellowship F32HD051383 (R.B.R.) and by NSF grant DEB-0445212 and NIH grant R01HD058635 (T.D.K.). Sequences generated in this study are deposited in GenBank under accession numbers GQ403984 to GQ403986.

Supporting Online Material

www.sciencemag.org/cgi/content/full/1174705/DC1
Materials and Methods
SOM Text
Figs. S1 and S2
Tables S1 to S7
Movie S1
References

8 April 2009; accepted 18 September 2009
Published online 1 October 2009;
10.1126/science.1174705
Include this information when citing this paper

Mutations in Two Independent Pathways Are Sufficient to Create Hermaphroditic Nematodes

Chris Baldi,[1] Soochin Cho,[2] Ronald E. Ellis[3]*

Although the nematode *Caenorhabditis elegans* produces self-fertile hermaphrodites, it descended from a male/female species, so hermaphroditism provides a model for the origin of novel traits. In the related species *C. remanei*, which has only male and female sexes, lowering the activity of *tra-2* by RNA interference created *XX* animals that made spermatids as well as oocytes, but their spermatids could not activate without the addition of male seminal fluid. However, by lowering the expression of both *tra-2* and *swm-1*, a gene that regulates sperm activation in *C. elegans*, we produced *XX* animals with active sperm that were self-fertile. Thus, the evolution of hermaphroditism in *Caenorhabditis* probably required two steps: a mutation in the sex-determination pathway that caused *XX* spermatogenesis and a mutation that allowed these spermatids to self-activate.

The genus *Caenorhabditis* includes nematodes that use two different mating systems, a gonochoristic one in which individuals are either male or female and an androdioecious one in which individuals are male or hermaphrodite. In *C. elegans* and *C. briggsae*, the *XX* animals are self-fertile hermaphrodites, which have both male and female traits. Their bodies appear female, but germ cells that differentiate during larval development become sperm, which move into the spermathecae during the first ovulation and are stored there for self-fertilization, whereas germ cells that differentiate during adulthood become oocytes, which can be fertilized either by self-sperm or male sperm. In *C. elegans*, a single pathway controls sexual fate for cells in the body and the germ line. In males, the secreted protein HER-1 inhibits the TRA-2 receptor, which allows a FEM protein/E3-ubiquitin-ligase complex to target the transcription factor TRA-1 for degradation (*1*, *2*). In hermaphrodites, TRA-1 is not degraded and represses male developmental genes such as *mab-3*, which regulates development of the intestine and male tail, and *fog-3*, which controls spermatogenesis (*1*, *2*).

The core members of the sex determination pathway in *C. elegans* are found in related species. In particular, *tra-2* (*3*, *4*), *fem-2* (*5*–*7*), *fem-3* (*7*, *8*), and *fog-3* (*9*) are conserved in both sequence and function in *C. elegans*, *C. briggsae*, and *C. remanei*. Furthermore, the interaction between TRA-2 and FEM-3 is conserved in all three species (*8*), and a TRA-2/TRA-1 interaction has been documented in *C. elegans* and *C. briggsae* (*10*).

In *C. elegans*, hermaphrodites lack HER-1 but still make sperm. This trait is due to repression of *tra-2* by FOG-2 and GLD-1, allowing spermatogenesis to occur late in larval development (*11*–*13*). *C. briggsae* lacks an ortholog of *fog-2* (*14*), but in this species the F-box protein SHE-1 promotes hermaphrodite spermatogenesis (*15*). In either case, a mutation in a single gene can cause hermaphrodites to become females (*11*, *15*). However, the phylogeny of this genus implies that the ancestor of *C. elegans* and *C. briggsae* was gonochoristic (*16*, *17*), and the mechanisms underlying the evolution of self-fertile hermaphrodites from male/female ancestors are unknown.

In *C. remanei*, which has male and female individuals, knocking down *tra-2* activity by RNA interference (RNAi) causes *XX* animals to develop male bodies and make sperm (*4*). Because genes that oppose *tra-2* are needed for hermaphrodite development in *C. elegans* and *C. briggsae* (*12*, *13*, *15*), we decreased but did not eliminate *tra-2* activity in *C. remanei* females, which resulted in hermaphrodite-like animals, pseudomales, females, and animals with masculinized germ lines (*18*). The hermaphrodite-like animals had normal female bodies, including a bilobed gonad like that found in females containing an ovary and spermatheca in each arm, connected by a central uterus (Fig. 1, A to C). The vulva was connected to the uterus and could lay eggs under control of the nervous system and sex muscles. These animals made both male and female germ cells, although they began oogenesis about a day later than females, probably because of the time devoted to spermatogenesis. Because they could not self-fertilize ($n = 0/27$), we call them pseudohermaphrodites. When we crossed individual pseudohermaphrodites with males, most of them laid eggs, although their broods were smaller than those of the wild type (47 ± 14 eggs and $n = 12$ for pseudohermaphrodites, compared with 252 ± 46 eggs and $n = 5$ for wild type; $P < 0.009$ in an unpaired t test). Thus, many of the oocytes found in pseudohermaphrodites are functional, and their self-infertility seemed to be caused by defective sperm.

In *C. elegans*, the major sperm protein stimulates ovulation (*19*) and forms the cytoskeleton of activated sperm, which allows sperm to crawl toward and fertilize oocytes (*20*). Because pseudohermaphrodite spermatids did not function, we assayed the major sperm protein and found that it was abundant (Fig. 1D). Next, we found that 78% of the pseudohermaphrodites ovulated within 1 day of producing oocytes ($n = 27$), compared with 0% of control females ($n = 30$). Because spermatids from pseudohermaphrodites stimulate ovulation, we concluded that they release major sperm protein. Although the spermatids were normal in these respects, differential interference contrast (DIC) optics revealed that they clustered in the ovaries and did not move into the spermathecae of young adults, suggesting that they had not activated (Fig. 1C, inset). Furthermore, older animals had spermatids in the uterus, but the ovaries and spermathecae were empty, suggesting that ovulation pushed inactive spermatids into the uterus, as in some *C. elegans* mutants (*21*).

To assay sperm activation, we examined adult pseudohermaphrodites and males and found that both released spermatids that remained round and inactive (Fig. 1E). By contrast, sperm from *C. elegans* adult hermaphrodites at this stage had already activated, produced pseudopodia, and begun to crawl (*22*). When exposed to media containing a mix of proteases that activates *C. remanei* male spermatids (*23*), the spermatids from pseudohermaphrodites produced pseudopods at a frequency that was not significantly different from that of their male counterparts (Fig. 1E, $P > 0.2315$ in an unpaired t test). Thus, pseudohermaphrodite spermatids do not activate in vivo but are capable of activation.

In *C. elegans*, male seminal fluid activates hermaphrodite spermatids (*24*). Furthermore, *C. elegans* males can mate with *C. remanei* females but do not produce embryos (*25*, *26*). However, crossing *C. elegans him-6* males with *C. remanei* pseudohermaphrodites yielded 142 eggs. Thirteen of these eggs (9%) developed into adult females, although 120 died as embryos and 9 died during larval development. Crossing pseudohermaphrodites with *Cr-fog-3(RNAi)* males, which cannot sire progeny because they only make oocytes, showed that *C. remanei* seminal fluid also activated spermatids, because eight mothers produced a total of 16 inviable eggs.

We observed a variety of terminal phenotypes among the self-progeny in these crosses (fig. S1). Some embryos died before 200 min (when apoptosis normally begins), some shortly afterward, and some after morphogenesis. Eight progeny arrested as L2 larvae, and two of these had abnormal granules in their intestines. Control crosses of wild-type strains resulted in 5 to 10% embryonic death (fig. S2), probably because of balanced deleterious mutations found in all *C. remanei* strains (*27*). However, more than 25% of the embryos produced by pseudohermaphrodites crossed with *C. remanei* males died, including 40% during the first day of reproduction, when mothers switch from spermatogenesis to oogenesis. These data suggest that some of the pseudohermaphrodite oocytes are defective. Because the lethality among self-progeny was much higher than among cross-progeny (91% versus 25%), some of the self-sperm are probably defective, too.

[1]Graduate School of Biomedical Sciences, University of Medicine and Dentistry of New Jersey, Stratford, NJ 08084, USA. [2]Department of Biology, Creighton University, Omaha, NE 68178, USA. [3]Department of Molecular Biology, School of Osteopathic Medicine, University of Medicine and Dentistry of New Jersey, Stratford, NJ 08084, USA.

*To whom correspondence should be addressed. E-mail: ronellis@umdnj.edu

In *C. elegans*, *swm-1* encodes a protease inhibitor with two TIL domains, and a short inhibitor with only one, and prevents the premature activation of sperm in males (*28*). Analysis of predicted proteins suggests that *C. remanei*, *C. briggsae*, *C. brenneri*, and *C. japonica* all have conserved orthologs of *swm-1* (Fig. 2B and figs. S3 and S5). In addition, putative paralogs of SWM-1 were seen in *C. elegans* and *C. briggsae* (Fig. 2B and figs. S4 and S5). In the *C. elegans* genome, the paralog C25E10.8 is an adjacent duplicate of *swm-1* (fig. S5C). It is only 81% similar over 137 residues, and its reactive sites differ from SWM-1. Lastly, when deleted, C25E10.8 does not affect sperm activation (*28*). In *C. briggsae*, the paralog CBG19173 is also an adjacent duplicate (fig. S5A). It encodes a protein only 75% similar to Cbg-SWM-1 over 137 residues, and both of its reactive sites are different.

We dissected *C. remanei swm-1(RNAi)* males and saw that 65/94 sperm had activated to the spiky stage, whereas control spermatids were inactive. Thus, *C. remanei swm-1* appears to regulate sperm activation, like its *C. elegans* ortholog. When we characterized *tra-2(RNAi); swm-1(RNAi) XX* animals that produced both sperm and oocytes, we found that 53.3% were self-fertile hermaphrodites. Out of 103 eggs produced, 15 hatched and 10 grew to adulthood; all of the adults were female, as expected for *XX* self-progeny.

Thus, we propose that self-fertile hermaphrodites originated from the alteration of both the sex-determination and *XX* sperm-activation pathways.

In *C. elegans*, the development of self-fertile hermaphrodites requires that FOG-2 bind GLD-1 (*13*), which interacts with *tra-2* mRNAs to block their translation (*12*). Although there is no FOG-2/GLD-1 complex in *C. briggsae* (*14*), the novel gene *she-1* drives hermaphroditic development in that species, and genetic tests suggest that *she-1* also acts upstream of *tra-2* to regulate its activity (*15*). Lastly, our data show that lowering *tra-2* activity in *C. remanei* can create pseudohermaphrodites. Thus, mutations that affect *tra-2* activity might play a general role in the evolution of hermaphrodites, although it remains possible that other genes in the pathway are also important (*7*).

Because *C. elegans* germ cell fates can be affected by mutations that change either the HER-1 or TRA-1 binding sites on TRA-2 or the GLD-1 binding site in *tra-2* mRNA or that alter a protease that cleaves TRA-2 (*1*), *tra-2* might be more sensitive to changes in upstream regulators than other genes. In addition, it might be better positioned to alter germline fates, because TRA-2 acts through the FEM proteins to control TRA-1 stability and also binds TRA-1 directly (*1*) (Fig. 3A). Thus, mutations that cause hermaphroditic development by targeting *tra-2* might be more frequent than mutations that act elsewhere to cause hermaphroditic development.

Changes to the sex-determination pathway are not sufficient to create self-fertile hermaphrodites because spermatids in affected animals do not self-activate. In *C. elegans*, mutations in *spe-8*, *spe-12*, *spe-19*, *spe-27*, or *spe-29* block activation of spermatids in hermaphrodites but not in males (*29*, *30*), so the signals that activate spermatids might differ between the sexes. This difference could be due to selection, because male spermatids must remain inactive before mating to improve transfer (*28*), but hermaphrodite spermatids need to activate during ovulation to avoid being swept out of the gonad.

Before mating, sperm activation in *C. elegans* males is blocked by SWM-1. Because *spe-29; swm-1* hermaphrodites have active sperm but *spe-29* hermaphrodites do not, SWM-1 also functions in *XX* animals (*28*). This result can be explained by the expression of SWM-1 in germ cells during spermatogenesis, as implied by genetic mosaic analyses (*28*). Thus, mutations that prevented *swm-1* from blocking sperm activation in *XX* animals, without compromising its role in males, might have been required for the evolution of a hermaphroditic mating system.

Although the gonochoristic species do not form a clade (*16*, *17*), their SWM-1 proteins were more similar to each other than to those of the hermaphrodites (Fig. 2, A and B). Furthermore, maximum

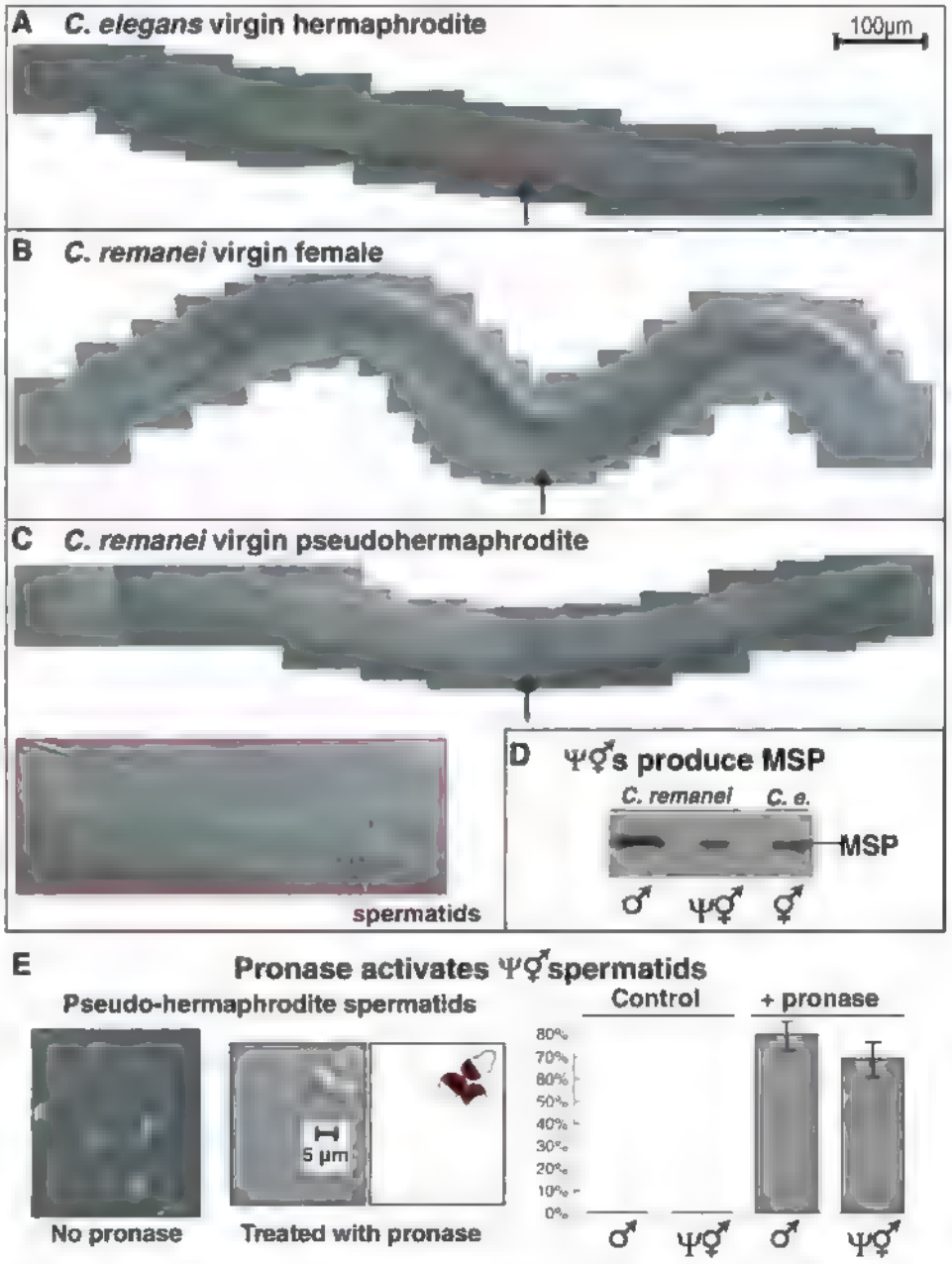

Fig. 1. Some *tra-2(RNAi)* animals are hermaphrodites with inactive spermatids. DIC photomicrographs of (**A**) *C. elegans* virgin hermaphrodite, (**B**) SB146 *C. remanei* virgin female, and (**C**) SB146 *C. remanei tra-2(RNAi)* pseudohermaphrodite. The inset shows a closeup of the proximal end of the ovary from (C), which is boxed in red. Developing embryos are false-colored red, stacked oocytes are false-colored yellow, and the vulva is marked by an arrow. (**D**) Western blot probed with antibodies to *C. elegans* (*C.e.*) major sperm protein (MSP) isolated from samples of 10 individual animals of the indicated species and sex; *C. remanei* animals were from strain PB4641. (**E**) DIC photomicrographs of spermatids from pseudohermaphrodites in sperm media (left) or in sperm media with pronase (right). In the diagram, activated spermatids are diagrammed red with clear pseudopods to the right of the micrograph. (Right graph) Frequency of activation of spermatids from males and pseudohermaphrodites. Error bars indicate 95% confidence intervals.

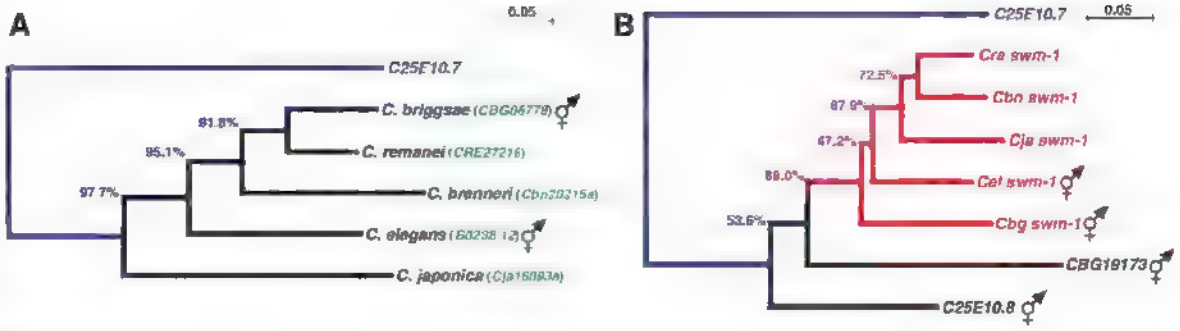

Fig. 2. SWM-1 is a conserved regulator of sperm activation. (**A**) Phylogeny of the *elegans* group of nematodes (*16*, *17*), as exemplified by a neighbor-joining analysis of the B0238.12 family of TIL domain proteins (green). Bootstrap replication values are shown at the node of each branch, and the TIL protein C25E10.7 is the outgroup [blue, see (*18*)]. (**B**) Neighbor-joining tree of the SWM-1 family of proteins.

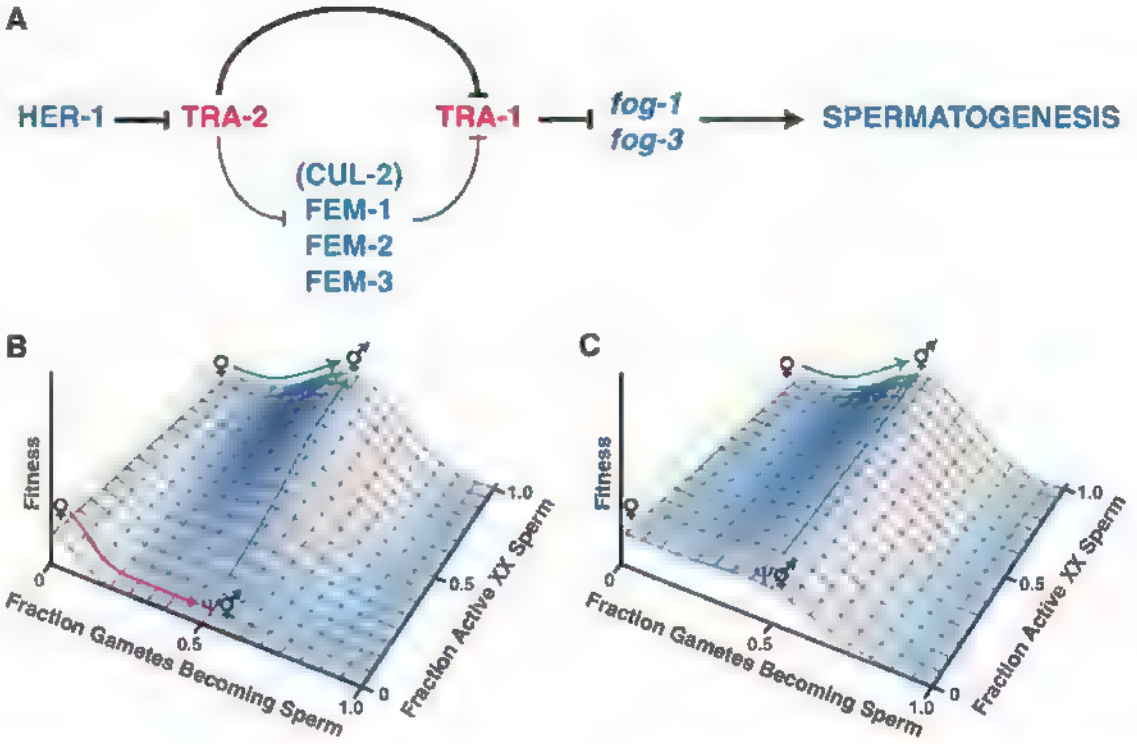

Fig. 3. Evolution of self-fertile hermaphrodites. (**A**) Model of the sex-determination pathway in *C. remanei*, indicating the branch at TRA-2. Proteins promoting spermatogenesis are blue, and those promoting oogenesis are red. (**B**) Model of an adaptive landscape in which pseudohermaphrodites are under negative selection because of the resources devoted to sperm production. Red arrows indicate paths opposed by selection, green indicates paths favored by selection, and yellow marks neutral paths. (**C**) Model of an adaptive landscape in which the negative effect of delayed oogenesis in pseudohermaphrodites is offset by self-fertilization after mating.

likelihood tests indicate that the ratio of nonsynonymous to synonymous substitutions (called Ka/Ks) along the hermaphroditic *swm-1* branches differs from that of the rest of the tree [$P < 0.0018$; see (*18*)]. Thus, the type of mating system appears to influence the selective pressures acting on *swm-1*. This difference might have been caused by positive selection on some residues of SWM-1 during the evolution of hermaphroditism. Alternatively, it might be due to a relaxation of negative selection on SWM-1 in hermaphrodites. In either case, these changes could have been facilitated by the presence of paralogs of *swm-1*, which only exist in the hermaphroditic taxa.

On the basis of our results, we suggest two models describing the evolution of hermaphroditism. Both models assume that selection would strongly favor the ability of individual *XX* animals to colonize new environments because these nematodes reproduce in large numbers and can quickly exhaust local food sources. Such an advantage would be needed to offset problems caused by inbreeding depression in originally outbreeding populations of nematodes (*27*). (i) *XX* animals first acquired the ability to activate self sperm by a neutral mutation. If so, a subsequent mutation conferring the ability to produce *XX* sperm and self-fertilize would have immediately been under positive selection when sexual partners were rare (left path, Fig. 3, B and C). (ii) *XX* animals first acquired the ability to produce spermatids and oocytes. Because our data imply that such animals could not self-fertilize, the production of spermatids should have resulted in reduced fitness (right path, Fig. 3B). However, selection against these incipient hermaphrodites would be alleviated if self-sperm were occasionally activated by male seminal fluid (Fig. 3C). Because *C. remanei* females are attractive to males of related species (*31*), a pseudohermaphrodite that mated with such a male would be stimulated to have self-progeny. However, a *C. remanei* female that mated with a male of another species would not have offspring. Despite this possibility, we favor the model in Fig. 3B.

In *Drosophila*, male wing spots have been independently gained or lost in different lineages because of mutations in cis regulatory elements that drive the *yellow* gene (*32*). Similarly, independent duplications of the gene encoding a pancreatic ribonuclease, followed by similar functional changes, occurred in leaf-eating monkeys (*33*). However, both examples involve novel traits that were created by modification of only a single gene. Thus, they differ from this study, which focuses on a novel trait that seems to have required independent changes in at least two regulatory pathways. To explain these changes, we favor stepwise models, in which a neutral mutation allowed for selection to act on a second, favorable change. Several species closely related to *C. remanei* have been isolated recently and will allow us to test whether the evolution of hermaphroditism follows our model throughout the *Caenorhabditis* genus.

References and Notes

1. R. E. Ellis, *Curr. Top. Dev. Biol.* **83**, 41 (2008)
2. D. Zarkower, in *Wormbook*, the *C. elegans* research community, Ed., 10.1895/wormbook.1.84.1 (10 February 2006), www.wormbook.org.
3. P. E. Kuwabara, *Genetics* **144**, 597 (1996)
4. E. S. Haag, J. Kimble, *Genetics* **155** 105 (2000)
5. D. Hansen, D. Pilgrim, *Genetics* **149**, 1353 (1998)
6. P. Stothard, D. Pilgrim, *J. Mol. Evol.* **62**, 281 (2006).
7. R. C. Hill *et al.*, *Dev. Cell* **10**, 531 (2006).
8. E. S. Haag, S. Wang, J. Kimble, *Curr. Biol.* **12**, 2035 (2002)
9. P. J. Chen, S. Cho, S. W. Jin, R. E. Ellis, *Genetics* **158**, 1513 (2001)

10. S. Wang, J. Kimble, *EMBO J.* **20**, 1363 (2001)
11. T. Schedl, J. Kimble, *Genetics* **119**, 43 (1988)
12. E. Jan, C. K. Motzny, L. E. Graves, E. B. Goodwin, *EMBO J.* **18**, 258 (1999).
13. R. Clifford *et al.*, *Development* **127**, 5265 (2000)
14. S. Nayak, J. Goree, T. Schedl, *PLoS Biol.* **3**, e6 (2005)
15. Y. Guo, S. Zang, R. E. Ellis, *Current Biol.*, in press, available at www.cell.com/currentbiology/abstract/S0960-9822(09)01752-7
16. S. Cho, S. W. Jin, A. Cohen, R. E. Ellis, *Genome Res.* **14**, 1207 (2004)
17. K. Kiontke *et al.*, *Proc. Natl. Acad. Sci. U.S.A.* **101**, 9003 (2004)
18. Materials and methods are available as supporting material on *Science* Online
19. M. A. Muller *et al.*, *Science* **291**, 2144 (2001)
20. T. M. Roberts, M. Stewart, *Curr. Opin. Cell Biol.* **7**, 13 (1995).
21. A. N. Minnich, C. Sadler, S. Ward, *Genetics* **143**, 213 (1996)
22. S. Ward, E. Hogan, G. A. Nelson, *Dev. Biol.* **98**, 70 (1983)
23. B. Geldziler *et al.*, *Dev. Genes Evol.* **216**, 198 (2006)
24. D. C. Shakes, S. Ward, *Dev. Biol.* **134**, 189 (1989)
25. S. E. Baird, M. E. Sutherlin, S. W. Emmons, *Evolution* **46**, 585 (1992)
26. S. E. Baird, W. C. Yen, *Evol. Dev.* **2**, 9 (2000)
27. A. Barmere *et al.*, *Genome Res.* **19**, 470 (2009)
28. G. M. Stanfield, A. M. Villeneuve, *Curr. Biol.* **16**, 252 (2006)
29. S. W. L'Hernault, in *WormBook* the *C. elegans* research community, Ed., 10.1895/wormbook.1.85.1 (20 February 2006), www.wormbook.org
30. B. Geldziler, I. Chatterjee, A. Singson, *Dev. Biol.* **283**, 424 (2005)
31. J. R. Chasnov, W. K. So, C. M. Chan, K. L. Chow, *Proc. Natl. Acad. Sci. U.S.A.* **104**, 6730 (2007)
32. B. Prud'homme *et al.*, *Nature* **440**, 1050 (2006)
33. J. Zhang, *Nat. Genet.* **38**, 819 (2006).
34. We thank the NSF for support (grant 0543828), D. Greenstein for antibodies, Y. Shirmann for technical assistance, A. Singson and S. L'Hernault for advice, and E. Moss and R. Dutch for comments on this manuscript

Supporting Online Material

www.sciencemag.org/cgi/content/full/326/5955/1002/DC1
Materials and Methods
Figs. S1 to S5
Table S1
References

8 May 2009; accepted 16 September 2009
10.1126/science.1176013

Amyloid-β Dynamics Are Regulated by Orexin and the Sleep-Wake Cycle

Jae-Eun Kang,[1] Miranda M. Lim,[1] Randall J. Bateman,[1,2,3] James J. Lee,[1] Liam P. Smyth,[1] John R. Cirrito,[1,2] Nobuhiro Fujiki,[4] Seiji Nishino,[4] David M. Holtzman[1,2,3,5]*

Amyloid-β (Aβ) accumulation in the brain extracellular space is a hallmark of Alzheimer's disease. The factors regulating this process are only partly understood. Aβ aggregation is a concentration-dependent process that is likely responsive to changes in brain interstitial fluid (ISF) levels of Aβ. Using in vivo microdialysis in mice, we found that the amount of ISF Aβ correlated with wakefulness. The amount of ISF Aβ also significantly increased during acute sleep deprivation and during orexin infusion, but decreased with infusion of a dual orexin receptor antagonist. Chronic sleep restriction significantly increased, and a dual orexin receptor antagonist decreased, Aβ plaque formation in amyloid precursor protein transgenic mice. Thus, the sleep-wake cycle and orexin may play a role in the pathogenesis of Alzheimer's disease.

Alzheimer's disease (AD) is the most common cause of dementia. The accumulation of the amyloid-β (Aβ) peptide in the brain extracellular space is a critical event in the pathogenesis of AD. Aβ is produced by neurons and secreted into the brain interstitial fluid (ISF). An initiating factor in AD pathogenesis occurs when soluble, monomeric Aβ undergoes a conformational change and converts into forms such as oligomers, protofibrils, and fibrils. The accumulation of these forms of Aβ is concentration dependent and confers toxicity (*1*). Elucidating factors that regulate soluble Aβ levels is important for understanding AD pathogenesis. Synaptic activity regulates the release of Aβ from neurons into the ISF (*2*, *3*). How ISF Aβ is regulated by normal physiology is poorly understood.

To investigate ISF Aβ metabolism, we monitored hippocampal Aβ levels using in vivo microdialysis in both wild-type mice and human *APP* transgenic (Tg2576) mice, which express a mutated form of human amyloid precursor protein (APP) (*4*). ISF Aβ was assessed in Tg2576 mice at 3 months of age, several months earlier than Aβ deposition begins. We found diurnal variation of ISF Aβ levels. Aβ levels were significantly increased during the dark period compared to the light period (Fig. 1A). ISF Aβ levels fluctuated over a 24-hour period: mean levels during the light period were ~75% of mean Aβ levels during the dark period (Fig. 1B). ISF Aβ levels were significantly correlated with the amount of time spent awake (Fig. 1, C and D). Conversely, ISF Aβ levels were negatively correlated with the amount of time spent asleep. This negative correlation was even stronger with non-REM (rapid eye movement) sleep (fig. S1). Despite fluctuations in ISF Aβ levels, full-length APP, APP C-terminal fragments, and $Aβ_{1-40}$ and $Aβ_{1-42}$ were not significantly different in total tissue homogenates of hippocampus between dark and light periods (fig. S2). Thus, the pool of ISF Aβ is likely to be regulated independently from total intracellular and membrane-associated Aβ.

Next, we assessed whether diurnal Aβ fluctuation was also present in C57BL6, wild-type mice. Similar to Tg2576 mice, C57BL6 mice also showed a significant difference in ISF Aβ levels between dark and light phases, when samples were pooled over longer periods of time (Fig. 1, E and F). Thus, the diurnal variation in Aβ is intrinsic to normal cellular physiology.

To determine the underlying mechanism of the diurnal variation in ISF Aβ levels, we tested whether the light stimulus itself could affect ISF Aβ levels. Using C57BL6 mice, we measured ISF Aβ levels over 2 days under constant dim light conditions. Diurnal fluctuations of ISF Aβ still occurred, as did normal sleep-wake behavior (Fig. 1, G and H). Thus, ISF Aβ fluctuations are linked to the sleep-wake cycle and not to light or dark exposure.

To see whether the diurnal fluctuation of ISF Aβ is present in humans, we assessed cerebrospinal fluid (CSF) levels of Aβ in 10 young healthy male volunteers via lumbar catheters over a 33-hour period and found clear evidence of diurnal fluctuation of Aβ in the CSF. Aβ levels increased throughout the first day with a peak in the evening, then decreased overnight, and again increased throughout the second day (Fig. 1I).

Because Aβ levels correlated with wakefulness, we asked whether manipulating sleep behavior would alter ISF Aβ levels. Mice were forced into wakefulness for 6 hours at the beginning of the second 12-hour light period when they would naturally be asleep. During sleep deprivation (SD), ISF Aβ levels were significantly higher compared to ISF Aβ levels during the normal light period 24 hours previously (Fig. 2, A to C). Following SD, mice spent more time sleeping and had an immediate reduction in ISF Aβ levels. Thus, the state of wakefulness, and not time of day, is associated with increased ISF Aβ levels.

Restraint stress in Tg2576 mice can acutely increase ISF Aβ mediated by corticotropin releasing factor (CRF) (*5*). $αCRF_{9-41}$, an antagonist of CRF receptors, was administered by reverse microdialysis at the beginning of SD. In the presence of the CRF receptor antagonist, ISF Aβ levels were still significantly higher compared to ISF Aβ levels during the normal light period 24 hours previously (Fig. 2, D to F). The SD-induced increase in ISF Aβ did not significantly differ in the presence or absence of the CRF antagonist, thereby excluding the CRF stress pathway as mechanism of action for SD to increase Aβ levels.

We next asked what molecular mechanism might mediate the diurnal fluctuation of Aβ levels. Orexin is a molecule that regulates wakefulness and other physiological functions, and is strongly implicated in narcolepsy and cataplexy, as well as disorders of sleep and arousal (*6*). Orexin release from hypothalamic neurons shows a diurnal fluctuation similar to that of ISF Aβ (*7*).

[1]Department of Neurology, Washington University, St. Louis, MO 63110, USA. [2]Hope Center for Neurological Disorders, Washington University, St. Louis, MO 63110, USA. [3]Alzheimer's Disease Research Center, Washington University, St. Louis, MO 63110, USA. [4]Sleep and Circadian Neurobiology Laboratory, Department of Psychiatry and Behavioral Sciences, Stanford University, Palo Alto, CA 94304, USA. [5]Department of Developmental Biology, Washington University, St. Louis, MO 63110, USA.

*To whom correspondence should be addressed. E-mail: holtzman@neuro.wustl.edu

Orexin neurons project to the hippocampus where orexin receptors are expressed, and this is the location where we monitored ISF Aβ (*8*). We examined whether orexin administration would modulate ISF Aβ levels. Intracerebroventricular (icv) infusion of orexin-A (1.5 pmol/hour) was given for 6 hours at the beginning of the light period. This dose induces wakefulness in rodents (*9*). During orexin infusion, ISF Aβ levels were significantly increased compared to ISF Aβ levels measured during the light period of the preceding day (Fig. 3, A and B). Infusion of vehicle did not significantly affect ISF Aβ (fig. S3, A and B).

The orexin family (orexin-A and orexin-B) has two receptor subtypes, orexin receptor 1 (OXR1) and orexin receptor 2 (OXR2). We asked whether endogenous orexin signaling via orexin receptors is involved in the diurnal variation of Aβ levels. We infused a dual orexin receptor antagonist, almorexant, during in vivo microdialysis for ISF Aβ. Icv administration of almorexant for 24 hours suppressed ISF Aβ levels and abolished the natural diurnal variation of Aβ (Fig. 3, D and E). Removal of almorexant immediately restored the diurnal rhythm in ISF Aβ levels during the next 24-hour period. Control icv infusions of vehicle did not affect ISF Aβ levels (fig. S3, C and D). Almorexant decreased the total amount of time spent awake by ~10% (Fig. 3F). Thus, endogenous orexin signaling via orexin receptors is required for the diurnal rhythm of ISF Aβ levels.

Because sleep-wake behavior modulates ISF Aβ levels, we investigated whether chronic sleep deprivation could ultimately affect Aβ plaque deposition in the brain. APP transgenic mice of the APPswe/PS1dE9 genotype were subjected to chronic sleep restriction for 20 hours daily for 21 days. Sleep-restricted animals showed markedly greater Aβ plaque deposition compared to their age-matched littermate controls (Fig. 4, A to G). We also observed significantly greater Aβ plaque burden using Tg2576 mice (fig. S4). We next asked whether chronic orexin receptor blockade could decrease Aβ plaque deposition in APPswe/PS1dE9 mice at an age when plaques are just forming. Systemic treatment with almorexant once daily for 8 weeks significantly decreased Aβ plaque formation in several brain regions compared to vehicle-treated age-matched control mice (Fig. 4H).

Here, we demonstrated diurnal variation in Aβ levels in the brain of awake and behaving animals. Perturbations in both orexin signaling and the sleep-wake cycle had acute effects upon Aβ dynamics. Furthermore, chronic sleep restriction accelerates Aβ plaque burden, whereas en-

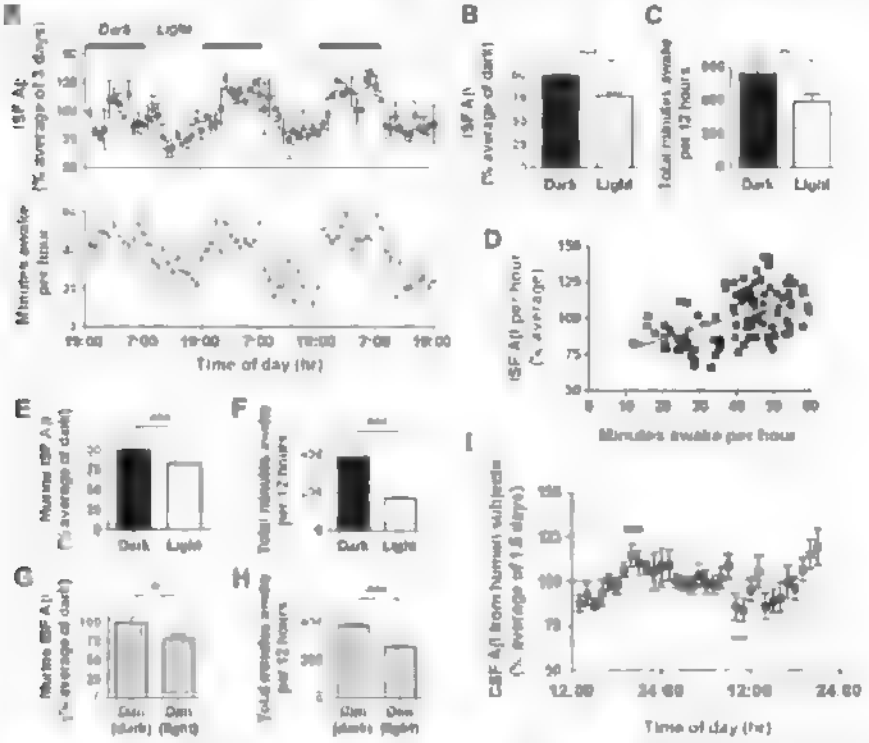

Fig. 1. Diurnal rhythm of ISF Aβ levels in the hippocampus of mice and CSF Aβ levels in human subjects. (**A**) (Top) ISF human Aβ levels expressed as a percentage of basal ISF Aβ levels over six light-dark periods in Tg2576 mice ($n = 8$). (Bottom) Total number of minutes spent awake per hour in the same mice. (**B** and **C**) Mean ISF Aβ levels were 24.4% higher (***$P < 0.0001$, $n = 8$) and the number of minutes awake was 167 min higher (**$P = 0.007$, $n = 7$) during dark versus light periods. (**D**) ISF Aβ levels correlate with the number of minutes awake per hour (correlation coefficient $r = 0.53$, ***$P < 0.0001$, $n = 7$). (**E** and **F**) Mean ISF Aβ levels and minutes awake over 2 days in C57BL6 mice. Under 12 hours dark/12 hours light conditions, ISF Aβ levels were 18.5% higher (***$P < 0.0001$, $n = 10$) and the number of minutes awake was 223 min higher (***$P = 0.0001$, $n = 5$) during the dark periods. (**G** and **H**) Under constant dim light conditions, ISF Aβ levels were 22.7% higher (*$P = 0.05$, $n = 10$) and the number of minutes awake was 114 min higher (***$P = 0.0003$, $n = 5$) during the typical hours for the dark phase. (**I**) CSF $Aβ_{1-40}$ levels from human subjects expressed as a percentage of basal CSF $Aβ_{1-40}$ levels over 33 hours ($n = 10$). Mean peak CSF $Aβ_{1-40}$ levels (black bar) at 7 to 9 p.m. were 27.6% higher than mean trough CSF Aβ levels (gray bar) at 9 to 11 a.m. (112.3 ± 6% versus 84.7 ± 6%, respectively, $P = 0.004$). Data shown are the means ± SEM.

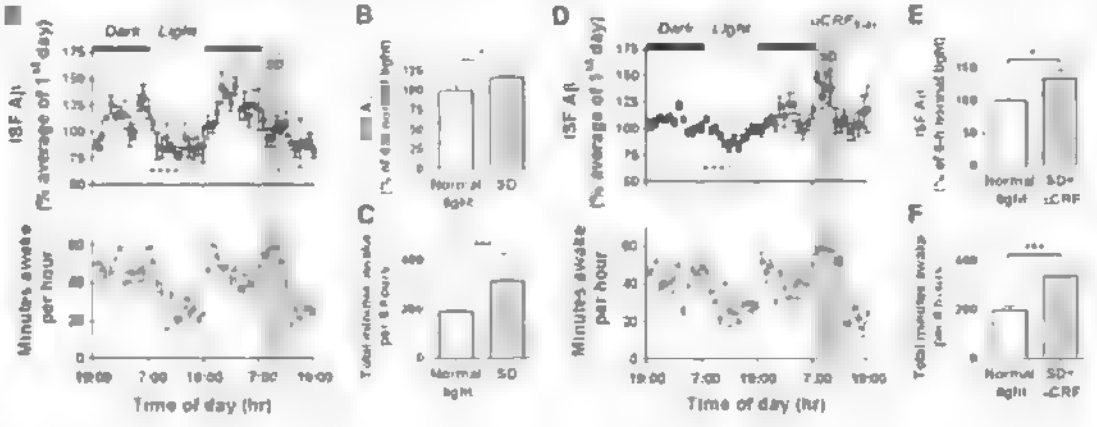

Fig. 2. Acute sleep deprivation alters ISF Aβ diurnal rhythm independently of CRF receptor signaling in Tg2576 mice. (**A**) Mice underwent acute sleep deprivation (SD, gray dashed line) for 6 hours at the beginning of the light period. This prevented the normal decrease in ISF Aβ levels that occurs during this period ($n = 8$). (**B**) Mean ISF Aβ levels during SD were 16.8% higher compared to those during the light period 24 hours earlier [black dashed line in (A), *$P = 0.05$, $n = 8$]. (**C**) Animals spent 126 more minutes awake during SD (***$P < 0.0001$, $n = 5$). (**D**) Mice underwent acute SD (gray dashed line) at the beginning of the light period. $αCRF_{9-41}$ (860 pmol) was infused into the hippocampus from 30 min before SD until the end of the light period ($n = 8$). (**E**) Mean ISF Aβ levels during SD with $αCRF_{9-41}$ infusion were 33.7% higher compared to those during the light period 24 hours earlier [black dashed line in (D), *$P = 0.01$, $n = 8$]. (**F**) Mice spent 136 more minutes awake during SD with $αCRF_{9-41}$ infusion (***$P < 0.0001$, $n = 5$). Data represent the mean ± SEM.

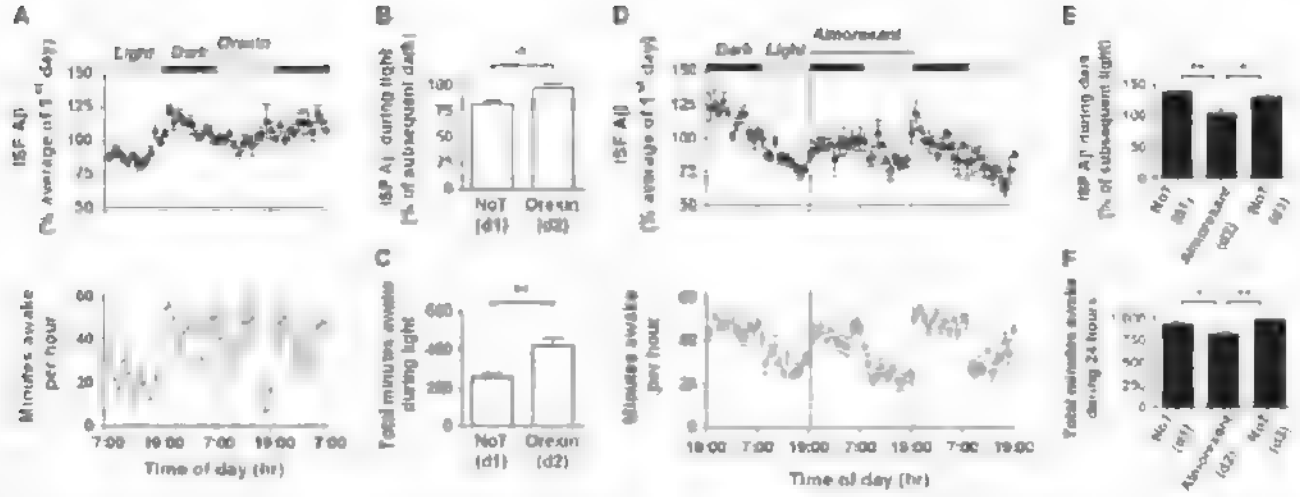

Fig. 3. Effects of orexin and a dual orexin receptor antagonist on ISF Aβ levels in Tg2576 mice. **(A)** After 24 hours of baseline measurement, orexin (1.5 pmol/hour) was infused icv for 6 hours at the beginning of the light period. This sustained ISF Aβ levels from the dark period and kept the mice awake longer. **(B** and **C)** Infusion with orexin increased Aβ levels during the light period and thereby abolished the normal 20% difference between the dark and light period (*$P = 0.01$, $n = 7$). Orexin increased the time spent awake by 163 min (**$P = 0.009$, $n = 5$), compared to that during the light period 24 hours previously. **(D)** After 24 hours of baseline measurement, almorexant (13.9 nmol/hour) was infused icv for 24 hours from the beginning of the dark period ($n = 8$). This continued to suppress ISF Aβ levels from the light period. **(E)** Mean ISF Aβ levels differed by 29% between the dark and light period during the control days, whereas there was no difference between the dark and light period during the 24-hour infusion of almorexant (*$P < 0.05$, $n = 8$). **(F)** During almorexant treatment, the time spent awake was decreased by 108 min over the 24-hour period compared to control days (*$P < 0.05$, $n = 13$). Data represent the mean ± SEM. NoT, no treatment; d, day.

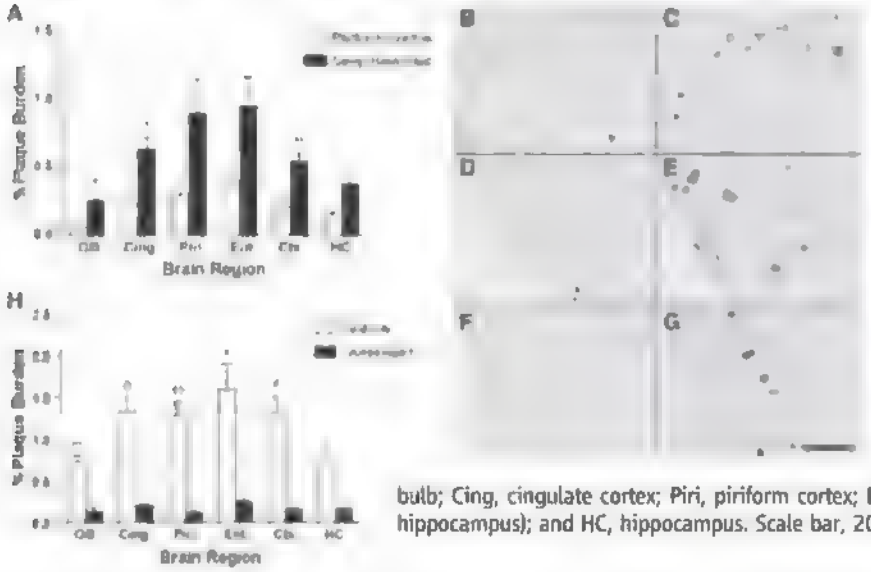

Fig. 4. Aβ plaque deposition after chronic sleep restriction and chronic orexin receptor blockade in APPswe/PS1dE9 transgenic mice **(A)** Mice that underwent chronic sleep restriction for 21 days showed significantly greater Aβ plaque deposition in multiple subregions of the cortex compared to age-matched control mice (**$P < 0.0008$, *$P < 0.008$, $n = 9$ to 11 mice per group, Bonferroni-adjusted $P < 0.0083$ for multiple t tests). For hippocampus, $P < 0.009$. Representative photomicrographs of Aβ plaques are shown in **(B)** control and **(C)** sleep-restricted olfactory bulb, **(D)** control and **(E)** sleep-restricted piriform cortex, and **(F)** control and **(G)** sleep-restricted entorhinal cortex. **(H)** Mice treated with daily intraperitoneal injections of almorexant for 8 weeks showed significantly less Aβ plaque deposition in multiple subregions of the cortex compared to age-matched vehicle controls (**$P < 0.0008$, *$P < 0.008$, $n = 5$ mice per group, using Bonferroni-adjusted $P < 0.0083$ for multiple t tests; for cingulate cortex and hippocampus, $P < 0.009$). OB, olfactory bulb; Cing, cingulate cortex; Piri, piriform cortex; Ent, entorhinal cortex; Ctx, cortex (immediately dorsal to dorsal hippocampus); and HC, hippocampus. Scale bar, 200 μm.

hancing sleep via orexin receptor blockade markedly inhibits Aβ plaque accumulation.

One factor that influences Aβ levels is synaptic activity. Periods of wakefulness are associated with a net increase in synaptic strength, and periods of sleep are associated with a net decrease in synaptic strength (*10*–*12*). Differences in synaptic activity between sleep and wake states, specifically via orexin signaling, may underlie the dynamic fluctuations in ISF Aβ levels.

How might changes in hourly ISF Aβ levels contribute to eventual Aβ plaque deposition? Recent work with a γ-secretase inhibitor has shown that changes in ISF Aβ levels as little as 20% block plaque formation and growth over weeks (*13*). Thus, behavioral and pharmacological manipulations of wakefulness that resulted in changes in ISF Aβ of 20 to 25% likely caused the observed changes in Aβ accumulation.

Sleep is a complex behavioral state whose ultimate functions remain poorly understood. Sleep disturbances, in addition to being prominent in neurodegenerative diseases (*14*), could exacerbate a fundamental process leading to neurodegeneration, and optimization of sleep time could potentially inhibit aggregation of toxic proteins and slow the progression of AD.

References and Notes

1. D. J. Selkoe, *Nat. Cell Biol.* **6**, 1054 (2004).
2. F. Kamenetz *et al.*, *Neuron* **37**, 925 (2003).
3. J. R. Cirrito *et al.*, *Neuron* **48**, 913 (2005).
4. K. Hsiao *et al.*, *Science* **274**, 99 (1996).
5. J. E. Kang, J. R. Cirrito, H. Dong, J. G. Csernansky, D. M. Holtzman, *Proc. Natl. Acad. Sci. U.S.A.* **104**, 10673 (2007).
6. T. S. Kilduff *et al.*, *J. Neurosci.* **28**, 11814 (2008).
7. Y. Yoshida *et al.*, *Eur. J. Neurosci.* **14**, 1075 (2001).
8. C. Peyron *et al.*, *J. Neurosci.* **18**, 9996 (1998).
9. Z. L. Huang *et al.*, *Proc. Natl. Acad. Sci. U.S.A.* **98**, 9965 (2001).
10. V. V. Vyazovskiy, C. Cirelli, M. Pfister-Genskow, U. Faraguna, G. Tononi, *Nat. Neurosci.* **11**, 200 (2008).
11. G. F. Gilestro, G. Tononi, C. Cirelli, *Science* **324**, 109 (2009).
12. J. M. Donlea, N. Ramanan, P. J. Shaw, *Science* **324**, 105 (2009).
13. P. Yan *et al.*, *J. Neurosci.* **29**, 10706 (2009).
14. J. F. Gagnon, D. Petit, V. Latreille, J. Montplaisir, *Curr. Pharm. Des.* **14**, 3430 (2008).

15. We thank E. D. Herzog and G. M. Freeman Jr. for assistance and P. J. Shaw for discussion. This work was supported by NIH grants AG025824, AG030946, N5065667, AG029524 and MH072525, Neuroscience Blueprint Center Core Grant P30 N5057105; Cure Alzheimer's Fund; Alzheimer's Association Zenith Award, and Eli Lilly.

Supporting Online Material

www.sciencemag.org/cgi/content/full/1180962/DC1
Materials and Methods
Figs. S1 to S4
References

24 August 2009; accepted 11 September 2009
Published online 24 September 2009.
10.1126/science.1180962
Include this information when citing this paper

Microwave Synthesizer

The Initiator 2.5 microwave synthesizer is designed to offer fast and scalable reactions and has been tailored for synthetic chemistry. The new system offers improved heating performance, guided run setup, and improved data management. It features 400 watts of power to deliver precise heating control. It allows chemists to share methods and results easily through either a USB port or a network. A built-in computer with intuitive software automatically converts conventional parameters to microwave conditions. The system is capable of heating a sample for up to 96 hours. It offers total automation with an eight-position and 60-position robot for rapid optimization of reaction conditions and analog synthesis.
Biotage
For information +46-18-56-59-00
www.biotage.com

Cell Density Meter

The CO 8000 is a simple, reliable instrument that measures the density of cells grown in suspension by measuring optical density at 600 nm, which makes the instrument suitable for yeast and bacterial cultures. Completely portable, the CO 8000 is hand-held and has a rechargeable battery. It can be used in incubation cabinets, under anaerobic conditions, and even in fume hoods or safety cabinets. It can be cleaned easily and accepts a variety of cuvettes and tubes. The built-in memory stores up to 99 sample results for later download to a computer. The LED source and fiber optics give stable results and require no maintenance or warm-up.
Biochrom
For information +44-(0)-1223-427811
www.biochrom.co.uk

Vision Spectrophotometer

The Vision Spectrophotometer includes 16 predefined methodologies for nucleic acid quantitation, protein assays, cell density measurements, and dye-labeled polymerase chain reaction probe detection. It can also accommodate 90 custom protocols. It combines these life science methods with rapid scanning, kinetics capabilities, and concentration capabilities. The Vision Spectrophotometer has novel Gifford optics for high energy combined with a xenon source for long life. It includes an integral cuvette tray for storage of expensive cells and sample support. An optional integrated printer and wireless Bluetooth connectivity are available.
Hoefer
For information 800-227-4750
www.hoeferinc.com

Benchtop LC/MS System

The Exactive system is a benchtop liquid chromatography/mass spectrometry (LC/MS) system designed for high throughput and high-performance screening and compound identification applications. The system leverages the manufacturer's Orbitrap mass-analyzer technology to provide precise and reliable information. It is fast, easy to use, cost effective, and suitable for new users in routine analytical laboratories. The Exactive LC/MS streamlines many of the technical steps that normally require specialized setup and operation. An intuitive software interface makes the system easy to use in both expert and "walk-up" mode, while ensuring precise mass identification of target compounds over a wide concentration range.
Thermo Fisher Scientific
For information 508-742-5254
www.thermofisher.com

Microscope Stage Incubator

The Okalab electric carbon dioxide microscope stage incubator is a low-cost, one-button solution for long-term studies. It fits all XY microscope stages and is suitable for high magnification microscopy and multipoint experiments. It features both chamber and temperature feedback mechanisms. This incubator can be customized using a wide range of interchangeable microscope stage inserts, an optional humidifying and preheating module, and optional Read Temperature Software.
Warner Instruments
For information 800-599-4203
www.warnerinstruments.com

Multidimensional Gas Chromatography

The Multi-Dimensional Gas Chromatography system expands the capabilities of chemists who perform target compound analyses in complex sample matrices, including natural product extracts, food and flavor components, and biological extracts. The multidimensional system increases separation power by combining two capillary columns of different selectivity for a more efficient separation of the target analytes from a complex sample matrix. The improved separation of the analytes from the matrix interferences allows more positive identification and improved quantitative analysis of the target analytes. The key hardware component of the system is a capillary-optimized pressure-switching device ("multi-Deans switch") that directs flow from the first column directly to a monitor detector or to the second column and detector. This device has no moving parts, but is based on the use of an advanced electronic flow controller to balance the pressure on both sides of the transfer line between columns.
Shimadzu
For information 800-477-1227
www.ssi.shimadzu.com

Electronically submit your new product description or product literature information! Go to **www.sciencemag.org/products/newproducts.dtl** for more information

Newly offered instrumentation, apparatus, and laboratory materials of interest to researchers in all disciplines in academic, industrial, and governmental organizations are featured in this space. Emphasis is given to purpose, chief characteristics, and availability of products and materials. Endorsement by *Science* or AAAS of any products or materials mentioned is not implied. Additional information may be obtained from the manufacturer or supplier.

POSITIONS OPEN

BRADLEY UNIVERSITY

ASSISTANT PROFESSOR, DEPARTMENT OF BIOLOGY

The Department of Biology invites applications for a tenure-track Assistant Professor position beginning fall 2010. We seek a creative, energetic individual whose research focuses at the organismal level using cellular or molecular approaches in animals. A Ph.D. is required and postdoctoral experience is preferred. The successful applicant is expected to teach upper level majors courses in his/her area of specialization, general biology courses, and a human anatomy and physiology course. In addition, the candidate is expected to establish a productive, funded research program in his/her area of expertise, and to contribute to the broader biology curriculum. The successful applicant is expected to pursue a research program and help sustain the University's emphasis on student-faculty scholarship collaboration. Applicants must demonstrate a strong commitment to undergraduate teaching and research, the promise of scholarly and pedagogical excellence in a liberal arts setting, and commitment to working with students of diverse backgrounds.

Qualified candidates should submit a letter of application, current vita, graduate and undergraduate transcripts, statements of teaching interests and research plans, and three letters of reference to: **Dr. Erich K. Stabenau, Chair, Biology Department, Bradley University, 1501 W. Bradley Avenue, Peoria, IL 61625**

Applications received by December 8, 2009, will receive priority consideration. Review of applications will continue until position is filled. Additional information regarding Bradley University and this position may be found at **websites: http://www.bradley.edu** and **http://www.bradley.edu/humanresources/opportunities/faculty.shtml.**

Bradley University is a distinctive, medium-size, comprehensive private institution of higher learning. Bradley is rich in tradition and poised to become one of the nation's best comprehensive universities. *Bradley University is an Equal Opportunity/Affirmative Action Employer. The administration, faculty, and staff are committed to attracting qualified candidates from underrepresented groups.*

FACULTY POSITION IN PATHOLOGY

Applications are invited for a full-time **ACADEMIC PATHOLOGIST** at the rank of **ASSISTANT/ASSOCIATE PROFESSOR** in the Department of Pathology, Microbiology and Immunology, University of South Carolina School of Medicine (USC SOM), Columbia. Candidates must have M.D., D.O., D.V.M., Ph.D., or equivalent degree in pathology or a related field. Candidates with strong teaching credentials in pathology who are interested primarily in teaching medical students will be considered for a full-time, nontenure-track faculty position. Tenure-track faculty candidates will also be considered, and are not only expected to teach pathology to medical students, but also to develop a strong research program. Basic science faculty at the USC SOM conduct research in a variety of areas including: cancer, biomedical engineering and regenerative medicine, neuroscience, complementary and alternative medicine, immunology, and HIV/AIDS, providing ample opportunities for productive collaborations. Shared instrumentation facilities at the USC SOM and at USC are world class and readily accessible. To apply, send your curriculum vitae and three references by surface mail to: **Dr. Mitzi Nagarkatti, Chair, Department of Pathology, Microbiology and Immunology, University of South Carolina School of Medicine, Columbia, SC 29208.** Or electronically to **e-mail: pathology@uscmed.sc.edu.** The search will start immediately and continue until the position is filled. *USC Columbia is an Equal Opportunity/Affirmative Action Employer and encourages applications from women and minorities.*

POSITIONS OPEN

UNIVERSITY OF SOUTH CAROLINA

CANCER RESEARCH

The Department of Pharmaceutical and Biomedical Sciences is seeking applications for a tenure-track position at the rank of **ASSISTANT PROFESSOR (website: http://www.scop.sc.edu)**. The candidate will have a Ph.D. degree, postdoctoral experience, and research interests in cancer pharmacology, cell biology, or drug discovery. The appointee will be expected to develop a strong, NIH-funded research program and participate in professional and graduate education. The Department has faculty members in Columbia (University of South Carolina) and Charleston (Medical University of South Carolina) who are members of the Center for Colon Cancer Research (**website: http://www.ccer.sc.edu**), South Carolina Cancer Center, Hollings Cancer Center, and Centers for Drug Discovery and Cancer Therapeutics. The appointment is on the Columbia campus.

Interested candidates should submit curriculum vitae, statement of research interests, and the names of three references to: **Dr. Michael Wyatt, Department of Pharmaceutical and Biomedical Sciences, South Carolina College of Pharmacy, University of South Carolina, Columbia, SC 29208. E-mail: wyatt@scop.sc.edu.** Electronic submission is encouraged. Review of applications will begin on January 5, 2010, and will continue until the position is filled.

The University of South Carolina is an Affirmative Action/Equal Opportunity Employer.

TENURE-TRACK ASSISTANT PROFESSOR MAMMALIAN PHYSIOLOGY or CELL BIOLOGY

The Department of Biological Sciences invites applications for a tenure-track Assistant Professor in mammalian physiology or cell biology, to support the Department's undergraduate and graduate programs. Areas of expertise and specialization are open. Of particular interest will be candidates working in regulation and health-related biology.

Successful applicants will hold a Ph.D. and possess postdoctoral experience; they will be expected to establish a vigorous, externally funded research program to complement our growing doctoral program. The Department expects candidates will be strongly committed to undergraduate and graduate education in their areas of expertise.

Biological Sciences is housed in the award-winning Dow Environmental Sciences and Engineering Building. Additional information about this position, the Biological Sciences Department, and its programs can be found at **website: http://www.bio.mtu.edu**

Send curriculum vitae, statement of research and teaching interests, and three letters of recommendation via e-mail or post to the search committee:

E-mail: biosearchcommittee@mtu.edu
Biological Sciences Search Committee
Department of Biological Sciences
1400 Townsend Drive
Michigan Technological University
Houghton, MI 49931-1295

Review of applications will begin December 7, 2009, and continue until the position is filled.

In addition to the present search, strategic faculty hiring initiatives with up to 10 new positions in Health Basic Sciences, Technologies, and Medical Informatics and in Next Generation Energy Systems are underway, and qualified candidates are encouraged to send a separate application, following the How to Apply guidelines at **website: http://mtu.edu/sfhi**

Michigan Tech is an ADVANCE institution, one of a limited number of universities in receipt of NSF funds in support of our commitment to increase diversity and the participation and advancement of women in science, technology, engineering, and mathematics. Michigan Technological University is an Equal Opportunity Educational Institution/Equal Opportunity Employer. Minorities and women are encouraged to apply.

San Francisco Bay Area

Dean of the School of Science

Saint Mary's College of California invites nominations and applications for the position of Dean of the School of Science. We seek a leader who will build upon a record of success and continue to develop our outstanding undergraduate science and mathematics programs. An independent institution of 3400 students, Saint Mary's draws upon three principal traditions: Catholicism, the liberal arts, and the educational vision of the De La Salle Christian Brothers. We provide our students with an outstanding educational experience characterized by vibrant and innovative teaching, personal contact between professor and student, and collaborative research experiences. Departments and programs in the School of Science include: biochemistry, biology, chemistry, environmental science & studies, health science, mathematics & computer science, physics and astronomy, psychology, 3+2 engineering program and 2+2 pre-nursing program.

The Dean is responsible for the overall academic excellence of the School: recruitment and development of outstanding faculty and staff, promotion of pedagogical and curricular renewal, and improvement of educational effectiveness. The Dean is expected to foster a rich intellectual community, support faculty and student research, and effectively manage the administrative affairs of the School. The Dean also represents the School to constituencies inside and outside the College and assists in obtaining external resources for the School and the College. The Dean is the primary advocate for the nearly 50 full-time faculty who display a strong commitment to teaching, research, and mentoring of students. At the same time, the Dean ensures that the programs and policies of the School are consistent with the College's mission and overall direction.

In addition to an understanding of and commitment to the Catholic, Lasallian, and Liberal Arts mission of the College, the successful candidate will possess an earned Doctorate in an appropriate field, along with evidence of teaching excellence, high-quality scholarship and service, as well as solid administrative skills and a record of open and collaborative leadership.

Position is available summer 2010. Salary is commensurate with experience, qualifications and internal equity considerations. Review of application materials begins **Dec. 11, 2009**. Please send application electronically as a Microsoft Word attachment and include a cover letter, curriculum vitae and a list of five references with names, titles, e-mails and telephone numbers. References will not be contacted until the candidate approves. All nominations and expressions of interest will be kept in strict confidence. Please direct inquiries, nominations and applications to:

Dr. Robert Kaffer
FENNELL ASSOCIATES HIGHER EDUCATION SERVICES
bobkaffer@gmail.com
(303) 423-4617 (Denver) • www.fennellassociates.org

Saint Mary's College of California is an Equal Opportunity Employer

ASSOCIATE LABORATORY DIRECTOR ENVIRONMENT & LIFE SCIENCES

Brookhaven National Laboratory (BNL) seeks an Associate Laboratory Director (ALD) to provide leadership of a newly created directorate that includes the Environmental Sciences, Biology and Medical Departments with a combined staff of 225. The ALD reports to the Laboratory Director. The Laboratory is especially interested in developing programs that link its existing world-class research on the response of ecosystems to rising CO_2 concentrations to its climate-change related molecular biology research, and to its analysis and modeling capabilities. Important related assets include BNL's synchrotron, nano-science and computing capabilities in addition to its nearness to Stony Brook University (www.sunysb.edu), which enables close collaboration and joint appointments.

Qualifications include an advanced degree and a distinguished research career in environmental, climate or biological science, and experience managing a large research program in a federally funded environment. Demonstrated ability to work with multiple sponsors at the federal and state level, as well as private industry, is highly desirable, as is experience with international organizations. Responsibilities include developing internationally recognized programs that are aligned with the mission of the Department of Energy; participating in lab-wide planning for Laboratory initiatives in energy and environmental sciences; linking directorate research and taking advantage of BNL's unique facilities; maintaining and enhancing excellence and productivity; developing outreach to universities and supporting collaborations between industrial partnerships and end users. The ALD is also responsible for operational and environmental performance, including safety.

For consideration please apply online at **www.bnl.gov/hr/careers**, responding to Position **#15077** (listed under Management). Brookhaven is an Equal Opportunity Employer committed to workforce diversity.

BROOKHAVEN NATIONAL LABORATORY

www.bnl.gov

CHAIR

Department of Pharmacology and Experimental Therapeutics
University of Maryland School of Medicine

UNIVERSITY OF MARYLAND
SCHOOL OF MEDICINE

Applications for the position of Chair of the Department of Pharmacology and Experimental Therapeutics at the University of Maryland School of Medicine (SOM) are invited from established, dynamic scientists with a creative vision of contemporary pharmacology. The Department was established in 1920, and currently has major research strengths in neuropharmacology, oncopharmacology and toxicology (see **http://pharmacology.umaryland.edu/**).

The successful candidate should have a superb record of scholarly activity, extramural funding and service, together with proven leadership, mentoring and administrative abilities, a legacy of building interdisciplinary programs and resources, and a commitment to further expand the high national and international visibility and prestige of the Department. Nominations and applications should be sent to **Dr. Meredith Bond, Chair, Search Committee for the Chair of Department of Pharmacology and Experimental Therapeutics, at pharmsearch@som.umaryland.edu**. Applicants should submit, by email, a letter summarizing their qualifications and interest in the position and an updated Curriculum Vitae. The letter should specify research, teaching, service, administrative experience, mentoring history and interdisciplinary achievements. All inquiries, nominations and applications will be treated confidentially. For more information, please visit the University of Maryland School of Medicine website at **http://medschool.umaryland.edu**. For questions or additional information, contact **Dr. Bond** directly at **mbond@som.umaryland.edu**. Review of applications will begin **December 1, 2009** and will continue until the position is filled.

University of Maryland is an Equal Opportunity/Affirmative Action Employer.

Staff Scientist, Laboratory of Immunology

The National Institute of Allergy and Infectious Diseases (NIAID) conducts and supports a global program of research to better understand, treat, and ultimately prevent infectious, immunologic, and allergic diseases. NIAID's Laboratory of Immunology, Lymphocyte Biology Section (LBS)/Program in Systems Immunology and Infectious Disease Modeling (PSIIM) has an opening for a staff scientist with expertise in optical imaging.

LBS/PSIIM's aim is to create a detailed understanding of immune responses to foreign pathogens or self antigens, as well as to develop new tools for predicting how the immune system will respond if perturbed, for example, by a vaccine. The laboratory uses optical imaging involving both 2-photon and confocal instruments in pursuing these goals (www.niaid.nih.gov/labs/aboutlabs/li/lymphocyteBiologySection/germain.htm).

The successful applicant will have primary responsibility for maintaining and operating four distinct 2-photon instruments (a custom dual laser, resonant scanner device; a Zeiss 510; a Zeiss 710; and a BioRad radiance 2100), two of which are also fully equipped confocal instruments. The successful applicant will work with LBS/PSIIM postdoctoral fellows in conducting their imaging studies as well as with staff from collaborating laboratories. Resources will be available to upgrade and modify these instruments, to acquire new instruments, and to develop novel imaging probes and methods. Software development will be encouraged, especially in collaboration with PSIIM computational staff.

Additionally, there will be opportunity for the successful applicant to design, conduct, and publish the results of biological imaging experiments. Strong technical applicants lacking an immunology background who are otherwise excellent fits to the imaging needs will be given full consideration. If hired, such an applicant will be provided opportunities for training and education in immunology and infectious diseases to facilitate development of a strong experimental research program in addition to technical activities and collaborative work with other members of LBS/PSIIM.

National Institute of Allergy and Infectious Diseases

To apply, send curriculum vitae, bibliography, three letters of recommendation, and a short statement about your skill set including how you see applying optical imaging to better understanding immunity (no more than two pages) by **January 31, 2010**, to Ronald Germain, M.D., Ph.D., Chief, LBS; Director, PSIIM, NIAID/NIH/HHS, 10 Center Drive, MSC 1892, Building 10, Room 11N311, Bethesda, MD 20892-1892 or rgermain@nih.gov.

For more information about NIAID and to view additional career opportunities, please visit **www.niaid.nih.gov/careers/ssds.**

HUMAN GENETICIST, Tenure-Track/Tenure Position
Laboratory of Translational Genomics

The newly formed intramural Laboratory of Translational Genomics (LTG) in the Division of Cancer Epidemiology and Genetics (DCEG), National Cancer Institute (NCI), National Institutes of Health (NIH), Department of Health and Human Services (DHHS), is recruiting a tenure-track/tenured investigator. The mission of the LTG is to investigate the genetic basis of strong association signals identified by candidate gene approaches, linkage analyses in high-risk families, or genome-wide association studies (GWAS), particularly loci identified by the ongoing Cancer Genetic Markers of Susceptibility (C GEMS) program involving GWAS of several major cancers. Investigators in the LTG are expected to develop an independent research portfolio in cancer genomics focused on (1) fine mapping and re-sequencing of loci relevant to cancer susceptibility and or outcomes, (2) investigation into the causal gene variants that provide biological plausibility for each locus, and (3) bioinformatic analyses of publicly available datasets derived from germline annotation of genetic variation and somatic alterations in cancers. Each investigator is expected to leverage the NCI resources in molecular epidemiology, high-throughput genotyping and whole genome scans, biostatistics and bioinformatics, as well as in basic and clinical sciences. The incumbent will receive research support for developing a state-of-the-art genomics laboratory, and recruiting two post-doctoral fellows/bioinformaticians and a technician.

Applicants must have an M D. and or Ph.D. in a relevant field, extensive post-doctoral experience, and a record of publications demonstrating potential for creative independent research in human cancer genetics. Facility with bioinformatics databases and high dimensional data are highly desirable along with strong communication skills. Interested individuals should send a cover letter, curriculum vitae and a brief summary of research accomplishments and goals, along with copies of three to five publications or preprints, and three letters of reference to: **Ms. Judy Schwadron, Division of Cancer Epidemiology and Genetics, National Cancer Institute, 6120 Executive Blvd. EPS/8073, Bethesda, MD 20892**

Recommendations can be included with the package or sent directly by the recommender to Ms. Schwadron. Candidates should submit applications by January 15, 2010; at this time, the committee will begin to look at suitable candidates. However, the search will continue until qualified scientists are found. Additional information about staff and ongoing research in the NCI Division of Cancer Epidemiology and Genetics is available at **http://www.dceg.cancer.gov**. Please contact **Dr. Stephen Chanock (phone 301-435-7559 at chanocks@mail.nih.gov) or Dr Peggy Tucker (phone 301-496-8031 at tuckerp@mail.nih.gov)** for questions about the position. DHHS and NIH are Equal Opportunity Employers.

Department of Health and Human Services
National Institutes of Health
National Heart, Lung, and Blood Institute

Deputy Scientific Director

The Division of Intramural Research (DIR) of the National Heart, Lung and Blood Institute (NHLBI) is seeking an exceptional candidate for the position of Deputy Scientific Director to provide leadership and support as an active partner with the Scientific Director in leading a large research program. The research program is wide in scope including both basic and clinical scientific research programs in such areas as heart and vascular disease, blood diseases, pulmonary, cardiology, hematology, cell biology, genetics, immunology, biophysics, and biochemistry. The existing faculty is an outstanding group of internationally recognized biomedical researchers covering a wide range of basic and clinical research topics (http: /dir.nhlbi.nih.gov/)

This position offers a unique and exciting opportunity for the right individual to share responsibility in providing visionary leadership to an organization dedicated to uncovering new knowledge and technologies, both basic and clinical. A candidate is sought who has a commitment to scientific excellence to help identify emerging areas of opportunity for collaboration and to work with members of the research community to implement strategies for successful research outcomes. The incumbent will serve as the liaison between the DIR and the NHLBI Board of Scientific Counselors (BSC) with full oversight responsibilities for the entire BSC process. He she will serve as a partner to establish relationships with regional hospitals to expand research opportunities and to impact clinical care. The incumbent will also build trans-NIH scientific and clinical collaborations and participate in trans-NIH initiatives. The candidate is expected to perform the specific duties listed above in addition to co-directing the intramural activities of the DIR with the Scientific Director.

Applicants must have an M D., Ph D., or both as well as senior-level research experience or knowledge of research programs in one or more scientific areas, related to the above mentioned DIR areas of interest. The candidate shall have administrative experience running a complex research program or institution. The candidate should be a strong communicator with the ability to work collaboratively to solve problems and to make informed decisions.

The successful candidate will be offered a competitive salary commensurate with experience and qualifications with a full benefits package (retirement, health & life insurance, leave, etc.). Appointees may be U.S citizens, resident aliens, or non-resident aliens with or eligible to obtain a valid employment authorized visa. Complete applications must be received by **December 18, 2009**. Review of applications is expected to begin in late December, but applications will be accepted until the position is filled. Please submit a curriculum vitae and three letters of reference in .pdf or Microsoft word format only (no paper applications will be accepted) to, **Robert S. Balaban, Ph.D., Scientific Director, NHLBI, c/o Tara Terndrup, nhlbideputysearch@mail.nih.gov**

Department of Health and Human Services (DHHS)
National Institutes of Health (NIH)
National Eye Institute (NEI)
Chief, Laboratory of Computational Medicine

The NEI seeks to develop a new program in computational analysis that fully employs human genomic, transcriptomic, proteomic, metabolomic, neurophysiological and clinical data sets to reconstruct biological networks characteristic of normal and disease states. The magnitude, diversity, rich information content, and hierarchical connectivity of these data sets require the utilization and development of novel quantitative tools. The goal is to understand human disease at a molecular level in order to develop mechanism-based therapeutic interventions.

We invite applications for head of a new laboratory of Computational Medicine within the NEI Intramural Research Program. This initiative seeks to integrate and translate knowledge from genetics and biology to a wide range of disease processes using systems, network, statistical and bioinformatics approaches.

- Examples in ocular biology amenable to a systems approach would include neuro-immune interactions, gene regulatory networks during disease pathogenesis, protein interaction pathways, neuron-glial-vascular biological networks in the retina, neuronal networks in the CNS, and developmental conditions and disorders.
- The research program has interest in developing novel computational methodologies for analyzing large genetic, biological, biomedical, neuronal, and functional data sets. Particular attention will be paid to genotype-phenotype correlations, gene-gene and gene-environment interactions. In parallel, we will actively seek to develop disease intermediate phenotypes that reflect the underlying biology and pathophysiology of disease.
- Data sets from large clinical trials, genetic studies (including GWAS), expression profiling in normal and disease conditions, and from the eyeGENE human research repository for monogenic ophthalmic diseases will be developed to reconstruct and understand ocular biological networks that link genetic perturbations, small molecule interactions, and physiological processes, to predict normal and disease states.

The NEI/NIH provides an exceptional environment of dedicated scientists as well as a wide range of resources. We currently envision that this program will be located in the newly constructed Porter Neuroscience complex that houses a diverse set of investigators from many different institutes. The successful candidate will be expected to recruit tenure-track faculty in areas that may include computational medicine or neuroscience, network biology, genetic or molecular epidemiology, cell and molecular biology, statistical genetics, bioinformatics, and biostatistics into the new Laboratory of Computational Medicine. Applicants should have a MD, MD/PhD or PhD and an outstanding record of accomplishments in genetics, epidemiology, neuroscience, cell and molecular biology, biostatistics, or a related quantitative discipline. Senior scientists would have the opportunity to maintain their participation in existing collaborative research in non-eye diseases if desired.

This position will remain open until filled. Applicants should submit curriculum vitae, bibliography, copies of their five most significant publications, a summary of research accomplishments, names of three references, and a detailed experimental plan for the development of this program. These materials should be sent to: **The Office of the Scientific Director, National Eye Institute, Attention: Ms. Mica Gordon (gordonm@nei.nih.gov), NIH Building 31, 31 Center Drive, Room 6A22, Bethesda, MD, 20892**

Department of Health and Human Services
National Institutes of Health
National Institute on Deafness and Other Communication Disorders
Tenure-Track Investigator Position

The Division of Intramural Research, National Institute on Deafness and Other Communication Disorders (NIDCD), is seeking a tenure-track scientist to establish an independent research program applicable to hearing and balance. We welcome applications from candidates with clinical, translational, or basic scientific interests or programs. Preference will be given to candidates whose experimental approaches complement those of our existing strong programs in the genetics, development and cell biology of hearing and balance. The successful candidate will join a dynamic group of scientists in a growing intramural program at the forefront of research on communication disorders.

The NIDCD offers an exceptional working environment including well-equipped research laboratories, the NIH Clinical Center, and numerous opportunities for collaboration. This position includes a generous start-up allowance, an ongoing commitment of research space, laboratory resources, and positions for personnel and trainees. Candidates must possess a Ph.D., M.D., or equivalent degree, post-doctoral research experience, and an outstanding publication record. Salary is commensurate with education and experience.

Please submit a curriculum vitae including bibliography, statement of research interests, an outline of your proposed research, and full contact information for three references to: **Ms. Linda De Iberri, Office of the Scientific Director, NIDCD, 5 Research Court, Room 2B28, Rockville, MD 20850 (deiberril@nidcd.nih.gov)**. Applications will be reviewed starting **January 2, 2010** and accepted until the position is filled. DHHS and NIH are Equal Opportunity Employers and encourage applications from women and minorities.

Wildlife Trust announces 11 New Positions in Emerging Disease Ecology

Wildlife Trust is expanding its research programs in emerging disease ecology and seeks outstanding candidates for eleven positions. Full position descriptions available at **www.wildlifetrust.org/jobs**.

SEVEN SCIENCE AND RESEARCH POSITIONS

- **Senior Disease Ecologist, Conservation Biologist or Veterinarian** with a Ph.D or DVM/Ph.D and substantial experience managing international conservation and disease ecology research and field programs. Duties include management of field teams and building an independent research program on infectious disease ecology and conservation biology in emerging disease hotspots (S. America, S. Asia, SE Asia).
- **Four positions: Post Doctoral Field Ecologist/Epidemiologist/Veterinarian** to conduct research on emerging diseases and run field programs in S. America, S Asia, and SE Asia surveying wildlife for our new USAID PREDICT program. Must have experience working in developing countries. Experience with free-ranging wildlife is preferred.
- **Post Doctoral Modeler/Epidemiologist/Ecologist** to study the dynamics of pathogens in wildlife, humans and domestic animals. Excellent spatial statistical and dynamic modeling skills required.
- **Modeling Research Assistant (graduate-level)** to analyze dynamics of pathogen spillover from wildlife and livestock to people. Strong statistical or dynamic modeling background required. Epidemiological skills an advantage.

TWO MOLECULAR BIOLOGY POSITIONS IN PATHOGEN DISCOVERY

Based at the Center for Infection and Immunity, Columbia University, in Prof. W. Ian Lipkin's laboratory, jointly supervised by Dr. Peter Daszak, Wildlife Trust

- **Post Doctoral Molecular Biologist** to employ cutting edge technology to discover novel viral pathogens in wildlife samples. Ph.D. in Biological or Molecular Sciences and strong laboratory background are required.
- **Laboratory Technician** to employ cutting edge technology to discover novel viral pathogens in wildlife samples. MS in Biological or Molecular Sciences and strong laboratory experience are required.

TWO ADMIN. POSITIONS AT WILDLIFE TRUST NEW YORK CITY HEADQUARTERS

- **International Grant and Program Manager**, responsible for federal grant administration, logistical operations for research programs, and international project coordination. International travel is required. B.S. or M.S. degree in a suitable field.
- **Program Assistant**, to manage office functions in New York. Candidate must have excellent organizational and communication skills. Experience in financial management and IT is an advantage.

Further details can be found at **www.wildlifetrust.org/jobs**. All positions are based in New York and require some international travel. Review of applications will begin **November 15, 2009**. Candidates should submit, in one attached document, a full *CV*, names and email addresses of 2 academic references, and a 2-page cover letter by email to **jobs@wildlifetrust.org** stating clearly the position of interest and career goals.

Worcester Polytechnic Institute

Department of Biology & Biotechnology Faculty Position

The Department of Biology & Biotechnology invites applications for a tenure track faculty position at the ASSISTANT PROFESSOR level (http://www.wpi.edu/Academics/Depts/BBT/). This position is part of a 'cluster hire' of 7 faculty positions this year in WPI's ongoing initiative in the life sciences (www.wpi.edu/go/lifesci). Areas of particular interest include ecology and environmental biology, cell and developmental biology, and systems biology. We are especially inviting candidates working with microbial systems, although a promising research program and a commitment to teaching are more important than the research topic or organism. The ideal candidate will enjoy an interdisciplinary environment, with opportunities to interact with faculty in environmental or biomedical engineering in focus areas including green energy, environmental studies, and regenerative medicine.

Faculty are expected to establish a vigorous, extramurally funded research program, and to fully participate in teaching at the undergraduate and/or graduate level.

Located in Worcester, MA, WPI is a highly selective private university with an undergraduate student body of over 3,200 and 1,100 full-time and part-time graduate students (M.S. and Ph.D.). WPI is consistently ranked among the top national universities in U.S. News & World Report.

Interested candidates should forward applications including a cover letter, curriculum vitae, a description of research plans, a statement of teaching philosophy, and a list of five references (with full contact information) to: Professor Eric Oversturn, Head, Department of Biology & Biotechnology at faculty-searchBBT@wpi.edu. Review of applications will continue until the position is filled.

To enrich education through diversity,
WPI is an affirmative action, equal opportunity employer.
A member of the Colleges of Worcester Consortium

THE UNIVERSITY OF CALIFORNIA AT BERKELEY

Department of Molecular and Cell Biology Faculty Position in Stem Cell Biology

The Department of Molecular and Cell Biology at Berkeley is seeking applicants for a faculty position in stem cell biology. Candidates at both the junior (non-tenured) and senior (tenured) faculty level will be considered. In addition to evidence of a strong research program, candidates are expected to have an interest in undergraduate and graduate teaching. The position will be a 9-month academic year appointment.

With regard to research, we seek individuals studying any aspect of stem cell biology, including (but not limited to) the use of stem cells to develop models of human biology or disease, molecular mechanisms of transcriptional regulation in pluripotent and differentiating stem cells, the regulation of stem cell renewal and differentiation during development, and the biology of cancer stem cells. The precise area is less important than a demonstrated record of excellence, originality and productivity in research. The successful candidate could choose to affiliate with any one of the five Divisions within the Department (Biochemistry and Molecular Biology, Genetics, Genomics and Development; Cell and Developmental Biology; Immunology and Pathogenesis; and Neurobiology). The stem cell biology program is to be housed in a new building currently nearing completion, the Li Ka-Shing Center for Biomedical and Health Sciences, which will also house programs in infectious disease, cancer biology, neuroscience and computational biology.

Applications and letters of reference should be submitted online through **http://mcb.berkeley.edu**. Applications should include a *curriculum vitae*; a list of publications; copies of three significant publications; a brief description of research accomplishments; and a statement of research objectives and teaching interests. In addition, junior applicants applying for a non-tenured position should arrange to have three letters of reference submitted. Potential reviewers should be referred to the Statement of Confidentiality found at: **http://apo.chance.berkeley.edu/evalltr.html**. The deadline for applications is **January 4, 2010**.

The University of California is an Affirmative Action/Equal Opportunity Employer

Careers with **Mass Appeal**

Ecosystem Ecology Assistant Professor

The Department of Biology at the University of Massachusetts Boston seeks applicants for a full-time tenure track Assistant Professor in ecosystem ecology or a closely related field starting in September 2010. Applications will be particularly welcome from candidates who are working on some aspect of global change, landscape ecology, or conservation in marine, aquatic, coastal and/or terrestrial ecosystems. Possible areas include land use/land cover change, watersheds/wetlands, carbon sequestration, invasive species and community interactions.

The successful applicant is expected to establish an externally funded research program and to be actively committed to teaching at both the undergraduate and graduate levels. There are excellent opportunities to collaborate and engage in multidisciplinary research with UMass Boston faculty. The University has a strong faculty and substantial research programs in environmental areas, and doctoral programs in Environmental Biology; Molecular, Cellular and Organismal Biology; and Environmental Sciences. Applicants must have a Ph.D. and postdoctoral (or equivalent professional) experience. Members of underrepresented groups and women are strongly encouraged to apply.

Please send a statement of teaching and research interests and goals, curriculum vitae, 3-5 representative reprints and three letters of reference. We prefer application material be sent electronically to biology@umb.edu. If e-files exceed 15mb, please send in smaller segments as multiple emails. Hard copies can be sent to: **Ecosystem Ecology Search, Biology Department, University of Massachusetts Boston, 100 Morrissey Blvd., Boston, MA 02125. For further information, visit the Biology Department website at www.bio.umb.edu, or contact either Co-Chair of the Search Committee Solange Brault at solange.brault@umb.edu or 617 287 6683, or Rob Stevenson at robert.stevenson@umb.edu, or 617-287-6579.**

Target date for receipt of applications is **Dec. 15, 2009**, but applications will be reviewed until the position is filled.

UMass Boston is an Affirmative Action, Equal Opportunity, Title IX employer

UMASS BOSTON

Discover Where Diverse Minds Meet.

Have you ever wanted to meet other scientists from diverse backgrounds? Build relationships not limited by geography or chance? Connect with people who share your interests, face similar challenges, and have overcome obstacles to become leaders in their fields? Find them all at **MySciNet**, the new online community from *Science*, *Science* Careers, and AAAS.

There's no charge for joining, and you may immediately:

- Make personal connections for a more successful, rewarding career
- Join groups of scientists focused on issues important to you – or create your own group
- Find organizations dedicated to helping diverse scientists
- Research employers committed to diversity and inclusion

This professional network helps you connect with other scientists and students based on race, ethnicity, gender, disability, sexual orientation, or military service, as well as career and scientific interests.

Whether you're a student embarking on your career or a seasoned professional who wants to share your experiences, MySciNet welcomes you. Help create a thriving community of inclusion. Get involved and connect with MySciNet today.

Community.ScienceCareers.org/MySciNet

MySciNet
An Inclusive Community

Sponsored by

Genentech
A Member of the Roche Group

Pfizer

Presented by

AAAS | Science | Science Careers

Partners

AWIS | EntryPoint! | NOGLSTP

AWG | National Postdoctoral Association | ΣΔΕ | SACNAS | AWM

FACULTY POSITION
Environmental Science
NYU ABU DHABI

New York University has established a new comprehensive liberal arts campus in Abu Dhabi, the capital of the United Arab Emirates. New York University Abu Dhabi (NYUAD) will consist of a highly selective liberal arts college (Arts, Humanities, Social Sciences, Sciences and Engineering), distinctive graduate programs, and a world-class institute for advanced research, scholarship, and creative work. NYUNY and NYUAD are integrally connected. The faculties work together, and the campuses form the foundation of a unique global network university, linked to NYU's other study and research sites on five continents.

As part of a multi-year hiring plan, New York University Abu Dhabi's Division of Science, Technology, Engineering and Mathematics invites applications for a senior rank faculty position in Environmental Science to begin September 1, 2010. Extraordinary applications at the associate or assistant professor level will also be considered. Broadly, we seek an individual with an outstanding record of accomplishment in research and teaching in one or more of the following branches of Environmental Science, theoretical, computational, or observational. The individual will develop a world-class research program in environmental science relating to worldwide or regional problems in climate, global change, or related disciplines. The recruited faculty will participate in teaching in an innovative three-semester course in science called "Foundations of Science," which is designed to integrate basic concepts from various science disciplines, and is required for all science majors at NYUAD. The candidate will also lead the establishment of a new interdisciplinary major in environmental studies. Strong links to research and teaching at NYU New York will be created through frequent exchange visits. The terms of employment are competitive compared to U.S. benchmarks and include housing and educational subsidies for children.

The deadline for submission is ***December 15, 2009.*** Applicants must submit a cover letter, curriculum vitae, statement of research and teaching interests, and the names and addresses of three references in PDF format in order to be considered. Please do not submit preprints or publications at this time. Complete instructions for the application process and additional information can be found at **http://nyuad.nyu.edu/human.resources/open.positions.html**. If you have any questions, please e-mail **nyuad.environmental@nyu.edu**.

NEW YORK UNIVERSITY ABU DHABI

NYU Abu Dhabi is an Equal Opportunity/Affirmative Action Employer

---

COLUMBIA UNIVERSITY
IN THE CITY OF NEW YORK

Neuroscience Faculty Recruitment

The Department of Neuroscience at Columbia University plans to recruit new faculty in two broad areas of neuroscience: (1) the analysis of motor and cognitive processes in awake, nonhuman primates, (2) the use of molecular and cellular approaches to study neural circuitry in genetically tractable model systems. We encourage applications at all levels, from Assistant to Full Professor.

Columbia University has an exceptionally strong and broad program in the neurosciences and aims to enhance interactions between basic and clinical research, and to link the neurosciences with other scientific disciplines within the University. New faculty will be affiliated with the Department of Neuroscience and with the Doctoral Program in Neurobiology and Behavior. There are many opportunities for interaction with other scientific departments and programs at the Medical Center and Morningside Heights campuses.

Applications must be received by November 30, 2009, and should be submitted online at

https://academicjobs.columbia.edu/applicants/Central?quickFind=52268

Columbia University takes affirmative action to ensure equal employment opportunity

---

THE UNIVERSITY of TENNESSEE
HEALTH SCIENCE CENTER

NEUROSCIENCE FACULTY POSITIONS

The Department of Anatomy and Neurobiology at the University of Tennessee Health Science Center seeks outstanding neuroscientists to fill one or two tenure track positions. Appointments can be at any rank (**ASSISTANT, ASSOCIATE, FULL PROFESSOR**). The Department is the center of a well-established, collaborative multidisciplinary neuroscience program. Our facilities include state-of-the-art laboratories, a unique mouse genetics reference population (**http://cgb.utmem.edu**) and we offer competitive salary and start-up packages. We seek candidates to complement existing departmental strengths, which include electrophysiological, anatomical, behavioral, and genetic approaches to understand normal and pathological brain function. For additional information, see departmental (**http://www.utmem.edu/anatomy-neurobiology/**) and Neuroscience Institute (**www.utmem.edu/neuroscience/**) websites. We are particularly interested in candidates using molecular/genetic and/or optical imaging approaches for the study of excitability, synaptic function, neural development, sensory or motor systems, or neurodegenerative diseases. The successful candidate is expected to establish or maintain an independent, extramurally funded research program, and contribute to the department's teaching mission. Candidates must have a Ph.D., M.D., or equivalent, and relevant postdoctoral experience.

Submit curriculum vitae, summary of current and proposed research programs, teaching experience and interests, and contact information for three to five references, in a single Word or PDF document to **bjsmith@utmem.edu**. For best consideration, applications should be received by **December 1, 2009**, however review of applications will begin immediately.

The University of Tennessee is an Affirmative Action Employer, and we encourage applications from women and underrepresented minorities. The University of Tennessee is an EEO/AA/Title VI/Title IX, Section 504/ADA/ADEA Employer.

THE UNIVERSITY of TENNESSEE
HEALTH SCIENCE CENTER

ENDOWED PROFESSORSHIP IN NEUROSCIENCE

The Department of Anatomy and Neurobiology at the University of Tennessee Health Science Center is seeking an outstanding neuroscientist to fill the Methodist Chair in Neuroscience. The tenure track appointment will be at the rank of **FULL PROFESSOR**. The Department is the center of a well-established, collaborative multidisciplinary neuroscience program with state-of-the-art laboratories and a unique mouse genetics reference population (**http://cgb.utmem.edu**). We seek a candidate to complement existing departmental strengths - see departmental (**http://www.utmem.edu/anatomy-neurobiology/**) and Neuroscience Institute (**www.utmem.edu/neuroscience/**) websites for additional information. We are particularly interested in collaborative scientists who study excitability, synaptic function, neural development, neurogenetics, sensory or motor systems, or neurodegenerative diseases using a modern arsenal of techniques. The successful candidate should have a distinguished research program, a record of sustained funding, strong current funding and is expected to contribute to the department's teaching mission. Candidates must have a Ph.D., M.D., or equivalent.

Submit curriculum vitae, summary of current and proposed research programs, teaching experience and interests, and contact information for three to five references, in a single Word or PDF document to **bjsmith@utmem.edu**. For best consideration, applications should be received by **December 1, 2009**, however review of applications will begin immediately.

The University of Tennessee is an Affirmative Action Employer, and we encourage applications from women and underrepresented minorities. The University of Tennessee is an EEO/AA/Title VI/Title IX, Section 504/ADA/ADEA Employer.

UNIVERSITY of IOWA
CARVER COLLEGE OF MEDICINE
University of Iowa Health Care

DIRECTOR, FRATERNAL ORDER OF EAGLES DIABETES RESEARCH CENTER

The Carver College of Medicine at The University of Iowa seeks candidates for the position of Director, Fraternal Order of Eagles Diabetes Research Center The University, in partnership with the Fraternal Order of Eagles, is establishing a comprehensive diabetes research center. This is an extraordinary opportunity, as substantial resources are available to recruit a director and several faculty members. In addition, the Center will be located on a 20,000 square feet floor of the Iowa Institute for Biomedical Discovery, which is under construction

The director is the spokesperson for the Center and represents it in interactions with the college, the university, as well as nationally Responsibilities include faculty recruitment and appointments; educational and research programs; fiscal planning and management; interaction with other departments and centers; and short term and long term strategic planning. In addition, the director is a member of the Medical Council, which provides input to the Dean.

Candidates must have previous records consistent with appointment as a tenured professor in an appropriate academic department. This includes a PhD or MD degree or equivalent and an outstanding record of accomplishments in research, teaching, and service. The successful candidate should have the demonstrated capacity to foster an environment in which excellence in research, teaching, and scholarship can flourish, as well as experience and interest in developing and leading research programs Desirable attributes include a record of innovative and effective administrative and fiscal leadership, a record of excellent interpersonal skills, demonstrated experience promoting a diverse workforce, and positive interactions with students, staff and faculty. An interest in interdisciplinary research programs is necessary

The Carver College of Medicine is part of a major research university and ranks 11th among public medical schools in National Institutes of Health funding The College and the University of Iowa Hospitals and Clinics are equal partners in UI Health Care. The hospital is one of the largest university-owned teaching hospitals in the United States and is adjacent to the Iowa City Department of Veterans Affairs Medical Center

The University of Iowa is located in Iowa City, a vibrant community located in the rolling hills of Southeastern Iowa. The community offers excellent schools, quality entertainment, literary, musical and cultural opportunities and Big 10 sporting events

The search committee will accept nominations and applications until the position is filled Nominations should include a brief statement of the attributes and qualities of the individual that make him or her ideally suited for this position, a *curriculum vitae*, and the names, addresses and telephone numbers of three references

To apply for this position visit our website at:
http://jobs.uiowa.edu/faculty
(Requisition # 57198)

Contact information:
Daryl Granner and Michael Welsh
Co-Chairs, Diabetes Center Director Search Committee
Attn: Nancy Grubb
Office of the Dean, 216 CMAB
The University of Iowa
Carver College of Medicine
Iowa City, IA 52242-1101

nancy-grubb@uiowa.edu
michael-welsh@uiowa.edu
daryl-granner@uiowa.edu

The University of Iowa is an Equal Opportunity and Affirmative Action Employer. Women and minorities are strongly encouraged to apply

IST AUSTRIA
Institute of Science and Technology

IST Austria is looking for

PROFESSORS

and

ASSISTANT PROFESSORS

IST Austria (Institute of Science and Technology Austria) is a new institute located near Vienna, dedicated to basic research at the highest international level. The Institute invites applications and nominations for Professors and Assistant Professors in Life Sciences, Physical Sciences, Mathematics and Computer Science, as well as in any multidisciplinary field.

The Institute (www.ist.ac.at), established by the Austrian Government, opened its campus in 2009. Its funding is substantial, allowing for over 500 employees and graduate students by 2016. IST Austria is entitled to award Ph.D. degrees and includes an English-language Graduate School. It aims to achieve an international mix of scientists and recruit them solely on the basis of their individual excellence and potential contribution to research

The Institute is recruiting leaders of independent research groups. Professors will have indefinite contracts and Assistant Professors will have fixed-term contracts for an initial period of five years, with a possible, but not automatic, renewal for two additional years. Before the end of this period, the scientist will be considered for an indefinite appointment as a Professor at IST Austria, the decision being based on merit only (as is the case for a "Tenure-Track Assistant Professor" at U.S. universities)

The selected candidates will receive a competitive salary and a substantial annual research budget, covering operating expenses and the cost of Ph.D. students, postdoctoral fellows, and technical staff. Additional costs of starting a new laboratory, including instruments and infrastructure, will be offered separately. Scientists are also expected to apply for external research grants.

Applications and nominations should be sent to professor@ist.ac.at or assistant.professor@ist.ac.at, depending on the relevant position. Applications must include a CV, a list of publications and a research plan. Nominations should include an appraisal of the achievements and scientific qualifications of the nominee

IST Austria is committed to Equality and Diversity. In particular female applicants are encouraged to apply

School of Biosciences

Postdoctoral Research position in the Future of Reefs in a Changing Environment - FORCE (Ref. H87N2381)

Salary in the range £26,391 to £31,513 per annum, depending on knowledge and experience
Fixed-term for 4 years
Position based at the University of Queensland, Brisbane, Australia

The School of Biosciences at the University of Exeter wishes to recruit a Postdoctoral Researcher to join the research group of Professor Peter Mumby on a four year research project funded by the EU. The post is available from 1 March 2010. You will join a diverse network of scientists that includes coral biologists, field ecologists, climate modellors and conservation biologists. This collaborative project will focus on modeling of climate change impacts and bioerosion on Caribbean coral reefs and will involve extensive travel in the region.

You must possess a PhD or equivalent in a related field of study, have a background in ecological modelling (although this does not have to involve coral reefs or marine ecosystems) and have an appropriate track record of publications. Experience in bioerosion and reef accretion/calcification is desirable. You should be a confident, independent scientist with knowledge in the discipline and of contemporary research methods and techniques to work within established research programmes, and willing to work collaboratively with partners in other institutions and disciplines. Although you will be employed by the University of Exeter, this position will be seconded to the University of Queensland and you will be required to travel extensively in the Caribbean region to liaise with project partners.

Postdoctoral Research position in Coral Reef Studies (Ref. H88N2307)

Salary will be in the range £26,391 to £30,594 per annum
Fixed-term for 3 years
Position based at the University of Queensland, Brisbane, Australia

The School of Biosciences at the University of Exeter wishes to recruit a Postdoctoral Researcher to join the research group of Professor Peter Mumby on a grant funded by the Natural Environment Research Council (NERC) from 1 January 2010. You will join a diverse network of scientists that include coral biologists, field ecologists, climate modellors, and conservation biologists. This project will focus on spatially-realistic modelling of coral and fish metapopulation dynamics.

You must possess a PhD or equivalent in a related field of study, have a background in ecological modelling (although this does not have to involve coral reefs or marine ecosystems) and have an appropriate track record of publications. You should be a confident, independent scientist with knowledge in the discipline and of contemporary research methods and techniques to work within established research programmes, and willing to work collaboratively with partners in other institutions and disciplines. Although you will be employed by the University of Exeter, this position will be seconded to the University of Queensland and you will be required to travel to Exeter to liaise with partners modelling climate change.

For further information on either of these posts please contact Professor Peter Mumby, e-mail: p.j.mumby@ex.ac.uk or telephone: +44 (0)1392 263798

To apply, please send your CV and covering letter with the contact details of three referees to Professor Peter Mumby, School of Biosciences, Hatherly Laboratories, University of Exeter, Prince of Wales Road, Exeter EX4 4PS (e-mail: p.j.mumby@ex.ac.uk) quoting the appropriate job reference number.

The closing date for completed applications is 25 November 2009

The University of Exeter is an equal opportunity employer and promotes diversity in its workforce and, whilst all applicants will be judged on merit alone, is particularly keen to consider applications from groups currently underrepresented in the workforce

UNIVERSITY OF EXETER

POSITIONS OPEN

UNIVERSITY OF MARYLAND
SCHOOL OF MEDICINE

POSTDOCTORAL FELLOWSHIP is available to study the molecular mechanisms of hypertension, focusing on the involvement of a newly discovered signaling network that regulates kidney salt transport. The NIH funded project builds on our group's recent discovery of the first essential hypertension susceptibility gene in the general population, STK39, illuminating a multigene kinase pathway and a specific environmental trigger (dietary salt) in the genesis of the disease. The successful applicant will employ state-of-the-art physiological approaches, novel molecular tools, and new transgenic models to explore the mechanisms by which STK39 participates in the genesis of hypertension. Experience with transgenic mouse physiology is highly desirable. Electronically send curriculum vitae and names of three references to: **Dr. Paul A. Welling, Department of Physiology, University of Maryland Medical School, e-mail: pwelling@umaryland.edu.**

The Harvard Kennedy School seeks to appoint a **PROFESSOR** of public policy with special interests in energy policy to teach, lead and conduct research, mentor graduate students and postdoctoral fellows, and engage with other faculty, policy makers, and the public. Requirements include a Doctorate in a relevant field (e.g., natural science, engineering, economics, or public policy) with strong capacity to integrate methods and insights across disciplinary boundaries and a record of research and scholarly publication with a focus on energy policy, technology innovation strategy, energy systems analysis, or a combination of these. Relevant teaching experience is desirable, as are close, substantive familiarity with one or more of the global challenges related to energy policy (e.g., climate change, energy security, energy regulation, energy for economic development) and previous or current engagement with the public and private sectors as well as international perspectives on these issues.

Applicants should send curriculum vitae, letters of recommendation, and papers and publications to: **Professor William Hogan, Harvard Kennedy School of Government, Harvard University, 79 JFK Street, Cambridge, MA 02138.** The deadline for receipt of applications is December 15, 2009.

Harvard University is an Affirmative Action/Equal Opportunity Employer. Qualified women and members of minority groups are specially urged to apply.

ANIMAL PHYSIOLOGIST

The Department of Biology at William Paterson University invites applications for a tenure-track position at the **ASSISTANT PROFESSOR** level. Ph.D. required. Postdoctoral research and teaching experience preferred. Candidates are expected to develop a research program involving students and utilizing molecular techniques. Teaching responsibilities will include courses in anatomy and physiology, molecular biology, and area of specialization. The facilities of the Department include new animal research laboratories (full-time technician), electron microscopy suite, and well-equipped molecular biology laboratories. The Department offers B.S. and M.S. degrees in biology and biotechnology.

Applicants should submit curriculum vitae, statements of research interests and teaching philosophy, and names, addresses and telephone numbers of three references to: **Dr. Lance S. Risley, Chairperson, Department of Biology, Science Hall, William Paterson University, 300 Pompton Road, Wayne, NJ 07470.** Review begins immediately and continues until the position is filled. *WPU NJ is an Affirmative Action/Equal Opportunity Institution, women and minorities are encouraged to apply.*

UMDNJ
ROBERT WOOD JOHNSON MEDICAL SCHOOL
University of Medicine & Dentistry of New Jersey

The Cancer Institute of New Jersey
Bringing research to life.

NCI CCC
A Comprehensive Cancer Center Designated by the National Cancer Institute

PATHOLOGY POSITION AVAILABLE IN CANCER RESEARCH PROGRAM

The Cancer Institute of New Jersey (CINJ), part of the University of Medicine & Dentistry of New Jersey (UMDNJ)-Robert Wood Johnson Medical School (RWJMS), seeks an active researcher with the skills and energy to integrate well with our existing multidisciplinary Cancer Programs. An attractive component of the program is the access to translational laboratories for clinical investigators. The CINJ seeks to expand significantly the breadth and scope of existing research programs. We are looking to identify a pathologist for this exciting and challenging position during this academic year.

Candidates must have an MD, MD/PhD or related degree. This position will include oversight for the Tissue Analytic Services core facility. It is anticipated that candidates will oversee a research program and be willing to collaborate with UMDNJ, RWJMS, CINJ, Rutgers University and Princeton University investigators with similar research interests. Primary academic appointment will be in the Department of Pathology and Laboratory Medicine, and resident member of The CINJ. Rank will be commensurate with experience and there is an excellent benefits package.

The Cancer Institute of New Jersey, part of a comprehensive educational health science and hospital complex with convenient access to public transportation and major highways, is located in New Brunswick, New Jersey, approximately one hour from New York City and Philadelphia, and in the middle of the Washington-Boston corridor. Moreover, the majority of pharmaceutical companies are located near The CINJ complex. This proximity allows for collaborations at several levels, which is the norm for The CINJ members.

Nominations, letters of interest, and CVs should be addressed to: **Isaac Y. Kim, MD, PhD, Co-Chair, Search Committee, c/o Louise Burke, 335 George Street, Suite 3700, New Brunswick, NJ 08901. Email: burkels@umdnj.edu**. UMDNJ is an Affirmative Action/Equal Employment Opportunity Employer, m/f/h v, and a member of the University Health System of New Jersey.

UCSF UNIVERSITY OF CALIFORNIA SAN FRANCISCO

Assistant/Associate Professor
Program in Craniofacial and Mesenchymal Biology

The Program in Craniofacial and Mesenchymal Biology seeks to hire a faculty member to be appointed at the Assistant or Associate Professor level in the Department of Cell and Tissue Biology, School of Dentistry. Membership in the Biomedical Sciences Graduate Program will be offered. Candidates are expected to establish a dynamic research program and to contribute to teaching and training programs.

We are interested in basic research scientists and clinician-scientists with research in one of the following areas: craniofacial development, mesenchymal stem cells, epithelial/mesenchymal interactions, or skeletal development and biology. Candidates should hold a Ph.D., M.D., or D.D.S. degree.

Applications should include a curriculum vitae, three to five names and addresses of references, a brief description of research accomplishments, and a statement of future research plans and teaching interests. Position will remain open until filled.

Applications should be sent by email to:

Chair, Craniofacial/Mesenchymal Biology Search
c/o Roger Mraz (roger.mraz@ucsf.edu)

UCSF seeks candidates whose experience, teaching, research, or community service has prepared them to contribute to our commitment to diversity and excellence.

UCSF is an affirmative action/equal opportunity employer. The University undertakes affirmative action to assure equal employment opportunity for underutilized minorities, and women, for persons with disabilities and for covered veterans. All qualified applicants are encouraged to apply, including minorities and women.

CHILDREN'S HOSPITAL BOSTON
HARVARD MEDICAL SCHOOL

Assistant/Associate Professor
In Auditory or Vestibular Neuroscience

The Department of Otolaryngology at Children's Hospital Boston, in collaboration with the Neurobiology Program, seeks applications to fill a full-time tenure-track Assistant/Associate Professor position. The successful candidate will hold either a PhD and/or MD degree and will join the interactive neuroscience community at Children's Hospital and Harvard Medical School. We seek an outstanding scientist that will establish a vigorous research program in neuroscience related to the auditory or vestibular systems. Areas of interest include development, cell and molecular biology and physiology of the auditory and vestibular systems. Modern laboratory space will be located in the new Children's Hospital Center for Life Science Building. The investigator will hold both Children's Hospital Boston and Harvard Medical School faculty appointments.

Please submit a current CV, a two- or three-page description of research interests and directions, and three to five reference letters to: **ORLjob@childrens.harvard.edu**.

For more information about the Neurobiology Program at CHB see: **http://www.childrenshospital.org/research/mult_progs/**

Equal Opportunity/Affirmative Action Employer

Institute for Advanced Sustainability Studies (IASS)

The IASS invites applications for the position of

Secretary-General (m/f)

The Secretary-General will be responsible for the scientific co-ordination and working capacity of the IASS. Upon nomination by IASS Executive Committee he/she will be elected through the General Assembly. The position of Secretary-General is a full-time position. The Secretary-General will conduct transactions of the Incorporated Association independently and according to the Terms of Reference of the Executive Board. The successful candidate will be responsible for the following tasks:

- Organisation of the scientific operations of the IASS and the execution of administrative tasks, directly concerning the scientific negotiations
- Support of the Executive Board in the preparation, execution and post-proceedings of General Assembly meetings and with meetings of the Strategy Advisory Board as well as all other relevant advisory bodies of the association
- Execution of strategic scientific dialogues as well as the development and expansion of scientific exchange and partnerships at highest level and according to the specification of the Executive Board

Additional requirements:

- Completed University education in a relevant discipline, doctorate degree
- Pronounced ability for interdisciplinary work at highest level
- Excellent communication skills in English, additional foreign language desired
- Well-founded knowledge and comprehension of the German and international innovative and research policy as well as the scientific base for sustainable development
- Several years of experience and knowledge in the management of an internationally aligned institution
- High degree of leadership and social skills as well as personal engagement, implementation expertise, organizational and team ability in scientific networks

Remuneration is based on the Civil Service Collective Wage Agreement (TVöD) according to the type and scope of responsibilities.

Equal opportunity is an integral part of IASS personnel policy.
The IASS encourages applications from qualified female candidates.

Handicapped applicants will be given preference in the case of equal qualifications.

Please submit your applications in written form stating the reference code IASS/GS within **14 days** after publication to: **Prof. Dr. Dr. h. c. mult. Klaus Töpfer, Executive Director, Institute for Advanced Sustainability Studies - IASS, Berliner Str. 130, 14467 Potsdam, Germany**

ETH

Eidgenössische Technische Hochschule Zürich
Swiss Federal Institute of Technology Zurich

Assistant Professor of Evolutionary Biology / Associate Professor of Evolutionary Biology

The Department of Environmental Sciences at ETH Zurich (www.env.ethz.ch) invites applications for a professorship in evolutionary biology at the associate (tenure) or assistant (tenure track) level.

Candidates with outstanding scientific track records in any related field will be considered, but preference may be given to applicants working on animal population biology and/or natural host-parasite systems. The candidate is expected to establish a world-class research group and to integrate into research activities in related fields at ETH Zurich.

The successful candidate will contribute to the teaching of undergraduate and graduate level courses for students of the Departments of Environmental Science and Biology. He or she will be expected to teach undergraduate level courses (German or English) and graduate level courses (English). The professorship will be equipped with a generous personnel and operational budget, but the candidate will be expected to obtain further funds for research through competitive grants.

Assistant professorships have been established to promote the careers of younger scientists. The initial appointment is for four years with the possibility of renewal for an additional two-year period and promotion to a permanent position.

Please submit your application together with a curriculum vitae and a list of refereed publications **to the President of the ETH Zurich, Prof Dr. Ralph Eichler, Raemistrasse 101, 8092 Zurich, Switzerland, no later than January 31, 2010.** With a view towards increasing the proportion of female professors, ETH Zurich specifically encourages female candidates to apply.

POSITIONS OPEN

ETSU
East Tennessee State University

CHAIR, DEPARTMENT OF CHEMISTRY
East Tennessee State University

Position: The Department of Chemistry at East Tennessee State University seeks an outstanding scholar and administrator for the position of Chair to begin August 2010. Applicants must meet the requirements for tenure at the rank of **PROFESSOR** in the Department of Chemistry.

The Department of Chemistry currently includes 10 tenure-track faculty, six research and adjunct faculty, and three staff members and offers undergraduate and Master's degree programs. With American Chemical Society–approved chemistry and biochemistry concentrations, we are known for our strong teaching record and a rapidly growing research effort. We have a modern suite of instrumentation. Please see **website: http://www.etsu.edu/chemists/.**

East Tennessee State University has an enrollment of over 14,000 students. We are a Carnegie Foundation doctoral research university, with associated Colleges of Pharmacy and Medicine. ETSU is located in Johnson City, a city of 57,000 in Northeast Tennessee between the Great Smokey Mountains and the Blue Ridge Mountains. The area offers many opportunities for outdoor recreation and enjoys a moderate climate with four distinct seasons.

Responsibilities: The chair is expected to foster and promote scholarly productivity and visibility of a diverse and active faculty while supporting innovative and high-quality teaching, must serve as an advocate for the Department, supporting efforts to secure external funding, and maintain effective liaisons with the campus and community.

Qualifications: Applicants must have a Ph.D. in chemistry with a proven record of scholarship, teaching excellence, leadership ability, and effective communication skills. A record of successful grantsmanship is preferred.

Application: Please submit a letter addressing responsibilities and qualifications outlined above, curriculum vitae, a statement of administrative philosophy, and names and contact information for five references to: **Michael S. Zavada, Department of Biological Sciences, Box 70703, East Tennessee State University, Johnson City, TN 37614.** Review of applications will begin November 16, 2009, and continue until the position is filled. *Affirmative Action/Equal Opportunity. We actively strive to increase diversity (see **website: http://www.etsu.edu/equity/**). Minorities and women are encouraged to apply.*

Yale

The Section of Cardiovascular Medicine seeks exceptional candidates to establish research programs in cardiovascular developmental biology and genetics. Successful individuals will have Ph.D. and/or M.D. degrees and will have a proven record of originality and productivity. The Section is undergoing a major expansion and houses a newly formed Yale Cardiovascular Research Center. Yale University School of Medicine has established a close affiliation with University College London, United Kingdom, that among other benefits provides access to extensive clinical and translational genetics resources at UCL. Although all extraordinary candidates will be considered, we are especially interested in **DEVELOPMENTAL BIOLOGISTS** utilizing zebrafish as their model, who will be able to establish and operate a zebrafish research facility, and in **GENETICISTS** involved in translational genetics research, who will be able to run or participate in a clinical cardiovascular genetics program in addition to basic research efforts.

Please electronically send your curriculum vitae with a list of publications, a summary of research (two pages), and a research plan (three pages) along with the names of three references by December 1, 2009, to **e-mail: michael.simons@yale.edu.**

ETH

Eidgenossische Technische Hochschule Zürich
Swiss Federal Institute of Technology Zurich

Assistant Professor (Tenure Track) of Micro- or Nanofluidics

The new Department of Biosystems Science and Engineering at ETH Zurich (www.bsse.ethz.ch) in Basel invites applications for a professorship in Micro- or Nanofluidics. The successful candidate is expected to develop a strong and visible research program in the area of micro- or nanofluidic technologies that are relevant to Systems Biology and Synthetic Biology. Research topics include but are not limited to techniques for single-cell handling (growth and storage), single-cell or single-molecule characterization and analysis, targeted system manipulations, fluidic techniques for massively parallel cell assays, dosage and synthesis of biorelevant compounds, or nanotechnological approaches to subcellular-resolution or single-molecule analysis and manipulation.

Candidates should have a Ph.D. degree with a solid background in technology and engineering. They are expected to develop cutting-edge technologies and to intensely collaborate with biology and bioinformatics groups in our interdisciplinary Department. The ideal applicant should have successful proof of obtaining support for independent research projects and have a strong publication record reflecting innovative, interdisciplinary, and collaborative approaches to important problems in biology, biotechnology, and/or medicine. In addition, commitment to teaching and the ability to lead a research group are expected. The position is planned an assistant professorship (tenure track) with the option of an upgrade depending on the candidate's credentials and qualifications. She or he will be expected to teach under-graduate level courses (German or English) and graduate level courses (English).

Assistant professorships have been established to promote the careers of younger scientists. The initial appointment is for four years with the possibility of renewal for an additional two-year period and promotion to a permanent position.

Please submit your application together with a curriculum vitae, a list of publications, and statements on future teaching and research activities **to the President of ETH Zurich, Prof. Dr. Ralph Eichler, Raemistrasse 101, 8092 Zurich, Switzerland, no later than January 31, 2010.** With a view toward increasing the number of female professors, ETH Zurich specifically encourages qualified female candidates to apply.

University of Cincinnati

PROFESSOR (28UC0913)

Applications are invited for a full-time retinal cell biologist position in the Crawley Vision Research Center in the Department of Ophthalmology at The University of Cincinnati Medical Center. Duties will involve participation in ongoing projects in vision neuroscience research. The position includes an appointment at the rank of assistant/ associate/ professor or professor. The title, rank, and track will be commensurate with experience. Salary and Benefits: commensurate with faculty rank and experience.

The University of Cincinnati Medical Center has an outstanding core facility in transgenic and gene targeting, genomic DNA microarray and proteomics/mass spectrometry. The Crawley Vision Research Center in the Department of Ophthalmology is well equipped for molecular biology, cell biology, histology, and small animal surgery. The Department is expanding its research program in establishing an interdisciplinary Vision Research Center in the Medical Center.

Min. Quals.: Doctoral degree or equivalent in life sciences.

Ideal Qualifications: Individuals using molecular and genetic approaches for innovative research in Ocular Surface and Retinal Cell Biology and Age-related Macular Degeneration are particularly encouraged to apply.

To apply for this position (**28UC0913**), please see www.jobsatuc.com

The University of Cincinnati is an affirmative action/equal opportunity employer. UC is a smoke-free work environment.

UNIVERSITY OF Cincinnati

ETH

Eidgenössische Technische Hochschule Zürich
Swiss Federal Institute of Technology Zurich

Assistant Professor of Plant Ecology / Associate Professor of Plant Ecology

The Department of Environmental Sciences at ETH Zurich (www.env.ethz.ch) invites applications for a professorship in plant ecology at the level of associate (tenure) or assistant (tenure track) professor. Candidates with outstanding scientific track record in the general field of plant ecology will be considered, but prefe-rence may be given to candidates working on plant population or community ecology. The future professor is expected to establish a world-class research group and to integrate into research activities in related fields at ETH Zurich.

The successful candidate will be lecturing undergraduate and graduate level courses for students of the Department of Environmental Science and the Department of Biology. He or she will be expected to teach undergraduate level courses (German or English) and graduate level courses (English). This professorship will be equipped with a generous personnel and operational budget, but the candidate will be expected to obtain further funds for research through competitive grants.

Assistant professorships have been established to promote the careers of younger scientists. The initial appointment is for four years with the possibility of renewal for an additional two-year period and promotion to a permanent position.

Please submit your application together with a curriculum vitae and a list of refereed publications **to the President of ETH Zurich, Prof Dr. Ralph Eichler, Raemistrasse 101, 8092 Zurich, Switzerland, no later than January 31, 2010.** With a view toward increasing the number of female professors, ETH Zurich specifically encourages qualified female candidates to apply.

Dean, College of Agriculture & Life Sciences

http://www.cornell.edu/provost/searches/cals/

Cornell University invites applications and nominations for the position of Dean of its College of Agriculture & Life Sciences

Cornell, as the Land Grant University of the State of New York, is unique in pursuing its land grant mission within an Ivy League setting. The College of Agriculture & Life Sciences is a globally preeminent institution that, through its educational, research, and extension programs, develops the knowledge, technology, and human capacity to address some of the most challenging issues facing society in the environment, food and energy systems, and community and economic development. The College is committed to having a profound impact on the lives of its urban and rural stakeholders–from fundamental discovery through direct translation of research to nature, farms, homes, and offices throughout New York State, the nation, and the world. The Dean works closely with the University administration to maintain and advance these programs as well as relationships with the State of New York and the State University of New York (SUNY system). In addition, the Dean shares responsibility for leadership and advancement of Cornell Cooperative Extension with the Dean of the College of Human Ecology.

As chief academic and administrative officer, the Dean has the opportunity and primary responsibility for developing and implementing the strategic direction of the College of Agriculture & Life Sciences. The College has approximately 370 faculty, 500 non-professorial academics, 140 postdoctoral associates, 1,300 staff, and a student body of more than 3,300 undergraduate and 900 graduate students. As a member of Cornell's senior administrative team, the Dean reports to the Provost and works closely with other deans and executive officers on behalf of the university as a whole.

We seek a creative leader and accomplished scholar. The new Dean will be intellectually curious, will listen carefully, administer wisely, delegate judiciously, further expand research and teaching excellence, embrace diversity, actively engage multiple constituencies, communicate clearly, advocate boldly, respect the past, understand the present, and envision the future.

In keeping with Cornell University's commitment to building a culturally-diverse community, nominations of and applications from women and other underrepresented groups are particularly encouraged. Applications should include a statement of interest and a curriculum vitae. Applications and nominations will be kept strictly confidential. The review of materials will begin immediately and continue until the new Dean is selected.

Send materials to: **College of Agriculture & Life Sciences Dean Search Manager, 440 Day Hall, Cornell University, Ithaca, NY 14853-2801**. Or electronically to **calsdeansearch@cornell.edu**

Cornell University

Cornell University is an Affirmative Action/ Equal Opportunity Employer and Educator

Principal Investigator & Vice Director Position at National Institute of Biological Sciences, Beijing

NIBS

Principal Investigator: National Institute of Biological Sciences, Beijing (NIBS) plans to start an expansion program and 20 to 25 multiple Principal Investigator (PI) positions are available. We expect PIs to lead independent laboratories in studying mechanism-based biological processes regardless of model systems. Candidates who are working on biochemistry, cell biology, chemical biology, plant biology, synthetic chemistry or animal model of mammalian system are particularly welcome. The candidate should have a Ph.D. degree and several years of postdoctoral training.

The initial appointment will be for 5 years, with full funding support by Chinese government. Renewal of appointment will be based on merit and is conditional upon passing reviews by international committees. In addition to generous start-up packages, core facilities and internationally competitive salaries and benefits, NIBS aims to provide its faculty members with an exciting environment, collegial and interactive colleagues, efficient administrative and support mechanisms, outstanding graduate students, and opportunities for substantial communications with the international scientific community, enabling PIs to conduct significant and creative researches. NIBS is particularly experienced in helping young scientists who are fresh out of their postdoctoral training to establish their laboratories quickly and efficiently. There is no limitation for different nationality and race, and foreign applicants are encouraged to apply.

Vice Director of translational Research: NIBS seeks to appoint an experienced leader in translational research as the vice director, who will oversee translational research at NIBS. Candidates with an MD, MD/Ph.D. or PhD with extensive industrial experience are particularly encouraged to apply.

Further information about NIBS and the position is available at **http://www.nibs.ac.cn.**

Applicants should send their CVs and research interests for PI and work plan for vice director (limited to 3 pages) in English to the following email address: **lixiaohong@nibs.ac.cn.** They should also arrange 3 recommendation letters to be sent to the same address.

POSITIONS OPEN

MOREHOUSE SCHOOL OF MEDICINE

CHAIR OF MICROBIOLOGY, BIOCHEMISTRY AND IMMUNOLOGY
at Morehouse School of Medicine

Morehouse School of Medicine invites applications from candidates holding the Ph.D. and/or M.D. degree(s) for the position of Chairperson of the Department of Microbiology, Biochemistry and Immunology. Applicants must have the credentials for appointment to the rank of **ASSOCIATE PROFESSOR** or higher and a track record of research funding. The successful applicant is expected to (i) continue key departmental service to the educational mission of the medical and graduate programs, (ii) identify and develop a sustainable departmental research focus; (iii) articulate a vision for this multidisciplinary Department; (iv) encourage collaboration within MSM and with national and international institutions, and (v) advance the strong mission of Morehouse School of Medicine (**website: http://www.msm.edu/Documents/Administration/marcom_FactSheet.pdf**). The Department consists of 15 faculty members at or above the rank of assistant professor whose research foci are infectious disease, cancer biology, and nutritional biochemistry (see **website: http //www.msm.edu/Academics/Microbiology_Biochemistry and Immunology htm**)

Interested applicants should submit curriculum vitae and a letter of interest that includes a description of the candidate's broad vision of a medical school department either electronically (**e-mail: gwaymon@msm.edu**) or by surface mail to: **Peter MacLeish, Ph.D., Chair, MBI Chair Search Committee, 226 MRC, Morehouse School of Medicine, 720 Westview Drive, S.W., Atlanta, GA 30310.** Correspondence will be kept confidential. Review of candidates will begin on January 15, 2010, and will continue until the position is filled.

The Morehouse School of Medicine is an Affirmative Action/ Equal Opportunity Employer and encourages applications from women and underrepresented minority candidates.

ANATOMY AND CELL BIOLOGY
East Carolina University

The Brody School of Medicine at East Carolina University (ECU) in Greenville, North Carolina, is actively recruiting for two faculty positions in the Department of Anatomy and Cell Biology. Tenure track or fixed-term appointment at the **ASSOCIATE** or **ASSISTANT PROFESSOR** level is available, based on qualifications. We are seeking applicants with a strong interest in graduate student education and experience teaching the basic human anatomical sciences. Research programs must complement the strengths of ongoing research in the Department.

For detailed information about the positions, please access the Human Resources website and apply using the online application process to position **#957506 ecu.peopleadmin.com/applicants/Central?quickFind=60691** or **#957508 ecu.peopleadmin.com/applicants/Central?quickFind=60652.**

ECU is a constituent institution of the University of North Carolina; view our departmental **website: http://www.ecu.edu/anatomy.**

An Equal Opportunity/ Affirmative Action University that accommodates the needs of individuals with disabilities.

ASSISTANT PROFESSOR: CHEMISTRY. Central Michigan University seeks a dynamic and creative scientist for a tenure-track Assistant Professor position in the Department of Chemistry and the interdisciplinary Science of Advanced Materials (SAM, Ph.D. program to begin August 2010. This position adds to a newly formed group exploring new materials for alternative/renewable energy applications. The preferred candidate will develop a competitive, externally funded research program in electrochemistry with additional emphasis on the synthesis and characterization of inorganic-based materials or nanomaterials. For more information and to apply see **website: http://www.fps.cmich.edu/jobs/CST_CHM.asp.** *Equal Opportunity Employer*

TEXAS STATE UNIVERSITY
SAN MARCOS
The rising STAR of Texas

Department of Chemistry and Biochemistry
TWO FACULTY POSITIONS

ORGANIC or ORGANOMETALLIC CHEMISTRY: Candidates for this position must have a PhD or equivalent degree in Chemistry or related field, post doctoral experience or equivalent, and a research area that complements existing faculty research in the department. The successful candidate will teach undergraduate and graduate courses in the area of organic chemistry, as well as other specialized courses commensurate with their area of expertise. In addition, a successful candidate will be expected to establish an externally funded research program involving both undergraduate and graduate students.

Applicants should submit a CV, a summary of research plans, a short description of teaching philosophy, unofficial undergraduate and graduate transcripts, and the contact information for three personal references to **Dr. Chad J. Booth, Chair: Organic Chemistry Search, Department of Chemistry and Biochemistry, Texas State University-San Marcos, 601 University Dr., San Marcos, TX 78666.** In order to assure full evaluation, materials must be submitted by **January 4, 2010**.

CHEMICAL EDUCATION: A doctoral degree is required. Preference will be given to candidates who have a doctoral degree in chemistry, biochemistry, or chemical education. A doctoral degree in education with a minimum of 18 hours of graduate coursework in chemistry or biochemistry will be considered. The successful candidate will teach courses in chemistry or biochemistry and have the opportunity to expand upon the existing undergraduate teaching certification programs in chemistry and physical science. Responsibilities will include working to recruit, retain, mentor and supervise pre-service secondary chemistry teachers, engage in externally funded scholarly activities in chemical education, and build university, school and community partnerships in science education. Preference will be given to those candidates who have experience working with secondary schools, post-doctoral or equivalent research experience in chemical education, and a documented record of teaching excellence.

Applicants should submit a CV, a one to two page summary of research plans, a short description of teaching philosophy, unofficial undergraduate and graduate transcripts, and arrange for three letters of recommendation to be sent to **Dr. Debra A. Feakes, Department of Chemistry and Biochemistry, Texas State University-San Marcos, 601 University Dr., San Marcos, TX 78666**. In order to assure full evaluation, materials must be submitted by **January 4, 2010**.

Texas State University-San Marcos is a doctoral-granting university located in the burgeoning Austin-San Antonio corridor, the largest campus in The Texas State University System, and among the largest in the state. Over 30,800 students at Texas State choose from 101 bachelor's, and 88 master's and 9 doctoral programs offered by eight colleges. With a diverse campus community including 33% of the student body from ethnic minorities, Texas State is one of the top 20 producers of Hispanic baccalaureate graduates in the nation. Additional information about Texas State and its nationally recognized academic programs is available at http://www.txstate.edu. The Department of Chemistry and Biochemistry currently has 20 faculty members and almost 350 majors who are strongly encouraged to participate in research. For more information, please visit **www.txstate.edu/chemistry**

Texas State University-San Marcos is an Equal Opportunity Employer, women and members of underrepresented minorities and individuals with disabilities are encouraged to apply.

Assistant Professor of Insect Vector Biology
School of Integrative Biology
University of Illinois at Urbana-Champaign

The School of Integrative Biology and the Department of Entomology at the University of Illinois, Urbana-Champaign, seek an outstanding scientist with a background and experience in insect vector biology for a full-time, 9-month, tenure-track faculty position at the assistant professor level to begin August 2010. Candidates must have a Ph.D. or equivalent in a relevant field by August 2010. The successful candidate will be expected to develop an externally funded research program, teach at the undergraduate and graduate level, and collaborate with other faculty to develop research initiatives in insect vector biology.

The University of Illinois provides a highly collaborative and supportive academic environment, with opportunities for interactions with the Institute for Genomic Biology; Center for Zoonoses Research; GIS and Spatial Analysis Laboratory; the Program in Ecology, Evolution, and Conservation Biology; the National Center for Supercomputer Applications; the Roy J. Carver Biotechnology Center; the Beckman Institute for Advanced Science and Technology; and the Illinois State Natural History Survey and Geological Survey.

Urbana-Champaign, located 120 miles south of Chicago, offers a variety of cultural opportunities that showcase the area's diverse ethnic population, superb public and private schools, quality public transportation, and a rapidly expanding community of high-tech businesses.

The anticipated starting date for the position is on or about August 16, 2010. Salary is commensurate with experience. To ensure full consideration please create your candidate profile through **https://jobs.illinois.edu** and upload your application letter, curriculum vitae, summary of research and plans, and contact information for three or more personal references by the close date of **December 11, 2009**. For further information contact: **Vector Biology Search Committee**, **sib@life.illinois.edu** or **217 333-3488**. Applicants may be interviewed before the closing date; however, no hiring decision will be made until after that date.

The University of Illinois is an Affirmative Action/Equal Opportunity Employer. The administration, faculty, and staff embrace diversity and are committed to attracting qualified candidates who also embrace and value diversity and inclusivity.

UNIVERSITY OF LIVERPOOL

Faculty of Health and Life Sciences
School of Biomedical Sciences
MRC Centre for Drug Safety Science

Chair in Pharmacology

Salary negotiable

The University of Liverpool invites applications for a Chair of Pharmacology based in the School of Biomedical Sciences and recently awarded prestigious MRC Centre for Drug Safety Science. This is an opportunity for an outstanding individual with a proven track record.

You will have an established independent research programme which will complement and enhance the existing strengths in Pharmacology and the MRC Centre. Candidates with an established track record in research in any relevant field of Pharmacology, Toxicology or Medicinal Chemistry will be welcomed. High quality laboratory research space exists, and there is an opportunity to develop further refurbished research laboratories.

Informal enquiries to Professor Kevin Park, Head of the School of Biomedical Sciences and Director of the MRC Centre on 0151 794 5543, email: b.k.park@liv.ac.uk

Job Ref: A-508334/S **Closing Date: 8 January 2010**

For full details, or to request an application pack, visit www.liv.ac.uk/working/job_vacancies/ or e-mail jobs@liv.ac.uk
Tel 0151 794 2210 (24 hr answerphone)
please quote job ref in all enquiries.

COMMITTED TO DIVERSITY AND EQUALITY OF OPPORTUNITY

POSITIONS OPEN

UT SOUTHWESTERN MEDICAL CENTER

THE UNIVERSITY OF TEXAS SOUTHWESTERN MEDICAL CENTER

ASSISTANT PROFESSORS. The Department of Physiology invites outstanding scientists with Ph.D., M.D., or equivalent degrees to apply for tenure-track Assistant Professor positions. Candidates who use innovative optical, mechanical, electrical, molecular biological, or computational methods with important applications to physiological systems, ranging from individual genes and proteins to cells and organs, are encouraged to apply. However, the scientific excellence of the candidates is more important than the specific area of research.

These positions are part of the continuing growth of the Department at one of the country's leading academic medical centers and will be supported by significant laboratory space on our new campus, competitive salaries, and exceptional startup packages. The University of Texas Southwestern Medical Center is the scientific home to four Nobel Prize laureates, 17 members of the National Academy of Sciences, and 17 members of the Institute of Medicine. UT Southwestern conducts more than 3,500 research projects annually totaling more than $400 million.

Applicants should submit curriculum vitae along with a brief statement of research plans and should arrange to have three letters of reference sent to: **James Stull, Ph.D., c/o Ronald Doris, Department of Physiology, The University of Texas Southwestern Medical Center, 5323 Harry Hines Boulevard, Dallas, TX 75390-9040.** *UT Southwestern strongly encourages applications from women, minorities, and people with physical challenges. An Equal Opportunity Employer.*

OPEN-RANK FACULTY
Department of Biological Sciences
University of Delaware

The Department of Biological Sciences at the University of Delaware is seeking to fill an open-rank Faculty Position. The University, as a member of the Delaware Health Science Alliance (**website: http://www.delawarehsa.org/**), has established research initiatives in cardiovascular biology, rehabilitation medicine, neuroscience, and cancer biology for which the Department of Biological Sciences plays a central role. Priority will be given to those applicants whose area of research focus is translational biology in cardiovascular or rehabilitation medicine.

Requirements for the position include a Ph.D. or equivalent degree, a minimum two years of postdoctoral experience, and a strong commitment to both research and education at the graduate and undergraduate levels. A successful candidate is expected to develop or continue an active research program, pursue extramural funding, and participate in undergraduate and graduate education.

This position will occupy recently renovated laboratory space, receive a competitive salary and startup package, and have access to state-of-the-art core facilities within the Department (**website: http://www.bio.udel.edu/**), the Center for Translational Cancer Research (**website: http://www.udel.edu/ctcr/**), and the Delaware Biotechnology Institute (**website: http://www.dbi.udel.edu/**). The Department of Biological Sciences consists of 35 faculty and currently has 90 students in its M.S./Ph.D. program.

Please submit complete curriculum vitae, a two- to three-page description of research interests and plans as well as one to two pages of teaching plans, and the names of three references with contact information either to: **Dr. Ulhas P. Naik, Chair, Search Committee, Department of Biological Sciences, University of Delaware, Newark, DE 19716-1590** or to our **website: http://www.udel.edu/bio/news/facultysearch/**. Review of applications will begin upon receipt, but the application deadline is December 31, 2009. The starting date for this position is September 1, 2010.

The University of Delaware is an Equal Opportunity Employer which encourages application from minority group members and women.

POSITIONS OPEN

TENURE-TRACK FACULTY POSITION

The Department of Nuclear Medicine (**website: http://nm.snu.ac.kr/eman.php**) and the Department of Molecular Medicine and Biopharmaceutical Sciences (**website: http://mmbs.snu.ac.kr**), Seoul National University, Seoul, Korea, invite a full-time, tenure-track faculty who will charge innovative research using nanomedicine (focusing on brain research and oncology) and education for postgraduate M.D. or Ph.D. candidates in English. Our expertise and current topics are in vivo molecular imaging revealing the expression of specific genes, biomarkers, and cell trafficking using multimodal imaging, nanoparticles as well as radioisotope. Our Department was designated as International Atomic Energy Agency Collaborating Center for Nuclear Medicine and Molecular Imaging for research and training from 2004. Applicants must have an M.D. or Ph.D. degree and be citizens of a foreign country. Please, inquire or send electronically curriculum vitae and a short statement to **Prof. Dong Soo Lee, e-mail: dsl@snu.ac.kr** until January 1, 2010.

JOINT FACULTY POSITION
Duke University
Department of Biomedical Engineering
Duke Global Health Institute

The Department of Biomedical Engineering (BME) at Duke University and the Duke Global Health Institute (DGHI) seek a faculty candidate who will lead the development of bioengineering tools for applications to global health. We are particularly interested in individuals with expertise in developing point-of-care diagnostics and the modeling of the spread of infectious disease. Rank is open and will depend on the qualifications and experience of the candidate. While applications from candidates with expertise in all areas of BME applied to global health are encouraged, we are particularly interested in candidates with expertise related to nanotechnology and biomaterials, gene and drug delivery, imaging, genomic technologies, and biomolecular modeling.

We seek applicants with a vision of collaboration and a research and teaching focus that is cross-disciplinary. Candidates must have a Doctorate in biomedical engineering, or a related field of science or engineering, and an outstanding record of accomplishment. The successful candidate will be expected to develop an active, externally funded research program, to build strong ties between DGHI and BME, initiate collaborative research with other faculty at Duke University and the Medical Center, and have a strong commitment to teaching at the undergraduate and graduate levels.

The application materials must include curriculum vitae (with address, telephone number, and e-mail address); statements of research and teaching interests, and names, addresses, telephone numbers, and e-mail addresses of three references. For full consideration, please submit your application by December 31, 2009.

Please submit application electronically to **website: https://academicjobsonline.org/ajo/Duke/BiomedicalEngineering/237.**

Duke University is an Affirmative Action/Equal Opportunity Employer. Applications from women and underrepresented minority groups are strongly encouraged.

FACULTY POSITIONS IN BIOLOGY
The American University of Beirut

The Biology Department at the American University of Beirut is seeking to fill **ASSISTANT PROFESSORSHIPS** in the following fields: molecular microbiology, population genetics, bioinformatics, plant biology, and biochemistry to begin September 15, 2010. Appointments at higher rank will be considered. For more information please visit our **website: http://www.aub.edu.lb/fas.** Applications will be accepted until January 15, 2010. *The American University of Beirut is an Affirmative Action, Equal Opportunity Employer.*

POSITIONS OPEN

RUTGERS

ASSISTANT PROFESSORS
in Center for Computational and Integrative Biology

The newly created Center for Computational and Integrative Biology (CCIB) on the Rutgers University-Camden campus seeks broadly trained experimental and theoretical researchers for two tenure-track Assistant Professor positions beginning fall 2010. The CCIB is an interdisciplinary research center with participating faculty members from the departments of Biology, Chemistry, Computer Science, Mathematics (including statistics), and Physics. In keeping with the CCIB's interdisciplinary thrust and Rutgers's appointment procedures, we seek two successful candidates who will hold tenure-track positions in two different home departments from among the following CCIB participating departments: Biology, Chemistry, Physics, and Computer Science. The mission of the CCIB is to determine the quantitative organizational principles of complex biological systems, using interdisciplinary approaches (see **website: http://www.camden.rutgers.edu/deptpages/biology/CCIB/Pages/About.htm**). The CCIB will start new doctoral and Master's programs in Computational and Integrative Biology in 2010. Successful applicants will be expected to develop productive, well-funded research programs and should take a strongly collaborative approach consistent with the mission of the CCIB. The positions entail teaching undergraduate and graduate courses in the area of the applicant's expertise. Ph.D. required and postdoctoral experience expected. Applicants should send a letter of interest, curriculum vitae, representative publications, and three letters of recommendation to: **Dr. Joseph V. Martin, Center for Computational and Integrative Biology, Rutgers University, Camden, NJ 08102.** Review of applications will begin January 15, 2010, and continue until the positions are filled. *Rutgers is an Equal Opportunity/Affirmative Action Employer. Women and minorities are strongly encouraged to apply. Rutgers University is the recipient of the National Science Foundation ADVANCE: Institutional Transformation Award to increase the participation of women in academic science and engineering careers.*

ASSISTANT PROFESSOR
MIT Department of Earth, Atmospheric and Planetary Sciences

The MIT Department of Earth, Atmospheric and Planetary Sciences (EAPS) seeks applicants for a tenure-track faculty position in climate within its Program in Atmospheres, Oceans, and Climate. Areas of specific interest include theory, models and observations of present and past climates, the cryosphere, and biogeochemical cycles. Preference will be given to candidates at the junior faculty level.

Requirements: The successful candidate will have a Ph.D. or near completion of degree, or completion of Ph.D. by start date of employment. Candidates will also have a strong record of accomplishment in their discipline, a strong commitment to teaching and student advising, and a keen interest in relating their work to complementary work in the climate sciences at MIT. Joint appointments with other MIT departments are also potentially negotiable where appropriate.

More information about this position can be obtained by writing: **Prof. Raffaele Ferrari, MIT Room 54-1420, Cambridge, MA 02139. E-mail: rferrari@mit.edu.**

A completed application will include curriculum vitae, a statement of research and teaching objectives, and the names of five potential references.

Applications are being accepted at Academic Jobs Online (**website: https://academicjobsonline.org/ajo**). To receive full consideration, a completed application must be received.

Search contact: **Mr. Michael Richard, Human Resources Administrator, EAPS, 54-926 Massachusetts Institute of Technology, 77 Massachusetts Avenue, Cambridge, MA 02139-4307. E-mail: mjr@mit.edu; telephone: 617-253-5184; fax: 617-253-8298.**

MIT is an Equal Opportunity/Affirmative Action Employer. Applications from women, minorities, veterans, older workers, and individuals with disabilities are strongly encouraged.

2010 Novartis Immunology Prizes

The 2010 Novartis Prizes, one for Basic Immunology and one for Clinical Immunology are awarded for outstanding achievements in the understanding of immunology and major immunological discoveries that lead to therapeutic applications in such fields as transplantation, haematopoiesis, cancer immunology, immunity to infectious diseases, rheumatology, dermatology and asthma. For more information, please visit www.novartisimmunologyprizes.org

The next Novartis Immunology Prizes will be awarded at the XIVth International Congress of Immunology in Kobe, Japan on 23 August 2010 in a special Award Ceremony during Monday afternoon.

Each prize is worth SFr 100 000

Nominations in English should comprise a summary of the research work up to 2 pages, a curriculum vitae, a bibliography and reprints of not more than 3 key published papers in English or with extended summaries in English.

The deadline for entries is 24 January 2010.

They should be sent, including an electronic version of the summary, to:
Dr Erik Wiskott, Novartis Prizes for Immunology, P.O. Box 360, CH 4013, Basel, Switzerland. Tel/Fax: +41 61 421 9019 E-mail: erik.wiskott@novartis.com

Judges: Andrew McMichael (Chair), Tadamitsu Kishimoto, Bernard Malissen, Philippa Marrack, Hidde Ploegh, David H. Sachs, Jan de Vries.

NOVARTIS

Trustee

The National Gallery in London is home to one of the world's greatest collections of Western European paintings.

A new Trustee is sought for appointment early in 2010.

You should have a love of paintings, share the Gallery's commitment to making its great collection freely accessible to the widest possible audience and be prepared to assist in fundraising for acquisitions and other major projects.

On this occasion, we wish to appoint a Trustee from a scientific background, with an interest in promoting public understanding of the role of science in museums and to chair the Gallery's Scientific Consultative Group. Experience of running an academic institution or department or Government Research Council connections might be helpful. The Gallery has Independent Research Organisation status for the AHRC and the EPSRC.

All Trustees are expected to attend six Board meetings (and one strategy weekend) each year, to assist by serving on committees of the Board, and to attend other events at the Gallery. As the Chair of the Scientific Consultative Group you would need to devote approximately two extra days a year to the work of that Group.

For an information pack and details of how to apply, please visit our website at www.nationalgallery.org.uk/trustee-appointments email trusteeappointments@ng-london.org.uk or telephone the Secretary to the Board on 020 7747 2801.

Applications should arrive no later than 4 December 2009. Interviews are expected to take place in London on Tuesday 19 January 2010.

The National Gallery and DCMS operate an equal opportunities policy.

THE NATIONAL GALLERY

dcms

McGill

The Louis and Artur Lucian Award For Research in Circulatory Diseases

Each year a Committee from the McGill University Faculty of Medicine confers the Louis and Artur Lucian Award ($60,000 Cdn.) for outstanding research in the field of circulatory diseases. The purpose of this Award is to honour a scientific investigator or group of investigators whose contribution to knowledge in this field is deemed worthy of special recognition. The successful recipient is invited to spend a short period of time at McGill University to give a formal Lucian Lecture and to have interchanges with members of the McGill community. Submissions should be received on or before March 19, 2010.

For further information and to download the nomination form, please check the following website, **http://www.mcgill.ca/lucianaward** or contact:

Dr. Jacques Genest, Chair
The Louis and Artur Lucian Award Committee
Royal Victoria Hospital - McGill University Health Centre
Cardiovascular Research Laboratories, H7.14
687 Pine Avenue West
Montreal, Quebec, CANADA H3A 1A1
Tel: (514) 934-1934, Ext. 34631
FAX: (514) 843-2843

POSITIONS OPEN

UNIVERSITY of ROCHESTER MEDICAL CENTER

TENURED/TENURE-TRACK FACULTY POSITION
at The University of Rochester Eye Institute

The University of Rochester Eye Institute seeks an exceptional scientist to fill a tenured and/or tenure-track faculty position at the **ASSISTANT, ASSOCIATE,** or **FULL PROFESSOR** level. Rank will be commensurate with experience. Applicants must have an M.D. and/or Ph.D. degree and have scientific interests in vision research, including but not limited to eye development, genetics, diseases, stem cells, and gene therapy. Emphasis will be placed on the applicants' proven track record of high-quality research and publications and on the promise of their future research plans.

Successful applicants will be expected to establish vigorous, independent research programs, form productive collaborations, and if appropriate, pursue translation of their research. The ideal applicants will benefit from preexisting expertise within the University community in neuroscience, optics, and mouse genetics.

Review of applications will commence December 1, 2009, and continue until the position is filled. Qualified applicants should submit their curriculum vitae, the names and contact information of three or more references, a brief summary of research accomplishments, and an outline of future research plans to: **Lin Gan, Ph.D., University of Rochester Eye Institute, 601 Elmwood Avenue, Box 659, Rochester, NY 14642. E-mail: lin_gan@urmc.rochester.edu.** *The University of Rochester is an Affirmative Action, Equal Opportunity Employer.*

POSTDOCTORAL POSITION
in Translational Immunology
Yale University School of Medicine

Postdoctoral position to study the molecular biology of the innate immune response is available at the Yale School of Medicine. Candidates should have a Ph.D. degree and must have published experience in molecular biology or immunology. The research will be under the supervision of **Richard Bucala, M.D.-Ph.D.,** in the Departments of Internal Medicine and Pathology. Please electronically submit your curriculum vitae along with a copy of prior publications and the names of two references to **e-mail: richard.bucala@yale.edu.** *Yale is an Affirmative Action/Equal Opportunity Employer.*

UT SOUTHWESTERN MEDICAL CENTER

POSTDOCTORAL POSITIONS available to study mechanisms of chromatin-dependent transcription and posttranslational modification of transcription factors, cofactors, and chromatin modifiers. Current focuses include functional interplays between AP-1, C/EBP, YY1, p53, Brd4, and HPV E2 and E6 in regulating cellular and viral gene transcription. Applicants should electronically send curriculum vitae and names of references to: **Dr. Cheng-Ming Chiang, e-mail: cheng-ming.chiang@utsouthwestern.edu** at UT Southwestern Medical Center at Dallas, Texas. Visit **website: http://www.utsouthwestern.edu/findfac/research/0,2357,95126,00.html.**

UT Southwestern is an Equal Opportunity, Affirmative Action Employer.

POSITIONS OPEN

The Mind RESEARCH NETWORK
For Neurodiagnostic Discovery

SENIOR FACULTY/RESEARCH SCIENTIST
University of New Mexico
and The Mind Research Network

Up to three senior faculty positions available to lead the research at The Mind Research Network (MRN), Albuquerque, New Mexico, an independent research organization (**website: http://www.mrn.org**), with a joint appointment as a tenure-track faculty member either at the University of New Mexico or another institution in the United States. Significant startup fund and highly competitive salary from MRN. Strong external funding is prerequisite. Successful candidate should have expertise in one or more of the following areas: human brain development, schizophrenia, addiction, health psychology, and neuroinformatics, based on one or more of the following technologies: magnetic resonance imaging, magnetoencephalography, electroencephalography, neuropsychology, and genetics. To apply, please send curriculum vitae, a description of research and teaching interests, and three letters of recommendation to: **MRN, Attn: Human Resources/Chair of MRN/UNM Search Committee, 1101 Yale Boulevard N.E., Albuquerque, NM 87106-4188.** To send application materials electronically, use **e-mail: hr@mrn.org** with the subject Senior Faculty/Research Scientist. For questions, please contact the chair, **Dr. Kent Hutchison, e-mail: khutchison@mrn.org.** The committee will begin reviewing applications as they are received focused on a deadline. *Equal Opportunity Employer, Minorities/Females/Persons with Disabilities/Veterans.*

ASSISTANT PROFESSOR
Department of Biology/Neurosciences Program
The University of Scranton

The Biology Department and the interdisciplinary Neuroscience Program of The University of Scranton are seeking applications for a tenure-track position at the level of Assistant Professor, to begin in August 2010. We are especially interested in applicants with specializations that include, but are not limited to, neuroethology or evolutionary approaches to neurosciences. Applicants should be able to contribute to the Neuroscience Research Methods Lecture and Laboratory and to the Biology Department's core courses, and will have the opportunity to develop upper level courses in their specialty. A research program that involves mentorship of undergraduates is also expected. The Biology Department and Neuroscience Program will be housed in a new state-of-the-art unified science center as of fall 2011. Visit **websites: http://academic.scranton.edu/department/biology/** and **http://academic.scranton.edu/department/neuro/** for more information about the Biology Department and the Neuroscience Program. Ph.D. required by start date; postdoctoral experience preferred. Applications, including a cover letter, curriculum vitae, statements of teaching philosophy and research interests, selected reprints, and three letters of reference, should be sent to: **Dr. Robert Waldeck, Chair of Search Committee, Department of Biology, The University of Scranton, Scranton, PA 18510-4625.** Electronic submission of applications should be directed to **e-mail: waldeckr2@scranton.edu.** Review of applications will begin December 1, 2009, and will continue until the position is filled. The University of Scranton is a Catholic and Jesuit university. The University's mission statement may be found at **website: http://www.scranton.edu/mission.** *The University is committed to developing a diverse faculty, staff, and student body and to modeling an inclusive campus community. In keeping with this commitment, veterans, minority persons, women, and persons with disabilities are encouraged to apply. An Equal Opportunity/Affirmative Action Employer/Educator.*

POSITIONS OPEN

UT TYLER

The University of Texas at Tyler invites applications for the position of **CHAIR** of the Department of Biology to begin August 2010. Additional information is available at **website: http://www.uttyler.edu/biology/.**

The successful candidate will have a Ph.D. or equivalent research degree in one of the biological sciences, administrative and teaching experience, and a record of distinguished scholarly achievements and funded research appropriate for a tenured appointment.

Please electronically submit a letter of application, curriculum vitae, statements of research plans, teaching philosophy and leadership philosophy, and names and e-mail addresses of at least four references to **Dr. Sheldon Davis, e-mail: sdavis@uttyler.edu.**

Review of applications will begin immediately and continue until the position is filled. *Women and minorities are strongly encouraged to apply. Applicants must be prepared to furnish the university with proof of eligibility to work in the United States. UT Tyler is an Equal Employment Opportunity/Affirmative Action Employer. This position is security-sensitive and subject to Texas Education Code Section 51.215, which authorizes the employer to obtain criminal history record information.*

PHYSIOLOGIST

Applications are invited for a tenure-track **ASSISTANT PROFESSOR** position to begin August 2010. Teaching responsibilities will include undergraduate courses in human and animal physiology and an upper division class in area of expertise. Establishment of a funded research program involving M.S. graduate students and undergraduates is expected. Area of research in any branch of physiology will be considered. Postdoctoral experience preferred. Applicants should submit a letter of application, curriculum vitae, reprints, along with statements of research and teaching interests and should have three letters of recommendation sent by December 31, 2009, to: **Dr. Frank Paladino, Search Committee Chair, Department of Biology, Indiana-Purdue University Fort Wayne, 2101 Coliseum Boulevard, Fort Wayne, IN 46805-1499.** Or electronically to **e-mail: paladino@ipfw.edu. Website: http://www.ipfw.edu/bio/.** *Employment is contingent on a satisfactory background records history check. IPFW is an Affirmative Action/Equal Access Employer fully committed to a diverse work force.*

MARKETPLACE

Call for Papers

Science Signaling

Science Signaling, from the publisher of ***Science***, AAAS, features top-notch, peer-reviewed, original research weekly. Submit your manuscripts in the following areas of cellular regulation:

- Biochemistry
- Bioinformatics
- Cell Biology
- Development
- Immunology
- Microbiology
- Molecular Biology
- Neuroscience
- Pharmacology
- Physiology and Medicine
- Systems Biology

Science Signaling is indexed in CrossRef and MEDLINE.

Submit your research at:
www.sciencesignaling.org/about/help/research.dtl

Subscribing to the weekly ***Science Signaling*** ensures that you and your lab have the latest cell signaling resources. For more information visit **www.ScienceSignaling.org**

Science Signaling
AAAS